

AD-A181 802

DTIC FILE COPY

REPORT DOCUMENTATION PAGE

| | | | |
|---|--|---|--------------------------------|
| 1a. REPORT SECURITY CLASSIFICATION Unclassified | | 1d. RESTRICTIVE MARKINGS (2) | |
| 2a. SECURITY CLASSIFICATION AUTHORITY | | 3. DISTRIBUTION/AVAILABILITY OF REPORT Approved for public release, distribution unlimited | |
| 2b. DECLASSIFICATION/DOWNGRADING SCHEDULE | | | |
| 4. PERFORMING ORGANIZATION REPORT NUMBER(S) | | 5. MONITORING ORGANIZATION REPORT NUMBER(S) AFOSR TR. 87-0824 | |
| 6a. NAME OF PERFORMING ORGANIZATION Mechanical Engineering University of Florida | 6b. OFFICE SYMBOL (If applicable) | 7a. NAME OF MONITORING ORGANIZATION Air Force Office of Scientific Research /NA | |
| 6c. ADDRESS (City, State and ZIP Code) 237 MEB University of Florida Gainesville, FL 32611 | | 7b. ADDRESS (City, State and ZIP Code) AFOSR/NA, Bldg 410 BOLLING AFB DC 20332-6448 | |
| 8a. NAME OF FUNDING/SPONSORING ORGANIZATION Air Force Office of Scientific Research | 8b. OFFICE SYMBOL (If applicable) AFOSR/NA | 9. PROCUREMENT INSTRUMENT IDENTIFICATION NUMBER AFOSR Grant 85-0113 | |
| 8c. ADDRESS (City, State and ZIP Code) Building 410 Bolling AFB, DC 20332-6448 | | 10. SOURCE OF FUNDING NOS. | |
| | | PROGRAM ELEMENT NO. 61102F | PROJECT NO. 2308 |
| | | TASK NO. A1 | WORK UNIT NO. |
| 11. TITLE (Include Security Classification) High Speed Flow in Tubes | | | |
| 12. PERSONAL AUTHOR(S) Elmer Hansen and Tom I-P. Shih | | | |
| 13a. TYPE OF REPORT Final | 13b. TIME COVERED FROM 2-85 TO 2-87 | 14. DATE OF REPORT (Yr., Mo., Day) 1987, April 14 | 15. PAGE COUNT 273 |
| 16. SUPPLEMENTARY NOTATION | | | |
| 17. COSATI CODES | | 18. SUBJECT TERMS (Continue on reverse if necessary and identify by block number) | |
| FIELD | GROUP | SUB-GR. | |
| | | Interior Ballistics | |
| | | Gas Gradients | |
| | | Unsteady Boundary Layers | |
| 19. ABSTRACT (Continue on reverse if necessary and identify by block number) Four interior ballistic models were developed for analyzing the flow field inside tubes that launch high-speed projectiles. The first model was developed for analyzing inviscid interior ballistic flow; The second model was developed for analyzing the unsteady, two-dimensional, momentum and thermal wall boundary layers in ballistic devices. The third model was developed for analyzing viscous interior ballistic flow; Finally, the fourth model is an analytical model that predicts the density and pressure variation between the breech and the base of the projectile. Results obtained were compared with experimental data. Results indicated that the following parameters have significant effects on the interior ballistic flow: covolume of the gas; cross-sectional area changes as a function of axial distance; relative velocity between the propellant grains and the combustion gas; ratio of the specific heats as a function of local temperature; the effects of friction and the heat transfer in the boundary layer; propellant burning rate as a function of local pressure. The effect of heat transfer was to (and) | | | |
| 20. DISTRIBUTION/AVAILABILITY OF ABSTRACT UNCLASSIFIED/UNLIMITED <input checked="" type="checkbox"/> SAME AS PRT. <input type="checkbox"/> DTIC USERS <input type="checkbox"/> | | 21. ABSTRACT SECURITY CLASSIFICATION Unclassified | |
| 22a. NAME OF RESPONSIBLE INDIVIDUAL Dr. Julian M. Tishkoff | | 22b. TELEPHONE NUMBER (Include Area Code) 202-767-4935 | 22c. OFFICE SYMBOL AFOSR/NA |

UNCLASSIFIED

SECURITY CLASSIFICATION OF THIS PAGE

AFOSR-TR- 87-0824

produce a significant (9+%) effective barrel volume increase. The down bore pressure and density gradients were found to be governed by the projectile acceleration and the length from breech to projectile. *Keywords: Interior ballistics; Gas gradients;*

*Unsteady boundary layers; Boundary layer flow;
Viscous flow; Gun barrels; Gun propellants;*

(10/1/87)

| | |
|--------------------|--|
| Accession For | |
| NIIS CRM&I | <input checked="checked" type="checkbox"/> |
| DTIC TAB | <input type="checkbox"/> |
| Unannounced | <input type="checkbox"/> |
| Justification | |
| By | |
| Distribution/ | |
| Availability Codes | |
| Avail and/or | |
| Dist | Special |
| A1 | |



UNCLASSIFIED

SECURITY CLASSIFICATION OF THIS PAGE

UNIVERSITY OF FLORIDA



High Speed Flow in Tubes

AFOSR Grant 85-0113

Elmer Hansen and Tom I-P. Shih

April 14, 1987

This technical information
approved for public release.
Distribution is unlimited.
MATTHEW J. KERPER
Chief, Technical Information Division

Computational Fluid Dynamics Laboratory

DEPARTMENT OF MECHANICAL ENGINEERING

Gainesville, Florida 32611

DTIC
ELECTE
JUL 06 1987
S A D

This document has been approved
for public release and sale; its
distribution is unlimited.

2
AFOSR-TR. 87-0824

Approved for public release;
distribution unlimited.

High Speed Flow in Tubes

AFOSR Grant 85-0113

Elmer Hansen and Tom I-P. Shih

April 14, 1987

AIR FORCE OFFICE OF SCIENTIFIC RESEARCH (AFSC)
NOTICE OF TRANSMITTAL TO DTIC
This technical report has been reviewed and is
approved for public release IAW AFR 190-12.
Distribution is unlimited.
MATTHEW J. KERPER
Chief, Technical Information Division

DTIC
SELECTED
JUL 6 1987

87 7 1 095

TABLE OF CONTENTS

Nomenclature

1. Introduction

- 1.1 Background
- 1.2 Objectives
- 1.3 Literature Survey
- 1.4 Overview of Report

2. Inviscid Flows inside Tubes

- 2.1 Introduction
- 2.2 Description of Problem
- 2.3 Formulation of Problem
- 2.4 Numerical Method of Solution
- 2.4 Results

3. Boundary Layer Flows inside Tubes

- 3.1 Introduction
- 3.2 Description of Problem
- 3.3 formulation of Problem
- 3.4 Numerical Method of Solution
- 3.5 Results

4. Viscous Flows inside Tubes

- 4.1 Introduction
- 4.2 Description of Problem
- 4.3 Formulation of Problem
- 4.4 Numerical Method of Solution
- 4.5 Results

5. Analytical Model of Pressure and Density Gradients

- 5.1 Physical Mechanisms Causing Pressure and Density Gradients
- 5.2 Equations of Motion for Unsteady Flows
- 5.3 Comparisons of Analytical Model with Experimental Data

6. Summary of Accomplishments

Acknowledgements

References

- Appendix A Governing Equations for Inviscid and Viscous
 Flows inside Tubes and Numerical Method of Solution
- Appendix B Boundary Layer Equations and Numerical Method of
 Solution
- Appendix C Simplified Analysis of Pressure and Density Gradients

NOMENCLATURE

| | |
|---------------|--|
| a | - $\partial A / \partial \xi$ |
| a_g | - acceleration of the combustion gases |
| \bar{a}_g | - acceleration of the combustion gases averaged over the distance L_p |
| a_p | - acceleration of projectile |
| a_s | - acceleration of propellant grain |
| \bar{a}_s | - average acceleration of propellant grain |
| a_p^* | - adjusted acceleration |
| A | - tube cross sectional area at a given axial location |
| A_b | - propellant burning surface area per unit volume |
| A_p | - cross sectional area of projectile |
| A^+ | - damping constant |
| CD_1 | - (propellant grain) / (combustion gas) velocity ratio |
| C_1 | - outer mixing length constant |
| C_D | - coefficient of drag of cylindrical propellant grain |
| C_{ps} | - propellant grain specific heat capacity |
| d_i | - propellant grain perforate diameter |
| D | - propellant grain drag force |
| e | - combustion gas energy averaged over tube cross section |
| f | - friction factor |
| Fa | - acceleration number |
| F_{net} | - net force acting on a control volume within the tube |
| F_{pnet} | - net force acting on the projectile |
| h | - combustion gas static enthalpy |
| h_c | - combustion gas convective coefficient |
| h_o | - combustion gas enthalpy at $T=300K$ |
| h_{sg} | - specific energy release |
| H | - combustion gas stagnation enthalpy |
| H_1 | - combustion gas static enthalpy |
| k | - conductivity |
| $k_{pu\xi}$ | - $\partial k_{pu} / \partial \xi$ |
| $k_{pu\tau}$ | - $\partial k_{pu} / \partial \tau$ |
| $k_{pu^2\xi}$ | - $\partial k_{pu^2} / \partial \xi$ |
| $k_{eu\xi}$ | - $\partial k_{eu} / \partial \xi$ |
| K | - Von Karman constant |
| K_1 | - nondimensional density ratio |
| K_2 | - nondimensional length acceleration |
| K_{pu} | - density flux K factor |

K_{pu}^2 - momentum flux K factor
 K_{eu} - energy flux K factor
 l - length of a propellant grain
 l_o - Prandtl mixing length, inner region
 l_i - Prandtl mixing length, outer region
 l_{pr} - Prandtl mixing length
 L - distance x between breech and projectile
 L_f - distance from breech to open end of tube
 L_p - distance between breech and projectile
 L_s - distance between breech and propellant grain nearest projectile
 m_{mass} - molar mass of combustion gas
 m_c - propellant mass
 m_p - mass of projectile
 M - mach number of projectile relative to atmosphere
 \dot{M}_s - volumetric rate of propellant consumption
 n_v - number of propellant grains per unit volume
 P - pressure
 Pr - Prandtl number
 P_{atm} - external (atmospheric) air pressure
 P_{ave} - average chamber pressure
 P_{cr} - pressure at which projectile motion begins
 P_f - "frontal" pressure, external pressure acting on front of projectile
 P_{pb} - pressure acting on base of projectile
 q_w - tube wall heat flux
 r - radial coordinate, distance from centerline
 \bar{r} - time averaged radius of a propellant grain
 r_b - propellant linear burning speed
 r_i - inner (perforate) radius of propellant grain
 r_o - outer radius of propellant grain
 R - tube radius
 Re_D - Reynolds number of combustion gases based on tube diameter
 R_{atm} - gas constant for air
 R_{cg} - gas constant for the combustion gases
 t - time
 T - temperature
 \bar{T} - combustion gas temperature averaged over tube cross sectional area
 T_{atm} - external (atmospheric) air temperature
 T_{ig} - ignition temperature of propellant
 T_{init} - initial temperature of propellant
 T_w - tube wall boundary temperature

| | |
|-------------|---|
| \bar{u} | - combustion gas velocity averaged over tube cross sectional area |
| \hat{u} | - combustion gas internal energy |
| \hat{u}_0 | - combustion gas internal energy at $T=300K$ |
| u | - velocity of gas |
| u_s | - propellant grain velocity |
| $u_s \xi$ | - $\partial u_s / \partial \xi$ |
| u_p | - velocity of projectile |
| U | - calculation velocity |
| \hat{U} | - predicted calculation velocity |
| U_p | - velocity of projectile |
| U_s | - velocity of propellant grain closest to projectile |
| v | - radial velocity |
| w | - propellant grain web thickness |
| x | - dimensional coordinate |
| y | - radial coordinate, distance from wall |
| Y^+ | - turbulent viscosity parameter |

Greek

| | |
|---------------|---|
| α | - diffusivity |
| δ | - kinetic energy of mass of gas at u_p / kinetic energy of gas |
| δ_q | - heat penetration length |
| δ_v | - velocity boundary layer thickness |
| δ_1 | - displacement thickness for compressible flow in tubes |
| δ_2 | - momentum thickness for compressible flow in tubes |
| δ_3 | - energy thickness for compressible flow in tubes |
| δ_ρ | - density thickness for compressible flow in tubes |
| δ_T | - temperature boundary layer thickness |
| γ | - specific heat ratio C_p/C_v |
| ζ | - radial coordinate, distance from wall |
| η | - covolume |
| λ | - nondimensional coordinate, from projectile to breech |
| μ | - absolute (or dynamic) viscosity |
| ξ | - nondimensional distance, from breech to projectile |
| π | - nondimensional constant, 3.14159 |
| ρ | - density of gas |
| $\bar{\rho}$ | - combustion gas density averaged over tube cross section |

ρ_m - average density
 ρ_{m1} - density times velocity average
 ρ_{m2} - density times velocity squared average
 ρ_s - propellant grain density
 ρ_s' - density of a grain including gas within perforation
 τ - time in transformed domain
 τ_w - tube wall shear stress
 u - (propellant grain cross sectional area)
 /(tube cross sectional area)
 u' - porosity: (volume of gas)/(total volume)

Subscripts

atm - atmosphere
 b - breech
 CIL - CIL 3331 combustion gas
 CO - carbon monoxide gas
 CO₂ - carbon dioxide gas
 e - boundary layer edge
 H₂ - hydrogen gas
 H₂O - water vapor
 i - axial grid location for gas coordinate system
 i* - axial grid location for propellant grain coordinate system
 j - radial grid location
 p - piston
 N₂ - nitrogen gas
 st - steel
 T - turbulent
 w - tube wall
 x - position x
 ξ - position ξ
 \emptyset - initial

Superscripts

n - current time level
 $\bar{n}+1$ - predictor time level
 n+1 - next time level

Chapter 1

INTRODUCTION

1.1 Background

The unsteady, compressible flow inside tubes that launch high-speed projectiles (e.g., ballistic devices) is complex. For a tube with geometry similar to that shown in Fig. 1.1, the flow is initiated when propellant grains within the region bounded by the breech, tube wall, and projectile ignites, causing pressure to rise. Once the pressure exceeds some critical value, the projectile starts to accelerate, moving away from the breech towards the open end of the tube.

The motion of the projectile causes the formation of momentum and thermal boundary layers next to the tube wall and a series of expansion waves at the base of the projectile. The expansion waves formed at the base of the projectile first propagate towards the breech, but later reflect between the breech and the base of the projectile. These expansion waves accelerate the combustion gas and propellant grains behind the projectile. As the projectile travels towards the open end of the tube, the speed of the projectile increases and variations in velocity, density, temperature, and pressure from the breech to the base of the projectile become more pronounced.

In order to design high-performance ballistic devices, it is necessary to have a good understanding of the physics taking place inside tubes that launch high-speed projectiles. The objective of this investigation is to provide such an understanding by constructing an interior ballistic model based on fundamental principles.

In the next section, the detailed objectives of this investigation along with the approach used to meet the objectives are described. Afterwards in Section 1.3, a brief literature survey is given. Finally in Section 1.4, an outline of this report is given to guide the reader.

1.2 Objectives and Approach

The major objectives of this investigation are to

1. Study how velocity, density, temperature, and pressure vary both temporally and axially inside tubes that launch high-speed projectiles.
2. Explain the underlying physics affecting how velocity, density, temperature, and pressure vary along the tube (e.g., the effects of the momentum and thermal boundary layers).
3. Explain how ballistic design parameters (e.g., geometry of tube) affect the performance (i.e., muzzle speed and peak pressure) of ballistic devices.

The approach employed to meet the objectives of this investigation was as follows: first develop a simple but physically meaningful interior ballistic model and later modify that model by adding more physics to create a more comprehensive model. The first interior ballistic model developed was based on equations valid for one-

dimensional, inviscid flows with mass generation. Later, that model was extended by adding viscous and heat transfer effects in order to study the effects of the thermal and momentum boundary layers on the flow.

Both of the interior ballistic models developed in this investigation were based on the conservation equations of mass, momentum, and energy. Since the dominating physics occur along the axial direction of the tube and not along the radial or azimuthal directions, the conservation equations were integrated analytically in the radial and azimuthal directions to facilitate analysis (see Fig. 1.1). For the interior ballistic model involving viscous and thermally-conducting fluids, the effects of the momentum and thermal boundary layers next to the tube wall were accounted for by parameters (referred to as K factors) describing the variation of velocity, temperature, and density in the radial direction. The K factors were determined by boundary-layer equations for unsteady compressible flows.

In the next section, a review is given of the different types of interior ballistic models used for studying physics inside tubes that launch high-speed projectiles.

1.3 Literature Survey

Interior ballistic models describing the physics inside tubes that launch high-speed projectiles (such as ballistics devices) can be classified into five types:

1. Empirical Models
2. Quasi One-Dimensional Models

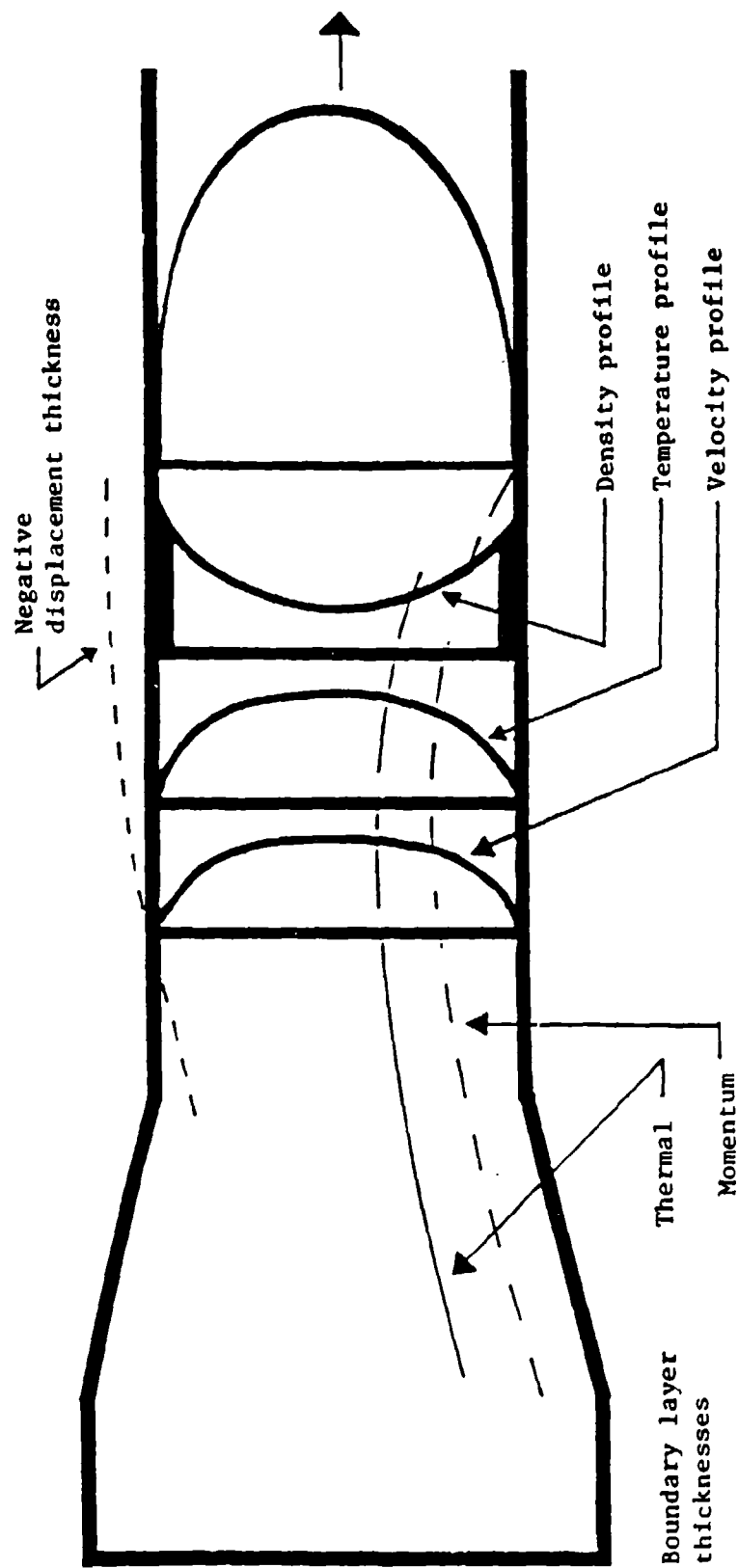


Figure 1.1

High speed flow inside tubes that launch high speed projectiles.

3. One-Dimensional Models

4. Quasi Multi-Dimensional Models

5. Multi-Dimensional Models

Below, each of the above five types of interior ballistic models are described.

Empirical Models

Empirical models are constructed by fitting curves through extensive amounts of experimental data obtained from a variety of different ballistic devices and propellants. Examples of empirical models are described in Refs. 1 - 5.

Though empirical models have their merits and uses, they cannot do two things. First, they cannot predict the physics inside ballistic devices for which experimental data do not exist. Second, even for problems in which there is adequate experimental data, empirical models cannot explain the underlying physics controlling the ballistic devices.

Quasi One-Dimensional Models (Also known as Lumped-Parameter Models)

Quasi one-dimensional (1-D) models are based on simplified versions of the conservation equations of mass, momentum and energy valid for 1-D, unsteady flows. Such models are referred to as quasi 1-D instead of 1-D because one or more flow variables such as density or pressure are assumed to depend only on time and not on position along the tube so that only some of the 1-D effects are accounted for.

Quasi 1-D models still require a number of empirical inputs. Most of these models require empirical models for the rate at which propellants burn, heat transfer rate from the walls, shear stress at the walls, gas velocity as a function of time and position along the tube, and gas pressure as a function of position along the tube. Velocity and pressure variations are often modelled as isentropic processes with empirical correction factors. Propellant burn rates are typically modelled by empirical relations relating the burn rate to the gas pressure and surface area of the propellants.

Quasi 1-D models vary considerably in complexity. These models range from relatively simple models which can only account for the effects of a few ballistic parameters to very complex models that can account for a large number of ballistic parameters. Examples of quasi 1-D models are given in Refs. 5 - 21.

Since quasi 1-D models are based on the conservation equations, these models have a wider range of applicability than empirical models. Specifically, these models can be applied to analyze ballistic devices for which experimental data are not available and can reveal some of the underlying physics controlling the ballistic devices.

Here, it should be noted that since (1) empirical inputs are still needed and (2) some 1-D effects and all of the two- and three-dimensional effects are not accounted for, there are still a number of physics that cannot be adequately accounted for by quasi 1-D models.

One-Dimensional Models

A type of model one step more complex than the quasi 1-D models is the 1-D model. The 1-D models are based on the conservation equations of mass, momentum, and energy valid for 1-D, unsteady flows.

Unlike the quasi 1-D models, 1-D models do not require empirical inputs for the variations of velocity and pressure along the tube. 1-D models can calculate velocity and pressure variations based on the conservation principles. As a result, 1-D models can be applied to study physics such as pressure waves.

Similar to quasi 1-D models, 1-D models still need empirical input regarding propellant burn rates, heat transfer rate from the walls, and shear stress at the walls. Thus, there are still situations in which a 1-D model may be inadequate.

Examples of 1-D models are given in Refs. 22 - 25.

Quasi Multi-Dimensional Models

Since the flow inside ballistic devices is primarily in the axial direction along the tube, it is reasonable to assume 1-D flow. However, by assuming 1-D flow the following empirical data must be supplied: the heat transfer rate from the walls, the shear stress at the walls, and the effects of the momentum and thermal boundary layers next to the walls on the inviscid flow (core flow).

One way to eliminate the need for empirical data for heat transfer and shear stress at the walls and still retain the simplicity of 1-D models is to construct quasi multi-dimensional models.

Quasi multi-dimensional models are models that can account for all of the 1-D effects as well as some (but not all) of the two- and three-

dimensional (2- and 3-D) effects. Quasi multi-dimensional models are derived from the conservation equations of mass, momentum, and energy valid for 2- or 3-D, unsteady flows by neglecting variations of certain flow variables along certain directions or by integrating the conservation equations along certain directions.

Gough [Refs. 26 and 27] has developed quasi 2-D models for analyzing burning of propellants. The authors of this report know of no investigators who have developed quasi multi-dimensional models to describe the flowfield between the breech and the base of the projectile taking into account the effects of the momentum and thermal boundary layers next to the tube wall. As mentioned in the previous section, such a model was developed in this study.

Multi-Dimensional Models

Multi-dimensional models are based on the conservation equations of mass, momentum, and energy for 2-D or 3-D, unsteady flows. Such models have the potential to describe completely the physics inside ballistic devices. However, at the present time existing computers prohibit the direct simulation of turbulence, detailed dynamics of the interaction between gas and solid propellants, and detailed chemical kinetics of propellant combustion.

In view of the limited understanding of inter-phase drag and two-phase turbulent transport properties (among others), the authors of this report believe that multi-dimensional models are not warranted at this time (i.e., quasi multi-dimensional models should be sufficient).

1.4 Outline of Report

To guide the reader in reading this report, a description of how this report is written is given here.

In Chapter 2, the details of an interior ballistic model developed for analyzing inviscid flows inside tubes that launch high-speed projectiles are presented. In Chapter 3, the mathematical model constructed for studying the unsteady, momentum and thermal boundary layers next to the tube wall are presented. In Chapter 4, the quasi multi-dimensional model developed for studying viscous flows inside tubes that launch high-speed projectiles are presented. In Chapter 5, a simple model is constructed for predicting how pressure and density vary from the breech to the base of the projectile. Finally, in Chapter 6, a summary is given of the important discoveries and contributions made.

Chapter 2

INVISCID FLOWS INSIDE TUBES

2.1 Introduction

In this chapter, an interior ballistic model for analyzing inviscid flow inside tubes that launch high-speed projectiles is described. The interior ballistic model is based on the conservation equations of mass, momentum and energy valid for one-dimensional, unsteady, compressible flow of an inviscid and thermally-nonconducting fluid with mass generation.

Previous investigators have developed interior ballistic models similar to the one presented in this chapter [Refs. 20-24]. The interior ballistic model presented in this chapter differs from the interior ballistic models described in Refs. 20-24 in the governing equations, in the numerical method of solution, and in the way in which boundary conditions were implemented.

In the next section, the problem of inviscid flow inside tubes is described in detail. Afterwards, in Section 2.3, the equations governing inviscid flow inside tubes are described. In Section 2.4, the numerical method used to obtain solutions is explained. (The combination of governing equations and numerical method of solution is referred to as the interior ballistic model.) In Section 2.5, the results generated by the interior ballistic model are presented.

2.2 Description of Problem

A schematic diagram of a typical tube assembly studied in this investigation is shown in Fig. 2.1. The tube assembly consists of a projectile and a tube that is closed at one end (the breech).

The region between the breech and the projectile initially contains a homogeneous mixture of solid propellant and inviscid combustion gas at a pressure of 3.45×10^6 Pa (500 psia) and temperature of 300 K. The exterior of the tube assembly is exposed to air maintained at a pressure of 1×10^5 Pa (14.7 psia) and a temperature of 300 K.

Two other tube assemblies (operating under identical conditions) are shown in Figs. 2.2 and 2.3. All three tube assemblies have the same initial interior volume and the same radius at the open end of the tube. Tables 2.1-2.3 present the equations and parameters needed to specify the geometry of the tube assemblies.

The physical process which takes place within a tube assembly proceeds as follows: at time $t=0$, combustion begins and the pressure, temperature and density of the combustion gas rapidly increase. After the pressure has exceeded a critical (starting) pressure P_{cr} , the projectile is free to move without sliding friction. The pressure difference across the projectile then causes it to accelerate and move away from the breech. The process is considered to have ended when the projectile exits the tube.

For the inviscid interior ballistic problem, we are interested in evaluating the influence of various parameters on gun performance. Table 2.4 shows a list of parameters necessary to specify the problem. Equations, equation numbers, and values for these parameters are presented in Tables 2.1-2.3 and in Tables 2.5-2.6 (see Section 2.5).

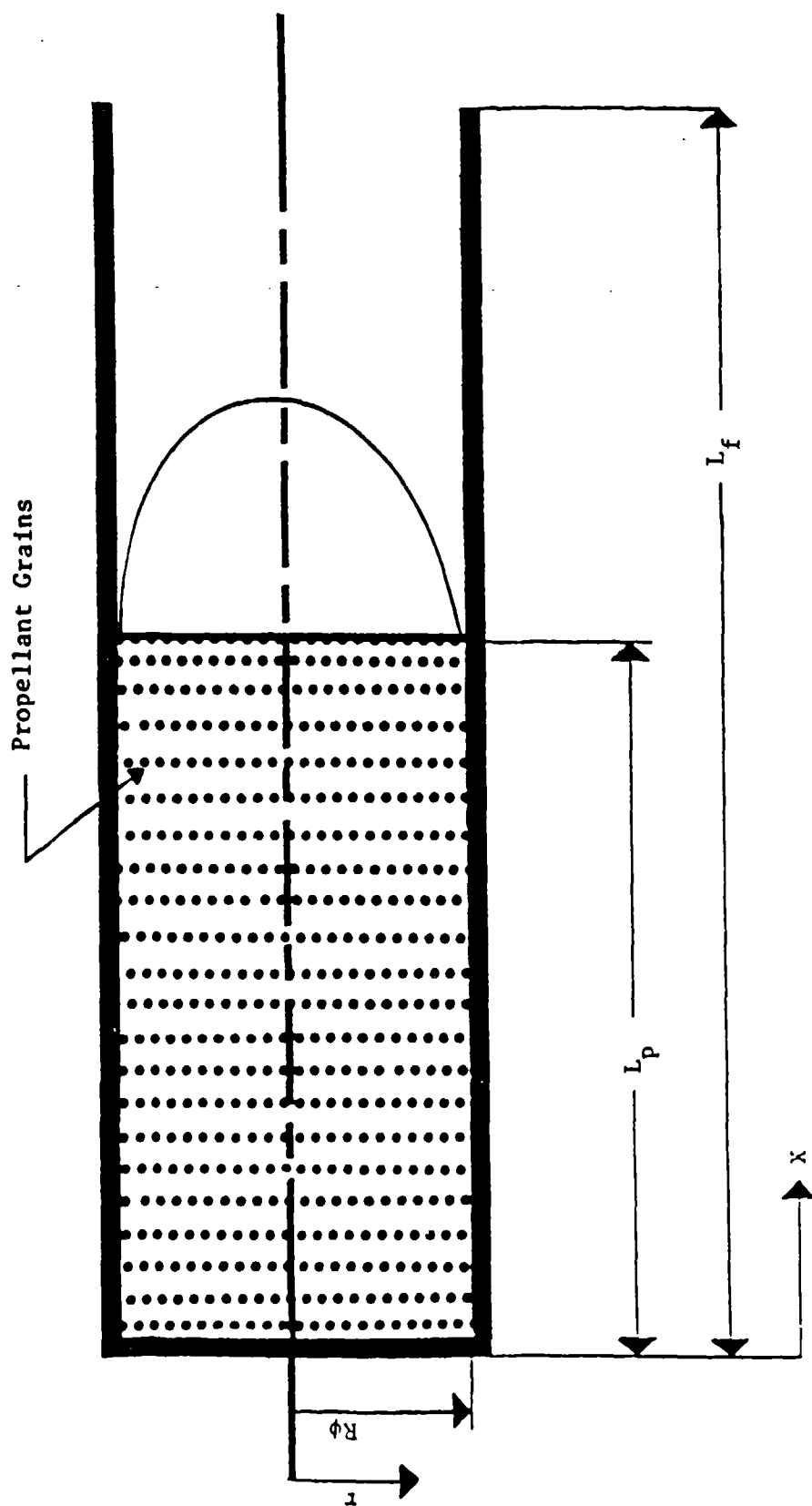


Figure 2.1

A tube assembly of constant radius.

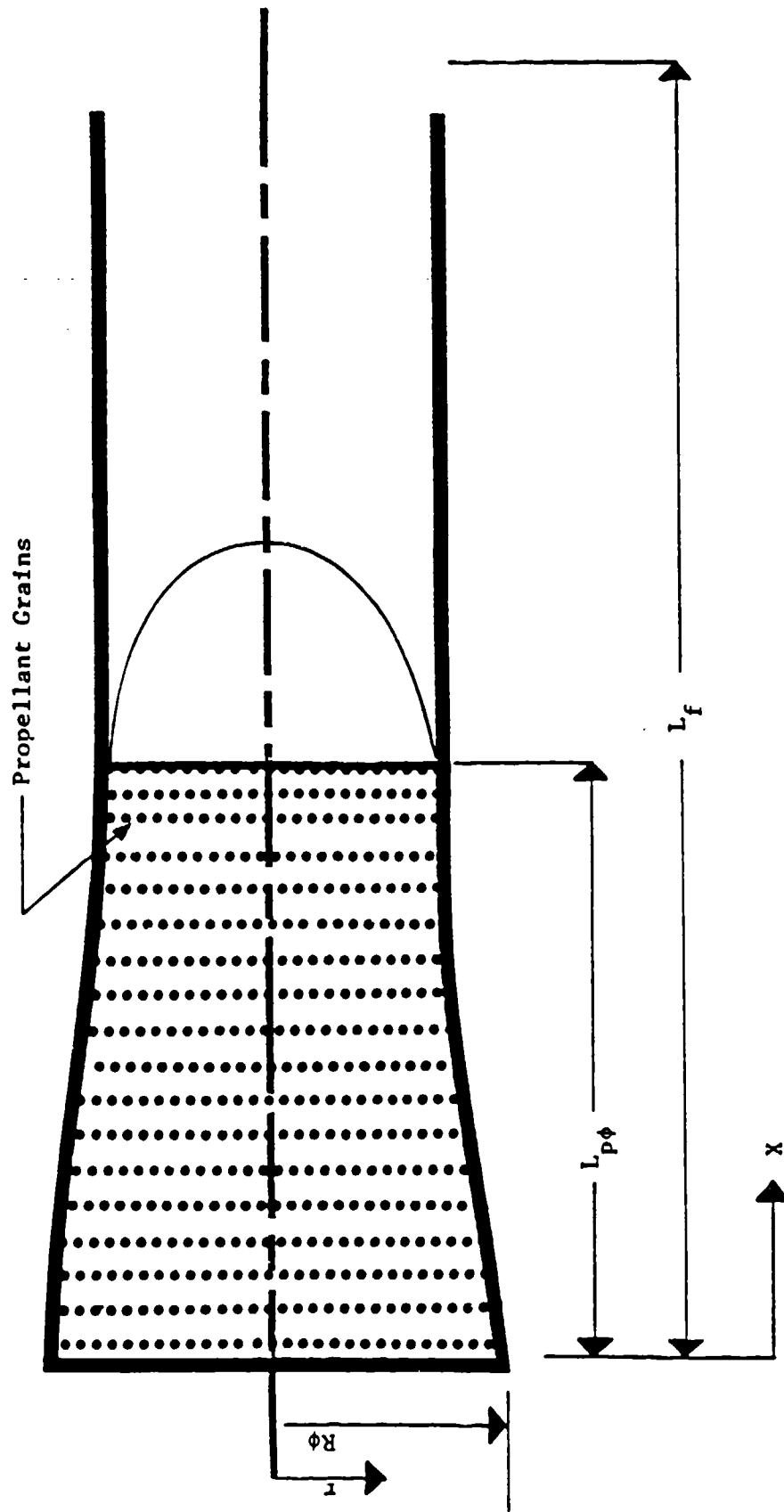


Figure 2.2

A tube assembly whose radius varies smoothly over the initial projectile displacement ($L_{p\phi}$) and then becomes constant.

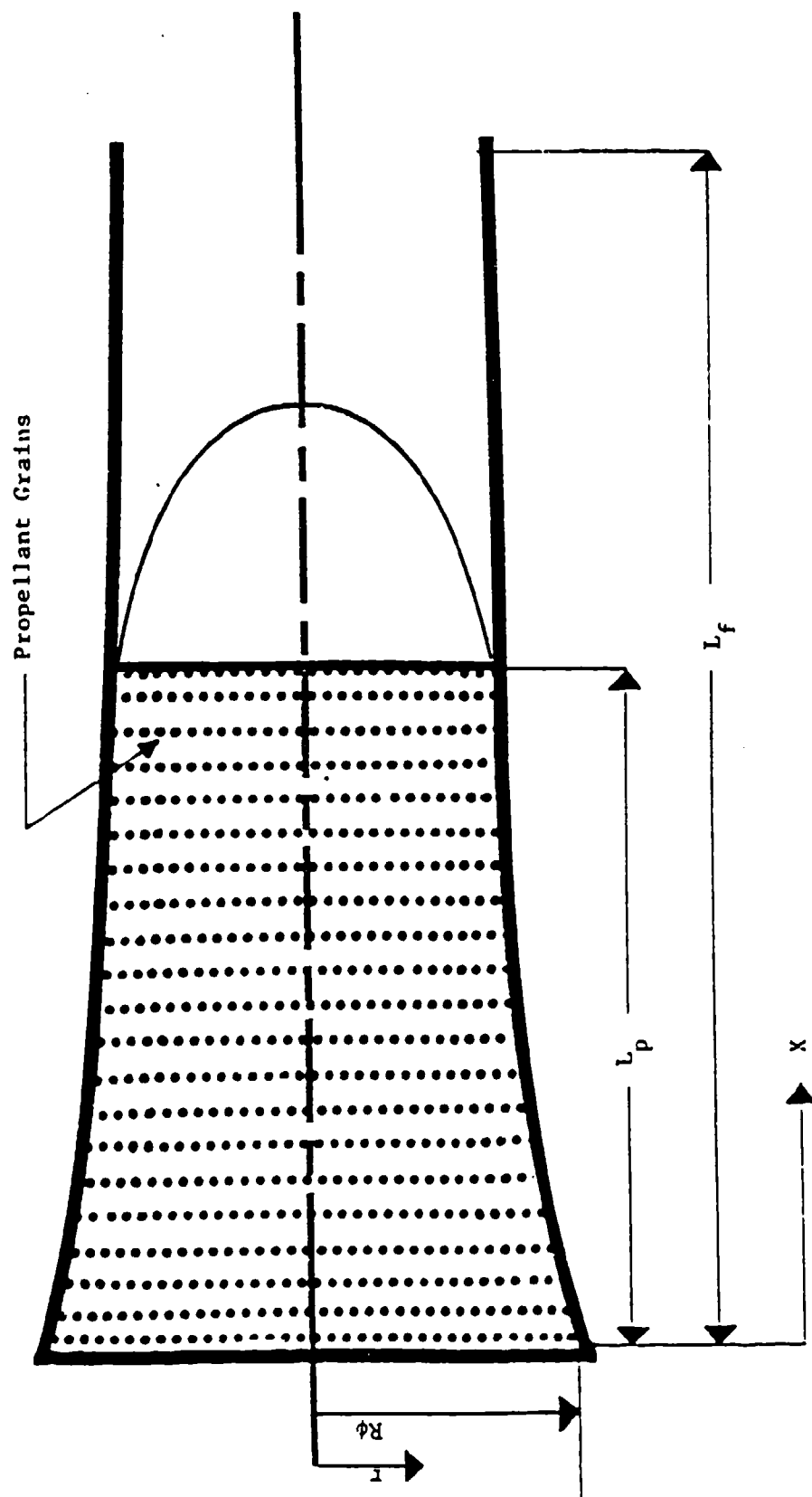


Figure 2.3

A tube assembly whose radius varies smoothly over the tube assembly length (L_f).

Table 2.1

Equations describing geometry of the tube assembly shown in Figure 2.1

| Equation | Eq. No. |
|--|---------|
| $R(0 \leq x \leq L_f) = R_\phi$ | (2.1) |
| $A(0 \leq x \leq L_f) = \pi R_\phi^2$ | (2.2) |
| $\frac{\partial A(0 \leq x \leq L_f)}{\partial x} = 0$ | (2.3) |

R_ϕ (the tube radius at $x=0$) = 0.0150 m, $L_{p\phi}$ (the initial distance from the breech to the projectile) = 0.2202 m, and L_f (the distance from the breech to the open end of the tube) = 2.1920 m.

Table 2.2

Equations describing geometry of the tube assembly shown in Figure 2.2

| Equation | Eq. No. |
|---|---------|
| $R(0 \leq x \leq L_{p\phi}) = R_{\phi} \left[0.25 \left(\frac{x}{L_{p\phi}} \right)^2 - 0.5 \left(\frac{x}{L_{p\phi}} \right) + 1 \right]$ | (2.4) |
| $R(L_{p\phi} \leq x \leq L_f) = R_{\phi}$ | (2.5) |
| $A(0 \leq x \leq L_{p\phi}) = \pi R_{\phi}^2 \left[0.0625 \left(\frac{x}{L_{p\phi}} \right)^4 - 0.25 \left(\frac{x}{L_{p\phi}} \right)^3 + 0.75 \left(\frac{x}{L_{p\phi}} \right)^2 - \left(\frac{x}{L_{p\phi}} \right) + 1 \right]$ | (2.6) |
| $A(L_{p\phi} \leq x \leq L_f) = \pi R_{\phi}^2$ | (2.7) |
| $\frac{\partial A(0 \leq x \leq L_{p\phi})}{\partial x} = \frac{\pi R_{\phi}^2}{L_{p\phi}} \left[0.25 \left(\frac{x}{L_{p\phi}} \right)^3 - 0.75 \left(\frac{x}{L_{p\phi}} \right)^2 + 1.5 \left(\frac{x}{L_{p\phi}} \right) - 1 \right]$ | (2.8) |
| $\frac{\partial A(L_{p\phi} \leq x \leq L_f)}{\partial x} = 0$ | (2.9) |

R_{ϕ} (the tube radius at $x=0$) = 0.0200 m, $L_{p\phi}$ (the initial distance from the breech to the projectile) = 0.1770 m, and L_f (the distance from the breech to the open end of the tube) = 2.1488 m.

Table 2.3

Equations describing geometry of the tube assembly shown in Figure 2.3

| Equation | Eq. No. |
|--|---------|
| $R(0 \leq x \leq L_f) = R_0 \left[0.25 \left(\frac{x}{L_f} \right)^2 - 0.5 \left(\frac{x}{L_f} \right) + 1 \right]$ | (2.10) |
| $A(0 \leq x \leq L_f) = \pi R_0^2 \left[0.0625 \left(\frac{x}{L_f} \right)^4 - 0.25 \left(\frac{x}{L_f} \right)^3 + 0.75 \left(\frac{x}{L_f} \right)^2 - \left(\frac{x}{L_f} \right) + 1 \right]$ | (2.11) |
| $\frac{\partial A(0 \leq x \leq L_f)}{\partial x} = \frac{\pi R_0^2}{L_f} \left[0.25 \left(\frac{x}{L_f} \right)^3 - 0.75 \left(\frac{x}{L_f} \right)^2 + 1.5 \left(\frac{x}{L_f} \right) - 1 \right]$ | (2.12) |

R_0 (the tube radius at $x=0$) = 0.0150 m, L_{p0} (the initial distance from the breech to the projectile) = 0.1276 m, and L_f (the distance from the breech to the open end of the tube) = 2.0994 m.

Table 2.4

Parameters needed to specify the inviscid interior ballistic problem

| <u>Tube Geometry Parameters</u> | <u>Propellant Parameters</u> |
|--|--|
| *radius (R) | *type |
| *cross-sectional area (A) | *grain geometry |
| *initial breech-to-projectile axial distance (L_{p0}) | *initial mass (m_{c0}) |
| *axial distance from the breech to the open end of the tube (L_f) | *covolume (η) |
| | *density (ρ_s) |
| | *initial web thickness (w_0) |
| | *specific heat capacity (C_{ps}) |
| | *initial temperature (T_{init}) |
| | *ignition temperature (T_{ig}) |
| | *linear burning speed (r_b) |
| | *specific energy release (h_{sg}) |
| | *initial velocity (u_{s0}) |
| | *propellant grain-combustion gas velocity ration (CD_1) |
| | *drag coefficient (C_D) |
| | *initial axial distance between the breech and most remote propellant grain (L_{s0}) |
| <u>Projectile Parameters</u> | |
| *mass (m_p) | |
| *initial velocity (U_{p0}) | |
| *pressure at which projectile motion begins (P_{cr}) | |
| <u>Air Parameters</u> | |
| *Temperature (T_{atm}) | |
| *Pressure (P_{atm}) | |
| *Specific heat ratio (γ_{atm}) | |
| *Gas constant (R_{atm}) | |
| <u>Combustion Gas Parameters</u> | |
| *molar mass (mmass) | |
| *initial temperature (T_0) | |
| *initial pressure (P_0) | |
| *initial velocity (U_0) | |

2.3 Formulation of Problem

Introduction

This section presents the assumptions and the governing equations used to describe the inviscid interior ballistic problem. The governing equations have been classified into the following three groups:

1. Conservation Equations - the set of coupled 1st order partial differential equations which describe the conservation of mass, momentum and energy.
2. Constitutive Equations - a group of equations which describe dependencies between two or more variables in the conservation equations.
3. Auxiliary Equations - a group of equations resulting from models developed for terms in either the conservation equations or the constitutive equations.

In this section, the conservation equations governing this problem are presented first. Afterwards the constitutive and auxiliary equations for this problem are presented. Here, it is noted that only the final forms of these equations are presented. The derivation of these equations are given in this section or in Appendix A.

Conservation Equations

The following assumptions were made to facilitate the derivation of the conservation equations for the inviscid interior ballistic problem:

- 1) The problem is unsteady and one-dimensional in the axial direction.
- 2) The propellant grains can be treated as a continuum.
- 3) The propellant grains are incompressible.
- 4) The propellant grains are distributed homogeneously across the cross-sectional area of the tube at any axial location.
- 5) There is no interaction between the propellant grains and the tube wall.
- 6) There is no heat transfer.
- 7) The combustion gas is an inviscid fluid.

With these assumptions, the inviscid conservation equations can be written as follows (see Appendix A for derivation):

Continuity of Propellant Grains

$$\frac{\partial v}{\partial t} = -v \frac{\partial u_s}{\partial x} - u_s \frac{\partial v}{\partial x} - \frac{u_s}{A} - \dot{M}_s \frac{v}{\rho_s} \quad (2.13)$$

Continuity of Combustion Gas

$$\begin{aligned} \frac{\partial \bar{\rho}}{\partial t} = & \frac{\bar{\rho} \bar{u}}{A} \frac{\partial A}{\partial x} - \frac{\partial (\bar{\rho} \bar{u})}{\partial x} + \left(\frac{v}{1-v} \right) \dot{M}_s \left(1 - \bar{\rho} / \rho_s \right) \\ & + \frac{\bar{\rho}}{(1-v)} \left[(\bar{u} - u_s) \frac{\partial v}{\partial x} - v \left(\frac{\partial u_s}{\partial x} + \frac{u_s}{A} \frac{\partial A}{\partial x} \right) \right] \end{aligned} \quad (2.14)$$

Conservation of Momentum for the Combustion Gas

$$\begin{aligned} \frac{\partial(\bar{\rho}\bar{u})}{\partial t} = & - \frac{\partial(\bar{\rho}\bar{u}^2)}{\partial x} + [\bar{\rho}\bar{u}(\bar{u}-u_s) + P] \frac{\partial v}{\partial x} - \frac{\partial P}{\partial x} \\ & - \bar{\rho}\bar{u} \left\{ \frac{[\bar{u} + (\frac{v}{1-v})u_s]}{A} \frac{\partial A}{\partial x} + (\frac{v}{1-v}) \left[\frac{\partial u_s}{\partial x} + \frac{\dot{M}_s}{\rho_s} \right] \right\} \end{aligned} \quad (2.15)$$

Conservation of Energy for the Combustion Gas

$$\begin{aligned} \frac{\partial \bar{e}}{\partial t} = & - \frac{\partial(\bar{e}\bar{u})}{\partial x} + (\frac{1}{1-v})[\bar{e}(\bar{u}-u_s) + P\bar{u}] \frac{\partial v}{\partial x} - \frac{\partial(P\bar{u})}{\partial x} - \frac{\bar{u}(\bar{e}+P)}{A(1-v)} \frac{\partial A}{\partial x} \\ & - \frac{\bar{e}v}{(1-v)} \frac{\partial u_s}{\partial x} + (\frac{v}{1-v})\dot{M}_s \{ [h_{sg} - C_{ps}(T_{ig} - T_{init}) - (h(\bar{T}) \\ & - h(T_{ig}))] - \frac{\bar{e}}{\rho_s} \} \end{aligned} \quad (2.16)$$

where the terms of Eqs. (2.13)-(2.16) are defined as

- 1) A = the tube cross-sectional area
- 2) $v = A_s/A$ = the ratio of propellant cross-sectional area to tube cross-sectional area
- 3) u_s = the propellant grain velocity
- 4) \dot{M}_s = the rate of propellant consumption per unit volume
- 5) ρ_s = the propellant grain density
- 6) $\bar{\rho}$ = the combustion gas density averaged over the tube cross-sectional area at some axial location
- 7) \bar{u} = the combustion gas velocity averaged over the tube cross-sectional area at some axial location
- 8) P = the combustion gas pressure
- 9) \bar{T} = the combustion gas temperature averaged over the tube

cross-sectional area at some axial location

- 10) \bar{e} = the combustion gas energy per unit volume averaged over the tube cross-sectional area at some axial location
- 11) h_{sg} = the chemical energy released per unit mass of propellant
- 12) C_{ps} = the specific heat capacity of the propellant
- 13) T_{ig} = the ignition temperature of the propellant [Ref. 28]
- 14) T_{init} = the initial temperature of the propellant
- 15) $h(\bar{T})$ = the enthalpy of the combustion gas at temperature \bar{T}
- 16) $h(T_{ig})$ = the enthalpy of the combustion gas at temperature T_{ig}

The conservation equations given by Eqs. (2.13)-(2.16) contain more dependent variables than the number of such equations. These conservation equations are closed by the constitutive and the auxiliary equations described in the next two sections.

Constitutive Equations

A modified ideal gas equation

An equation of state which describes the relationship between combustion gas pressure, specific volume and temperature is needed. In order to account for the deviation caused by the specific volume of the propellant grains, an additional term η , the covolume, is employed with the ideal gas equation in the following manner [Ref. 14]:

$$P\left(\frac{1}{\rho} - \eta\right) = R_{cg} \bar{T} \quad (2.17)$$

where

η = the covolume of the propellant grains

R_{cg} = a gas constant particular to the combustion gas

Energy per unit volume

A constitutive relationship for energy was derived after making the following assumption: the internal energy and kinetic energy modes are the only significant energy modes for the combustion gas. Therefore, the combustion gas internal energy and kinetic energy terms can be combined in the following manner:

$$\bar{e} = \bar{\rho}(\hat{u}(\bar{T}) + \frac{1}{2} \bar{u}^2) \quad (2.18)$$

where $\hat{u}(\bar{T})$ = the combustion gas internal energy.

Propellant grain velocity

The last constitutive relationship used in this analysis describes the dependency between propellant grain velocity and combustion gas velocity. This relationship is defined as

$$u_g = CD_1 \bar{u} \quad (2.19)$$

where CD_1 = the propellant grain-combustion gas velocity ratio.

Auxiliary Equations

Combustion gas internal energy

In order to evaluate the effects of the large temperature range of the interior ballistic problem, the following two internal energy models were developed:

- 1) A polynomial expression in which specific heat at constant volume, C_v , is a function of temperature. The derivation of this expression is presented in Appendix A [Refs. 29, 30 and 31]. The resulting equation is

$$\begin{aligned} \hat{u}(\bar{T}) = & [-7.1259 \times 10^4 + 4.9224 \times 10^7 (\bar{T}^{-2}) - 1.2872 \times 10^6 (\bar{T}^{-1}) \\ & + 2.8007 \times 10^5 (\bar{T}^{-.5}) + 1.6310 \times 10^4 (\ln \bar{T}) - 2.3833 \times 10^3 (\bar{T}^{.25}) \\ & - 1.8069 \times 10^3 (\bar{T}^{.5}) + 6.2205 \times 10^1 (\bar{T}) - 8.8221 (\bar{T}^{1.25}) \\ & + 1.2517 (\bar{T}^{1.5}) - 5.7297 \times 10^{-3} (\bar{T}^{1.75}) - 5.5657 \times 10^{-3} (\bar{T}^2) \\ & + 8.066 \times 10^{-8} (\bar{T}^3)] (1000/\text{mmass}) \text{J/kg} \end{aligned} \quad (2.20)$$

where mmass = the molar mass of the combustion gas.

- 2) A simpler expression in which the specific heat ratio, γ , is assumed to be a constant [Ref. 31]. The resulting expression is

$$\hat{u}(\bar{T}) = \hat{u}_0 + [R_{cg}/(\gamma-1)]\bar{T} (1000/\text{mmass}) \text{J/kg} \quad (2.21)$$

where \hat{u}_0 = a reference internal energy at $\bar{T} = 300^\circ\text{K}$.

Combustion gas enthalpy

Because of the insertion of the covolume term in Eq. (2.17), the equation for combustion gas enthalpy becomes

$$h(\bar{T}) = h_0 + \hat{u}(\bar{T}) + R_{cg}\bar{T} + nP \quad (2.22)$$

where $\hat{u}(\bar{T})$, R_{cg} , \bar{T} , n , and P have been previously defined and h_0 = a reference enthalpy at $\bar{T} = 300^\circ\text{K}$ [Ref. 31].

Propellant grain-combustion gas velocity ratio

For the inviscid interior ballistic problem, it was assumed that no net force acts on the propellant grains. Therefore, the equation for the propellant grain-combustion gas velocity ratio becomes

$$CD_1 = 0 \quad (2.23)$$

Rate of propellant consumption per unit volume

The following assumptions were made to facilitate the derivation of an equation for the rate of propellant consumption per unit volume, \dot{M}_g :

- 1) \dot{M}_g is a function of time and axial position along the tube.
- 2) The linear burning speed, r_b , is a function of pressure only.

- 3) The propellant grains are incompressible.
- 4) The total burning surface area (A_{bt}) is constant.
- 5) The propellant grains are single-perforate cylinders.
- 6) The burning surface area of the ends of a propellant particle (A_{be}) is small in comparison to the burning surface area of the inner and outer cylindrical surfaces of the propellant particle (A_b).
- 7) The number of propellant grains (n) is a function of time and axial position along the tube.

Based on these assumptions, the following equation for \dot{M}_s was derived:

$$\dot{M}_s = \rho_s \left[A_{bt} \left(\frac{A_{vdx}}{L} \right) \right] r_b \quad (2.24)$$

$$\int_0^L A_{vdx}$$

where A_{bt} is the total burning surface area. The details of this derivation are given in Appendix A.

Projectile velocity

By using Newton's second law, the projectile acceleration can be expressed as

$$a_p = \frac{F_{pnet}}{m_p} \quad (2.25)$$

where

- 1) F_{pnet} = the net force acting on the projectile in the axial direction
2. m_p = the mass of the projectile.

By assuming that the projectile slides freely and that the effects of gravity can be neglected, F_{pnet} can be expressed as

$$F_{pnet} = (P_{pb} - P_f)A_p \quad (2.26)$$

where

- 1) P_{pb} = the combustion gas pressure acting on the base of the projectile
- 2) P_f = the "frontal" pressure, i.e., the external pressure acting on the front of the projectile
- 3) A_p = the cross-sectional area of the projectile.

The projectile acceleration may also be expressed in differential form as

$$a_p = \frac{dU_p}{dt} \quad (2.27)$$

where U_p is the projectile velocity.

Combining Eqs. (2.25)-(2.27) yields the following equation:

$$\frac{dU_p}{dt} = \frac{(P_{pb} - P_f)}{m_p} A_{pb} \quad (2.28)$$

The frontal pressure P_f in Eq. (2.26) may be found using the following assumptions:

- 1) The atmospheric specific heat ratio γ_{atm} is constant.
- 2) Quasi-steady conditions hold in front of the projectile.
- 3) The pressure increase in front of the projectile (due to projectile motion) can be modeled as an isentropic compression

in the axial direction when the Mach number (relative to the atmosphere) is less than or equal to 1.

- 4) The pressure increase in front of the projectile (due to projectile motion) can be modeled as compression across a normal shock when the Mach number (relative to the atmosphere) exceeds 1.

Under these assumptions, the Mach number may be expressed as

$$M = U_p / \sqrt{\gamma_{atm} R_{atm} T_{atm}} \quad (2.29)$$

and the frontal pressure may be expressed as

$$P_f = P_{atm} \left(1 + \frac{\gamma_{atm}-1}{2} M^2 \right)^{\frac{2}{\gamma_{atm}-1}} \quad (2.30)$$

where $M \leq 1$ or

$$P_f = P_{atm} \left(1 + \frac{\gamma_{atm}-1}{2} M^2 \right)^{\frac{\gamma_{atm}}{\gamma_{atm}-1}} \left(\frac{2\gamma_{atm}}{\gamma_{atm}+1} M^2 - \frac{\gamma_{atm}-1}{\gamma_{atm}+1} \right) \quad (2.31)$$

where $M > 1$ [Ref. 32].

The differential expression for projectile acceleration can be discretized and approximated at time level $n+1$ by the following expression [Ref. 33]:

$$\left(\frac{dU}{dt} \right)_p^{n+1} = \frac{U_p^{n+1} - U_p^n}{\Delta t} + O(\Delta t) \quad (2.32)$$

Substitution of Eq. (2.32) into the discretized form of Eq. (2.28) results in the following first-order accurate equation for projectile

velocity at time level $n+1$:

$$U_p^{n+1} = U_p^n + \left(\frac{P_b^{n+1} - P_f^{n+1}}{m_p} \right) A_p^{n+1} \Delta t \quad (2.33)$$

Projectile displacement

The projectile displacement (L_p) can be found from the formula

$$L_p(t) = L_p(t_0) + \int_{t_0}^t \frac{dU_p}{dt} dt \quad (2.34)$$

This equation may be discretized and approximated at time level $n+1$ by the following expression:

$$L_p^{n+1} = L_p^n + \frac{U_p^{n+1} + U_p^n}{2} \Delta t \quad (2.35)$$

2.4 Numerical Method of Solution

Solutions for the conservation equations (Eqs. (2.13)-(2.16)) were obtained by a finite difference method. Since finite difference methods provide solutions only at grid points and time levels, both the spatial domain and the duration of interest of Eqs. (2.13)-(2.16) must be discretized.

Discretization of the Spatial Domain

The spatial domain of interest for this problem is the distance from the breech to the base of the projectile as shown in Fig. 2.1. Typical values for this length interval range from a fraction of a meter to a few meters. This continuous length interval must be replaced by a system of grid points. The system chosen for this problem is shown in Fig. 2.4 and consists of a fixed number of uniformly distributed grid points. The spacing between the grid points increases as the distance between the spatial domain boundaries increases.

For problems with deforming spatial domains, the system of grid points used here has two principal advantages over grid systems that employ stationary grid points:

- 1) It avoids the problem of "uncovering" grid points as the projectile travels down the tube. Therefore, interpolation schemes for projectile base boundary values are unnecessary, making numerical boundary conditions much easier to implement.
- 2) It minimizes the number of grid points necessary to resolve the problem since no grid points need to be added as the

projectile travels down the tube.

These advantages have the effect of increasing computational efficiency and simplifying coding requirements.

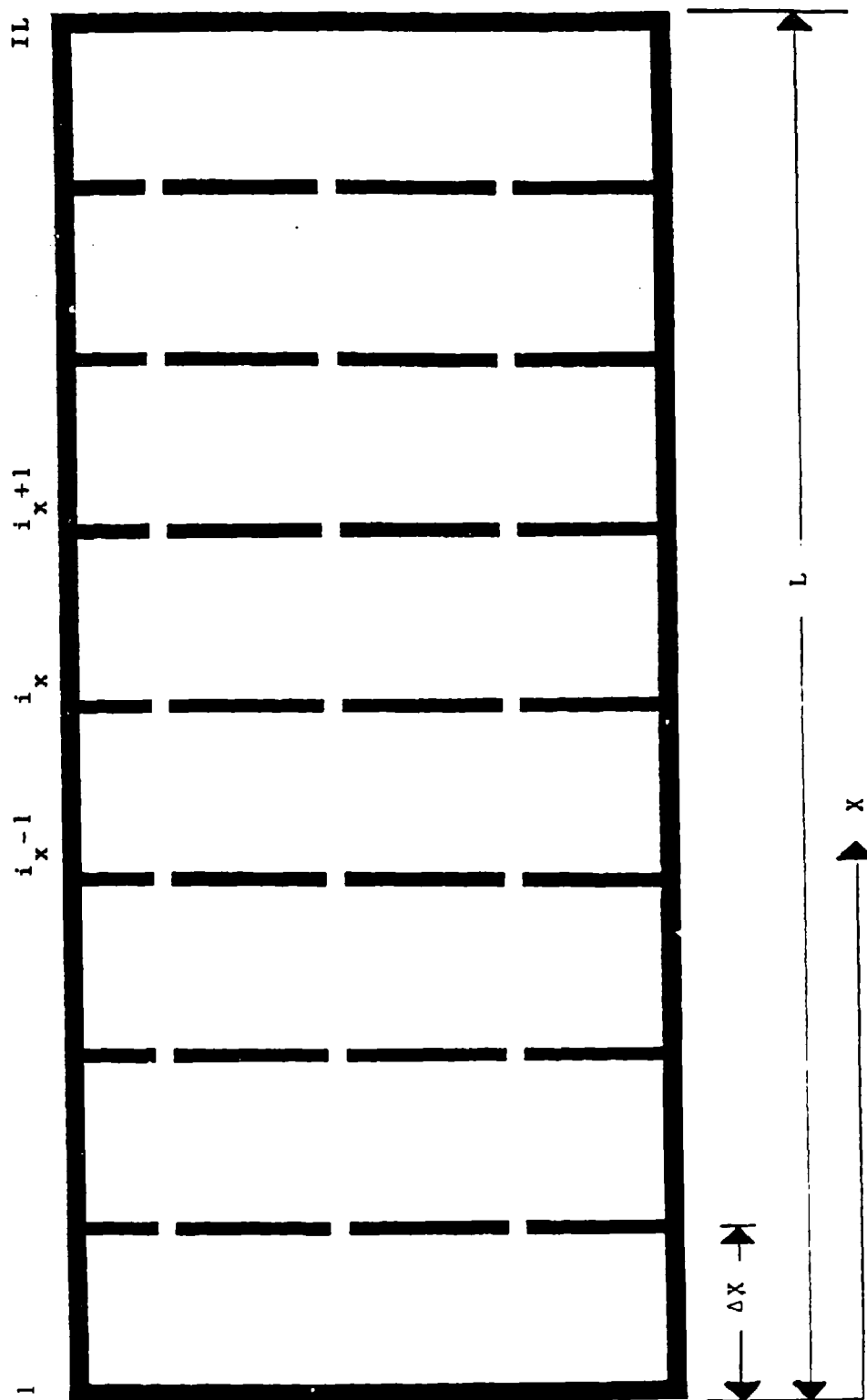


Figure 2.4
 Discretization of the Spatial Domain where $L=L_p$ (the projectile displacement) or L_s (the displacement of the propellant grain closest to the projectile).

Discretization of the Temporal Domain

The duration of interest for this problem is the time interval from the start of combustion to the time when the projectile exits the tube. Typical values for this time interval are on the order of a few milliseconds. This continuous time interval must be replaced by a finite number of time levels which satisfy the most limiting of the following two criteria:

- 1) The time step size (increment between two successive time levels) must be small enough to ensure numerical stability.
- 2) The time step size must be small enough to ensure temporal accuracy.

In this study, a constant time step size of 2 μ sec was used.

Derivation of the Finite Difference Equations

The derivation of the finite difference equations (FDE's) needed to obtain a solution to the inviscid problem involved three major steps:

- 1) The partial differential equations (PDE's) given by Eqs. (2.13)-(2.16) were transformed from the (x,t) coordinate system to the (ξ,τ) coordinate system.
- 2) The spatial and temporal domains of the transformed PDE's were discretized (see Fig. 2.5) and FDE's at the interior grid points were derived from the transformed PDE's.
- 3) FDE's at the boundary grid points (see Fig. 2.5) were derived from the transformed PDE's and from physical constraints.

In this section, the conservation equations resulting from the

coordinate transformation between (x,t) and (ξ,τ) used in step 1 are presented first. Next, the FDE's derived in steps 2 and 3 are shown.

Coordinate transformation

It is difficult to derive FDE's at grid points that move. One way to simplify the derivation of FDE's at moving grid points is to map moving grid points in the (x,t) coordinate system onto a (ξ,τ) coordinate system where all grid points are stationary.

To accomplish this transformation, the independent variables ξ and τ were defined such that

$$\xi = x/L \quad (2.37)$$

$$\tau = t \quad (2.38)$$

where for Eq. (2.13),

$L = L_g$, the distance between the breech and propellant grain closest to the projectile base.

and for Eqs. (2.14)-(2.16),

$L = L_p$, the distance between the breech and the base of the projectile.

Differentiation for a dependent variable $()$ with respect to x and t can be expressed in terms of differentiation with respect to ξ and τ as follows:

$$\frac{\partial ()}{\partial x} = \frac{1}{L} \frac{\partial ()}{\partial \xi} \quad (2.39)$$

$$\frac{\partial(\quad)}{\partial t} = \frac{\partial(\quad)}{\partial \tau} - \frac{U_f}{L} \frac{\partial(\quad)}{\partial \xi} \quad (2.40)$$

where for Eq. (2.13)

$U_f = U_s$, the velocity of the propellant grain closest to the projectile base.

and for Eqs. (2.14)-(2.16)

$U_f = U_p$, the velocity of the projectile.

By using the transformation equations presented in this section, the conservation equations (Eqs. (2.13)-(2.16)) can be rewritten as follows:

Continuity of Propellant Grains

$$\frac{\partial v}{\partial \tau} = \frac{U_s}{L_s} \xi \frac{\partial v}{\partial \xi} - \frac{1}{L_s} \left[\frac{\partial(vu_s)}{\partial \xi} - \frac{vu_s}{A} \frac{\partial A}{\partial \xi} \right] - \frac{\dot{M}_v}{\rho_s} \quad (2.41)$$

Continuity of Combustion Gas

$$\begin{aligned} \frac{\partial \bar{\rho}}{\partial \tau} = & \frac{U_p}{L_p} \xi \frac{\partial \bar{\rho}}{\partial \xi} - \frac{\bar{\rho} \bar{u}}{AL_p} \frac{\partial A}{\partial \xi} - \frac{1}{L_p} \frac{\partial(\bar{\rho} \bar{u})}{\partial \xi} + \frac{v}{(1-v)} \dot{M}_s \left(1 - \frac{\bar{\rho}}{\rho_s} \right) \\ & + \frac{\bar{\rho}}{(1-v)L_p} \left[(\bar{u} - u_s) \frac{\partial v}{\partial \xi} - v \left(\frac{\partial u_s}{\partial \xi} + \frac{u_s}{A} \frac{\partial A}{\partial \xi} \right) \right] \end{aligned} \quad (2.42)$$

Conservation of Momentum for the Combustion Gas

$$\begin{aligned} \frac{\partial(\bar{\rho} \bar{u})}{\partial \tau} = & \frac{1}{L_p} \left\{ U_p \xi \frac{\partial(\bar{\rho} \bar{u})}{\partial \xi} - \frac{\partial(\bar{\rho} \bar{u}^2)}{\partial \xi} + [\bar{\rho} \bar{u}(\bar{u} - u_s) + P] \frac{\partial v}{\partial \xi} - \frac{\partial P}{\partial \xi} \right\} \\ & - \frac{\bar{\rho} \bar{u}}{L_p} \left\{ \frac{[\bar{u} + (\frac{v}{1-v})u_s]}{A} \frac{\partial A}{\partial \xi} + \left(\frac{v}{1-v} \right) \left[\frac{\partial u_s}{\partial \xi} + \frac{\dot{M}_s L_p}{\rho_s} \right] \right\} \end{aligned} \quad (2.43)$$

Conservation of Energy for the Combustion Gas

$$\begin{aligned}
\frac{\partial \bar{e}}{\partial \tau} = & \frac{1}{L_p} \left\{ U_p \xi \frac{\partial \bar{e}}{\partial \xi} - \frac{\partial (\bar{e} \bar{u})}{\partial \xi} + \left(\frac{1}{1-v} \right) [\bar{e}(\bar{u} - u_s) + P \bar{u}] \frac{\partial v}{\partial \xi} - \frac{\partial (P \bar{u})}{\partial \xi} - \frac{U(\bar{e} + P)}{A(1-v)} \frac{\partial A}{\partial \xi} \right. \\
& \left. - \frac{\bar{e} v}{(1-v)} \frac{\partial u_s}{\partial \xi} \right\} + \left(\frac{v}{1-v} \right) \dot{M}_s \{ h_{sg} - C_{ps} (T_{ig} - T_{init}) \\
& - [h(\bar{T}) - h(T_{ig})] \} - \frac{\bar{e}}{\rho_s}
\end{aligned} \tag{2.44}$$

The transformed conservation equations can now be discretized and applied at individual grid points. For conservation equations that have been transformed with L_p as the scaling parameter (Eqs. (2.14)-(2.16)), a representative grid point is indicated by the symbol i (see Fig. 2.5). The propellant grain continuity equation (Fig. 2.13) has been transformed with L_g as the scaling parameter. A representative grid point for this equation is indicated by the symbol i^* (see Fig. 2.5).

It should be noted here that there is not a direct correspondence between values at locations i^* and i since L_g does not equal L_p in general. Consequently, values in the i^* grid point system must be mapped onto the i grid point system. This mapping procedure is accomplished by an interpolative scheme which is described in Appendix A.

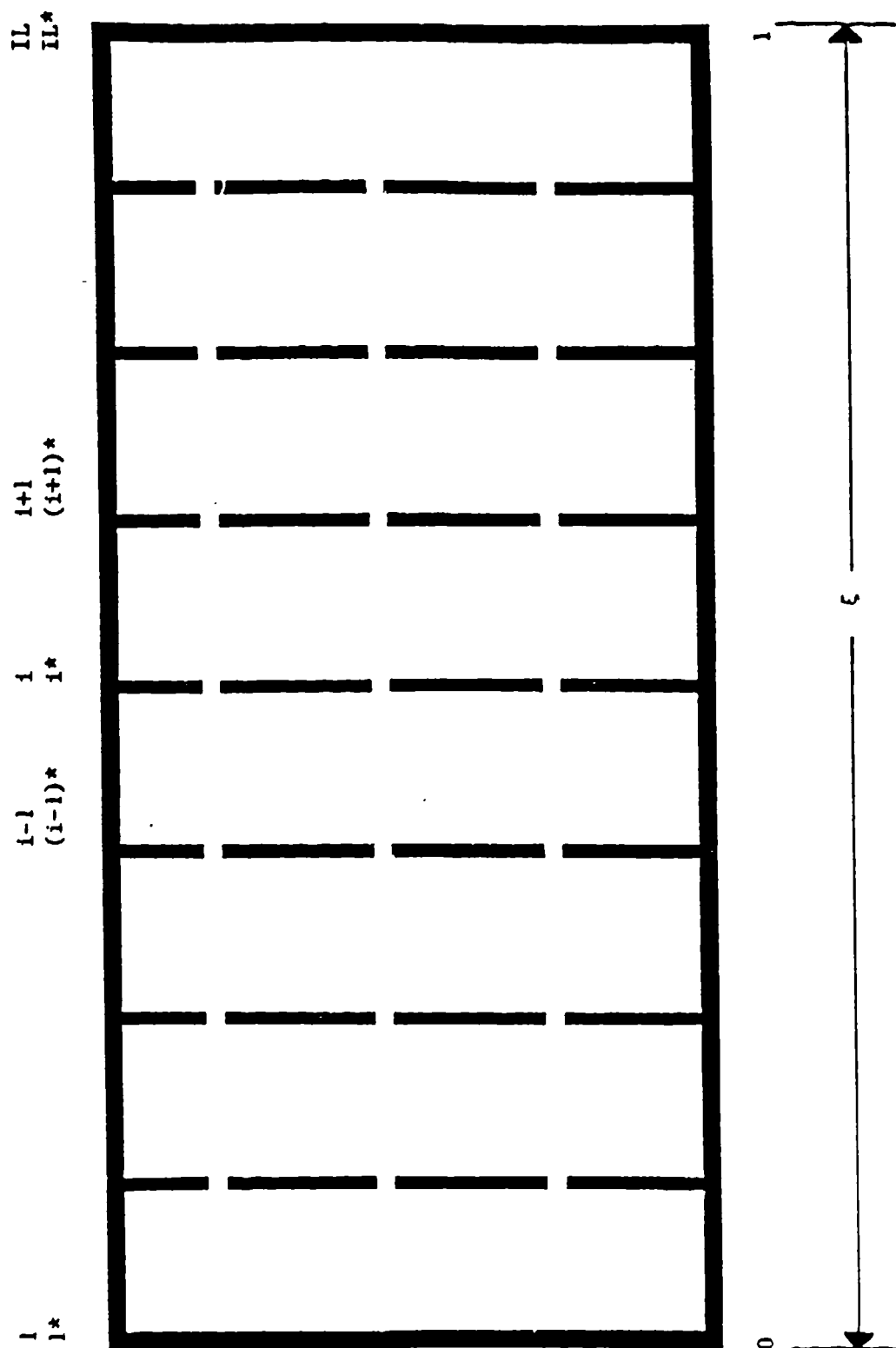


Figure 2.5

Discretization of the Transformed Spatial Domain where $\xi = x/L_p$ or x/L_s
 (i grid points correspond to the case where $\xi = x/L_p$ and i^* gridpoints
 correspond to the case where $\xi = x/L_s$)

Finite Difference Equations

The finite difference equations (FDE's) used to obtain solutions to the transformed conservation equations (Eqs. (2.39)-(2.42)) were obtained by implementing MacCormack's predictor-corrector scheme. This explicit method is second order accurate in both space and time. In this section, the resulting FDE's for the interior grid points are presented first. Then the FDE's for both the breech and projectile base boundaries are presented.

Finite difference equations at interior grid points

For each interior grid point i and i^* , the FDE's are derived by using MacCormack's predictor-corrector scheme to approximate the transformed PDE's. The resulting interior grid point FDE's at the predictor time level of $\overline{n+1}$ and the corrector time level of $n+1$ are presented as follows:

Continuity of Propellant Grains (Interior Point Predictor)

$$\begin{aligned}
 \overline{v_{i^*}^{n+1}} &= v_{i^*}^n + \left(\frac{\Delta \tau}{L_s}\right)^n \left(\frac{1}{\Delta \xi}\right) \{ (u_{s,i^*}^n)^n (v_{i^*}^n - v_{(i-1)^*}^n) \\
 &\quad - [(v_{u,s,i^*}^n - (v_{u,s,i^*}^n - (v_{u,(i-1)^*}^n)] - \left(\frac{v_{u,s}}{A}\right)_{i^*}^n a_{i^*}^n \Delta \xi \\
 &\quad - \left(\frac{\dot{M}_s v_{L_s}}{\rho_s}\right)_{i^*}^n \Delta \xi \}
 \end{aligned} \tag{2.45}$$

Continuity of Propellant Grains (Interior Point Corrector)

$$\begin{aligned}
\bar{v}_{1*}^{n+1} &= \frac{1}{2} [\bar{v}_{1*}^n + \bar{v}_{1*}^{n+1}] + \frac{1}{2} \left(\frac{\Delta \tau}{L_s} \right)^{n+1} \left(\frac{1}{\Delta \xi} \right) \{ U_s^{n+1} \bar{\epsilon}_{1*} (\bar{v}_{(1+1)*}^{n+1} \\
&- \bar{v}_{1*}^{n+1}) - [(\bar{v} u_s)_{(1+1)*}^{n+1} - (\bar{v} u_s)_{1*}^{n+1}] - \left(\frac{v u_s}{A} \right)_{1*}^{n+1} a_{1*}^{n+1} \Delta \xi \\
&- \left(\frac{\dot{M}_s v L_s}{\rho_s} \right)_{1*}^{n+1} \Delta \xi \}
\end{aligned} \quad (2.46)$$

Continuity of Combustion Gas (Interior Point Predictor)

$$\begin{aligned}
\bar{\rho}_1^{n+1} &= \bar{\rho}_1^n + \left(\frac{\Delta \tau}{L_p} \right)^n \left(\frac{1}{\Delta \xi} \right) \{ U_p^n \bar{\epsilon}_{1*} (\bar{\rho}_1^n - \bar{\rho}_{1-1}^n) - [(\bar{\rho} \bar{u})_1^n - (\bar{\rho} \bar{u})_{1-1}^n] \\
&+ \left(\frac{\bar{\rho}}{1-v} \right)_1^n [\bar{u}_1^n - u_s^n] (\bar{v}_1^n - \bar{v}_{1-1}^n) \} - \left(\frac{\Delta \tau}{L_p} \right)^n \left\{ \left(\frac{a}{A} \right)_1^n (\bar{\rho} \bar{u})_1^n \right. \\
&+ \left(\frac{v}{1-v} \right)_1^n \bar{\rho}_1^n [(u_{s\xi})_1^n + \left(\frac{u_s}{A} \right)_1^n a_1^n] \} + \Delta \tau \left(\frac{v}{1-v} \right)_1^n \dot{L}_1 \\
&- \left(\frac{\bar{\rho}}{\rho_s} \right)_1^n (\dot{M}_s)_1^n
\end{aligned} \quad (2.47)$$

Continuity of Combustion Gas (Interior Point Corrector)

$$\begin{aligned}
\bar{\rho}_1^{n+1} &= \frac{1}{2} (\bar{\rho}_1^n + \bar{\rho}_1^{n+1}) + \left(\frac{1}{2} \right) \left(\frac{\Delta \tau}{L_p} \right)^{n+1} \left(\frac{1}{\Delta \xi} \right) \{ U_p^{n+1} \bar{\epsilon}_{1*} (\bar{\rho}_{1+1}^{n+1} - \bar{\rho}_1^{n+1}) \\
&- [(\bar{\rho} \bar{u})_{1+1}^{n+1} - (\bar{\rho} \bar{u})_1^{n+1}] + \left(\frac{\bar{\rho}}{1-v} \right)_1^{n+1} [\bar{u}_1^{n+1} - (u_s)_{1*}^{n+1}] (\bar{v}_{1+1}^{n+1} - \bar{v}_1^{n+1}) \} \\
&- \left(\frac{1}{2} \right) \left(\frac{\Delta \tau}{L_p} \right)^{n+1} \left\{ \left(\frac{a}{A} \right)_1^{n+1} (\bar{\rho} \bar{u})_1^{n+1} + \left(\frac{v}{1-v} \right)_1^{n+1} \bar{\rho}_1^{n+1} [(u_{s\xi})_1^{n+1} \right. \\
&+ \left. \left(\frac{u_s}{A} \right)_1^{n+1} a_1^{n+1}] \right\} + \left(\frac{\Delta \tau}{2} \right) \left(\frac{v}{1-v} \right)_1^{n+1} [1 - \left(\frac{\bar{\rho}}{\rho_s} \right)_1^{n+1}] (\dot{M}_s)_1^{n+1}
\end{aligned} \quad (2.48)$$

Conservation of Momentum for the Combustion Gas (Interior Point Predictor)

$$\begin{aligned}
 (\bar{\rho}\bar{u})_1^{n+1} = & (\bar{\rho}\bar{u})_1^n + \left(\frac{\Delta\tau}{L_p}\right)^n \left(\frac{1}{\Delta\xi}\right) \{U_p^n \xi_1 [(\bar{\rho}\bar{u})_1^n - (\bar{\rho}\bar{u})_{1-1}^n] - [(\bar{\rho}\bar{u}^2)_1^n \\
 & - (\bar{\rho}\bar{u}^2)_{1-1}^n] + [(\bar{\rho}\bar{u})_1^n (\bar{u}-u_s)_1^n + p_1^n] \left(\frac{1}{1-v}\right)_1^n (v_1^n - v_{1-1}^n) \\
 & - (p_1^n - p_{1-1}^n)\} - \left(\frac{\Delta\tau}{L_p}\right)^n (\bar{\rho}\bar{u})_1^n \left\{ [\bar{u}_1^n + \left(\frac{v}{1-v}\right)_1^n (u_s)_1^n \left(\frac{a}{A}\right)_1^n \right. \\
 & \left. + \left(\frac{v}{1-v}\right)_1^n (u_{s\xi})_1^n \right\} - \left(\frac{v}{1-v}\right)_1^n \Delta\tau \left(\frac{\bar{\rho}\bar{u}}{\rho_s}\right)_1^n (\dot{M}_s)_1^n \quad (2.49)
 \end{aligned}$$

Conservation of Momentum for the Combustion Gas (Interior Point Corrector)

$$\begin{aligned}
 (\bar{\rho}\bar{u})_1^{n+1} = & \frac{1}{2} [(\bar{\rho}\bar{u})_1^n + (\bar{\rho}\bar{u})_1^{n+1}] + \left(\frac{1}{2}\right) \left(\frac{\Delta\tau}{L_p}\right)^{n+1} \left(\frac{1}{\Delta\xi}\right) (U_p^{n+1} \xi_1 [(\bar{\rho}\bar{u})_{1+1}^{n+1} \\
 & - (\bar{\rho}\bar{u})_1^{n+1}] [(\bar{\rho}\bar{u}^2)_{1+1}^{n+1} - (\bar{\rho}\bar{u}^2)_1^{n+1}] + [(\bar{\rho}\bar{u})_1^{n+1} (\bar{u}-u_s)_1^{n+1} \\
 & + p_1^{n+1}] \left(\frac{1}{1-v}\right)_1^{n+1} (v_{1+1}^{n+1} - v_1^{n+1}) - (p_{1+1}^{n+1} - p_1^{n+1})\} \\
 & - \left(\frac{1}{2}\right) \left(\frac{\Delta\tau}{L_p}\right)^{n+1} (\bar{\rho}\bar{u})_1^{n+1} \left\{ [\bar{u}_1^{n+1} + \left(\frac{v}{1-v}\right)_1^{n+1} \left(\frac{a}{A}\right)_1^{n+1} \right. \\
 & \left. + \left(\frac{v}{1-v}\right)_1^{n+1} (u_{s\xi})_1^{n+1} \right\} - \frac{\Delta\tau}{2} \left(\frac{v}{1-v}\right)_1^{n+1} \left(\frac{\bar{\rho}\bar{u}}{\rho_s}\right)_1^{n+1} (\dot{M}_s)_1^{n+1} \quad (2.50)
 \end{aligned}$$

Conservation of Energy for the Combustion Gas (Interior Point Predictor)

$$\bar{e}_1^{n+1} = \bar{e}_1^n + \left(\frac{\Delta\tau}{L_p}\right)^n \left(\frac{1}{\Delta\xi}\right) (U_p^n \xi_1 (\bar{e}_1^n - \bar{e}_{1-1}^n) - [(\bar{e}\bar{u})_1^n - (\bar{e}\bar{u})_{1-1}^n])$$

$$\begin{aligned}
& - [(Pu)_1^n - (Pu)_{1-1}^n] + \left(\frac{1}{1-v}\right)_1^n [(\bar{e}u)_1^n - (\bar{e}u_s)_1^n + (\bar{P}u)_1^n] (v_1^n - v_{1-1}^n) \\
& - \left(\frac{\Delta\tau}{L_p}\right)_1^n [(\bar{e}u)_1^n + \left(\frac{v}{1-v}\right)_1^n (\bar{e}u_s)_1^n + (\bar{P}u)_1^n] \left(\frac{a}{A}\right)_1^n + \left(\frac{v}{1-v}\right)_1^n \bar{e}_1^n (u_{s\xi})_1^n \\
& + \Delta\tau \left(\frac{v}{1-v}\right)_1^n (\dot{M}_s)_1^n \{ [h_{sg} - C_{ps}(T_{1g} - T_{init}) - (h(\bar{T}_1^n) \\
& - h(T_{1g}))] - \left(\frac{\bar{e}}{\rho_s}\right)_1^n \} \quad (2.51)
\end{aligned}$$

Conservation of Energy for the Combustion Gas (Interior Point Corrector)

$$\begin{aligned}
\bar{e}_1^{n+1} &= \frac{1}{2} (\bar{e}_1^n + \bar{e}_1^{n+1}) + \left(\frac{1}{2}\right) \left(\frac{\Delta\tau}{L_p}\right)^{n+1} \left(\frac{1}{\Delta\xi}\right) \{ U_p^n \xi_1 (\bar{e}_{1+1}^{n+1} - \bar{e}_1^n) \\
& - [(\bar{e}u)_{1+1}^{n+1} - (\bar{e}u)_1^{n+1}] - [(\bar{P}u)_{1+1}^{n+1} - (\bar{P}u)_1^{n+1}] + \left(\frac{1}{1-v}\right)_1^{n+1} [(\bar{e}u)_1^{n+1} \\
& - (\bar{e}u_s)_1^{n+1} + (\bar{P}u)_1^{n+1}] (v_{1+1}^{n+1} - v_1^{n+1}) \} - \left(\frac{1}{2}\right) \left(\frac{\Delta\tau}{L_p}\right)^{n+1} \{ [(\bar{e}u)_1^{n+1} \\
& + \left(\frac{v}{1-v}\right)_1^{n+1} (\bar{e}u_s)_1^{n+1} + (\bar{P}u)_1^{n+1}] \left(\frac{a}{A}\right)_1^{n+1} + \left(\frac{v}{1-v}\right)_1^{n+1} \bar{e}_1^{n+1} (u_{s\xi})_1^{n+1} \} \\
& + \left(\frac{\Delta\tau}{2}\right) \left(\frac{v}{1-v}\right)_1^{n+1} (\dot{M}_s)_1^{n+1} \{ [h_{sg} - C_{ps}(T_{1g} - T_{init}) \\
& - (h(\bar{T}_1^{n+1}) - h(T_{1g}))] - \left(\frac{\bar{e}}{\rho_s}\right)_1^{n+1} \} \quad (2.52)
\end{aligned}$$

where all other variables have previously been defined and

$$a = \frac{\partial A}{\partial \xi} \quad (2.53)$$

Finite difference equations at boundary grid points

Finite difference equations for the breech and projectile base boundaries were defined by first applying the transformed conservation equations (Eqs. (2.39)-(2.42)) at the boundaries subject to the following constraints:

$$1) \quad \bar{u}(\xi=0, \tau) = 0 \quad (2.54)$$

$$2) \quad \bar{u}(\xi=1, \tau) = U_p \quad (2.55)$$

$$3) \quad \frac{\partial v}{\partial \xi}(\xi=1, \tau) = 0 \quad (2.56)$$

Then, MacCormack's predictor-corrector scheme was used with three-point, one-sided differencing to approximate the resulting boundary conservation equations. Boundary FDE's at the predictor time level of $\bar{n+1}$ and corrector time level of $n+1$ are presented as follows:

Continuity of Propellant Grains

Breech Boundary Predictor

$$\begin{aligned} \bar{v}_{1*}^{\bar{n+1}} &= v_{1*}^n - \left(\frac{\Delta \tau}{L_s}\right)^n \left(\frac{1}{\Delta \xi}\right) \left[2(vu_s)_2^n + \frac{1}{2}(vu_s)_3^n \right] \\ &+ \left(\frac{\dot{M}_s v L_s}{\rho_s}\right)_{1*}^n \Delta \xi \end{aligned} \quad (2.57)$$

Breech Boundary Corrector

$$\begin{aligned} v_{1*}^{n+1} &= \frac{1}{2} (v_{1*}^n + \bar{v}_{1*}^{\bar{n+1}}) - \left(\frac{1}{2}\right) \left(\frac{\Delta \tau}{L_s}\right)^{\bar{n+1}} \left(\frac{1}{\Delta \xi}\right) \left[2(vu_s)_2^{\bar{n+1}} + \frac{1}{2}(vu_s)_3^{\bar{n+1}} \right] \\ &+ \left(\frac{\dot{M}_s v L_s}{\rho_s}\right)_{1*}^{\bar{n+1}} \Delta \xi \end{aligned} \quad (2.58)$$

Projectile Base Boundary Predictor

$$\overline{v_{IL}^{n+1}} = \overline{v_{(IL-1)}^{n+1}} \quad (2.59)$$

Projectile Base Boundary Corrector

$$\overline{v_{IL}^{n+1}} = \overline{v_{(IL-1)}^{n+1}} \quad (2.60)$$

Continuity of Combustion Gas

Breech Boundary Predictor

$$\begin{aligned} \overline{\rho_1^{n+1}} = \overline{\rho_1^n} - \left(\frac{\Delta \tau}{L_p}\right)^n \left(\frac{1}{\Delta \xi}\right) [2(\overline{\rho u})_2^n - \frac{1}{2}(\overline{\rho u})_3^n] - \left(\frac{\Delta \tau}{L_p}\right)^n \left[\left(\frac{v}{1-v}\right)_1^n \overline{\rho_1^n} (u_{s\xi})_1^n\right] \\ + \Delta \tau \left(\frac{v}{1-v}\right)_1^n [1 - \left(\frac{\rho}{\rho_s}\right)_1^n] (\dot{M}_s)_1^n \end{aligned} \quad (2.61)$$

Breech Boundary Corrector

$$\begin{aligned} \overline{\rho_1^{n+1}} = \frac{1}{2} (\overline{\rho_1^n} + \overline{\rho_1^{n+1}}) - \left(\frac{1}{2}\right) \left(\frac{\Delta \tau}{L_p}\right)^{n+1} \left(\frac{1}{\Delta \xi}\right) [2(\overline{\rho u})_2^{n+1} - \frac{1}{2}(\overline{\rho u})_3^{n+1}] \\ - \frac{\Delta \tau}{2} \left(\frac{\Delta \tau}{L_p}\right)^{n+1} \left[\left(\frac{v}{1-v}\right)_1^{n+1} \overline{\rho_1^{n+1}} (u_{s\xi})_1^{n+1}\right] \\ + \left(\frac{\Delta \tau}{2}\right) \left(\frac{v}{1-v}\right)_1^{n+1} [1 - \left(\frac{\rho}{\rho_s}\right)_1^{n+1}] (\dot{M}_s)_1^{n+1} \end{aligned} \quad (2.62)$$

Projectile Base Predictor

$$\begin{aligned}
\overline{\rho_{IL}^{n+1}} &= \overline{\rho_{IL}^n} + \left(\frac{\Delta\tau}{L_p}\right)^n \left(\frac{1}{\Delta\xi}\right) \left\{ U_p^n \left(\frac{3}{2} \overline{\rho_{IL}^n} - 2\overline{\rho_{IL-1}^n} + \frac{1}{2} \overline{\rho_{IL-2}^n} \right) \right. \\
&\quad - \left[\frac{3}{2} (\overline{\rho\bar{u}})_{IL}^n - 2(\overline{\rho\bar{u}})_{IL-1}^n + \frac{1}{2} (\overline{\rho\bar{u}})_{IL-2}^n \right] \\
&\quad + \left(\frac{\bar{\rho}}{1-\bar{v}} \right)_{IL}^n [\overline{u_{IL}^n} - (u_s)_{IL}^n] \left[\frac{3}{2} \overline{v_{IL}^n} - 2\overline{v_{IL-1}^n} + \frac{1}{2} \overline{v_{IL-2}^n} \right] \Big\} \\
&\quad - \left(\frac{\Delta\tau}{L_p} \right)^n \left\{ \left(\frac{a}{A} \right)_{IL}^n (\overline{\rho\bar{u}})_{IL}^n + \left(\frac{v}{1-\bar{v}} \right)_{IL}^n \overline{\rho_{IL}^n} [(u_{s\xi})_{IL}^n + \left(\frac{u_s}{A} \right)_{IL}^n a_{IL}^n] \right\} \\
&\quad + \Delta\tau \left(\frac{v}{1-\bar{v}} \right)_{IL}^n \left[1 - \left(\frac{\bar{\rho}}{\rho_s} \right)_{IL}^n \right] (\dot{M}_s)_{IL}^n \quad (2.63)
\end{aligned}$$

Projectile Base Corrector

$$\begin{aligned}
\overline{\rho_{IL}^{n+1}} &= \frac{1}{2} (\overline{\rho_{IL}^n} + \overline{\rho_{IL}^{n+1}}) + \left(\frac{1}{2} \right) \left(\frac{\Delta\tau}{L_p} \right)^n \left(\frac{1}{\Delta\xi} \right) \left\{ U_p^{n+1} \left(\frac{3}{2} \overline{\rho_{IL}^{n+1}} - 2\overline{\rho_{IL-1}^{n+1}} + \frac{1}{2} \overline{\rho_{IL-2}^{n+1}} \right) \right. \\
&\quad - \left[\frac{3}{2} (\overline{\rho\bar{u}})_{IL}^{n+1} - 2(\overline{\rho\bar{u}})_{IL-1}^{n+1} + \frac{1}{2} (\overline{\rho\bar{u}})_{IL-2}^{n+1} \right] \\
&\quad + \left(\frac{\bar{\rho}}{1-\bar{v}} \right)_{IL}^{n+1} [\overline{u_{IL}^{n+1}} - (u_s)_{IL}^{n+1}] \left[\frac{3}{2} \overline{v_{IL}^{n+1}} - 2\overline{v_{IL-1}^{n+1}} + \frac{1}{2} \overline{v_{IL-2}^{n+1}} \right] \Big\} \\
&\quad - \frac{1}{2} \left(\frac{\Delta\tau}{L_p} \right)^{n+1} \left\{ \left(\frac{a}{A} \right)_{IL}^{n+1} (\overline{\rho\bar{u}})_{IL}^{n+1} + \left(\frac{v}{1-\bar{v}} \right)_{IL}^{n+1} \overline{\rho_{IL}^{n+1}} [(u_{s\xi})_{IL}^{n+1} \right. \\
&\quad + \left. \left(\frac{u_s}{A} \right)_{IL}^{n+1} a_{IL}^{n+1}] \right\} + \frac{\Delta\tau}{2} \left(\frac{v}{1-\bar{v}} \right)_{IL}^{n+1} \left[1 - \left(\frac{\bar{\rho}}{\rho_s} \right)_{IL}^{n+1} \right] (\dot{M}_s)_{IL}^{n+1} \quad (2.64)
\end{aligned}$$

Conservation of Momentum for the Combustion Gas

Breach Boundary Predictor

$$(\bar{\rho}\bar{u})_1^{n+1} = 0 \quad (2.65)$$

Breach Boundary Corrector

$$(\bar{\rho}\bar{u})_1^{n+1} = 0 \quad (2.66)$$

Projectile Base Boundary Predictor

$$(\bar{\rho}\bar{u})_{IL}^{n+1} = \bar{\rho}_{IL}^{n+1} \bar{u}_p^{n+1} \quad (2.67)$$

Projectile Base Boundary Corrector

$$(\bar{\rho}\bar{u})_{IL}^{n+1} = \bar{\rho}_{IL}^{n+1} \bar{u}_p^{n+1} \quad (2.68)$$

Conservation of Energy for the Combustion Gas

Breach Boundary Predictor

$$\begin{aligned} \bar{e}_1^{n+1} = & \bar{e}_1^n - \left(\frac{\Delta\tau}{L_p}\right)^n \left(\frac{1}{\Delta\xi}\right) \left\{ [2(\bar{e}\bar{u})_2^n - \frac{1}{2}(\bar{e}\bar{u})_3^n] + [2(P\bar{u})_2^n - \frac{1}{2}(P\bar{u})_3^n] \right\} \\ & - \left(\frac{\Delta\tau}{L_p}\right)^n \left(\frac{v}{1-v}\right)_1^n \bar{e}_1^n (u_{s\xi})_1^n + \Delta\tau \left(\frac{v}{1-v}\right)_1^n (\dot{M}_s)_1^n \{ [h_{sg} - c_{ps}(T_{ig} - T_{init}) \\ & - (h(\bar{T}_1^n) - h(T_{ig}))] - \left(\frac{\bar{e}}{\rho_s}\right)_1^n \} \end{aligned} \quad (2.69)$$

Breach Boundary Corrector

$$\begin{aligned}
\bar{e}_1^{n+1} = & \frac{1}{2} (\bar{e}_1^n + \bar{e}_1^{n+1}) - \left(\frac{1}{2}\right) \left(\frac{\Delta \tau}{L_p}\right)^{n+1} \left(\frac{1}{\Delta \xi}\right) \{ [2(\bar{e}\bar{u})_2^{n+1} - \frac{1}{2} (\bar{e}\bar{u})_3^{n+1}] \\
& - [2(P\bar{u})_3^{n+1} - \frac{1}{2} (P\bar{u})_3^{n+1}] \} - \left(\frac{1}{2}\right) \left(\frac{\Delta \tau}{L_p}\right)^{n+1} \left(\frac{v}{1-v}\right)_1^{n+1} \bar{e}_1^{n+1} (u_{s\xi})_1^{n+1} \\
& + \left(\frac{\Delta t}{2}\right) \left(\frac{v}{1-v}\right)_1^{n+1} (\dot{M}_s)_1^{n+1} \{ [h_{sg} - c_{ps}(T_{ig} - T_{init}) - (h(\bar{T}_1^{n+1}) \\
& - h(\bar{T}_1^{n+1}) - h(T_{ig}))] - \left(\frac{\bar{p}}{\rho_s}\right)_1^{n+1} \} \quad (2.70)
\end{aligned}$$

Projectile Base Predictor

$$\begin{aligned}
\bar{e}_{IL}^{n+1} = & \bar{e}_{IL}^n + \left(\frac{\Delta \tau}{L_p}\right)^n \left(\frac{1}{\Delta \xi}\right) \{ U_p^n \left(\frac{3}{2} \bar{e}_{IL}^n - 2\bar{e}_{IL-1}^n + \frac{1}{2} \bar{e}_{IL-2}^n\right) \\
& - \left[\frac{3}{2} (P\bar{u})_{IL}^n - 2(P\bar{u})_{IL-1}^n + \frac{1}{2} (P\bar{u})_{IL-2}^n\right] \\
& + \left(\frac{1}{1-v}\right)_{IL}^n [(\bar{e}\bar{u})_{IL}^n - (\bar{e}u_s)_{IL}^n + (P\bar{u})_{IL}^n] \left(\frac{3}{2} v_{IL}^n - 2v_{IL-1}^n + \frac{1}{2} v_{IL-2}^n\right) \} \\
& - \left(\frac{\Delta \tau}{L_p}\right)^n \{ [(\bar{e}\bar{u})_{IL}^n + \left(\frac{v}{1-v}\right)_{IL}^n (\bar{e}u_s)_{IL}^n + (P\bar{u})_{IL}^n] \left(\frac{a}{A}\right)_{IL}^n \\
& + \left(\frac{v}{1-v}\right)_{IL}^n \bar{e}_{IL}^n (u_{s\xi})_{IL}^n \} + \Delta \tau \left(\frac{v}{1-v}\right)_{IL}^n (\dot{M}_s)_{IL}^n \{ [h_{sg} - c_{ps}(T_{ig} - T_{init}) \\
& - (h(\bar{T}_{IL}^n) - h(T_{ig}))] - \left(\frac{\bar{p}}{\rho_s}\right)_{IL}^n \} \quad (2.71)
\end{aligned}$$

Projectile Base Corrector

$$\begin{aligned}
\bar{e}_{IL}^{n+1} = & \frac{1}{2} (\bar{e}_{IL}^n + \bar{e}_{IL}^{n+1}) + \left(\frac{1}{2}\right) \left(\frac{\Delta \tau}{L_p}\right)^{n+1} \left(\frac{1}{\Delta \xi}\right) \{U_p^n \left(\frac{3}{2} \bar{e}_{IL}^{n+1} - 2\bar{e}_{IL-1}^{n+1} + \frac{1}{2} \bar{e}_{IL-2}^{n+1}\right) \\
& - \left[\frac{3}{2} (\bar{P}\bar{u})_{IL}^{n+1} - 2(\bar{P}\bar{u})_{IL-1}^{n+1} + \frac{1}{2} (\bar{P}\bar{u})_{IL-2}^{n+1}\right] + \left(\frac{1}{1-v}\right)_{IL}^{n+1} [(\bar{e}u_s)_{IL}^{n+1} \\
& + (\bar{P}\bar{u})_{IL}^{n+1}] \left(\frac{3}{2} v_{IL}^{n+1} - 2v_{IL-1}^{n+1} + \frac{1}{2} v_{IL-2}^{n+1}\right) \\
& - \left(\frac{1}{2}\right) \left(\frac{\Delta \tau}{L_p}\right)^{n+1} \{[(\bar{e}u)_{IL}^{n+1} + \left(\frac{v}{1-v}\right)_{IL}^{n+1} (\bar{e}u_s)_{IL}^{n+1} + (\bar{P}\bar{u})_{IL}^{n+1}] \left(\frac{a}{A}\right)_{IL}^{n+1} \\
& + \left(\frac{v}{1-v}\right)_{IL}^{n+1} \bar{e}_{IL}^{n+1} (u_{s\xi})_{IL}^{n+1}\} + \left(\frac{\Delta \tau}{2}\right) \left(\frac{v}{1-v}\right)_{IL}^{n+1} \{[h_{sg} - c_{ps}(T_{ig} - T_{init}) \\
& - (h(\bar{T}_{IL}^{n+1}) - h(T_{ig}))]\} - \left(\frac{\bar{p}}{\rho_s}\right)_{IL}^{n+1} \} \quad (2.72)
\end{aligned}$$

Summary of the Solution Procedure

At this point all the equations needed to specify the inviscid interior ballistic problem have been developed. A solution procedure for this problem proceeds as follows:

- I) Specify the input parameters listed in table 2-4, for all grid points i and i^* .
- II) Specify initial values for the dependent variables v , \bar{p} , $\bar{p}\bar{u}$ and \bar{e} for all grid points i and i^* .
- III) Find the values of the dependent variables at the predictor

time level $\overline{n+1}$ in the following manner:

Predictor

- 1) Find $v_{i*}^{\overline{n+1}}, v_i^{\overline{n+1}}$.
 - a) find $v_{i*}^{\overline{n+1}}$ at all interior i^* points by using Eq. (2.44)
 - b) find $v_{i*}^{\overline{n+1}}$ by using Eq. (2.57)
 - c) find $v_{IL*}^{\overline{n+1}}$ by using Eq. (2.58)
 - d) find $v_i^{\overline{n+1}}$ at all i grid points by interpolating between $v_{i*}^{\overline{n+1}}$ values at i^* grid points (see Appendix A)
 - e) store all values of $v_{i*}^{\overline{n+1}}$ and $v_i^{\overline{n+1}}$ for use in the corrector FDE's.
- 2) Find $\bar{\rho}_i^{\overline{n+1}}, (\bar{\rho}u)_i^{\overline{n+1}}$ and $\bar{e}_i^{\overline{n+1}}$.
 - a) find $\bar{\rho}_i^{\overline{n+1}}, (\bar{\rho}u)_i^{\overline{n+1}}$ and $\bar{e}_i^{\overline{n+1}}$ at all interior i grid points by using Eqs. (2.47), (2.49) and (2.51)
 - b) find $\bar{\rho}_i^{\overline{n+1}}$ and $\bar{\rho}_{IL}^{\overline{n+1}}$ by using Eq. (2.61) and Eq. (2.63)
 - c) find $(\bar{\rho}u)_i^{\overline{n+1}}$ by using Eq. (2.63)
 - d) guess the value of $(\bar{\rho}u)_{IL}^{\overline{n+1}}$ by using a one-sided difference version of Eq. (2.49)
 - e) find $\bar{e}_i^{\overline{n+1}}$ and $\bar{e}_{IL}^{\overline{n+1}}$ by using Eq. (2.68) and Eq. (2.71)

- 3) Find \bar{u}_i^{n+1} , \bar{T}_i^{n+1} and \bar{p}_i^{n+1} .
 - a) find \bar{u}_i^{n+1} at all i grid points by dividing $(\bar{\rho u})_i^{n+1}$ by $\bar{\rho}_i^{n+1}$
 - b) find \bar{T}_i^{n+1} at all i grid points by applying either of the internal energy equations (Eq. (2.20) or Eq. (2.21)) in Eq. (2.18) where all variables are discretized (i) predictor variables and \bar{e}_i^{n+1} , $\bar{\rho}_i^{n+1}$ and \bar{u}_i^{n+1} are known
 - c) find \bar{p}_i^{n+1} at all i grid points by using Eq. (2.17) where $\bar{\rho}_i^{n+1}$ and \bar{T}_i^{n+1} are now known
- 4) Find \bar{U}_p^{n+1} , $(\bar{\rho u})_{IL}^{n+1}$, and \bar{L}_p^{n+1} .
 - a) find \bar{P}_f^{n+1} (the projectile frontal pressure) by using Eq. (2.30) or Eq. (2.31)
 - b) find \bar{U}_p^{n+1} by using Eq. (2.33) where all variables are discretized (i) predictor variables
 - c) find $(\bar{\rho u})_{IL}^{n+1}$ by using Eq. (2.67)
 - d) find \bar{L}_p^{n+1} by using Eq. (2.35) where all variables are discretized (i) predictor variables
- 5) Find $(\bar{CD}_1)_1^{n+1}$, \bar{U}_s^{n+1} , and \bar{L}_s^{n+1} .
 - a) find $(\bar{CD}_1)_1^{n+1}$ at all i grid points by using Eq. (2.23) where all variables are discretized (i) predictor variables

- b) solve for u_s^{n+1} and L_s^{n+1} by using the iterative method described in Appendix A
- 6) Find $(u_s)_i^{n+1}$, $(u_s)_{i*}^{n+1}$, $(u_{s\xi})_{i*}^{n+1}$, and $(u_{s\xi})_i^{n+1}$.
- a) find $(u_s)_i^{n+1}$ at all i grid points by using Eq. () where all variables are discretized (1) predictor variables
- b) find $(u_s)_{i*}^{n+1}$ at all $i*$ grid points by interpolating between $(u_s)_i^{n+1}$ values at i grid points (see Appendix A)
- c) find $(u_{s\xi})_{i*}^{n+1}$ at all $i*$ grid points by using backward differencing of $(u_s)_{i*}^{n+1}$ for grid points $(2+IL)*$ and one-sided differencing of $(u_s)_{i*}^{n+1}$ at grid point 1
- d) find $(u_{s\xi})_i^{n+1}$ at all i grid points by interpolating between $(u_{s\xi})_{i*}^{n+1}$ values at $i*$ grid points (see Appendix A)
- 7) Find $(\dot{M}_s)_i^{n+1}$ and $(\dot{M}_s)_{i*}^{n+1}$.
- a) find $(\dot{M}_s)_i^{n+1}$ at all i grid points by using Eq. (2.24) where all variables are discretized (1) predictor variables and $(r_b)_i$ depends on p_i^{n+1}
- b) find p_{i*}^{n+1} at all $i*$ grid points by interpolating between p_i^{n+1} values at i grid points (see Appendix A)

- c) find $(\dot{M}_s)_{i*}^{n+1}$ at all i^* grid points by using Eq. (2.24) where all variables are discretized (i^*) predictor variables and $(r_b)_{i*}$ depends on p_{i*}^{n+1}

- 8) Find R_i^{n+1} , A_i^{n+1} and a_i^{n+1} .

- a) use the set of equations which corresponds to the chosen tube geometry (see Tables 2.1-2.3) to find R_i^{n+1} , A_i^{n+1} and a_i^{n+1}

- 9) Find R_{i*}^{n+1} , A_{i*}^{n+1} and a_{i*}^{n+1} .

- a) find R_{i*}^{n+1} , A_{i*}^{n+1} and a_{i*}^{n+1} at all i^* grid points by interpolating between R_i^{n+1} , A_i^{n+1} and a_i^{n+1} values respectively at i grid points

IV) Find the values of the dependent variables at the corrector time level of $n+1$ in the following manner:

Corrector

- 1) Find v_{i*}^{n+1} , v_i^{n+1} .

- a) find v_{i*}^{n+1} at all interior i^* points by using Eq. (2.46)
- b) find v_{i*}^{n+1} by using Eq. (2.58)
- c) find v_{iL}^{n+1} by using Eq. (2.60)
- d) find v_i^{n+1} at all i grid points by interpolating between v_{i*}^{n+1} values at i^* grid points (see Appendix A)

- e) store all values of v_{1*}^{n+1} and v_1^{n+1} for use in the predictor FDE's.
- 2) Find $\bar{\rho}_1^{n+1}$, $(\bar{\rho}u)_1^{n+1}$, and \bar{e}_1^{n+1} .
- a) find $\bar{\rho}_1^{n+1}$, $(\bar{\rho}u)_1^{n+1}$, and \bar{e}_1^{n+1} at all interior i grid points by using Eqs. (2.48), (2.50) and (2.52)
- b) find $\bar{\rho}_1^{n+1}$ and $\bar{\rho}_{IL}^{n+1}$ by using Eq. (2.61) and Eq. (2.64)
- c) find $(\bar{\rho}u)_1^{n+1}$ by using Eq. (2.66)
- d) guess the value of $(\bar{\rho}u)_{IL}^{n+1}$ by using a one-sided difference version of Eq. (2.50)
- e) find \bar{e}_1^{n+1} and \bar{e}_{IL}^{n+1} by using Eq. (2.70) and Eq. (2.72)
- 3) Find \bar{u}_1^{n+1} , \bar{T}_1^{n+1} and P_1^{n+1} .
- a) find \bar{u}_1^{n+1} at all i grid points by dividing $(\bar{\rho}u)_1^{n+1}$ by $\bar{\rho}_1^{n+1}$
- b) find \bar{T}_1^{n+1} at all i grid points by applying either of the internal energy equations (Eq. (2.20) or Eq. (2.22)) in Eq. (2.18) where all variables are discretized (1) corrector variables and \bar{e}_1^{n+1} , $\bar{\rho}_1^{n+1}$ and \bar{u}_1^{n+1} are known

- o) find P_i^{n+1} at all i grid points by using Eq. (2.17) where $\bar{\rho}_i^{n+1}$ and \bar{T}_i^{n+1} are now known
- 4) Find U_p^{n+1} , $(\bar{\rho}u)_{IL}^{n+1}$, and L_p^{n+1} .
 - a) find P_f^{n+1} (the projectile frontal pressure) by using Eq. (2.30) or Eq. (2.31)
 - b) find U_p^{n+1} by using Eq. (2.33) where all variables are discretized (1) corrector variables
 - c) find $(\bar{\rho}u)_{IL}^{n+1}$ by using Eq. (2.68)
 - d) find L_p^{n+1} by using Eq. (2.35) where all variables are discretized (1) corrector variables
- 5) Find $(CD_1)_i^{n+1}$, U_s^{n+1} , and L_s^{n+1} .
 - a) find $(CD_1)_i^{n+1}$ at all i grid points by using Eq. (2.23) where all variables are discretized (1) corrector variables
 - b) solve for U_s^{n+1} and L_s^{n+1} by using the iterative method described in Appendix A
- 6) Find $(u_s)_i^{n+1}$, $(u_s)_{i*}^{n+1}$, $(u_{s\xi})_{i*}^{n+1}$, and $(u_{s\xi})_i^{n+1}$.
 - a) find $(u_s)_i^{n+1}$ at all i grid points by using Eq. (2.19) where all variables are discretized (1) corrector variables

- b) find $(u_s)_{i*}^{n+1}$ at all i^* grid points by interpolating between $(u_s)_1^{n+1}$ values at 1 grid points (see Appendix A)
 - c) find $(u_{s\xi})_{i*}^{n+1}$ by using forward differencing of $(u_s)_{i*}^{n+1}$ for grid points $(1 \leftrightarrow IL-1)^*$ and one-sided differencing of $(u_s)_{i*}^{n+1}$ at grid point 1
 - d) find $(u_{s\xi})_{i*}^{n+1}$ by interpolating between $(u_{s\xi})_{i*}^{n+1}$ values at i^* grid points (see Appendix A)
- 7) Find $(\dot{M}_s)_1^{n+1}$ and $(\dot{M}_s)_{i*}^{n+1}$.
- a) find $(\dot{M}_s)_1^{n+1}$ at all 1 grid points by using Eq. (2.24) where all variables are discretized (1) corrector variables and $(r_b)_1$ depends on P_1^{n+1}
 - b) find P_{i*}^{n+1} at all i^* grid points by interpolating between P_1^{n+1} values at 1 grid points (see Appendix A)
 - c) find $(\dot{M}_s)_{i*}^{n+1}$ at all i^* grid points by using Eq. (2.24) where all variables are discretized (i^*) corrector variables and $(r_b)_{i*}$ depends on P_{i*}^{n+1}
- 8) Find R_1^{n+1} , A_1^{n+1} and a_1^{n+1} .
- a) use the set of equations which corresponds to the chosen tube geometry (see Tables 2.1-2.3) to

find R_i^{n+1} , A_i^{n+1} and a_i^{n+1}

9) Find R_{i*}^{n+1} , A_{i*}^{n+1} and a_{i*}^{n+1} .

a) find R_{i*}^{n+1} , A_{i*}^{n+1} and a_{i*}^{n+1} at all i^* grid points by interpolating between R_i^{n+1} , A_i^{n+1} and a_i^{n+1} values respectively at i grid points

V) Repeat steps III and IV until the projectile has traveled a prescribed length L_f .

2.5 Results

In this section, the results of several computer simulations of inviscid interior ballistic flow are presented and compared. Salient gun performance parameters were determined and conclusions were drawn about their significance.

Description of Cases

A case study which isolated the effect of a parameter on gun performance was made for the inviscid interior ballistic problem. Table 2.5 lists the values or equations of parameters which did not change in these case studies. The assumptions common to all the inviscid interior ballistic case studies are listed as follows:

- 1) Combustion gas flow is unsteady and one-dimensional in the axial direction.
- 2) There is no heat transfer.
- 3) The combustion gas is inviscid (e.g., there is no wall shear force).
- 4) No net force is exerted on the propellant grains (i.e., the propellant grains do not move from their initial positions and there is no propellant grain drag force).

Table 2.6 lists the equations of parameters which were varied in the inviscid interior ballistic case studies. The sum of the parameters listed in Tables 2.5 and 2.6 specify the inviscid interior ballistic problem.

Case AA was the simplest inviscid interior ballistic case study.

Table 2.5

Specification in MKS units of parameters which remain
the same for all inviscid interior ballistic case studies

Projectile Parameters

$U_{p0} = 0.0$
 $P_{or} = 6.895 \times 10^6$
 $m_p = .375$

Air Parameters

$T_{atm} = 300$
 $P_{atm} = 1.0 \times 10^5$
 $\gamma_{atm} = 1.41$
 $R_{atm} = 296.82$

Combustion Gas Parameters

$m_{mass} = 24.0728$
 $T_0 = 300$
 $P_0 = 3.449 \times 10^6$
 $U_0 = 0.0$

Propellant Parameters

type = CIL 3331
 grain geometry = cylindrical,
 single perforate
 $m_{c0} = 0.148$
 $\rho_s = 1660.820$
 $w_0 = 86.868 \times 10^{-5}$
 $C_{ps} = 1539.25$
 $T_{init} = 300$
 $T_{ig} = 600$
 $h_{sg} = 4171.998 \times 10^3$
 $u_{s0} = 0.0$
 $C_D = 1.0$

Table 2.6
Parameters and equations which were varied in the
inviscid interior ballistic case studies

| Case | η | r_b | $\hat{u}(T)$ | tube geometry |
|------|---|------------------|-------------------------|---------------------------------|
| AA | 0.0 | $f(P_{ave})$ | given by Eq. (2.21) | given by Eqs. (2.1)-(2.3) |
| AB | $1.084 \times 10^{-3} (\frac{m^3}{kg})^*$ | $f(P_{ave})$ | given by Eq. (2.21) | given by Eqs. (2.1)-(2.3) |
| AC | $1.084 \times 10^{-3} (\frac{m^3}{kg})$ | $f(P_{local})^*$ | given by Eq. (2.21) | given by Eqs. (2.1)-(2.3) |
| AD | $1.084 \times 10^{-3} (\frac{m^3}{kg})$ | $f(P_{local})$ | given by Eq. (2.20)* | given by Eqs. (2.1)-(2.3) |
| AE | $1.084 \times 10^{-3} (\frac{m^3}{kg})$ | $f(P_{local})$ | given by Eq. (2.20) | given by Eqs. (2.10)-(2.12)* |

* Indicates a change in value from the previous case.

In addition to the general assumptions listed previously, the following simplifying assumptions were used to analyze this case:

- 1) The covolume (n) is zero (i.e., the equation of state (Eq. (2.17)) reduces to the ideal gas law).
- 2) The local linear burning rate (r_b) depends on the spatial-average pressure within the tube assembly.
- 3) The ratio of specific heats is constant (i.e., Eq. (2.21) is used to describe the combustion gas internal energy).
- 4) The tube assembly is a straight tube.

The rest of the inviscid interior ballistic cases reduce these simplifying assumptions one-by-one in the following manner:

- 1) Case AB is the same as case AA except that the covolume term is no longer zero (see Table 2.6 for the value of n).
- 2) Case AC is the same as case AB except that the local linear burning rate depends on local pressure.
- 3) Case AD is the same as case AC except that the ratio of specific heats is no longer constant (i.e., Eq. (2.20) is used to describe combustion gas energy).
- 4) Case AE is the same as case AD except that the tube assembly radius varies smoothly from the breech to the open end of the tube.

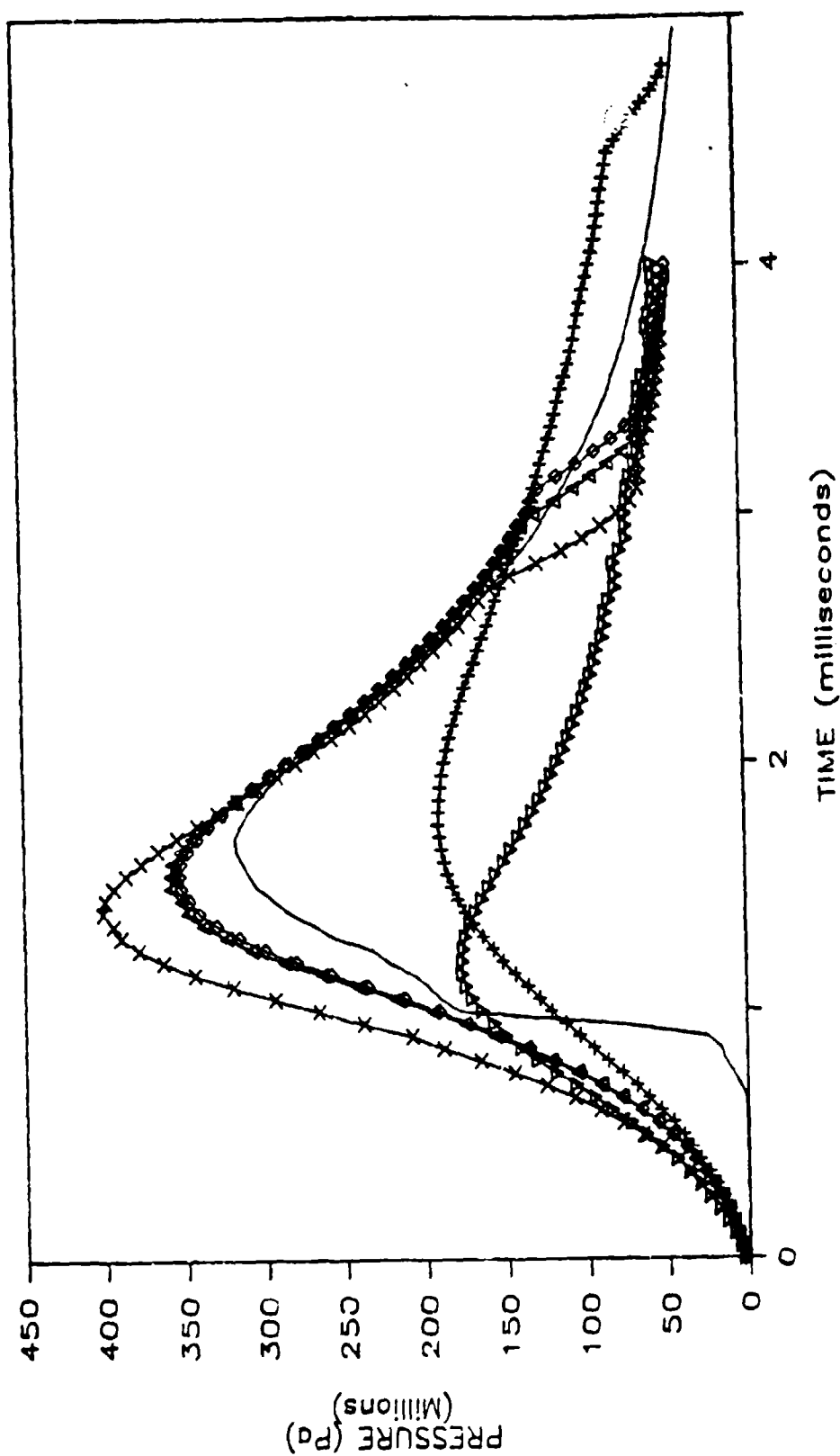


Figure 2.6

Breech pressure as a function of time for an actual gun firing and for the inviscid interior ballistic cases AA-AE. - denotes the experimentally determined pressure,

+ denotes case AA, \diamond denotes case AB, Δ denotes case AC, x denotes case AD, and V denotes case AE.

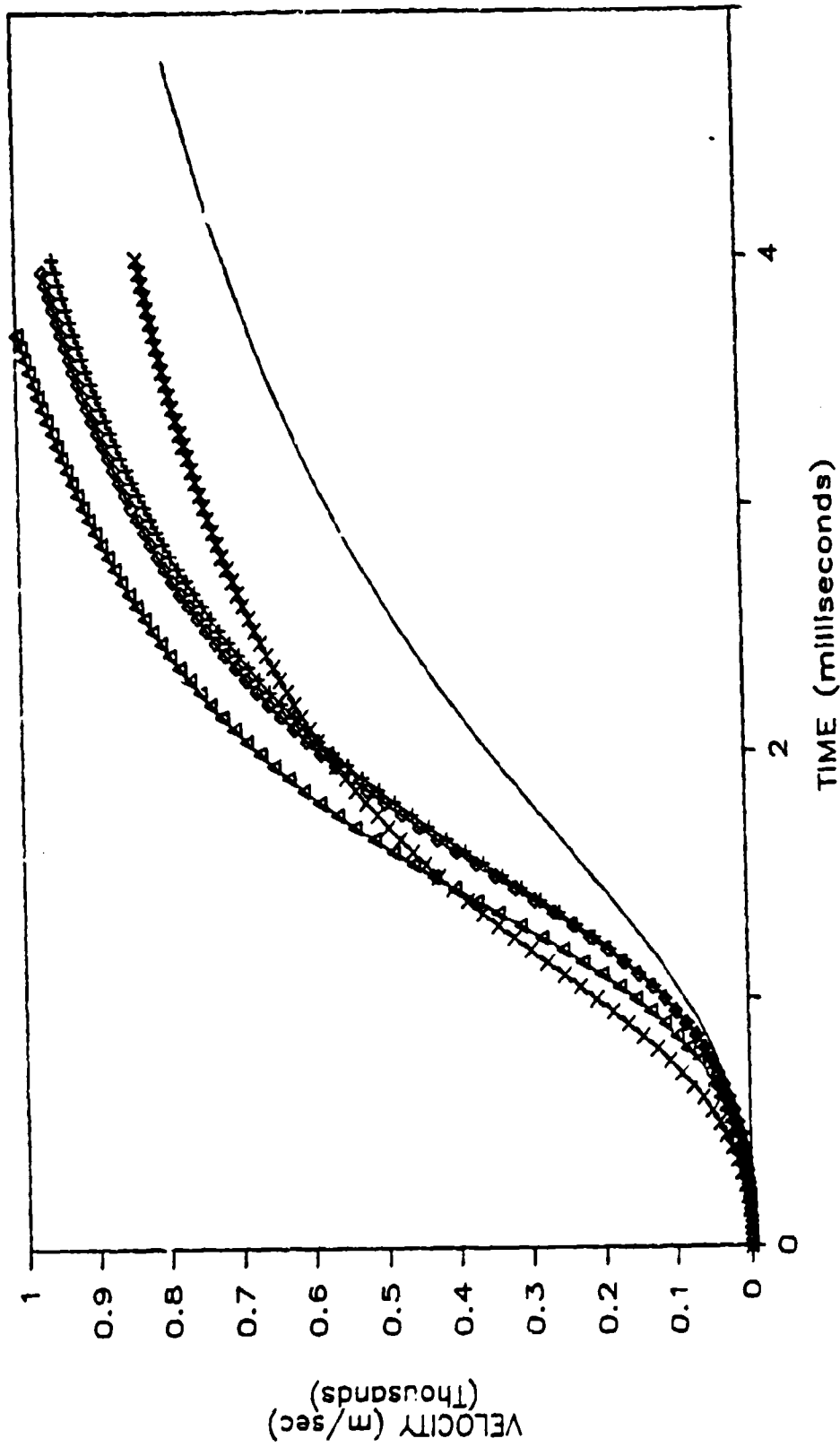


Figure 2.7

Projectile velocity as a function of time for the inviscid interior ballistic cases

AA-AE. - denotes case AA, + denotes case AB, \diamond denotes case AC

Δ denotes case AD, and x denotes case AE.

Table 2.7

Muzzle velocity, peak breech pressure, time of occurrence of
 peak breech pressure, and percent differences for inviscid interior
 ballistic cases AA-AE

| Case | U_{pf} (m/sec) | % Dif. | Peak P (10^5 Pa) | % Dif. | Time ($P_k P$) (milli-sec) | % Dif. |
|------|---------------------|--------|------------------------|--------|---------------------------------|--------|
| AA | 789 | | 1902 | | 1.70 | |
| AB | 948 | 20.3 | 3585 | 85.5 | 1.55 | -8.8 |
| AC | 961 | 1.4 | 3642 | 1.6 | 1.50 | -3.2 |
| AD | 897 | 3.7 | 4001 | 11.6 | 1.40 | -6.7 |
| AE | 830 | -16.7 | 1769 | -55.8 | 1.15 | -17.9 |

Case Performance

Figure 2.6 shows a plot of breech pressure versus time for an actual gun firing [Ref. 28] and for cases AA-AE. Figure 2.7 shows a plot of projectile velocity versus time for cases AA-AE. Table 2.7 lists the muzzle velocity, the peak breech pressure and the time of occurrence of peak breech pressure for cases AA-AE. It also lists the percent difference (from the previous case) of each of these quantities.

The effect of the covolume term (η) can be seen by comparing cases AA and AB. When compared to case AA, case AB shows a 20.3% gain in muzzle velocity, an 85.5% gain in peak breech pressure and an 8.8% decrease in the time needed to reach peak breech pressure. This is the largest change in gun performance found in the inviscid interior ballistic case studies. Accurate modeling of the covolume term is therefore seen to be of paramount importance.

The effect of using local pressure values to find the local linear burning rate can be seen by comparing cases AB and AC. When compared to case AB, case AC shows a 1.4% gain in muzzle velocity, a 3.2% increase in peak breech pressure, and a 1.6% decrease in the time needed to reach peak breech pressure. This shows one of the significant effects of the spatial pressure gradient on gun performance.

The effect of a non-constant specific heat ratio can be seen by comparing cases AC and AD. When compared to case AC, case AD shows a 3.7% gain in muzzle velocity, an 11.6% increase peak breech pressure, and a 6.7% decrease in the time needed to reach peak breech pressure. This significant change in gun performance indicates that interior ballistic modeling should account for a non-constant specific heat ratio.

The effect of a non-constant tube radius can be seen by comparing cases AD and AE. When compared to case AD, case AE shows a 16.7% decrease in muzzle velocity, a 55.8% decrease in peak breech pressure and a 17.9% decrease in the time needed to reach peak breech pressure.

This decrease in performance is accounted for by the larger increase in interior volume of the tube assembly (at the time of peak pressure) for case AE when compared to case AD. This volume increase lowers pressure and dominates the helpful effect of case AE's increased projectile cross-sectional area.

Since case AE shows the dramatic effect that tube geometry can have on gun performance, it is felt that more work should be done to find the tube geometry which optimizes gun performance.

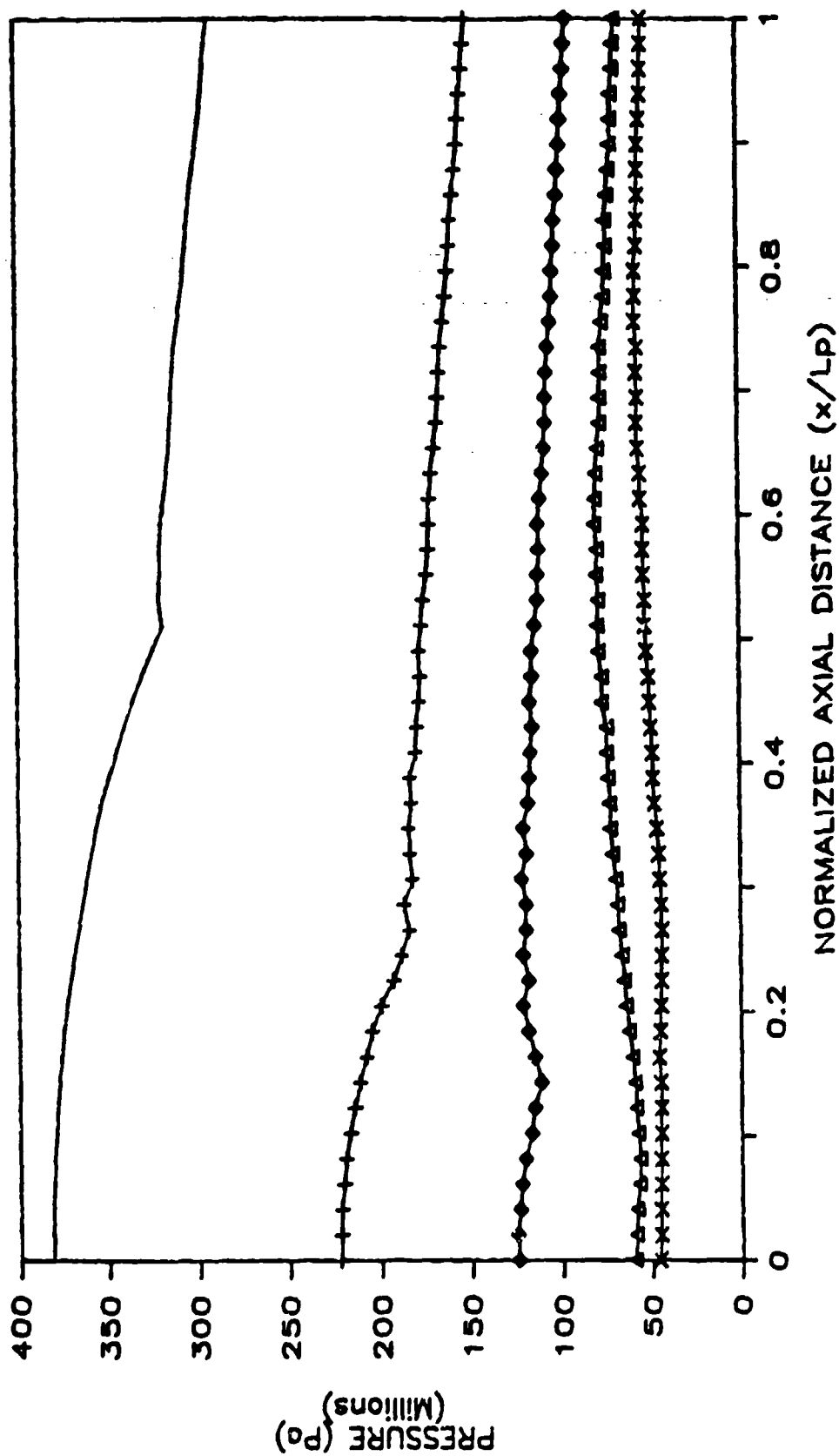


Figure 2.8

Pressure as a function of normalized axial distance at five projectile displacements (L_p)

where - indicates $L_p=0.44m$, + indicates $L_p=0.88m$, \diamond indicates $L_p=1.32m$, Δ indicates

$L_p=1.75m$, and x indicates $L_p=2.19m$.

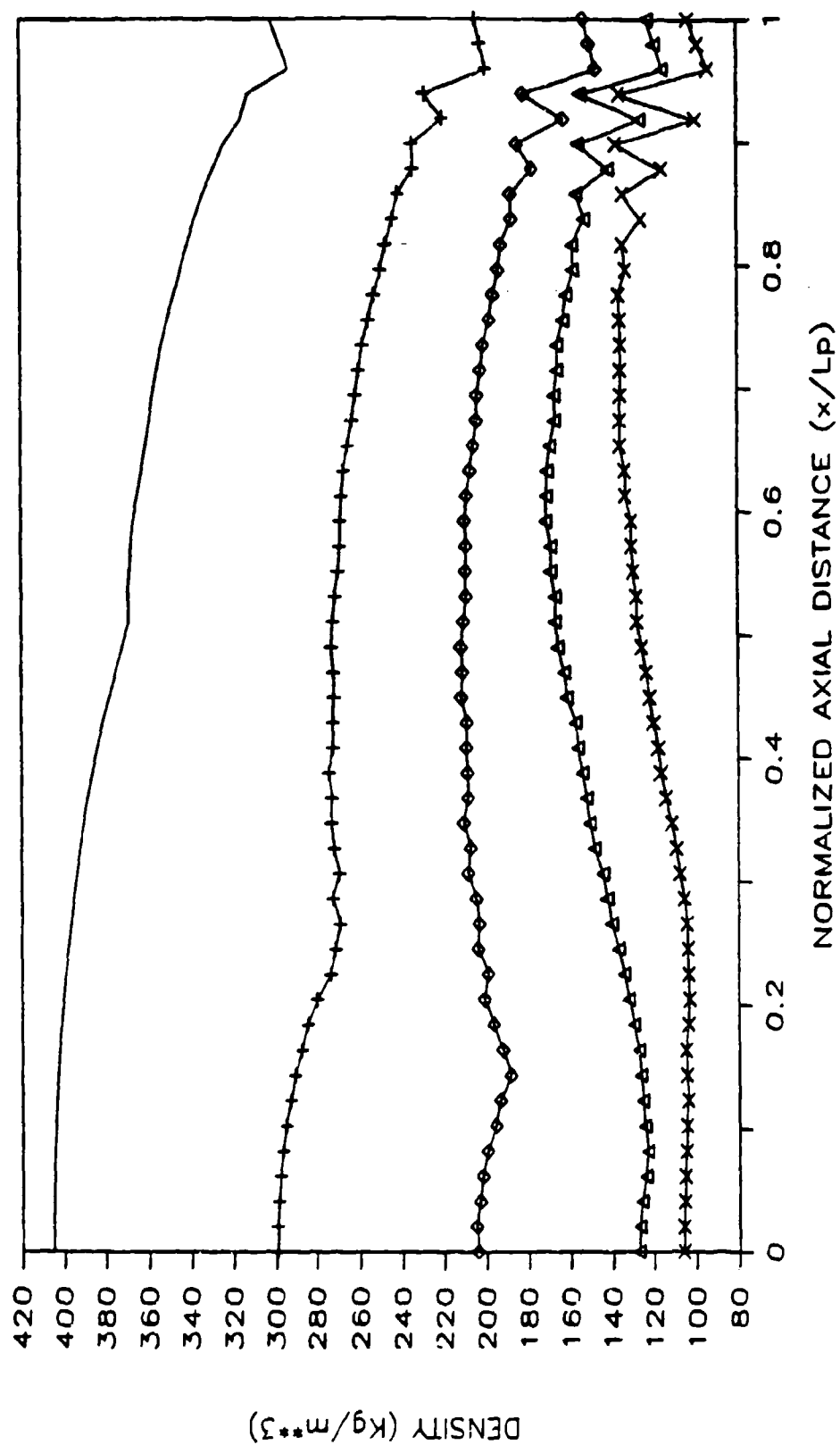


Figure 2.9

Density as a function of normalized axial distance at five projectile displacements

(Lp) where - indicates Lp=0.44m, + indicates Lp=0.88m, ◇ indicates Lp=1.32m,

Δ indicates Lp=1.75m, and x indicates Lp=2.19m.

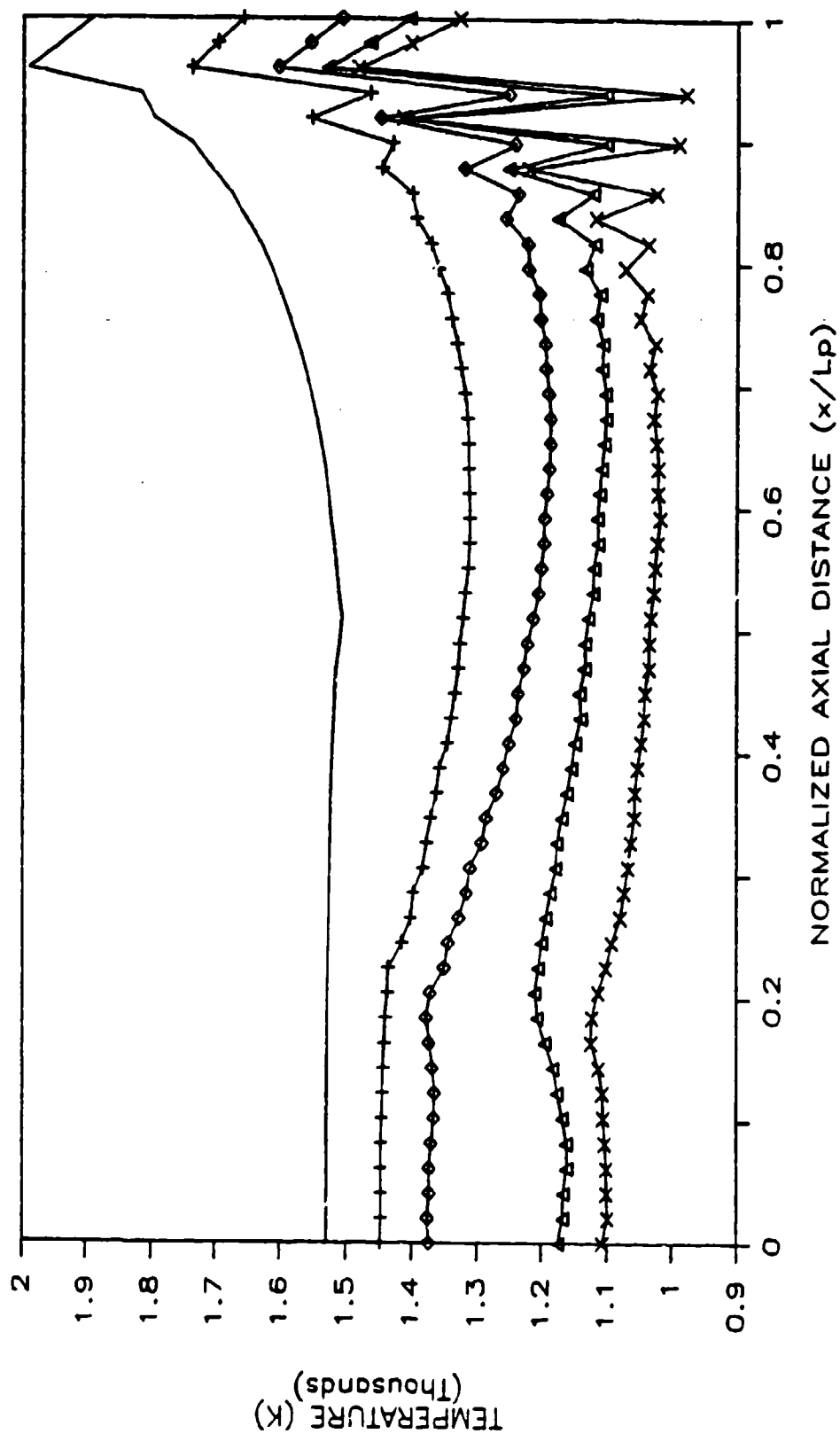


Figure 2.10

Temperature as a function of normalized axial distance at five projectile displacements

(L_p) where - indicates $L_p=0.44m$, + indicates $L_p=0.88m$, \diamond indicates $L_p=1.32m$, Δ indicates $L_p=1.75m$, and x indicates $L_p=2.19m$.

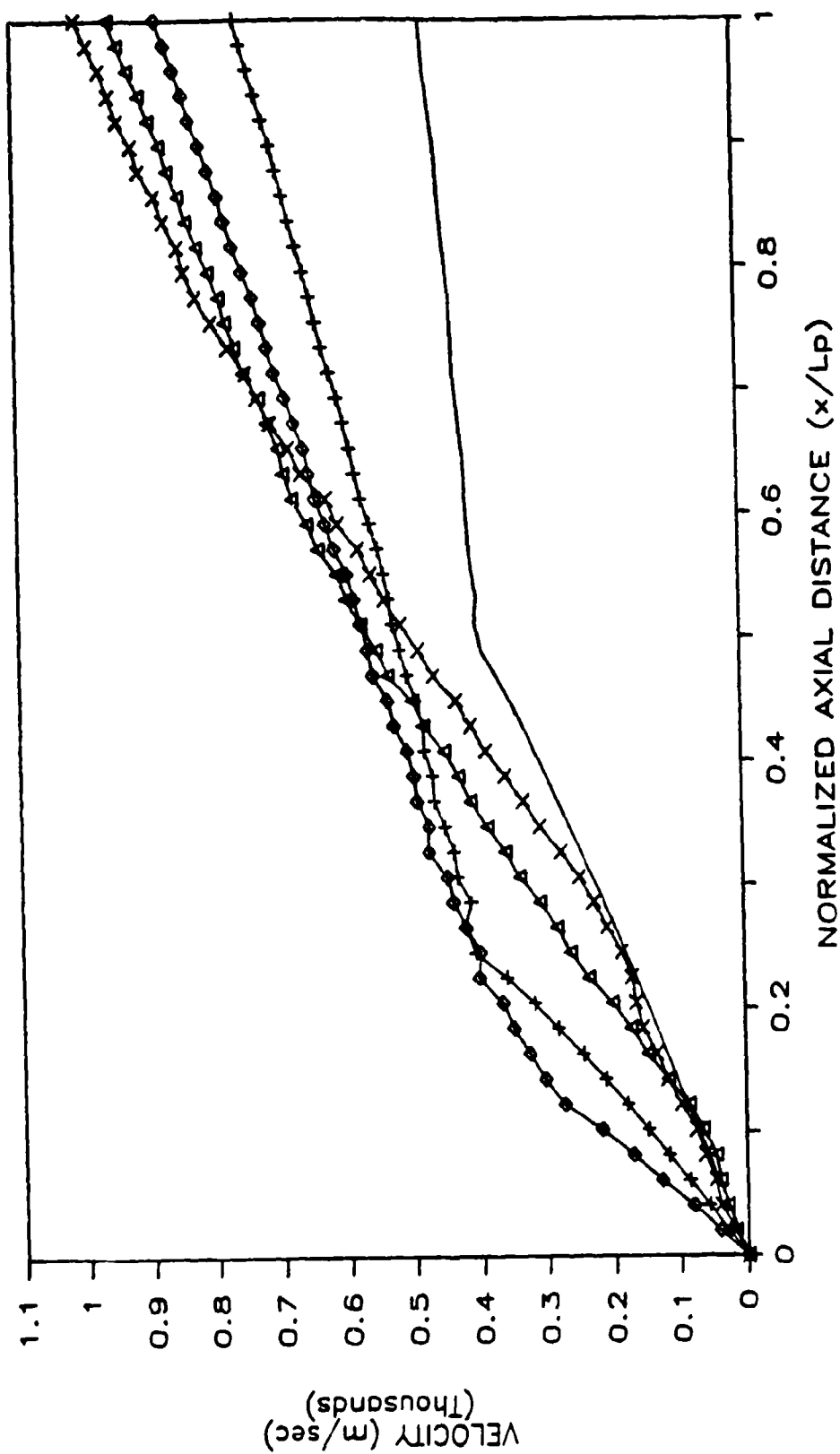


Figure 2.11

Velocity as a function of normalized axial distance at five projectile displacements (L_p)

where - indicates $L_p=0.44\text{m}$, + indicates $L_p=0.88\text{m}$, \diamond indicates $L_p=1.32\text{m}$, Δ indicates

$L_p=1.75\text{m}$, and x indicates $L_p=2.19\text{m}$.

Case AD Spatial Distributions

The data generated from case AD was chosen to illustrate the behavior of combustion gas spatial pressure, density, temperature and velocity distributions for the inviscid interior ballistic problem.

Figure 2.8 shows combustion gas pressure plotted against normalized axial distance (x/L_p) at five projectile displacements. The first half of the pressure plot corresponding to $L_p = 0.44$ m shows the effect that local pressure has on the propellant burning rate. Since the relationship between pressure and the propellant burning rate is non-linear (see Table A-1), the pressure plot in the burning region is also non-linear. The second half of the pressure plot corresponding to $L_p = 0.44$ m is essentially linear, which is typical of gas expansion with no combustion. The pressure plots corresponding to $L_p = 0.88$ m and $L_p = 1.32$ m show that the effect of the non-linear burning rate diminishes as the shot progresses and the propellant is consumed.

Figure 2.8 also shows that the slope of the axial pressure profile is initially negative with a 22% drop in pressure from the breech to the projectile base when $L_p = 0.44$ m. As the shot progresses, the axial pressure drop tends toward zero and when $L_p = 2.19$ m (at the end of the shot), there is only a 2% difference between breech pressure and projectile base pressure.

Figure 2.9 shows combustion gas density plotted against normalized axial distance at five projectile displacements. As in the plot of pressure profiles, the effect of the propellant burning rate's dependence on local pressure can be seen in the axial density profiles.

Figure 2.9 also shows that the slope of the axial density profile

is initially negative with a 26% drop in density from the breech to the projectile base when $L_p = 0.44$ m. As the shot progresses, this density drop between boundaries tends toward zero. At the end of the shot (when $L_p = 2.19$ m), there is actually a density increase of 4% at the base of the projectile when compared to the breech.

An interesting phenomenon indicated by Fig. 2.9 is that the density gradient in the region where no combustion is taking place is not constant. Another phenomenon shown by Fig. 2.9 are the oscillations in the density profiles near the projectile base boundary. These oscillations become more pronounced as the shot progresses and are non-physical in origin.

Figure 2.10 shows combustion gas temperatures plotted against normalized axial distance at five projectile displacements. These plots show that the axial gradient of temperature is nearly zero in the combustion region. In the region of no combustion, however, the temperature gradient is not constant.

Figure 2.10 shows that combustion gas temperature tends to rise when approaching the projectile base. This temperature increase appears to have been caused primarily by energy transport from the combustion region. The oscillations with temperature profiles near the projectile base boundary are a response to the numerically induced oscillations in combustion gas density.

Figure 2.11 shows combustion gas velocity plotted against axial distance at five projectile displacements. These plots show that the axial gradient of velocity is nearly constant in both the combustion region and the region of no combustion and that the magnitude of the axial gradient of velocity changes suddenly upon entry into the region

of no combustion.

Inspection of the velocity plots in Fig. 2.11 reveals that in the region where (x/L_p) is less than or equal to 0.5, the velocity first increases with time and then decreases with time. This phenomenon explains why the pressure gradient (see Fig. 2.8) tends toward zero since the deceleration of combustion gas implies that the driving potential (i.e., the pressure gradient) is being reduced.

Inspection of the velocity plots in Fig. 2.11 also shows that the axial velocity distribution approaches a linear profile as the shot progresses and the propellant is consumed.

Chapter 3

Boundary Layer Flows in Tubes

3.1 Introduction

The viscous effects which occur in the interior ballistic cycle were studied using a core flow driven unsteady boundary layer model. The core flow distributions of velocity, density, and temperature were used as edge conditions to drive the unsteady boundary layer formed on the inside of the tube.

The internal ballistic cycle boundary layer flow is typical of most boundary layer flows in that it occurs in a narrow region adjacent to the tube wall. The radial gradients of velocity and temperature are governed by the viscous mixing of the gas. The radial velocity and temperature gradients are steep as velocities range from zero at the tube wall to the core gas velocity and temperature increases from ambient at the wall to the core gas temperature.

The internal ballistic cycle boundary layer flow is different from typical boundary layer flows in that it is highly non-steady. The projectile velocity increases through time, from zero to over 950 meters/sec at the end of the cycle. Pressures drop from a peak of 3×10^8 Pa to 5×10^7 Pa near the projectile at the end of the cycle. Temperature differences are the largest at the beginning of the cycle with the tube wall temperature at 300 K and the chamber at 2800 K.

This boundary layer flow is different from typical boundary layer flows in that the velocity and thermal boundary layers have zero thickness at two locations instead of a single location. At the breech and the projectile, the velocity and thermal boundary layer thicknesses are zero. Going from the breech to the projectile, the boundary layer edges grow, reach a maximum distance from the tube wall, and return to zero.

The internal ballistic cycle boundary layer flow is also different in that the core velocities are driven by the expansion of the chamber volume and the effects of transient expansion waves from the projectile. These core values are imposed as a boundary condition at the edge of the boundary layer. In most tube flows, velocities are driven by a pressure difference between the pipe inlet and the pipe exit.

Although the boundary layer is thin, the effect of the boundary layer on the core is recognized as significant. As heat is transferred to the wall, a cool dense layer of gas forms next to the wall. A negative displacement thickness is produced and the streamlines of the core flow move toward the wall.

Some previous work has been done to study the boundary layer flow of the internal ballistic cycle. Most of this work takes advantage of the similarities between the gun and the shock tube. That is, the internal ballistic cycle boundary layer flow is often modelled as the boundary layer which results from flow through a constant speed shock. Mirels [Ref. 34] obtained the exact numerical solutions to steady compressible laminar boundary layers behind shock waves. Here the boundary layers look steady in a coordinate system fixed to the moving shock wave. Yalamanchili and Reddy [Ref. 35] extended this problem to include the effect of wall temperatures different from the freestream temperature.

Cook and Chapman [Ref. 36] studied the unsteady laminar boundary layer on a flat plate produced by a constant speed shock moving across the plate. The resulting velocity boundary layer had zero thickness at the plate leading edge and at the shock wave. Also, the velocity boundary layer thickness in this study was found to be less than the corresponding velocity boundary layer thickness for a flat plate flow or constant speed shock.

However, the shock approximation is not an appropriate model for this problem. First, the shock is assumed to move with constant velocity. The projectile does not move at constant velocity. Rather, the projectile starts from rest and its velocity may exceed 950 meters/second at the end of the cycle. This produces a rapidly changing freestream condition to which the boundary layer must adjust. Second, the gas velocity is assumed constant once the gas has passed through the shock. In the interior ballistic cycle, axial gradients are present, especially near the projectile. Third, although mass constantly crosses the plane of the shock; mass cannot pass through the projectile.

Burgles [Ref. 22] derived the momentum integral boundary layer equations for a non-steady, non-uniform flow developing in a tube. To facilitate finding a solution, Burgles assumed that the profile shape factor H_{12} (the ratio between displacement thickness δ_1 and momentum thickness δ_2) was constant along the tube length.

A better model was assumed necessary to understand the physics of the boundary layer flow of the interior ballistic cycle and to account properly for the effects of the heat transfer. The objective of the work described in this chapter was to model, calculate, and study the unsteady velocity and temperature boundary layers of the interior ballistic cycle. In this work, a solution technique was adapted from the general algorithm for unsteady compressible boundary layers by Kwon and Pletcher [Ref. 37]. The governing equations were solved using the primitive variables, u , v , T , and p . The governing partial differential equations were discretized using a fully implicit algorithm. Application of Newton linearization

resulted in tridiagonal systems, which were then solved using an efficient tridiagonal solution procedure.

Among the answers sought from the boundary layer model were the location of velocity and temperature boundary layer edges in both space and time. Integral variables such as density, displacement and momentum thicknesses were determined and used to describe viscous and thermal effects occurring in the boundary layer. A good understanding of these effects, will provide a physical basis for the incorporation of second order effects of high speed flow in tubes. These effects can then be used to improve one-dimensional internal ballistic models.

3.2 Description of Problem

An illustration of an idealized boundary layer on a barrel wall is shown in Fig. 3.1. The boundaries are the axisymmetric tube, the fixed breech wall and the movable projectile. A radial coordinate system is set on the breech along the centerline.

The interior ballistic cycle begins with combustion gases in the chamber enclosed by the tube, breech, and projectile. This gas is at high pressure and high temperature. The tube wall is fixed at ambient temperature. The projectile starts at an initial distance along the tube, with a fixed mass in the chamber. The seal between the projectile and the tube wall is assumed to prevent mass from leaving the chamber. The projectile does have mass, and accelerates away from the breech because of the high chamber pressure.

As the projectile accelerates, gas velocities along the centerline increase, driven by the volume expansion of the chamber. The work of Chapter 2 was used to produce these necessary velocities, pressures, and temperatures which drive the boundary layer flow. The no-slip condition on the tube wall creates a velocity gradient between the wall and the centerline. A boundary layer in velocity exists along the length of the tube. Along the breech, the no-slip condition forces all gas velocities to zero, and the velocity boundary layer thickness is zero. Along the projectile wall, the no-slip condition forces all gas velocities to be identical to the projectile velocity, making the velocity boundary layer thickness zero.

An additional characteristic of this flow is the unusually high tube wall shear stress near the projectile. As the projectile accelerates from the breech, new tube wall area is constantly being uncovered. The no-slip condition, $u(\text{wall})=0$, applies at all times along this new area. Gas velocities in the core near the projectile are approximate to

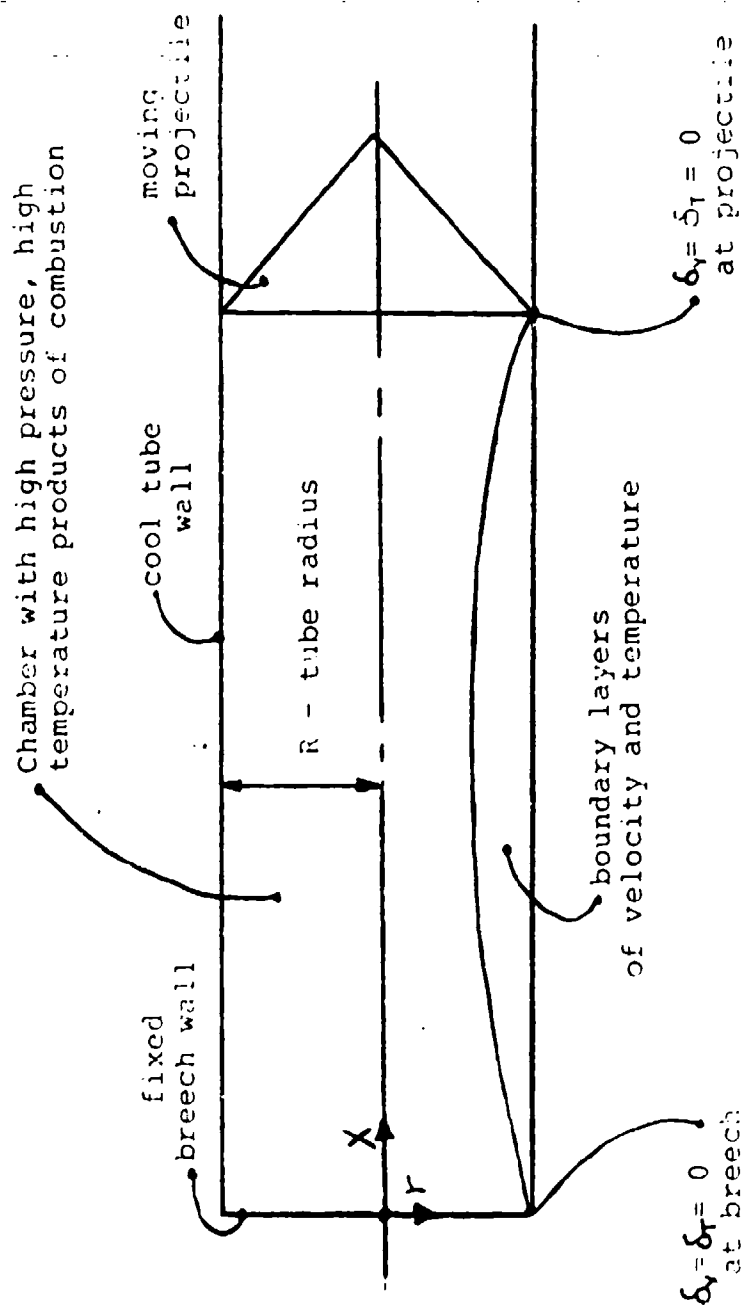


Fig. 3.1 Physical coordinate system for the interior ballistic problem

the projectile velocity itself. Inertial forces are much greater than viscous forces and the boundary layer is kept thin. The thin boundary layer, with high core velocity, creates a steep gradient and unusually high tube wall shear stress near the projectile.

As the projectile accelerates from the breech, the core gas temperature drops but remains relatively high compared to the cool wall, which is fixed at a low temperature. This gradient in gas temperature produces a thermal boundary layer along the length of the tube except at the breech and projectile wall. Along the breech and the projectile wall, all gas temperatures are set equal to the immediate core temperature, and the thermal boundary layer thickness is zero.

An additional characteristic of this flow is the negative displacement thickness produced by the tube wall. The tube wall, held at low temperature, produces a thin layer of dense gas into which mass is constantly being entrained. The radial velocity is negative and streamlines indicate a negative displacement thickness exists.

Very shortly after the start of the interior ballistic cycle, core gas velocities are high enough that momentum effects dominate over the free convection from the cool wall. It is assumed that the thermal boundary layer never reaches the centerline, and there is a substantial amount of core gas which never sees the effect of the cool wall.

Close to the projectile, heat transfer to the tube wall is significant. As the projectile accelerates, cool tube wall is constantly being uncovered. Because of this, the thermal boundary layer near the projectile is not given the opportunity to extend any appreciable distance into the core. The hot core and cool wall create a steep temperature gradient and high rate of heat transfer near the projectile throughout the entire cycle.

3.3 Formulation of Problem

The assumptions used to formulate the equations of motion governing the previously described boundary layer flow are:

- 1) Combustion gases at high pressure and high temperature fill a chamber. The mass of this gas remains constant in time as no gas is allowed to escape the chamber. Also throughout time, the tube wall is held fixed at its initial ambient temperature.
- 2) As the projectile accelerates, core velocities increase and boundary layers in velocity and temperature form. Because these boundary layers are thin and never reach the centerline, there is some core gas which appears to never see the effect of the cool tube wall.
- 3) Gradients in the radial direction are much stronger than gradients in the longitudinal direction. Second derivatives (which correspond to dissipation) in z are negligible to second derivatives in r .
- 4) The pressure gradient in the r direction inside the thin boundary layer is negligible as compared to the longitudinal pressure gradient. Pressure is a function only of z .
- 5) The radial velocity is small when compared to the longitudinal velocity.

These assumptions emphasize that the internal ballistic cycle is much like a typical boundary layer flow with a core flow and thin layers where velocity and temperature gradients exist. Such flow suggests the use of typical boundary layer equations:

Continuity

$$\frac{\partial \rho}{\partial t} + \frac{\partial(\rho v)}{r \partial r} + \frac{\partial(\rho u)}{\partial x} = 0 \quad (3.1)$$

X - Momentum

$$\rho \left(\frac{\partial u}{\partial t} + v \frac{\partial u}{\partial r} + u \frac{\partial u}{\partial x} \right) = \frac{\partial}{\partial r} \left(r \mu \frac{\partial u}{\partial r} \right) - \frac{\partial p}{\partial x} \quad (3.2)$$

Energy

$$\begin{aligned} \rho \left(\frac{\partial H}{\partial t} + u \frac{\partial H}{\partial x} + v \frac{\partial H}{\partial r} \right) - \frac{\partial p}{\partial t} - u \frac{\partial p}{\partial x} \\ = \frac{\partial}{\partial r} \left[r \left[\left(\frac{\mu}{Pr} + \frac{\mu_T}{Pr_T} \right) \frac{\partial H}{\partial r} + \left(\mu \left(1 - \frac{1}{Pr} \right) + \mu_T \left(1 - \frac{1}{Pr_T} \right) \right) u \frac{\partial u}{\partial r} \right] \right] \end{aligned} \quad (3.3)$$

For simplicity, the X-momentum equation will hereafter be called the momentum equation. The unknowns in these equations are:

- 1) longitudinal velocity, u
- 2) radial velocity, v
- 3) density, ρ
- 4) stagnation enthalpy, H

With three equations for four unknowns, at least one more equation is necessary to provide closure. Most often, this equation is an equation of state. However, no single equation exists which relates two or more of the above four unknowns. Three equations will be introduced, with two additional unknowns, temperature and static enthalpy. Since the combustion gas is at sufficiently high temperature, the ideal gas equation of state will be used:

$$P = \rho * R_{Cg} * T \quad (3.4)$$

where P = pressure at a point
 ρ = density at a point
 R_{Cg} = gas constant for the combustion gases
 T = gas temperature at a point

The introduction of T is another unknown. The next equation to be used is the static enthalpy equation:

$$H1 = H - (u^2)/2 \quad (3.5)$$

where $H1$ = static enthalpy at a point
 H = stagnation enthalpy at a point
 u = longitudinal velocity at a point

thermal gradients are steep. For these reasons, the longitudinal coordinate λ is chosen to be placed on the projectile and oriented toward the breech. It must be noted that any longitudinal grid point is dependent on space and time. That is $\lambda = \lambda(z, t)$.

The solution to the equations which govern the interior ballistic cycle boundary layer flow is obtained by marching in time. For a given time, the calculations sweep in the λ direction, from the projectile to the breech. This is opposite in direction to the actual gas flow itself and violates the principle that information is propagated only downstream in boundary layer flows and calculations. It is therefore necessary that the calculation variable also "flow" from the projectile to the breech. A bound for the longitudinal velocity of any gas particle is the projectile velocity. That is, no core gas particle has a longitudinal velocity which exceeds the projectile velocity. By choosing a calculation variable $U = u - u_p$, gas velocities properly orient from the projectile towards the breech.

The coordinate ζ is located on the wall and oriented perpendicular to the core flow. Since viscous effects near the wall are important, grid stretching is employed to cluster more points near the wall and fewer points in the core flow. Since the tube diameter remains constant in time and there is no advantage to changing the stretching function in time, the radial coordinate is not time dependent. The resulting coordinate system is illustrated in Fig. 3.2.

The previously discussed governing equations are transformed (the details are given in Appendix B). These new equations which govern the boundary layer of the interior ballistic cycle are:

Static enthalpy can be related to temperature using experimental data:

$$H_1 = H_1(T) \quad \text{or} \quad T = T(H_1) \quad (3.6)$$

The reciprocal equation, $T = T(H_1)$, assumes that the static enthalpy and temperature are monotonic.

These six equations apply to typical boundary layer flows. The internal ballistic cycle has several departures from the typical boundary layer:

- 1) The core flow occurs in a closed system rather than an open system. The projectile velocity represents a bounds to the core velocity. That is, no gas particle has a longitudinal velocity which exceeds the piston velocity.
- 2) The velocity and thermal boundary layers have zero thickness at two locations instead of a single location. At the breech and the projectile wall, the velocity and thermal boundary layer thicknesses are zero. As the boundary layer equations spatially "march" from one end of the tube to the other, the velocity and thermal boundary layers must reach a peak value and return to zero.
- 3) Core velocities are driven by the volume expansion. Since the projectile experiences acceleration throughout the entire ballistic cycle, the core velocities are also constantly changing in space and time.
- 4) Cool tube wall is constantly being uncovered. Typical boundary layer problems consider a fixed amount of wall area as part of an inertial coordinate system. This problem constantly exposes new tube wall area at the piston, which contributes to high shear stress and high rates of heat transfer near the projectile.

The last item above indicates that the dynamics of most interest occur near the projectile. Near the projectile, core velocities reach maximum values, and velocity and

Continuity

$$\frac{\partial \rho}{\partial \tau} + \lambda_t \frac{\partial \rho}{\partial \lambda} - \frac{1}{r} \zeta_y \frac{\partial}{\partial \zeta} (r \rho v) + \lambda_z \frac{\partial}{\partial \lambda} (\rho U) = 0 \quad (3.7)$$

Momentum

$$\begin{aligned} & \rho \left(\frac{\partial}{\partial \tau} (U + u_p) + (\lambda_t + \lambda_z (U + u_p)) \frac{\partial}{\partial \lambda} (U) - v \zeta_y \frac{\partial}{\partial \zeta} (U) \right) \\ &= \frac{1}{r} \zeta_y \frac{\partial}{\partial \zeta} (r (\mu + \mu_T) \zeta_y \frac{\partial}{\partial \zeta} (U)) - \lambda_z \frac{\partial P}{\partial \lambda} \end{aligned} \quad (3.8)$$

Energy

$$\begin{aligned} & \rho \left(\frac{\partial H}{\partial \tau} + (\lambda_t + \lambda_z (U + u_p)) \frac{\partial H}{\partial \lambda} - v \zeta_y \frac{\partial H}{\partial \zeta} \right) - \frac{\partial P}{\partial \tau} - (\lambda_t + \lambda_z (U + u_p)) \frac{\partial P}{\partial \lambda} \\ &= \frac{1}{r} \zeta_y \frac{\partial}{\partial \zeta} \left[r \left[\left(\frac{\mu + \mu_T}{Pr} \right) \zeta_y \frac{\partial H}{\partial \zeta} \right. \right. \\ & \quad \left. \left. + \left[\mu' \left(1 - \frac{1}{Pr} \right) + \mu_T \left(1 - \frac{1}{Pr_T} \right) \right] (U + u_p) \zeta_y \frac{\partial}{\partial \zeta} (U) \right] \right] \end{aligned} \quad (3.9)$$

Static Enthalpy

$$H1 = H - \frac{(U + u_p)^2}{2} \quad (3.10)$$

Gas Properties

$$T = T(H1) \quad (3.11)$$

Equation of State

$$P = \rho * R_{cg} * T \quad (3.12)$$

The unknowns in these equations are:

- 1) calculation velocity, U
- 2) radial velocity, v
- 3) density, ρ
- 4) stagnation enthalpy, H
- 5) static enthalpy, $H1$
- 6) temperature, T

The knowns in these equations are:

- 1) projectile velocity, u_p
- 2) pressure, P
- 3) viscosity, μ

- 4) turbulent viscosity, μ_T
- 5) Prandtl number, Pr
- 6) turbulent Prandtl number, Pr_T
- 7) gas constant, R_{cg}
- 8) metric coefficients, $\lambda_t, \lambda_z, \zeta_y$

The fluid property of turbulent viscosity μ_T is evaluated using a simple Prandtl mixing length model:

$$\mu_T = \rho * (l_{pr})^2 * \left| \frac{\partial u}{\partial y} \right| \quad (3.13)$$

where l_{pr} is the mixing length. The value of l_{pr} is dependent on whether a given gas particle is in the inner or outer region of the boundary layer. In the inner region, the mixing length $l_{pr} = l_i$ is evaluated by:

$$l_i = K * y * (1 - \exp(-y^+/A^+)) \quad (3.14)$$

$$y^+ = y \sqrt{\left| \frac{\partial u}{\partial y} \right|_w * \frac{\rho_w}{\mu_w}}$$

where K = Von Karman constant = 0.41
 Y = perpendicular distance from wall
 A^+ = damping constant = 26
 ρ_w = density at wall
 μ_w = absolute or dynamic viscosity at wall

In the outer region, the mixing length $l_{pr} = l_o$ is evaluated using:

$$l_o = C_1 * \delta_v \quad (3.15)$$

where $C_1 = 0.089$

δ_v = instantaneous velocity boundary layer thickness.

The switch from the inner region mixing length $l_{pr} = l_i$ to the outer region mixing length $l_{pr} = l_o$ is made when l_i exceeds l_o .

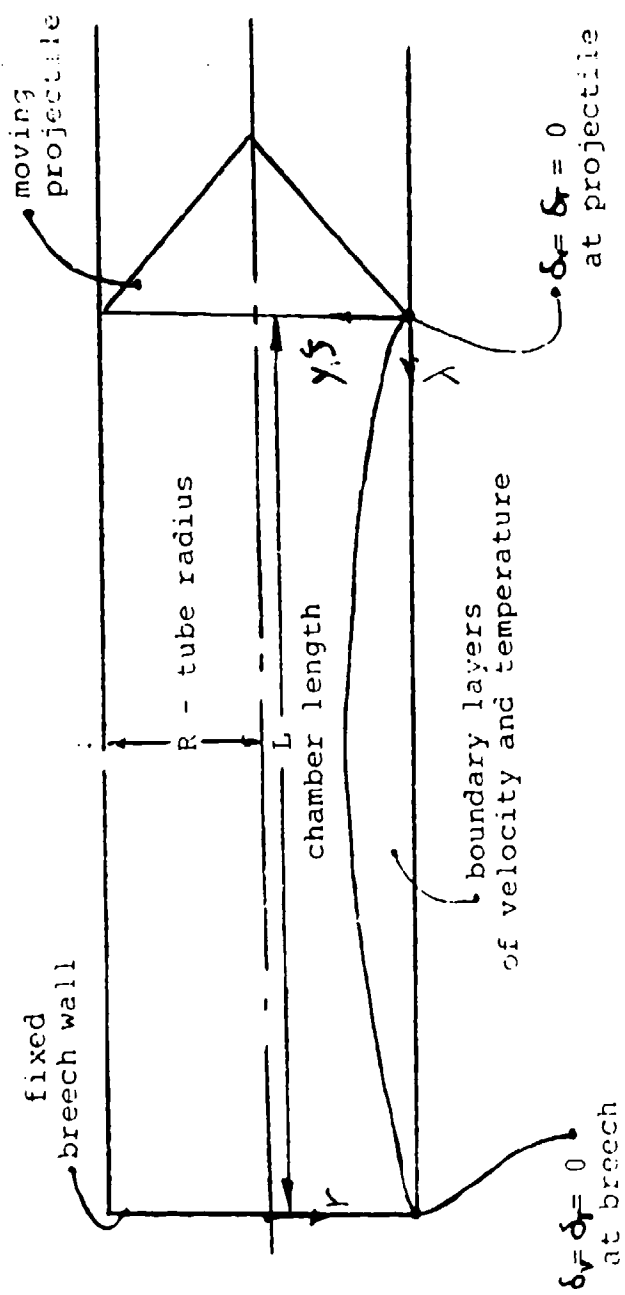


Fig. 3.2 Computational coordinate system for the interior ballistic problem

3.4 Numerical Method of Solution

In the previous section, the equations (3.7) to (3.12) were developed to describe the boundary layer flow of the interior ballistic cycle. There is no analytical solution to this set of non-linear partial differential equations. To solve these coupled equations on a digital computer requires that the continuous physical grid be discretized and that the partial differentials be replaced with finite difference formulas. Typical for boundary layer flows, the following techniques were applied to the momentum and energy equations:

- 1) Partial derivatives in time are forward differenced, involving only the current time step and the next time step forward in time.
- 2) Partial derivatives in the longitudinal direction are all of first order. Backward differencing is applied across the current grid point and the preceeding grid point.
- 3) Partial derivatives in the radial direction use at most three grid points, and are central differenced where possible.

The following techniques typical for boundary layer flows were applied to the continuity equation:

- 1) Partial derivatives in time are forward differenced, involving only the current time step and the next step forward in time.
- 2) Partial derivatives in the longitudinal direction are all of first order. To aid in properly determining mass flux, backward differencing is applied across the current grid point and the preceeding grid point, and across the respective pair of points nearer the tube wall.
- 3) Partial derivatives in the radial direction are all of first order. Backward differencing is applied across the current grid point and the neighboring point nearer the wall.

Except for the partial time derivative, some choice must be made for the time level of each term in the finite difference equations. Normally all of the spatial derivative terms are sought at the current time level (n) or the next time level ($n+1$). Time levels of the spatial derivatives are not mixed. The choice of time level often determines whether the method of solution is explicit or implicit. An explicit scheme results when there is only one unknown in each of the governing equations. An implicit scheme results when any equation contains more than one unknown. Iterative techniques or matrix solvers, or both, must be used to solve the implicit scheme coupled equations.

The equations which govern the interior ballistic cycle boundary layer flow cannot be solved explicitly:

- 1) The continuity equation has a time derivative across density (ρ), providing density at the new time level.
- 2) The momentum equation has a time derivative across calculation velocity (U), providing calculation velocity at the new time level.
- 3) The energy equation has a time derivative across stagnation enthalpy (H), providing stagnation enthalpy at the new time level.
- 4) With density known, the ideal gas equation of state provides temperature (T).
- 5) The temperature being known implies a static enthalpy (H_1) from gas property tables.
- 6) Static enthalpy (H_1) being known and the calculation velocity (U) being known implies a stagnation enthalpy (H) which is possibly different from that obtained in step 3.
- 7) The radial velocity (v) is never solved.

The logical step to development of an explicit scheme determine two values for the stagnation enthalpy (H), while failing to solve for the radial velocity (v). The equations

which govern the interior ballistic cycle boundary layer flow cannot be solved explicitly.

If the convention is retained that time levels within spatial derivatives are not mixed, then an implicit scheme must be used. All the spatial derivative terms are sought at the next time level $(n+1)$. Following the previously mentioned guidelines for finite differencing, the resulting equations are:

Continuity

$$\begin{aligned}
 & \left[\frac{1}{4\Delta\tau} \right] \left[(\rho_{1,j})^{n+1} + (\rho_{1-1,j})^{n+1} + (\rho_{1,j-1})^{n+1} + (\rho_{1-1,j-1})^{n+1} \right. \\
 & \quad \left. - (\rho_{1,j})^n - (\rho_{1-1,j})^n - (\rho_{1,j-1})^n - (\rho_{1-1,j-1})^n \right] \\
 & + \left[\frac{\lambda_{t1}}{2\Delta\lambda} + \frac{\lambda_{z1}u_p}{\Delta\lambda} \right] \left[(\rho_{1,j})^{n+1} - (\rho_{1-1,j})^{n+1} \right. \\
 & \quad \left. + (\rho_{1,j-1})^{n+1} - (\rho_{1-1,j-1})^{n+1} \right] \\
 & - \left[\frac{\zeta_{y1}}{r_j \Delta\zeta} \right] \left[r_j (\rho_{1,j} v_{1,j})^{n+1} - r_{j-1} (\rho_{1,j-1} v_{1,j-1})^{n+1} \right] \\
 & + \left[\frac{\lambda_{z1}}{\Delta\lambda} \right] \left[(\rho_{1,j} U_{1,j})^{n+1} - (\rho_{1-1,j} U_{1-1,j})^{n+1} \right. \\
 & \quad \left. + (\rho_{1,j-1} U_{1,j-1})^{n+1} - (\rho_{1-1,j-1} U_{1-1,j-1})^{n+1} \right] = 0 \quad (3.16)
 \end{aligned}$$

Momentum

$$\begin{aligned}
 & \left[\frac{(\rho_{1,j})^{n+1}}{\Delta\tau} \right] \left[(U_{1,j})^{n+1} - (U_{1,j})^n + (u_{p1,j})^{n+1} - (u_{p1,j})^n \right] \\
 & + \left[\frac{(\rho_{1,j})^{n+1}}{\Delta\lambda} \right] \left[(\lambda_{t1} + \lambda_{z1}(U_{1,j} + u_p))^{n+1} (u_{1,j})^{n+1} - (u_{1-1,j})^{n+1} \right] \\
 & - \left[\frac{(\rho_{1,j} v_{1,j})^{n+1}}{2\Delta\zeta} \right] \zeta_{y1} (u_{1+1,j} - u_{1-1,j})^{n+1} \\
 & = \frac{\zeta_{y1}}{\Delta\zeta r_j} \left[(r_{j+1/2}) \left(\frac{\mu_{1,j+1} + \mu_{1,j}}{2} + \frac{\mu_{T1,j+1} + \mu_{T1,j}}{2} \right) \zeta_{y,j+1/2} (u_{1,j+1} - u_{1,j})^{n+1} \right]
 \end{aligned}$$

$$\begin{aligned}
& - (r_{j-1/2}) \left(\frac{\mu_{1,j} + \mu_{1,j-1}}{2} + \frac{\mu_{T1,j} + \mu_{T1,j-1}}{2} \right) \zeta_{y,j-1/2} \frac{(u_{1,j} - u_{1,j-1})^{n+1}}{\Delta \zeta} \\
& - \left[(\lambda_{z1})^{n+1} \right] \left[(P_1 - P_{1-1})^{n+1} \right] / \Delta \lambda
\end{aligned} \tag{3.17}$$

Energy

$$\begin{aligned}
& \left[(\rho_{1,j})^{n+1} \right] \left[\frac{(H_{1,j})^{n+1} - (H_{1,j})^n}{\Delta \tau} \right] \\
& + \left[\frac{(\rho_{1,j})^{n+1}}{\Delta \lambda} \right] \left[(\lambda_{z1} + \lambda_{z1} (U_{1,j} + u_p))^{n+1} \right] \left[(H_{1,j})^{n+1} - (H_{1-1,j})^{n+1} \right] \\
& - \left[\frac{(\rho_{1,j} v_{1,j})^{n+1}}{2 \Delta \zeta} \right] \zeta_{y,j} \left[(H_{1,j+1} - H_{1,j-1})^{n+1} \right] \\
& - \frac{\zeta_{y,j}}{r_j \Delta \zeta} \left[r_{j+1/2} \right] \left(\frac{\mu_{1,j+1} + \mu_{1,j}}{Pr_{1,j+1} + Pr_{1,j}} + \frac{\mu_{T1,j+1} + \mu_{T1,j}}{Pr_{T1,j+1} + Pr_{T1,j}} \right) \\
& \quad \left[\zeta_{y,j+1/2} \right] \left[\frac{(H_{1,j+1} - H_{1,j})^{n+1}}{\Delta \zeta} \right] \\
& + \frac{\mu_{1,j+1} + \mu_{1,j}}{2} \left(1 - \frac{2}{Pr_{1,j} + Pr_{1,j+1}} + \frac{\mu_{T1,j+1} + \mu_{T1,j}}{2} \left(1 - \frac{2}{Pr_{T1,j+1} + Pr_{T1,j}} \right) \right) \\
& \quad * \left(\frac{(U_{1,j+1} + U_{1,j} + u_p)^{n+1}}{2} \right) \zeta_{y,j+1/2} \left(\frac{(U_{1,j+1} - U_{1,j})^{n+1}}{\Delta \zeta} \right) \\
& - \left[r_{j-1/2} \right] \left(\frac{\mu_{1,j} + \mu_{1,j-1}}{Pr_{1,j} + Pr_{1,j-1}} + \frac{\mu_{T1,j} + \mu_{T1,j-1}}{Pr_{T1,j} + Pr_{T1,j-1}} \right) \\
& \quad \left[\zeta_{y,j-1/2} \right] \left[\frac{(H_{1,j} - H_{1,j-1})^{n+1}}{\Delta \zeta} \right] \\
& - \left[\frac{\mu_{1,j} + \mu_{1,j-1}}{2} \left(1 - \frac{2}{Pr_{1,j} + Pr_{1,j-1}} + \frac{\mu_{T1,j} + \mu_{T1,j-1}}{2} \left(1 - \frac{2}{Pr_{T1,j} + Pr_{T1,j-1}} \right) \right) \right. \\
& \quad \left. * \left(\frac{(U_{1,j} + U_{1,j-1} + u_p)^{n+1}}{2} \right) \zeta_{y,j-1/2} \left(\frac{(U_{1,j} - U_{1,j-1})^{n+1}}{\Delta \zeta} \right) \right]
\end{aligned}$$

$$+ \left[\frac{(P_i)^{n+1} - (P_i)^n}{\Delta \tau} \right] + \left[(\lambda_{t1} + \lambda_{z1} (U_{i,j} + u_p))^{n+1} \right] \left[\frac{(P_{i,j})^{n+1} - (P_{i-1,j})^{n+1}}{\Delta \lambda} \right] \quad (3.18)$$

Static Enthalpy

$$(H_{i,j})^{n+1} = (H_i)^{n+1} - \frac{((U_{i,j} + u_p)^{n+1})^2}{2} \quad (3.19)$$

Gas Properties

$$(T_{i,j})^{n+1} = T((H_{i,j})^{n+1}) \quad (3.20)$$

Equation of State

$$(P_{i,j})^{n+1} = (\rho_{i,j})^{n+1} * R_{cg} * (T_{i,j})^{n+1} \quad (3.21)$$

The subscript (i) refers to the axial location of a computational grid point. This subscript (i) ranges from i=1 to i=IL, where IL is the number of axial grid points.

The subscript (j) refers to the radial location of a computational grid point. This subscript (j) ranges from j=1 to j=JL, where JL is the number of radial grid points.

The solution to the finite difference equations is obtained by marching in time. For a given time, calculations sweep in the λ direction, from the projectile to the breech. This is in the same direction as the flow, propagating information to the next i-station. At a give i-station, unknowns in the finite difference equations occur at the (j-1), (j), and (j+1) gridpoints.

The continuity, energy, static enthalpy, and gas property equations and the ideal gas equation of state are all linear and can be efficiently solved on a digital computer. However, the momentum equation is non-linear in calculation velocity (U) at the gridpoint (i,j). To efficiently solve the momentum equation on a digital computer, this $(U_{i,j})^2$ term must be linearized. Newton linearization is used:

$$(U^2)^{n+1} \equiv 2(\hat{U}U)^{n+1} - ((\hat{U})^{n+1})^2 \quad (3.22)$$

where U = calculation velocity
 \hat{U} = predicted calculation velocity,
 U from most recent iteration

The resulting linearized momentum equation is:

$$\begin{aligned} & \left[\frac{(\rho_{1,j})^{n+1}}{\Delta \tau} \right] \left[(U_{1,j})^{n+1} - (U_{1,j})^n + (u_{p1,j})^{n+1} - (u_{p1,j})^n \right] \\ & + \left[\frac{(\rho_{1,j})^{n+1}}{\Delta \lambda} \right] \left[(\lambda_{t1} + \lambda_{z1} u_p)^{n+1} \right] \left[(U_{1,j})^{n+1} - (U_{1-1,j})^{n+1} \right] \\ & + \left[\frac{(\rho_{1,j})^{n+1}}{\Delta \lambda} \right] \left[(\lambda_{z1})^{n+1} \right] \left[-(\hat{U}_{1,j})^{n+1}{}^2 - (2\hat{U}_{1,j}U_{1,j})^{n+1} + (U_{1,j}U_{1-1,j})^{n+1} \right] \\ & - \left[\frac{(\rho_{1,j}v_{1,j})^{n+1}}{2\Delta \zeta} \right] \zeta_{y,j} \left[(U_{i+1,j} - U_{i-1,j})^{n+1} \right] \\ & = \frac{\zeta_{y,j}}{\Delta \zeta r_j} \left[\begin{aligned} & (r_{j+1/2}) \frac{\mu_{1,j+1} + \mu_{1,j}}{2} + \frac{\mu_{T1,j+1} + \mu_{T1,j}}{2} \zeta_{y,j+1/2} \frac{(u_{1,j+1} - u_{1,j})^{n+1}}{\Delta \zeta} \\ & - (r_{j-1/2}) \frac{\mu_{1,j} + \mu_{1,j-1}}{2} + \frac{\mu_{T1,j} + \mu_{T1,j-1}}{2} \zeta_{y,j-1/2} \frac{(u_{1,j} - u_{1,j-1})^{n+1}}{\Delta \zeta} \end{aligned} \right] \\ & - \left[\frac{(\lambda_{z1})^{n+1}}{\Delta \lambda} \right] \left[(P_1 - P_{1-1})^{n+1} \right] \quad (3.23) \end{aligned}$$

The use of Newton linearization for the $(U_{1,j})^2$ term of the momentum equation necessitates the use of iteration in obtaining a solution at a given i -station. The iteration procedure starts with values of H , U , p , and v from the previous time level, adjusted for the projectile acceleration and increase in chamber length. The energy equation is solved for stagnation enthalpy (H). The linearized momentum

equation is solved for calculation velocity (U). The ideal gas equation of state is solved for density (ρ). The continuity equation is solved for radial velocity (v). The new values of H , U , ρ , and v are used as initial values for the next iteration and the iteration process is repeated until an acceptable solution is obtained. An acceptable solution for the time level ($n+1$) at the given i -station requires convergence by one of two criteria:

- 1) If the number of iterations for a given station reaches 30, oscillation around the correct answer is assumed. The oscillated values from the two most recent iterations are averaged to provide the answer at this i -station for this time level.
- 2) For every variable, at every (i,j) gridpoint:
 - a) If the absolute value for a variable at a point is less than $1E-4$, then convergence at this point, for this variable, for this time level is met.
 - or b) If the difference between successive iterations for a variable at a point is less than 00.01%, convergence at this point, for this variable, for this time level is met.

The fluid properties of viscosity (μ), temperature (T), and Prandtl number (Pr) have been calculated and stored in table form. These fluid properties are dependent on the static enthalpy:

$$\mu = \mu((H1_{i,j})^{n+1}) \quad T = T((H1_{i,j})^{n+1}) \quad Pr = Pr((H1_{i,j})^{n+1})$$

These fluid properties are updated during an iteration step by the solution of the energy equation for the stagnation enthalpy (H) and the solution of the linearized momentum equation for the calculation velocity (U), which together define the static enthalpy ($H1$).

The fluid property of turbulent Prandtl number (Pr_T) has been set to unity and requires no updating during iterations.

The fluid property of turbulent viscosity (μ_T) is evaluated using a simple Prandtl mixing length model. The turbulent viscosity is updated during an iteration step by the solution of the energy equation for the stagnation enthalpy, the solution of the linearized momentum equation for the calculation velocity (U), and the solution of the ideal gas equation of state for density (ρ).

Very shortly after the start of the interior ballistic cycle, core gas velocities are high enough that momentum effects dominate over the free convection from the cool wall. It is assumed that the thermal boundary layer never reaches the centerline, and there is a substantial amount of core gas which never sees the effect of the cool wall. Within this core gas, radial gradients in velocity or temperature do not exist and calculations are not necessary. At a given i -station, calculations are performed only to the boundary layer edge. The location of this boundary layer edge is determined in the following manner:

- 1) At a given i -station, the radial velocity gradient edge (JV) is defined as the first grid point from the wall where $u \geq 0.95 * u(\text{core})$.
- 2) At a given i -station, the radial temperature gradient edge (JT) is defined as the first grid point from the wall where $T \geq 0.95 * T(\text{core})$.
- 3) At a given i -station, the boundary layer edge is defined as the maximum of JV or JT, with an additional three grid points added to allow for velocity or temperature boundary layer growth.

The location of the boundary layer edge is updated after each iteration.

The core velocities, core pressures, and core temperatures which drive the internal ballistic cycle boundary layer flow are taken from the work of Chapter 2. These core values, determined by one-dimensional Euler equations where specific heat is non-constant, will not satisfy the boundary layer momentum or energy equations. Some adjustment of the core gradients is necessary:

- 1) Along the centerline, the radial velocity (v), and first and second derivatives in the radial direction are zero. The momentum and energy equation reduce to a coupled set of equations with unknowns of calculation velocity (U), pressure (P), and enthalpy (H). Imposing one of these three as an input profile specifies the profiles of the other two.
- 2) Velocities are considered of most importance, and the velocity profile is chosen to be the independent profile.
- 3) The momentum equation implies a pressure profile from the initial value of pressure on the projectile. The energy equation implies an enthalpy profile from the initial value of enthalpy on the projectile. Velocity and enthalpy prescribe the temperature profile. Since the pressure and enthalpy profiles are themselves dependent on the temperature, some iteration is necessary to obtain a convergent set of pressure and temperature profiles.

3.5 Results

To draw conclusions about boundary layer flow inside tubes, several parameters are examined.

The velocity boundary layer edge (δ_v) at a given i-station is defined as the first location away from the wall where the gas velocity equals 95% of the core velocity at that i-station.

The thermal boundary layer edge (δ_T) at a given i-station is defined as the first location away from the wall where the gas temperature equals 95% of the core temperature at that i-station.

For compressible flow inside tubes, the displacement thickness (δ_1) is given by:

$$\frac{\delta_1}{R} = 1 - \sqrt{1 + \frac{2}{R^2} \int_{r=R}^{r=0} \left[\frac{1 - \frac{\rho u}{\rho_e u_e}}{\rho_e u_e} \right] r dr}$$

For compressible flow inside tubes, the momentum thickness (δ_2) is given by:

$$\frac{\delta_2}{R} = 1 - \sqrt{1 + \frac{2}{R^2} \int_{r=R}^{r=0} \left[\frac{\rho u}{\rho_e u_e} \right] \left[\frac{1 - \frac{u}{u_e}}{u_e} \right] r dr}$$

For compressible flow inside tubes, the energy thickness (δ_3) is given by:

$$\frac{\delta_3}{R} = 1 - \sqrt{1 + \frac{2}{R^2} \int_{r=R}^{r=0} \left[\frac{\rho u}{\rho_e u_e} \right] \left[\frac{1 - \frac{u^2}{u_e^2}}{u_e^2} \right] r dr}$$

For compressible flow inside tubes, the density thickness (δ_ρ) is given by:

$$\frac{\delta_\rho}{R} = 1 - \sqrt{1 + \frac{2}{R^2} \int_{r=R}^{r=0} \left[1 - \frac{\rho}{\rho_e} \right] r dr}$$

The interior ballistic cycle occurs in an axisymmetric tube, so that $A = \pi R^2$, $dA = 2\pi r dr$, and the limits of integration go from the tube wall ($r=R$) to the centerline ($r=0$).

The work of Chapter 4 will model the interior ballistic problem as one-dimensional. In this model, integral averages over a cross sectional area remove radial dependence, so that mass, momentum, and energy are only axially dependent. To study the validity of this one-dimensional model, three ratios are examined:

$$K_{\rho u} = \frac{[1/A \int \rho u dA]}{[1/A \int \rho dA] [1/A \int u dA]}$$

$$K_{\rho u^2} = \frac{[1/A \int \rho u^2 dA]}{[1/A \int \rho dA] [1/A \int u^2 dA]}$$

$$K_{eu} = \frac{[1/A \int e u dA]}{[1/A \int e dA] [1/A \int u dA]}$$

where e is the total energy:

$$e = \rho(u(T) + 0.5u^2) = \rho \left[h - \frac{p}{\rho} + 0.5u^2 \right]$$

If $K_{\rho u}$, $K_{\rho u^2}$, K_{eu} are close to unity, the one-dimensional model is good. The interior ballistic cycle occurs in an axisymmetric tube, so that $A = \pi R^2$, $dA = 2\pi r dr$, and the limits of integration go from the centerline ($r=0$) to the tube wall ($r=R$).

The boundary layer flow of the interior ballistic

problem was examined using input data from Heiney's test case 536 [Ref. 14 and 29]. The projectile started at a distance of 0.22 meters from the breech. The chamber enclosed by the projectile and breech was filled with combustion gases at a pressure of 6.6×10^6 Pa and temperature of 2916 K. As shown in Fig. 3.3, input variations in pressure, temperature, and velocity were determined at the projectile base through time using the computer code of Ref. 14. A linear core velocity profile was assumed from the projectile to the breech. The pressure and temperature profiles are then determined from the momentum and energy equations respectively.

The first output parameter examined was the displacement thickness. Figure 3.4 shows that the displacement thickness is negative for most of space and time. A short time after the projectile passed a point in the tube wall, the cool temperature of the wall created a thin layer of dense gas next to the wall. Since the tube wall temperature is held fixed at ambient temperature, core gas is constantly entrained into this thin layer of dense gas and the displacement thickness at a point continues to grow in time. The movement of core gas towards the wall is expansion that does no useful work. The pressure times change in volume of this process is a measure of this energy loss.

Figure 3.5 shows the momentum thickness as a function of time and space for the test case 536. The momentum thickness is similar to the displacement thickness in that it is negative for the majority of space and time. The momentum thickness differs from the displacement thickness in that viscous forces have more influence. This is evident in the shape of the momentum thickness curve for fixed time. Near the breech, the core velocity is small and the resulting radial gradient of axial velocity is also small. Viscous effects near the breech are small, so that thermal effects dominate and the distributions of momentum and the displacement thicknesses have a similar slope. Near the

projectile, the gas velocities are high, causing large velocity gradients in the radial direction. Viscous effects dominate causing the momentum thickness curve to pass from negative to positive. Once positive, the momentum thickness reaches a maximum and returns to zero at the projectile. The peaks in momentum thickness correspond to peaks in the velocity boundary layer.

The ratio of the momentum thickness to the displacement thickness is known as the shape factor H_{12} . Figure 3.6 shows the shape factor H_{12} as a function of time and space for the test case 536. As the momentum thickness crosses from negative to positive, the shape factor H_{12} experiences a sign change. Examination of Figure 3.6 shows that the shape factor H_{12} is not constant in time. Figure 3.7 shows the shape factor H_{12} normalized over axial distance. Figure 3.7 further shows that the shape factor H_{12} is not constant in time. These suggest that the shape factor is not a good correlator.

Figure 3.8 shows the velocity boundary layer as a function of time and space. As predicted, this boundary layer has zero thickness at two locations, the breech and the projectile. It is seen that the velocity boundary layer is small as assumed, reaching a maximum thickness of four percent of the tube radius. The internal ballistic problem has the characteristic of removing points previously in the velocity boundary layer. At a given x location, the projectile passes and the boundary layer at this x location grows, peaks, and then decreases. This has significance in the fact that there are some points previously in the velocity boundary layer that are removed from the velocity boundary layer at this x location.

Figure 3.9 shows the thermal boundary layer as a function of time and space for the test case 536. As predicted, this boundary layer has zero thickness at two locations, the breech and the projectile. It is seen that the thermal boundary layer is small as assumed, reaching a

maximum thickness of 11 percent of the tube radius. The growth rate of the thermal boundary layer is approximately twice that of the velocity boundary layer. Further, all points enveloped in the thermal boundary layer remain within this thermal boundary layer through time.

The objective of the interior ballistic problem is to accelerate a projectile. This objective is accomplished by the high chamber pressure. The cool tube wall has the effect of increasing the effective chamber volume and decreasing the effective pressure which acts on the projectile. The final result is a decrease in the muzzle exit velocity of the projectile.

The density thickness (Fig. 3.10) provides a measure of this effective volume increase. An assumption made of the interior ballistic cycle was that the mass in the chamber is constant. For the proper density flux at any given cross section, the one dimensional model must increase the tube radius since density thickness is negative. As the effective volume increases, the effective pressure must decrease, assuming the combustion gas acts as an ideal gas:

$$P * V = m * R * T = \text{constant}$$

The change in effective volume is shown in Fig. 3.11.

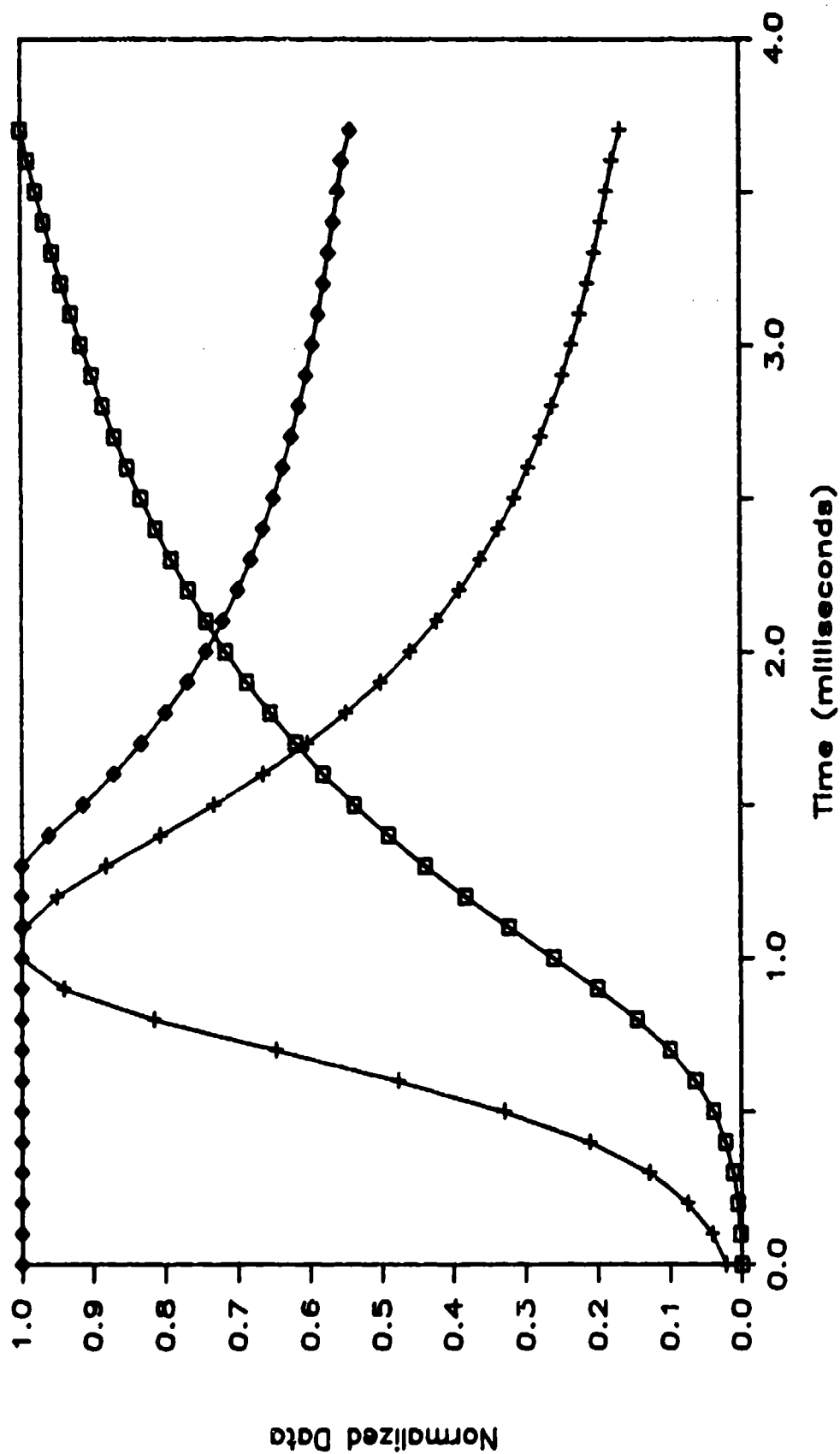


Fig. 3.3 Variations in velocity, pressure, and temperature for test case 536. \square Velocity (max=940 meters/sec)
 $+$ Pressure (max=3.1 x 10⁻⁸ Pa) \diamond Temperature (max=2917 K)

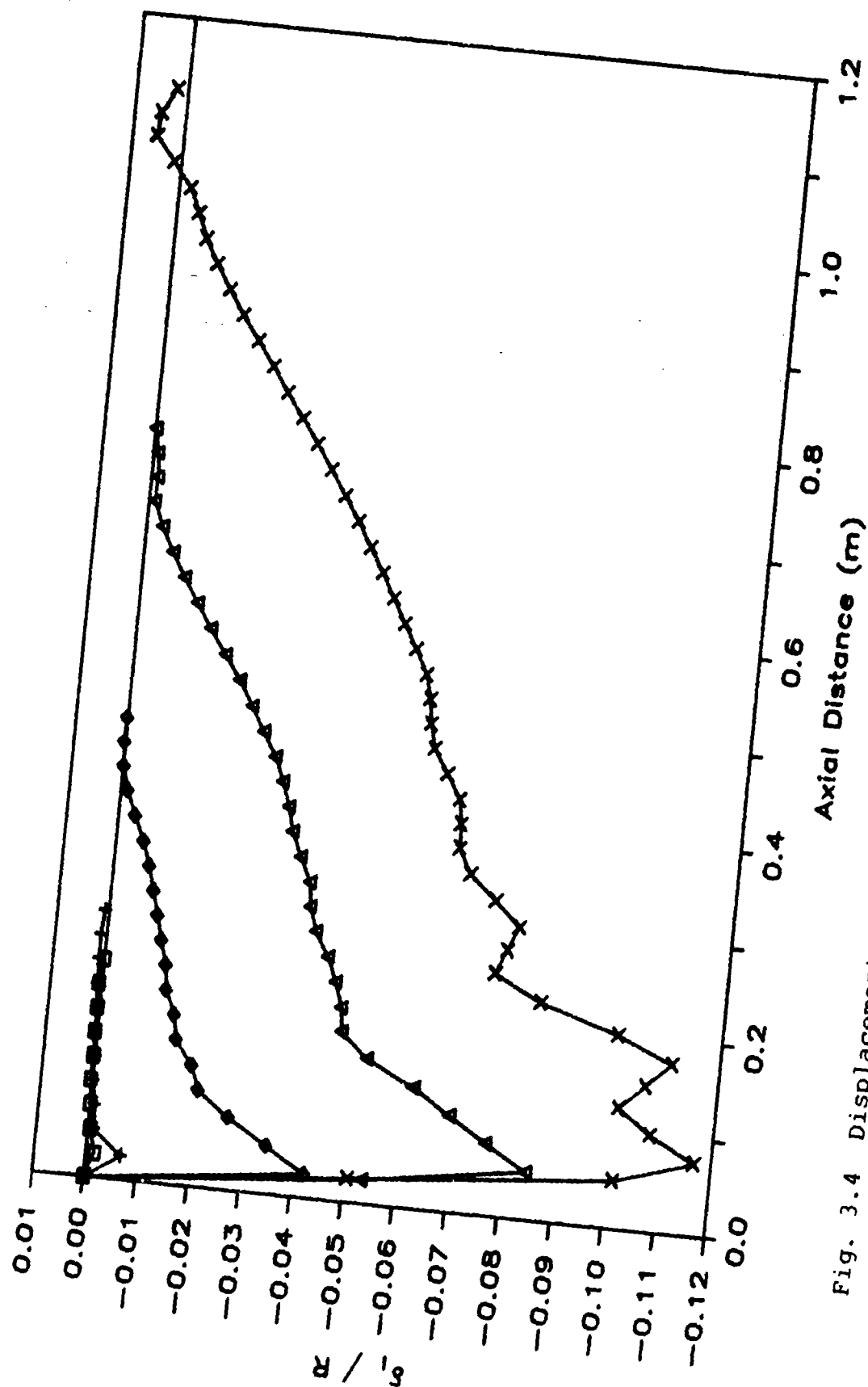


Fig. 3.4 Displacement thickness as a function of space and time for the test case 536. \square 500 μsec Δ 2000 μsec \diamond 1500 μsec

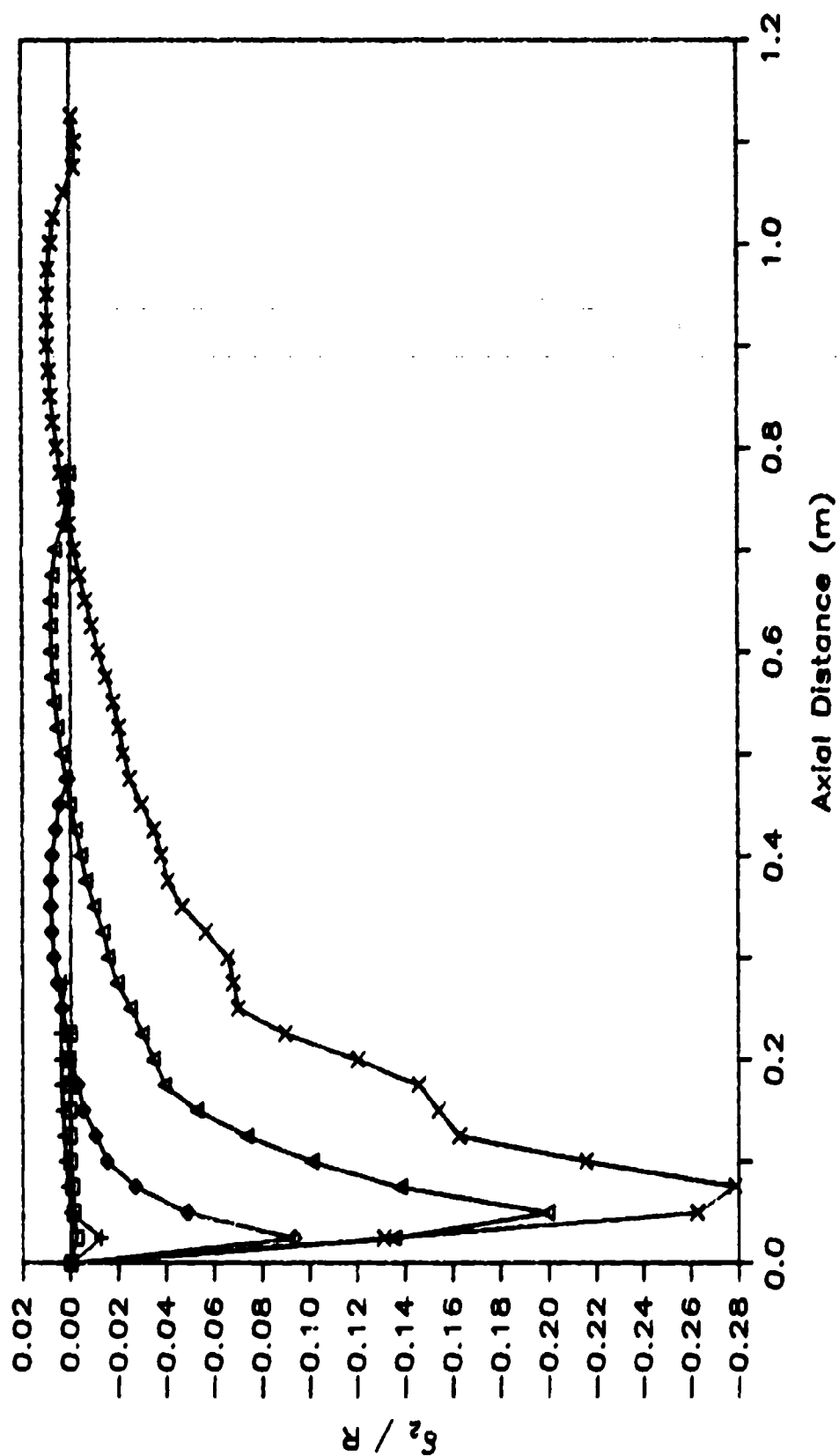


Fig. 3.5 Momentum thickness as a function of space and time for the test case 536. □ 500 μsec +1000 μsec Δ 1500 μsec x 2000 μsec

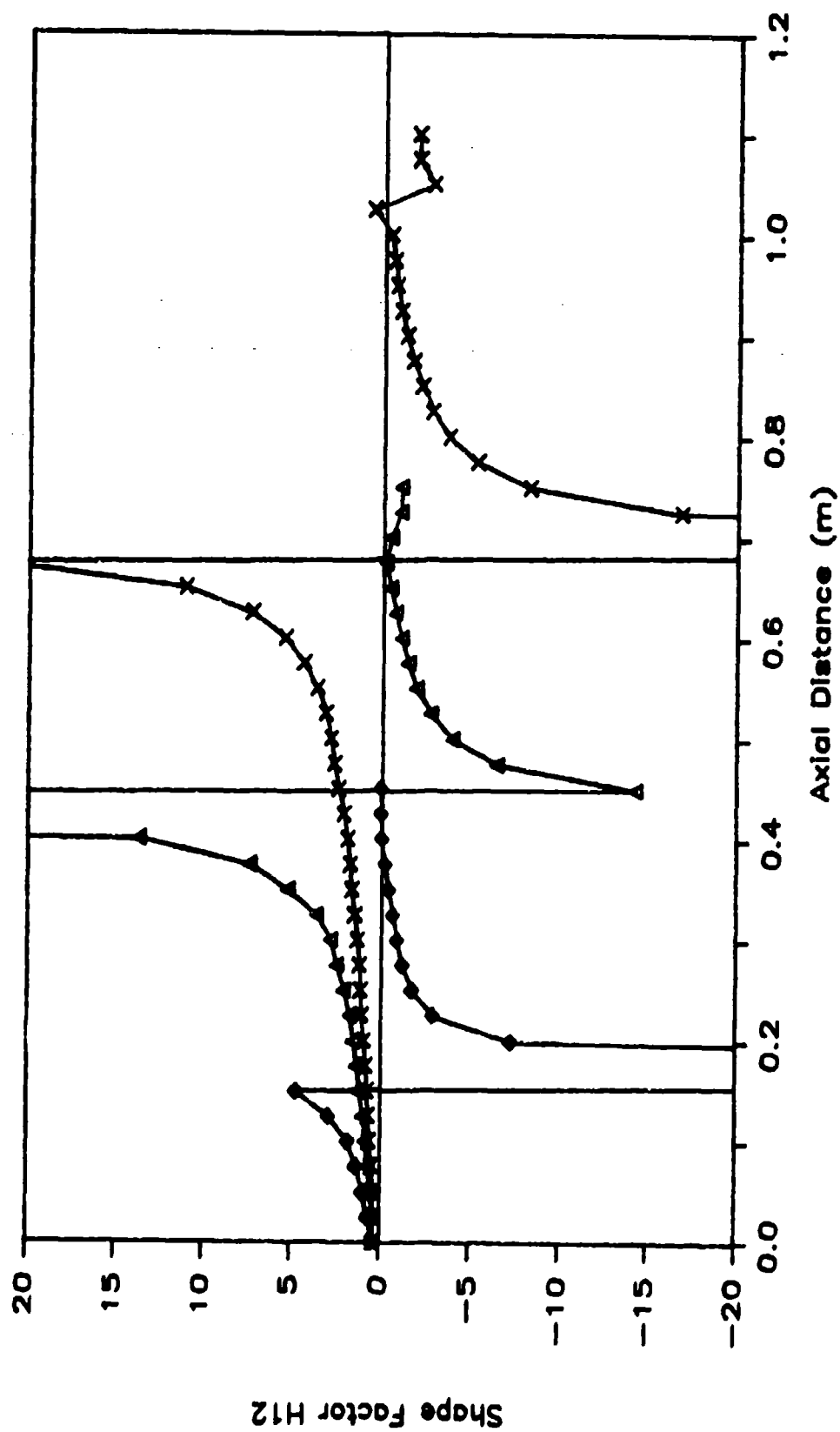


Fig. 3.6 Shape Factor H12 as a function of space and time for the test case 536. \diamond 1500 μsec Δ 2000 μsec \times 2500 μsec

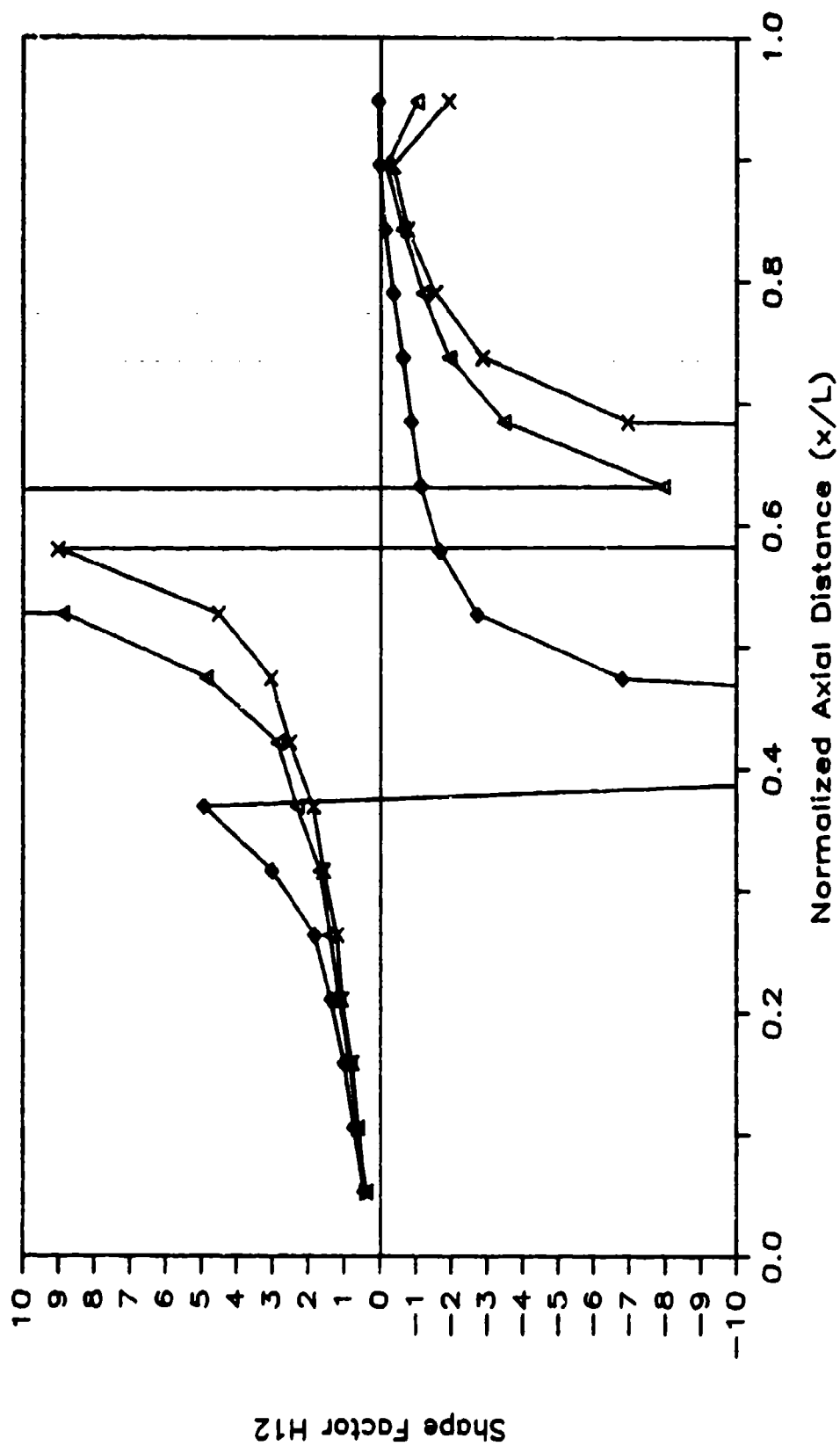


Fig. 3.7 Shape Factor H12 as a function time for the test case 536.
 ◇ 1500 μsec Δ 2000 μsec × 2500 μsec

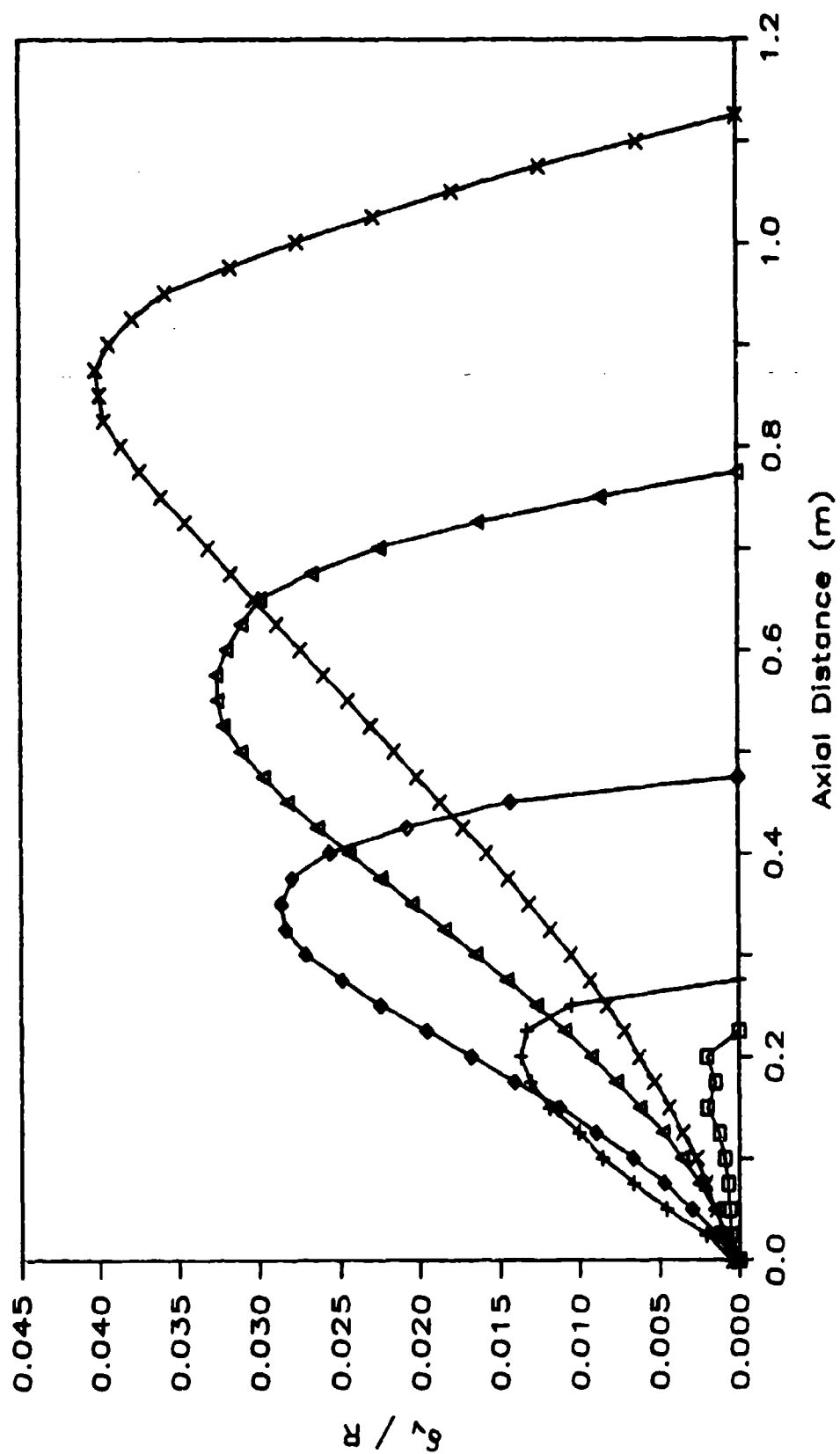


Fig. 3.8 Velocity Boundary Layer as a function of space and time for the test case 536. \square 500 μsec $+$ 1000 μsec \diamond 1500 μsec Δ 2000 μsec \times 2500 μsec

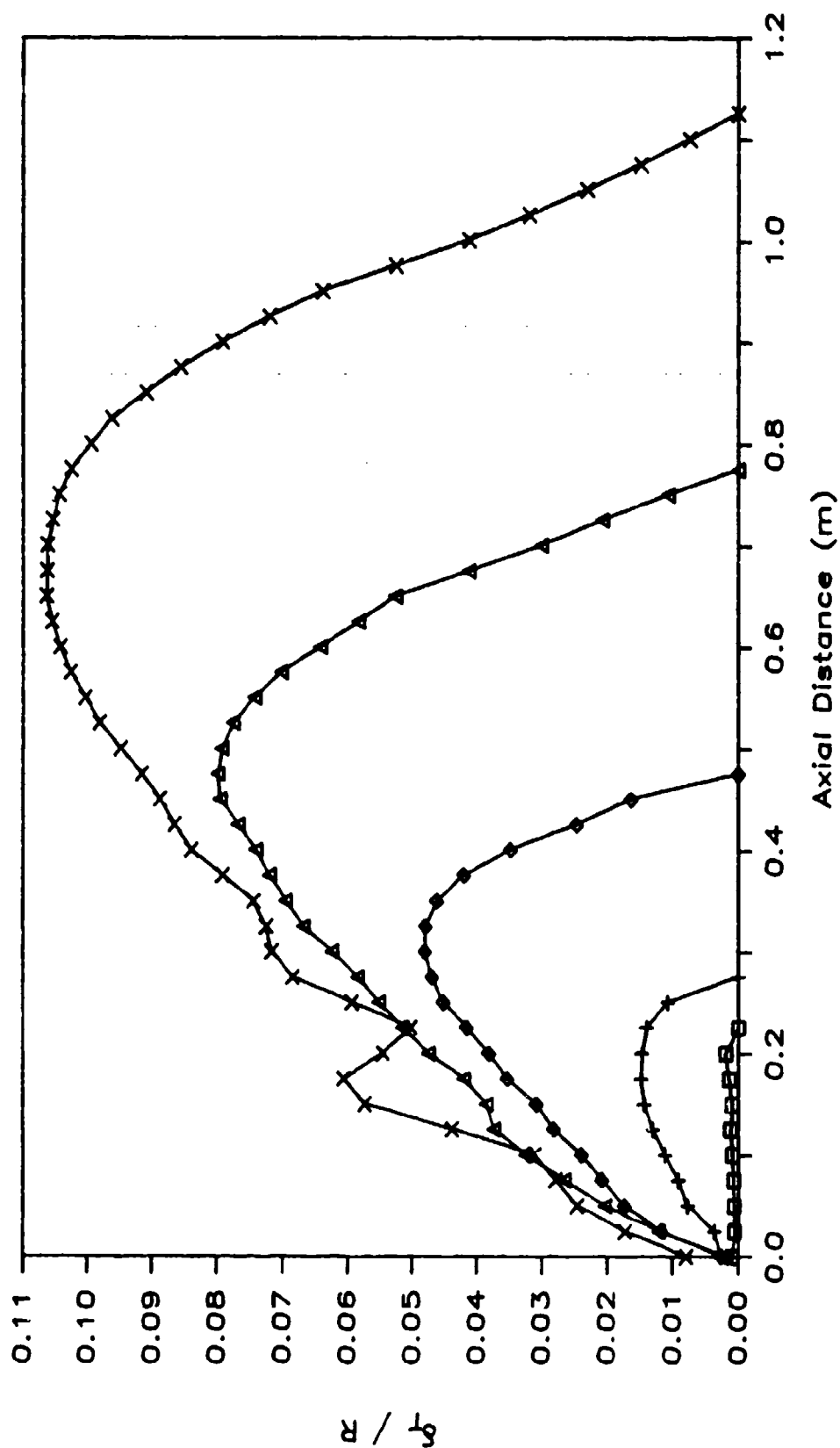


Fig. 3.9 Thermal Boundary Layer as a function of space and time for the test case 536. \square 500 μsec $+$ 1000 μsec \diamond 1500 μsec Δ 2000 μsec \times 2500 μsec

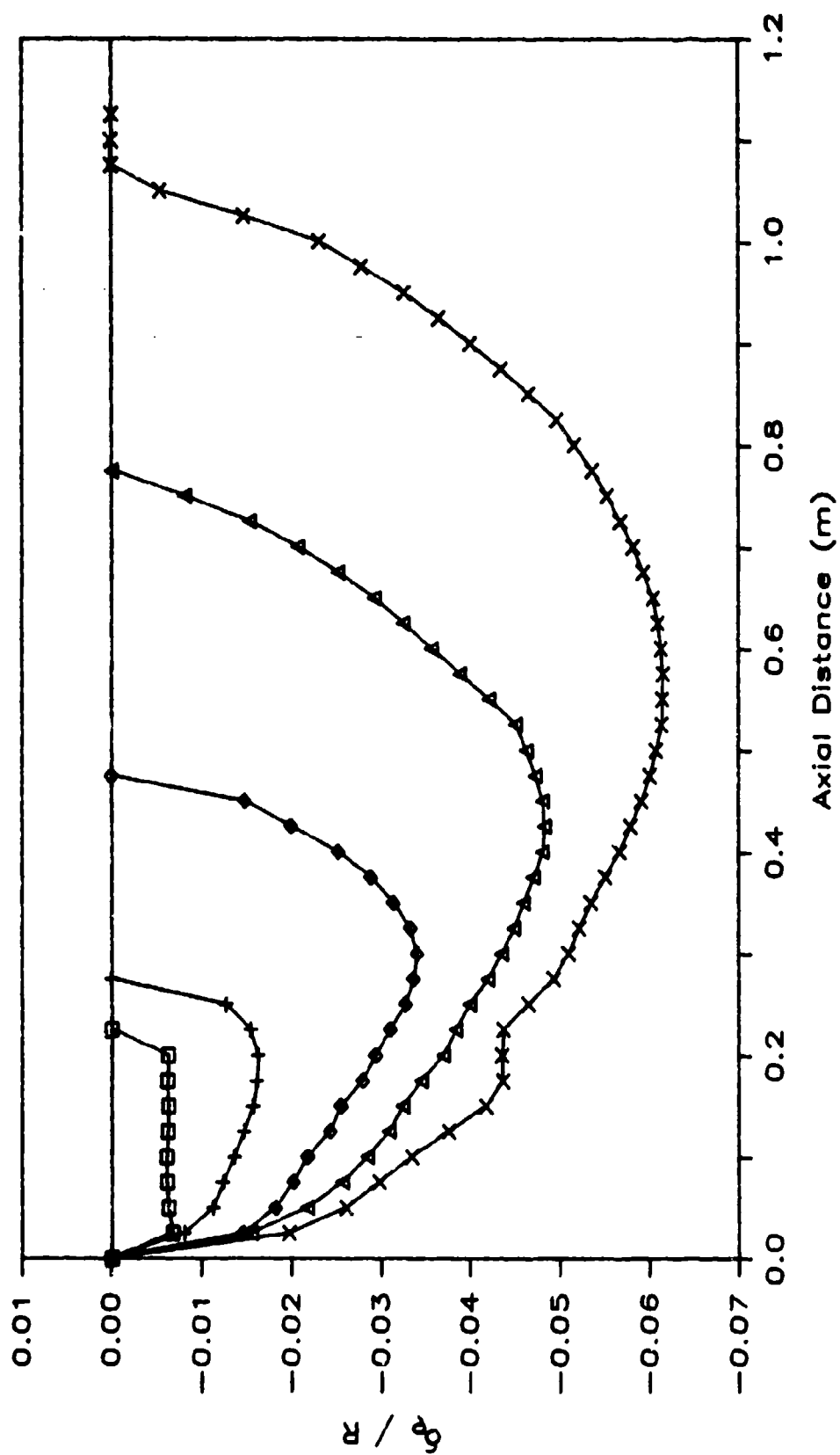


Fig. 3.10 Density Thickness as a function of space and time for the test case 536. \square 500 μsec \triangle 1000 μsec \diamond 1500 μsec \times 2000 μsec

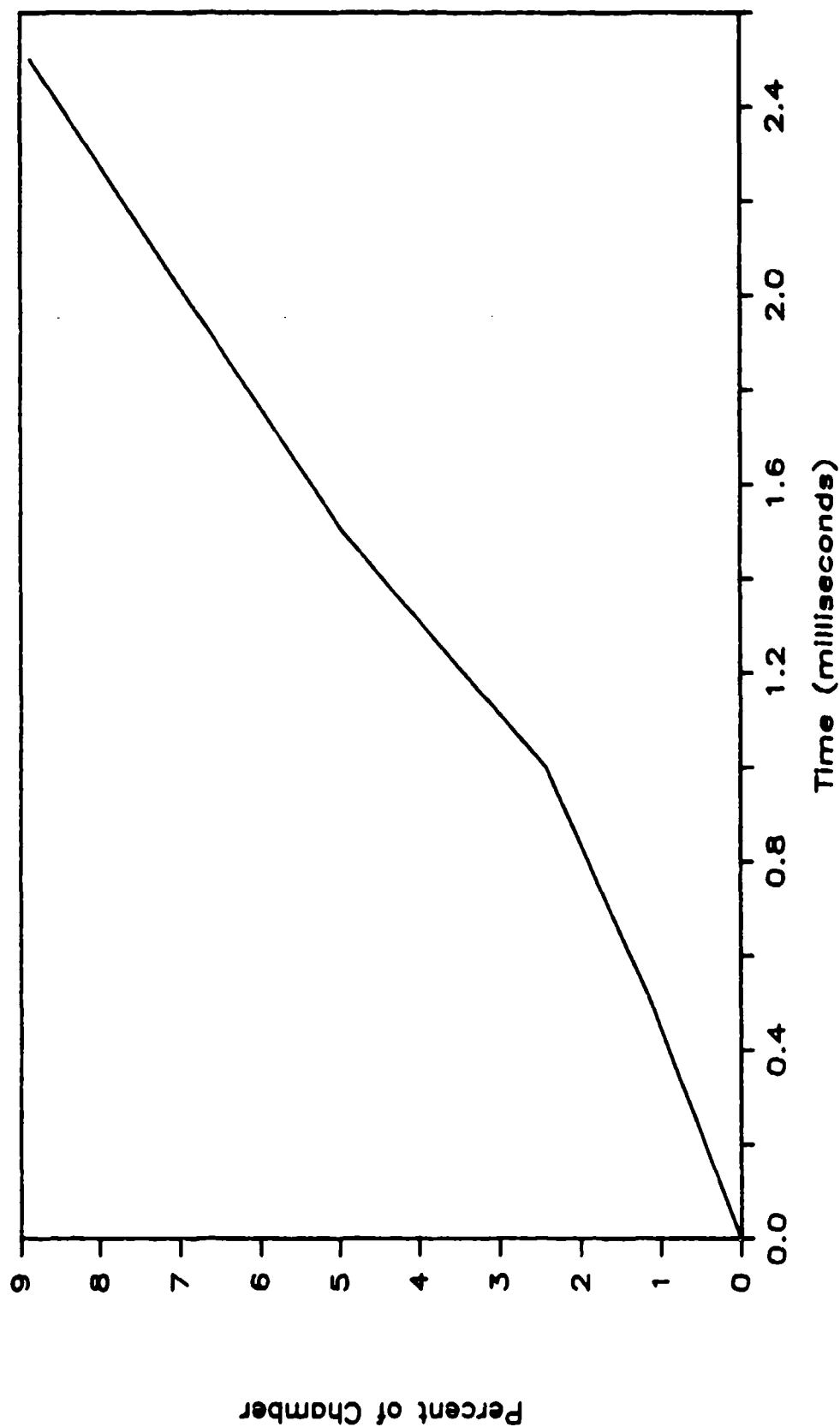


Fig. 3.11 Apparent Increase in Chamber Volume as a Function of Time
Caused by Negative Displacement Thickness

Chapter 4

VISCOUS FLOW INSIDE TUBES

4.1 Introduction

In this chapter, an interior ballistic model for analyzing viscous flow inside tubes that launch high-speed projectiles is described. The interior ballistic model is of the quasi multi-dimensional type (see Section 1.3) and is based on the interior ballistic model described in Chapter 2 and the model for the momentum and thermal boundary layers described in Chapter 3. The interior ballistic model described in this chapter is the first quasi multi-dimensional model ever developed for analyzing the flowfield between the breech and the base of the projectile which takes into account the effects of the momentum and thermal boundary layers next to the tube wall.

In the next section, the problem involving viscous flow inside tubes is described. Afterwards, in Section 4.3, the formulation of the problem is presented. In Section 4.4, the numerical method used to obtain solutions is described. Finally, in Section 4.5, the results are presented.

4.2 Description of Problem

The description of the viscous interior ballistic problem is the same as the description of the inviscid interior ballistic problem (see Section 2.2) except that the combustion gas is now considered to be a viscous fluid.

For the viscous interior ballistic problem, we are interested in evaluating the influence of viscosity, heat transfer, and the ratio of propellant grain velocity to combustion gas velocity on gun performance. Table 4.1 shows a list of parameters necessary to specify the problem. Equations, equation numbers, and values for these parameters are presented in Tables 2.1-2.3 and in Tables 4.2-4.3 (see Section 4.5).

Table 4.1

Parameters needed to specify the viscous interior ballistic problem

Tube Geometry Parameters

- radius (R)
- cross-sectional area (A)
- initial breech-to-projectile
axial distance (L_{p0})
- axial distance from the breech
to the open end of the tube (L_f)

Projectile Parameters

- mass (m_p)
- initial velocity (U_{p0})
- pressure at which projectile
motion begins (P_{cr})

Air Parameters

- Temperature (T_{atm})
- Pressure (P_{atm})
- Specific heat ratio (γ_{atm})
- Gas constant (R_{atm})

Combustion Gas Parameters

- molar mass (m_{mass})
- initial temperature (T_0)
- initial pressure (P_0)
- initial velocity (U_0)
- viscosity (μ)
- conductivity (k)
- friction factor (f)
- Prantl number (Pr)

Propellant Parameters

- type
- grain geometry
- initial mass (m_0)
- covolume (η)
- density (ρ_s)
- initial web thickness (w_0)
- initial propellant grain
length (λ_0)
- initial perforate
diameter (d_{i0})
- specific heat capacity (C_{ps})
- initial temperature (T_{init})
- ignition temperature (T_{ig})
- linear burning speed (r_b)
- specific energy release (h_{sg})
- initial velocity (u_{s0})
- propellant grain-combustion
gas velocity ratio (CD_1)
- drag coefficient (C_D)
- initial axial distance between
the breech and most remote
propellant grain (L_{s0})

Tube Wall Parameters

- initial temperature (T_{w0})
- diffusivity (α)

4.3 Formulation of Problem

Introduction

This section presents the assumptions and the governing equations used to describe the viscous interior ballistic problem. As in the inviscid formulation, the governing equations have been classified into the following three groups:

1. Conservation Equations - the set of coupled 1st order partial differential equations which describe the conservation of mass, momentum and energy.
2. Constitutive Equations - a group of equations which describe dependencies between two or more variables in the conservation equations.
3. Auxiliary Equations - a group of equations resulting from models developed for terms in either the conservation equations or the constitutive equations.

In this section, the conservation equations governing this problem are presented first. Afterwards, the constitutive and auxiliary equations for this problem are presented. Here, it is noted that only the final forms of these equations are presented. The derivation of these equations are given in this section or in Appendix A.

Conservation Equations

The conservation equations governing this problem are the mass, momentum and energy conservation equations. The following assumptions were made to facilitate the derivation of the conservation equations for the viscous interior ballistic problem:

- 1) The problem is unsteady and one-dimensional in the axial direction where radial effects are accounted for by the K-factor approach (see Appendix A).
- 2) Pressure varies in the axial direction only.
- 3) The propellant grains can be treated as a continuum.
- 4) The propellant grains are incompressible.
- 5) The propellant grains are distributed homogeneously across the cross-sectional area of the tube at any axial location.
- 6) There is no interaction between the propellant grains and the tube wall.
- 7) The combustion gas is a viscous fluid.

With these assumptions, the viscous conservation equations can be written as follows:

Continuity of Propellant Grains

$$\frac{\partial v}{\partial t} = -v \frac{\partial u_s}{\partial x} - u_s \frac{\partial v}{\partial x} - \frac{u_s}{A} - \dot{M}_s \frac{v}{\rho_s} \quad (4.1)$$

Continuity of Combustion Gas

$$\frac{\partial \bar{p}}{\partial t} = -K_{pu} \frac{\bar{p} \bar{u}}{A} \frac{\partial A}{\partial x} - \bar{p} \bar{u} \frac{\partial K}{\partial x} - K_{pu} \frac{\partial (\bar{p} \bar{u})}{\partial x} + \frac{\bar{p}}{(1-v)} [(K_{pu} \bar{u} - u_s) \frac{\partial v}{\partial x}]$$

$$- v \left(\frac{\partial u_s}{\partial x} + \frac{u_s}{A} \frac{\partial A}{\partial x} \right) + \left(\frac{v}{1-v} \right) \dot{M}_s (1 - \bar{\rho}/\rho_s) \quad (4.2)$$

Conservation of Momentum for the Combustion Gas

$$\begin{aligned} \frac{\partial(\bar{\rho}\bar{u})}{\partial t} = & \frac{1}{K_{\rho u}} \left\{ -K_{\rho u}^2 \frac{\partial(\bar{\rho}\bar{u}^2)}{\partial x} + [\bar{\rho}\bar{u} (K_{\rho u}^2 \bar{u} - K_{\rho u} u_s) + P] \frac{\partial v}{\partial x} - \frac{\partial P}{\partial x} \right\} \\ & - \frac{\bar{\rho}\bar{u}}{K_{\rho u}} \left\{ \frac{[K_{\rho u}^2 \bar{u} + \left(\frac{v}{1-v}\right) K_{\rho u} u_s]}{A} \frac{\partial A}{\partial x} + \left[\frac{\partial K_{\rho u}}{\partial t} + u \frac{\partial K_{\rho u}^2}{\partial x} \right. \right. \\ & \left. \left. + \left(\frac{v}{1-v}\right) K_{\rho u} \frac{\partial u_s}{\partial x} \right] \right\} + \left\{ \frac{\bar{u}}{K_{\rho u}} \frac{v}{(1-v)} \dot{M}_s [CD_1 - K_{\rho u} \bar{\rho}/\rho_s] \right. \\ & \left. - \frac{1}{K_{\rho u}(1-v)} [\tau_w 2\pi R/A + D/A] \right\} \quad (4.3) \end{aligned}$$

Conservation of Energy for the Combustion Gas

$$\begin{aligned} \frac{\partial \bar{e}}{\partial t} = & -K_{eu} \frac{\partial(\bar{e}\bar{u})}{\partial x} + \frac{1}{(1-v)} (K_{eu} \bar{e}\bar{u} + P\bar{u} - \bar{e}u_s) \frac{\partial v}{\partial x} - \frac{\partial(P\bar{u})}{\partial x} - \bar{e}\bar{u} \frac{\partial K_{eu}}{\partial x} \\ & - \frac{[(K_{eu} \bar{e}\bar{u} + P\bar{u}) + \left(\frac{v}{1-v}\right) \bar{e}\bar{u}]}{A} \frac{\partial A}{\partial x} - \frac{\bar{e}v}{(1-v)} \frac{\partial u_s}{\partial x} + \frac{v}{(1-v)} \dot{M}_s \{ [h_{sg} \\ & - C_{ps}(T_{ign} - T_{init}) - (h(\bar{T}) - h(T_{ign}))] - \frac{\bar{e}}{\rho_s} \} \\ & - \frac{1}{(1-v)} q_w \frac{2}{R} \quad (4.4) \end{aligned}$$

where the terms of Eqs. (4.1)-(4.4) are defined as

- 1) A = the tube cross-sectional area
- 2) $v = A_s/A$ = the ratio of propellant cross-sectional area to tube cross-sectional area

- 3) u_g = the propellant grain velocity
- 4) \dot{M}_g = the rate of propellant consumption per unit volume
- 5) ρ_g = the propellant grain density
- 6) $\bar{\rho}$ = the combustion gas density averaged over the tube cross-sectional area at some axial location
- 7) \bar{u} = the combustion gas velocity averaged over the tube cross-sectional area at some axial location
- 8) P = the combustion gas pressure
- 9) \bar{T} = the combustion gas temperature averaged over the tube cross-sectional area at some axial location
- 10) \bar{e} = the combustion gas energy per unit volume averaged over the tube cross-sectional area at some axial location
- 11) h_{sg} = the chemical energy released per unit mass of propellant
- 12) C_{ps} = the specific heat capacity of the propellant
- 13) T_{ig} = the ignition temperature of the propellant
- 14) T_{init} = the initial temperature of the propellant
- 15) $h(\bar{T})$ = the enthalpy of the combustion gas at temperature \bar{T}
- 16) $h(T_{ig})$ = the enthalpy of the combustion gas at temperature T_{ig}
- 17) $K_{\rho u} = \overline{\rho u} / \bar{\rho} \bar{u}$ = the density flux K-factor
- 18) $K_{\rho u^2} = \overline{\rho u^2} / \bar{\rho} \bar{u}^2$ = the momentum flux K-factor
- 19) $K_{eu} = \overline{eu} / \bar{e} \bar{u}$ = the energy flux K-factor
- 20) CD_1 = the propellant grain-combustion gas velocity ratio
- 21) τ_w = the tube wall shear stress
- 22) D = the propellant grain drag force
- 23) q_w = the tube wall heat flux

The conservation equations given by Eqs. (4.1)-(4.4) contain more dependent variables than the number of such equations. These

conservation equations are closed by the constitutive and the auxiliary equations described in the next two sections.

Constitutive Equations

The constitutive equations for the viscous interior ballistic problem are the same as those presented for the inviscid interior ballistic problem (see Section 2.2. These equations are restated here for convenience:

- 1) An equation of state given by

$$P\left(\frac{1}{\rho} - \eta\right) = R\bar{T} \quad (4.5)$$

- 2) A constitutive relationship for combustion gas energy given by

$$\bar{e} = \bar{p}(\hat{u}(T) + \frac{1}{2} \bar{u}^2) \quad (4.6)$$

- 3) The dependency between propellant grain velocity and combustion gas velocity given by

$$u_g = CD_1 \bar{u} \quad (4.7)$$

Auxiliary Equations

The combustion gas internal energy and enthalpy equations developed for the inviscid interior ballistic problem are also used for the viscous interior ballistic problem and are restated here for convenience:

Combustion Gas Internal Energy

$$\hat{u}(\bar{T}) = [-7.1259 \times 10^4 + 4.9224 \times 10^7 (\bar{T}^{-2}) - 1.2872 \times 10^6 (\bar{T}^{-1})]$$

$$\begin{aligned}
& + 2.8007 \times 10^5 (\bar{T}^{.5}) + 1.6310 \times 10^4 (\ln \bar{T}) - 2.3833 \times 10^3 (\bar{T}^{.25}) \\
& - 1.8069 \times 10^3 (\bar{T}^{.5}) + 6.2205 \times 10^1 (\bar{T}) - 8.8221 (\bar{T}^{1.25}) \\
& + 1.2517 (\bar{T}^{1.5}) - 5.7297 \times 10^{-3} (\bar{T}^{1.75}) - 5.5657 \times 10^{-3} (\bar{T}^2) \\
& + 8.066 \times 10^{-8} (\bar{T}^3)] (1000/\text{mmass}) \text{J/kg}
\end{aligned} \tag{4.8}$$

where mmass = the molar mass of the combustion gas.

Combustion Gas Enthalpy

$$h(\bar{T}) = h_o + \hat{u}(\bar{T}) + R_{cg} \bar{T} + \eta P \tag{4.9}$$

Propellant grain-combustion gas velocity ratio

Two formulas for the propellant grain-combustion gas ratio CD_1 were developed for the viscous interior ballistic problem. The first formula presented here describes a variable CD_1 while the second assumes that the propellant grain velocity equals the combustion gas velocity.

The formula derived for the variable, CD_1 , is intended to express only the most dominant physics involved in the interior ballistic combustion/expansion process. Therefore, simplifying assumptions which are more restrictive than those used to obtain the viscous conservation equations (Eqs. (4.1)-(4.4)) have been used here. These assumptions are as follows:

- 1) Quasi-steady conditions hold for all time dependent variables involved in this derivation.
- 2) The temporal gradient of CD_1 has a much smaller magnitude than either the temporal gradient of propellant grain velocity (u_g) or the temporal gradient of the combustion gas velocity (u), i.e.,

$$\left| \frac{\partial CD_1}{\partial t} \right| \ll \left| \frac{\partial u_g}{\partial t} \right| \text{ or } \left| \frac{\partial u}{\partial t} \right| \quad (4.10)$$

- 3) At any time, u is a linear function of the projectile velocity (U_p) and the projectile travel length (L_p), i.e.,

$$u = \left(\frac{x}{L_p} \right) U_p \quad (4.11)$$

- 4) The spatial gradient of CD_1 is negligible at any time, i.e.,

$$\frac{\partial CD_1}{\partial x} = 0 \quad (4.12)$$

- 5) All other forces felt by a propellant grain are negligible in comparison with the pressure drag force, i.e.,

$$F_{\text{net}} = F_d$$

- 6) The propellant grains are single perforate cylinders with a time-averaged radius r and constant length l .
- 7) The propellant grains are incompressible.
- 8) At any time, the combustion gas spatial density gradient is

negligible, i.e.,

$$\frac{\partial \bar{p}}{\partial x} = 0 \quad (4.13)$$

Under these assumptions, the following two equations were derived for CD_1 :

$$CD_1 = 1 + \frac{1}{2Fa} (1 - \sqrt{4Fa+1}) \quad (4.14)$$

$$Fa = \frac{2C_D \bar{\rho} U_p^2}{3\pi \rho_s a_p} \quad (4.15)$$

where

- 1) Fa = the acceleration ratio of propellant grains to combustion gas
- 2) a_p = the projectile acceleration
- 3) C_D = a drag coefficient

and $\bar{\rho}$, U_p , r , and ρ_s have previously been defined.

The second formula used for CD_1 describes the limiting case for the viscous interior ballistic problem. This formula is simply

$$CD_1 = 1 \quad (4.16)$$

The rate of propellant consumption per unit volume

Two formulas for finding the rate of propellant consumption per unit volume (\dot{M}_s) are presented here for the viscous interior ballistic problem. The first formula for \dot{M}_s was also used for the inviscid interior ballistic problem (see section 2.3) and is restated here for

convenience:

$$\dot{M}_s = \rho_s [A_{bt} \frac{v_{Adx}}{\int_0^L v_{Adx}}] r_b \quad (4.17)$$

The second formula for \dot{M}_s takes into account the non-constant burning surface area of individual propellant grains. The following assumptions were used in this derivation:

- 1) \dot{M}_s is a function of time and axial position along the tube.
- 2) The linear burning speed r_b is a function of pressure only.
- 3) The propellant grains are incompressible.
- 4) The propellant grains are single-perforate cylinders.
- 5) The number of propellant grains per unit volume (n) is a function of time and axial position along the tube.

Based on these assumptions, the following equation for \dot{M}_s was derived:

$$\dot{M}_s = \rho_s A_b r_b \quad (4.18)$$

where

$$1) \quad A_b = \frac{2\{[w_\phi + d_{1\phi}][l_\phi - R_b + w_\phi] - 2w_\phi R_b\}}{w_\phi \{[w_\phi + d_{1\phi} - 2R_b][l_\phi - R_b]\}} \quad (4.19)$$

$$2) \quad R_b = \int_0^t r_b dt \quad (4.20)$$

and

- 1) w_ϕ = the initial web thickness
- 2) $d_{1\phi}$ = the initial perforation diameter

3) l_0 = the initial propellant grain length

See Appendix A for detailed derivations of Eqs. (4.17)-(4.20).

Projectile velocity

Two formulas for finding the projectile velocity U_p at time level $n+1$ are presented here for the viscous interior ballistic problem. The first formula for U_p^{n+1} was also used for the inviscid interior ballistic problem (see Section 2.3) and is restated here for convenience:

$$U_p^{n+1} = U_p^n + \left(\frac{P_{pb} - P_s}{m_p} \right) A_p \Delta t \quad (4.21)$$

The second formula for U_p^{n+1} makes use of a second-order accurate approximation of the projectile acceleration. This approximation at time level $n+1$ is given by

$$\left(\frac{dU}{dt} \right)_p^{n+1} = \frac{3}{2} \left(\frac{U_p^{n+1} - U_p^n}{\Delta t} \right) - \frac{1}{2} \left(\frac{U_p^n - U_p^{n-1}}{\Delta t} \right) + O(\Delta t^2) \quad (4.22)$$

Substitution of Eq. (4.22) into the discretized form of Eq. (2.28) (developed in Section 2.3), results in the following second-order accurate equation for projectile velocity:

$$U_p^{n+1} = U_p^n + \frac{1}{3} (U_p^n - U_p^{n-1}) + \frac{2}{3} \frac{(P_{pb} - P_f)}{m_p} A_{pb} \Delta t \quad (4.23)$$

Projectile displacement

The equation which describes projectile displacement for the

viscous interior ballistic problem is the same equation that was developed to describe projectile displacement for the inviscid ballistic problem (see Section 2.3). This discretized equation is restated here for convenience:

$$L_p^{n+1} = L_p^n + \frac{U_p^{n+1} + U_p^n}{2} \Delta t \quad (4.24)$$

Wall shear stress

A simple formula for tube wall shear stress (τ_w) was derived by using the following assumptions:

- 1) Quasi-steady conditions are valid for this analysis.
- 2) The Reynolds number for the tube, Re_D , is greater than 5×10^5 .
- 3) The tube surface has a relative roughness of 0.002.

With these assumptions, it can be seen from the Moody friction factor diagram that the tube wall friction factor (f) is nearly constant with a value of about 0.02 [Ref. 38]. The friction factor is related to tube wall shear stress by the formula

$$f = \frac{4\tau_w}{\frac{1}{2} \rho u_m^2} \quad (4.25)$$

From this equation, it follows that the tube wall shear stress may be approximated as

$$\tau_w = \frac{1}{8} f \rho u_m^2 \quad (4.26)$$

Propellant grain drag force

A simple formula for the propellant grain drag force (D) was derived by using the following assumptions:

- 1) Quasi-steady conditions are valid for this analysis.
- 2) The drag coefficient for the propellant (C_D) is a constant.

With these assumptions and by making use of Eq. (4.7), the propellant grain drag force may be expressed as

$$D = \frac{1}{2} C_D \bar{\rho} \bar{u}^2 (1 - C_{D_1})^2 v A \quad (4.27)$$

Tube wall heat flux

Tube wall heat flux (q_w) for the viscous interior ballistic problem can be calculated quite easily if the temperature profile in the radial direction is known. A boundary layer analysis of this problem can provide this information (see Chapter 3) and q_w at some axial location x_a may then be found by Fourier's equation

$$q_w(x_a, t) = -k \frac{\partial T_w(x_a, t)}{\partial r} \quad (4.28)$$

where

- 1) k = the combustion gas thermal conductivity.
- 2) $T_w(x_a, t)$ = the tube wall boundary temperature.
- 3) r = a radial coordinate.

An estimate of the tube wall heat flux at some axial location x_a can

also be made by using the formula

$$q_w(x_a, t) = h_c(x_a, t)[\bar{T}(x_a, t) - T_w(x_a, t)] \quad (4.29)$$

where h_c is a local, time dependent combustion gas convection coefficient.

In order to derive an expression for the tube wall boundary temperature in Eq. (4.29), the following assumptions were made:

- 1) The heat transfer taking place is conductive heat transfer into the tube wall.
- 2) The effects of tube wall curvature may be neglected since the heat penetration distance into the tube wall ($\delta(t)$) is small.
- 3) The tube wall thermal properties are functions of temperature only.
- 4) The temperature profile in the tube wall at any axial location can be expressed as a second degree polynomial function of temperature.
- 5) Quasi-steady conditions are valid for all time-dependent variables.
- 6) The tube wall is initially at temperature T_1 .

With these assumptions, the following discretized formula for tube wall boundary temperature at location x_a and time $(n+1)\Delta t$ was derived:

$$T_w(x_a, (n+1)\Delta t) = \frac{T_1 + \left(\frac{h_c}{2k_{st}}\right)\delta((n+1)\Delta t)\bar{T}(x_a, (n+1)\Delta t)}{\left[1 + \left(\frac{h_c}{k_{st}}\right)\delta((n+1)\Delta t)\right]} \quad (4.30)$$

where the details of this derivation and formulas for h_0 , k_{st} and $\delta((n+1)\Delta t)$ are given in Appendix A [Refs. 38,39]. An alternate (and more accurate) approach to finding a value for h_0 is to use information gained from a boundary layer analysis of this problem (see Chap. 3).

K-factors

Realistic values for K-factors (K_{pu} , K_{pu}^2 , and K_{eu}) can be found from a boundary layer analysis of the viscous interior ballistic problem (see Chapter 3).

A simple model for K-factor variation which incorporates some of the most dominant physics is presented here:

$$K = 1 \pm 0.1 \sin(\pi(x/L_p)^2) \frac{L_p}{L_r} \quad (4.31)$$

4.4 Numerical Method of Solution

Solutions were found for the viscous conservation equations (Eqs. (4.1)-(4.4)) in the same manner that solutions were found for the inviscid conservation equations, i.e., by MacCormack's Predictor-Corrector finite-difference method. Refer to Section 2.4 for a discussion on the procedure used to approximate the conservation equations.

A summary of the procedure used to obtain finite difference equations (FDE's) which describe the viscous interior ballistic problem is given below:

- 1) The partial differential equations (PDE's) given by Eqs. (4.1)-(4.4) were transformed from the (x,t) coordinate system to the (ξ,τ) coordinate system.
- 2) The spatial and temporal domains of the transformed PDE's were discretized (see Fig. 2.5) and FDE's at the interior grid points were derived from the transformed PDE's.
- 3) FDE's at the boundary grid points (see Fig. 2.5) were derived from the transformed PDE's and from physical constraints.

Transformed Conservation Equations

By using the transformation equations presented in Section 2.3, the viscous conservation equations (Eqs. (4.1)-(4.4)) can be rewritten as follows:

Continuity of Propellant Grains

$$\frac{\partial v}{\partial \tau} = \frac{U_s}{L_s} \xi \frac{\partial v}{\partial \xi} - \frac{1}{L_s} \left[\frac{\partial (v u_s)}{\partial \xi} - \frac{v u_s}{A} \frac{\partial A}{\partial \xi} \right] - \frac{\dot{M}_s}{\rho_s} \quad (4.32)$$

Continuity of Combustion Gas

$$\begin{aligned} \frac{\partial \bar{\rho}}{\partial \tau} = & \frac{U_p}{L_p} \xi \frac{\partial \bar{\rho}}{\partial \xi} - \frac{1}{L_p} \left[\frac{K_{\rho u} \bar{\rho} \bar{u}}{A} \frac{\partial A}{\partial \xi} + \bar{\rho} \bar{u} \frac{\partial K_{\rho u}}{\partial \xi} + K_{\rho u} \frac{\partial \bar{\rho} \bar{u}}{\partial \xi} \right] + \frac{v}{(1-v)} \dot{M}_s \left(1 \right. \\ & \left. - \bar{\rho} / \rho_s \right) + \frac{\bar{\rho}}{(1-v)} \frac{1}{L_p} \left[(K_{\rho u} \bar{u} - u_s) \frac{\partial v}{\partial \xi} - v \left(\frac{\partial u_s}{\partial \xi} + \frac{u_s}{A} \frac{\partial A}{\partial \xi} \right) \right] \quad (4.33) \end{aligned}$$

Conservation of Momentum for the Combustion Gas

$$\begin{aligned} \frac{\partial (\bar{\rho} \bar{u})}{\partial \tau} = & \frac{1}{K_{\rho u} L_p} \left\{ U_p \xi K_{\rho u} \frac{\partial (\bar{\rho} \bar{u})}{\partial \xi} - K_{\rho u}^2 \frac{\partial (\bar{\rho} \bar{u}^2)}{\partial \xi} + \frac{1}{(1-v)} [\bar{\rho} \bar{u} (K_{\rho u}^2 \bar{u} \right. \\ & \left. - K_{\rho u} u_s) + P] \frac{\partial v}{\partial \xi} - \frac{\partial P}{\partial \xi} \right\} - \frac{\bar{\rho} \bar{u}}{K_{\rho u} L_p} \left\{ \frac{[K_{\rho u}^2 \bar{u} + (\frac{v}{1-v}) K_{\rho u} u_s]}{A} \frac{\partial A}{\partial \xi} \right. \\ & \left. + L_p \frac{\partial K_{\rho u}}{\partial \tau} - U_p \xi \frac{\partial K_{\rho u}}{\partial \xi} + \bar{u} \frac{\partial K_{\rho u}^2}{\partial \xi} + (\frac{v}{1-v}) K_{\rho u} \frac{\partial u_s}{\partial \xi} \right\} \\ & + \left\{ \frac{\bar{u}}{K_{\rho u}} \left(\frac{v}{1-v} \right) \dot{M}_s (CD_1 - K_{\rho u} \bar{\rho} / \rho_s) \right. \\ & \left. - \frac{1}{K_{\rho u} (1-v)} (2\tau_w / R + D/A) \right\} \quad (4.34) \end{aligned}$$

Conservation of Energy for the Combustion Gas

$$\begin{aligned} \frac{\partial \bar{e}}{\partial \tau} = & \frac{1}{L_p} \left\{ U_p \xi \frac{\partial \bar{e}}{\partial \xi} - K_{eu} \frac{\partial (\bar{e} \bar{u})}{\partial \xi} + \frac{1}{(1-v)} [K_{eu} \bar{e} \bar{u} - \bar{e} u_s + P \bar{u}] \frac{\partial v}{\partial \xi} \right. \\ & \left. - \frac{\partial (P \bar{u})}{\partial \xi} \right\} - \frac{1}{L_p} \left\{ \bar{e} \bar{u} \frac{\partial K_{eu}}{\partial \xi} + \frac{[K_{eu} \bar{e} \bar{u} + (\frac{v}{1-v}) \bar{e} u_s + P \bar{u}]}{A} \frac{\partial A}{\partial \xi} \right. \\ & \left. + (\frac{v}{1-v}) \bar{e} \frac{\partial u_s}{\partial \xi} \right\} + (\frac{v}{1-v}) \dot{M}_s \{ [h_{sg} - C_{ps} (T_{lg} - T_{init})] \} \end{aligned}$$

$$- (h(\bar{T}) - h(T_{ig})) - \frac{\bar{e}}{\rho_s} - \frac{2}{(1-v)} \frac{q_w}{R} \quad (4.35)$$

The transformed conservation equations can now be discretized and applied at individual grid points. For conservation equations that have been transformed with L_p as the scaling parameter (Eqs. (4.33)-(4.35)), a representative grid point is indicated by the symbol i (see Fig. 2.5). The propellant grain continuity equation (Eq. (4.32)) has been transformed with L_g as the scaling parameter. A representative grid point for this equation is indicated by the symbol i^* (see Fig. 2.5).

It should be noted here that there is not a direct correspondence between values at locations i^* and i since L_g does not equal L_p in general. Consequently, values in the i^* grid point system must be mapped onto the i grid point system. This mapping procedure is accomplished by an interpolative scheme which is described in Appendix A.

Finite Difference Equations

The finite difference equations (FDE's) used to obtain solutions to the transformed viscous conservation equations (Eqs. (4.32)-(4.35)) were obtained by implementing MacCormack's predictor-corrector scheme. This explicit method is second order accurate in both space and time. In this section, the resulting FDE's for the interior grid points are presented first. Then the FDE's for both the breech and projectile base boundaries are presented.

Finite difference equations at interior grid points

For each interior grid point i and i^* , the FDE's are derived by using MacCormack's predictor-corrector scheme to approximate the transformed PDE's. The resulting interior grid point FDE's at the predictor time level of $\overline{n+1}$ and the corrector time level of $n+1$ are presented as follows:

Continuity of Propellant Grains

Interior Predictor

$$\begin{aligned} \overline{v}_{i^*}^{n+1} = & v_{i^*}^n + \left(\frac{\Delta \tau}{L_s}\right)^n \left(\frac{1}{\Delta \xi}\right) \{U_s^n \xi_{i^*} (v_{i^*}^n - v_{(i-1)^*}^n) - [(vu_s)_{i^*}^n \\ & - (vu_s)_{(i-1)^*}^n] - (vu_s)_{i^*}^n \left(\frac{a}{A}\right)_{i^*}^n \Delta \xi - \left(\frac{\dot{M}_s v L_s}{\rho_s}\right)_{i^*}^n \Delta \xi \} \end{aligned} \quad (4.36)$$

Interior Corrector

$$\begin{aligned} v_{i^*}^{n+1} = & \left(\frac{1}{2}\right)(v_{i^*}^n + \overline{v}_{i^*}^{n+1}) + \left(\frac{1}{2}\right)\left(\frac{\Delta \tau}{L_s}\right)^{\overline{n+1}} \left(\frac{1}{\Delta \xi}\right) \{U_s^{\overline{n+1}} \xi_{i^*} (\overline{v}_{(i+1)^*}^{n+1} - \overline{v}_{i^*}^{n+1}) \\ & - [(vu_s)_{(i+1)^*}^{\overline{n+1}} - (vu_s)_{i^*}^{\overline{n+1}}] - (vu_s)_{i^*}^{\overline{n+1}} \left(\frac{a}{A}\right)_{i^*}^{\overline{n+1}} \Delta \xi \\ & - \left(\frac{\dot{M}_s v L_s}{\rho_s}\right)_{i^*}^{\overline{n+1}} \Delta \xi \} \end{aligned} \quad (4.37)$$

Continuity of the Combustion Gas

Interior Predictor

$$\begin{aligned}
\bar{\rho}_1^{n+1} = & \bar{\rho}_1^n + \left(\frac{\Delta\tau}{L_p}\right)^n \left(\frac{1}{\Delta\xi}\right) \{U_p^n \xi_1 (\bar{\rho}_1^n - \bar{\rho}_{1-1}^n) - (K_{\rho u})_1^n [(\bar{\rho}u)_1^n - (\bar{\rho}u)_{1-1}^n] \\
& + \left(\frac{\bar{p}}{1-v}\right)_1^n [(K_{\rho u}u)_1^n - (u_s)_1^n] (v_1^n - v_{1-1}^n) \} - \left(\frac{\Delta\tau}{L_p}\right)^n [(K_{\rho u})_1^n \left(\frac{a}{A}\right)_1^n \\
& + (K_{\rho u\xi})_1^n (\bar{\rho}u)_1^n + \left(\frac{v}{1-v}\right)_1^n \bar{\rho}_1^n [(u_{s\xi})_1^n + \left(\frac{a}{A}\right)_1^n (u_s)_1^n] \\
& + \Delta\tau \left(\frac{v}{1-v}\right)_1^n [1 - \left(\frac{\bar{p}}{\rho_s}\right)_1^n] (\dot{M}_s)_1^n
\end{aligned} \quad (4.38)$$

Interior Corrector

$$\begin{aligned}
\bar{\rho}_1^{n+1} = & \left(\frac{1}{2}\right) (\bar{\rho}_1^n + \bar{\rho}_1^{n+1}) + \left(\frac{1}{2}\right) \left(\frac{\Delta\tau}{L_p}\right)^{n+1} \left(\frac{1}{\Delta\xi}\right) \{U_p^{n+1} \xi_1 (\bar{\rho}_{1+1}^{n+1} - \bar{\rho}_1^{n+1}) \\
& - (K_{\rho u})_1^{n+1} [(\bar{\rho}u)_{1+1}^{n+1} - (\bar{\rho}u)_1^{n+1}] + \left(\frac{\bar{p}}{1-v}\right)_1^{n+1} [(K_{\rho u}u)_1^{n+1} \\
& - (u_s)_1^{n+1}] (v_{1+1}^{n+1} - v_1^{n+1}) \} - \left(\frac{1}{2}\right) \left(\frac{\Delta\tau}{L_p}\right)^{n+1} [(K_{\rho u})_1^{n+1} \left(\frac{a}{A}\right)_1^{n+1} \\
& + (K_{\rho u\xi})_1^{n+1} (\bar{\rho}u)_1^{n+1} + \left(\frac{v}{1-v}\right)_1^{n+1} \bar{\rho}_1^{n+1} [(u_{s\xi})_1^{n+1} + \left(\frac{a}{A}\right)_1^{n+1} (u_s)_1^{n+1}] \\
& + \left(\frac{\Delta\tau}{2}\right)^{n+1} \left(\frac{v}{1-v}\right)_1^{n+1} [1 - \left(\frac{\bar{p}}{\rho_s}\right)_1^{n+1}] (\dot{M}_s)_1^{n+1}
\end{aligned} \quad (4.39)$$

Conservation of Momentum for the Combustion Gas

Interior Predictor

$$\begin{aligned}
(\bar{\rho} \bar{u})_1^{n+1} = & (\bar{\rho} \bar{u})_1^n + \left(\frac{\Delta \tau}{L_p}\right)^n \left(\frac{1}{\Delta \xi}\right) \left(\frac{1}{K_{\rho u}}\right)_1^n \{U_p^n \xi_1 (K_{\rho u})_1^n [(\bar{\rho} \bar{u})_1^n - (\bar{\rho} \bar{u})_{1-1}^n] \\
& + \left(\frac{1}{1-v}\right)_1^n \{(\bar{\rho} \bar{u})_1^n [(K_{\rho u} \bar{u})_1^n - (K_{\rho u} u_s)_1^n] + P_1^n\} (v_1^n - v_{1-1}^n) - (P_1^n \\
& - P_{1-1}^n)\} - \left(\frac{\Delta \tau}{L_p}\right)^n \left(\frac{\bar{\rho} \bar{u}}{K_{\rho u}}\right)_1^n \{[(K_{\rho u} \bar{u})_1^n + \left(\frac{v}{1-v}\right)_1^n (K_{\rho u} u_s)_1^n] \left(\frac{a}{A}\right)_1^n \\
& + L_p^n (K_{\rho u \tau})_1^n - (U_p^n (\xi K_{\rho u \xi})_1^n + (K_{\rho u} \bar{u})_1^n + \left(\frac{v}{1-v}\right)_1^n (K_{\rho u} u_s)_1^n) \\
& + \left[\frac{\Delta \tau}{K_{\rho u} (1-v)}\right]_1^n \{(\bar{u} \dot{M}_s)_1^n [(CD_1)_1^n - \left(\frac{K_{\rho u} \bar{p}}{\rho_s}\right)_1^n] \\
& - 2\left(\frac{\tau_w}{R}\right)_1^n - \left(\frac{D}{A}\right)_1^n\}
\end{aligned} \tag{4.40}$$

Interior Corrector

$$\begin{aligned}
(\bar{\rho} \bar{u})^{n+1} = & \left(\frac{1}{2}\right) [(\bar{\rho} \bar{u})_1^n + (\bar{\rho} \bar{u})_1^{n+1}] \\
& + \left(\frac{1}{2}\right) \left(\frac{\Delta \tau}{L_p}\right)^{n+1} \left(\frac{1}{\Delta \xi}\right) \left(\frac{1}{K_{\rho u}}\right)_1^{n+1} \{U_p^{n+1} \xi_1 (K_{\rho u})_1^{n+1} [(\bar{\rho} \bar{u})_{1+1}^{n+1} \\
& - (\bar{\rho} \bar{u})_1^{n+1}] + \left(\frac{1}{1-v}\right)_1^{n+1} \{(\bar{\rho} \bar{u})_1^{n+1} [(K_{\rho u} \bar{u})_1^{n+1} - (K_{\rho u} u_s)_1^{n+1} \\
& + P_{1+1}^{n+1}] (v_{1+1}^{n+1} - v_1^{n+1}) - (P_{1+1}^{n+1} - P_1^{n+1})\} \\
& - \left(\frac{1}{2}\right) \left(\frac{\Delta \tau}{L_p}\right)^{n+1} \left(\frac{\bar{\rho} \bar{u}}{K_{\rho u}}\right)_1^{n+1} \{[(K_{\rho u} \bar{u})_1^{n+1} + \left(\frac{v}{1-v}\right)_1^{n+1} (K_{\rho u} u_s)_1^{n+1}] \left(\frac{a}{A}\right)_1^{n+1}
\end{aligned}$$

$$\begin{aligned}
& + \overline{L_p^{n+1}} (\overline{k_{\rho u \tau}}_1^{n+1} - \overline{U_p^{n+1}} (\overline{\xi k_{\rho u \xi}}_1^{n+1} + (\overline{k_{\rho u^2 \xi}}_1^{n+1} \overline{u})_1^{n+1} \\
& + (\frac{v}{1-v})_1^{n+1} (\overline{K_{\rho u s \xi}}_1^{n+1}) + (\frac{1}{2}) [\frac{\Delta \tau}{K_{\rho u (1-v)}}]_1^{n+1} \{ (\overline{u \dot{M}_s})_1^{n+1} [(\overline{CD}_1)_{1-1}^{n+1} \\
& - (\frac{K_{\rho u \rho}}{\rho_s})_1^{n+1}] - 2(\frac{\tau_w}{R})_1^{n+1} - (\frac{D}{A})_1^{n+1} \} \quad (4.41)
\end{aligned}$$

Conservation of Energy for the Combustion Gas

Interior Predictor

$$\begin{aligned}
\overline{e}_1^{n+1} &= \overline{e}_1^n + (\frac{\Delta \tau}{L_p})^n (\frac{1}{\Delta \xi}) \{ U_p^n \xi_1 (\overline{e}_1^n - \overline{e}_{1-1}^n) - (K_{eu})_1^n [(\overline{eu})_1^n - (\overline{eu})_{1-1}^n] \\
& - [(\overline{Pu})_1^n - (\overline{Pu})_{1-1}^n] + (\frac{1}{1-v})_1^n [(K_{eu} \overline{eu})_1^n - (\overline{eu}_s)_1^n + (\overline{Pu})_1^n] (v_1^n \\
& - v_{1-1}^n) \} - (\frac{\Delta \tau}{L_p})^n \{ (K_{eu \xi} \overline{eu})_1^n + [(K_{eu} \overline{eu})_1^n + (\frac{v}{1-v})_1^n (\overline{eu}_s)_1^n \\
& + (\overline{Pu})_1^n] (\frac{a}{A})_1^n + (\frac{v}{1-v})_1^n (\overline{eu}_{s \xi})_1^n \} + \Delta \tau (\frac{v}{1-v})_1^n (\dot{M}_s)_1^n \{ [h_{sg} \\
& - C_{ps} (T_{ig} - T_{init}) - (h(\overline{T}_1^n) - h(T_{ig})) \} - (\frac{\overline{e}}{\rho_s})_1^n \\
& - (\frac{\Delta \tau}{1-v})_1^n (q_w)_1^n (\frac{2}{R})_1 \quad (4.42)
\end{aligned}$$

Interior Corrector

$$\overline{e}_1^{n+1} = (\frac{1}{2}) (\overline{e}_1^n + \overline{e}_1^{n+1}) + (\frac{1}{2}) (\frac{\Delta \tau}{L_p})^n (\frac{1}{\Delta \xi}) \{ U_p^{n+1} \xi_1 (\overline{e}_{1+1}^{n+1} - \overline{e}_1^n)$$

$$\begin{aligned}
& - (K_{eu})_1^{n+1} [(\bar{eu})_{1+1}^{n+1} - (\bar{eu})_1^{n+1}] - [(P\bar{u})_{1+1}^{n+1} - (P\bar{u})_1^{n+1}] \\
& + \left(\frac{1}{1-v}\right)_1^{n+1} [(K_{eu}\bar{eu})_1^{n+1} - (\bar{eu}_s)_1^{n+1} + (P\bar{u})_1^{n+1}] (v_{1+1}^{n+1} - v_1^{n+1}) \\
& - \left(\frac{1}{2}\right) \left(\frac{\Delta\tau}{L_p}\right)_1^{n+1} \{ (k_{eu\xi}\bar{eu})_1^{n+1} + [(K_{eu}\bar{eu})_1^{n+1} + \left(\frac{v}{1-v}\right)_1^{n+1} (\bar{eu}_s)_1^{n+1} \\
& + (P\bar{u})_1^{n+1}] \left(\frac{a}{A}\right)_1^{n+1} + \left(\frac{v}{1-v}\right)_1^{n+1} (\bar{eu}_{s\xi})_1^{n+1} \} \\
& + \left(\frac{\Delta\tau}{2}\right) \left(\frac{v}{1-v}\right)_1^{n+1} (\dot{M}_s)_1^{n+1} [h_{sg} - C_{ps}(T_{1g} - T_{init}) \\
& - (h(\bar{T}_1^{n+1}) - h(T_{1g}))] - \left(\frac{\bar{e}}{\rho_s}\right)_1^{n+1} \\
& - \left(\frac{1}{2}\right) \left(\frac{\Delta\tau}{1-v}\right)_1^{n+1} (q_w)_1^{n+1} \left(\frac{2}{R}\right)_1
\end{aligned} \tag{4.43}$$

where all the terms of Eqs. (4.32)-(4.39) have previously been defined except for

$$1) \quad a = \frac{\partial A}{\partial \xi} \tag{4.44}$$

$$2) \quad k_{\rho u \xi} = \frac{\partial K_{\rho u}}{\partial \xi} \tag{4.45}$$

$$3) \quad k_{\rho u^2 \xi} = \frac{\partial K_{\rho u^2}}{\partial \xi} \tag{4.46}$$

$$4) \quad k_{eu\xi} = \frac{\partial K_{eu}}{\partial \xi} \tag{4.47}$$

$$5) \quad u_{s\xi} = \frac{\partial u_s}{\partial \xi} \tag{4.48}$$

Finite difference equations at boundary grid points

Finite difference equations for the breech and projectile base

boundaries were defined by first applying the transformed conservation equations (Eqs. (4.32)-(4.35)) at the boundaries subject to the following constraints:

$$1) \quad \bar{u}(\xi=0, \tau) = 0 \quad (4.49)$$

$$2) \quad \bar{u}(\xi=1, \tau) = u_p \quad (4.50)$$

$$3) \quad \frac{\partial v}{\partial \xi}(\xi=1, \tau) = 0 \quad (4.51)$$

$$4) \quad K_{\rho u}(\xi=0, \tau) = 1 \quad (4.52)$$

$$5) \quad K_{\rho u}(\xi=1, \tau) = 1 \quad (4.53)$$

$$6) \quad K_{\rho u^2}(\xi=0, \tau) = 1 \quad (4.54)$$

$$7) \quad K_{\rho u^2}(\xi=1, \tau) = 1 \quad (4.55)$$

$$8) \quad \frac{\partial K_{\rho u}}{\partial \tau}(\xi=0, \tau) = 0 \quad (4.56)$$

$$9) \quad \frac{\partial K_{\rho u}}{\partial \tau}(\xi=1, \tau) = 0 \quad (4.57)$$

Then, MacCormack's predictor-corrector scheme was used with three-point, one-sided differencing to approximate the resulting boundary conservation equations. Boundary FDE's at the predictor time level of $\overline{n+1}$ and corrector time level of $n+1$ are presented as follows:

Continuity of Propellant Grains

Breech Boundary Predictor

$$\overline{v_{1*}^{n+1}} = v_{1*}^n - \left(\frac{\Delta \tau}{L_s}\right)^n \left(\frac{1}{\Delta \xi}\right) \left[\left(\frac{1}{2} \right) (v u_s)_2^n - \left(\frac{1}{2} \right) (v u_s)_3^n \right]$$

$$+ \left(\frac{\dot{M}_s v L_s}{\rho_s} \right)_{1*}^n \Delta \xi \} \quad (4.58)$$

Breech Boundary Corrector

$$\begin{aligned} \overline{v_{1*}^{n+1}} &= \frac{1}{2} (\overline{v_{1*}^n} + \overline{v_{1*}^{n+1}}) - \left(\frac{1}{2} \right) \left(\frac{\Delta \tau}{L_s} \right)^{n+1} \left(\frac{1}{\Delta \xi} \right) \{ [(2) (\overline{v u_s})_{2*}^{n+1} - \left(\frac{1}{2} \right) (\overline{v u_s})_{3*}^{n+1}] \\ &+ \left(\frac{\dot{M}_s v L_s}{\rho_s} \right)_{1*}^{n+1} \Delta \xi \} \end{aligned} \quad (4.59)$$

Projectile Base Boundary Predictor

$$\overline{v_{IL*}^{n+1}} = \overline{v_{(IL-1)*}^{n+1}} \quad (4.60)$$

Projectile Base Boundary Corrector

$$\overline{v_{IL*}^{n+1}} = \overline{v_{(IL-1)*}^{n+1}} \quad (4.61)$$

Continuity of Combustion Gas

Breech Boundary Predictor

$$\begin{aligned} \overline{\rho_1^{n+1}} &= \overline{\rho_1^n} - \left(\frac{\Delta \tau}{L_p} \right)^n \left(\frac{1}{\Delta \xi} \right) \{ (2) (\overline{\rho u})_2^n - \left(\frac{1}{2} \right) (\overline{\rho u})_3^n \} - \left(\frac{\Delta \tau}{L_p} \right)^n \left[\left(\frac{v}{1-v} \right)_1^n (\overline{\rho u_{s\xi}})_1^n \right] \\ &+ \Delta \tau \left(\frac{v}{1-v} \right)_1^n \left[1 - \left(\frac{\overline{\rho}}{\rho_s} \right)_1^n \right] (\dot{M}_s)_1^n \end{aligned} \quad (4.62)$$

Breach Boundary Corrector

$$\begin{aligned}
\bar{\rho}_1^{n+1} = & \frac{1}{2} (\bar{\rho}_1 + \bar{\rho}_1^{n+1}) - \left(\frac{1}{2}\right) \left(\frac{\Delta \tau}{L_p}\right)^{n+1} \left(\frac{1}{\Delta \xi}\right) [(2)(\bar{\rho} \bar{u})_2^{n+1} - \left(\frac{1}{2}\right)(\bar{\rho} \bar{u})_3^{n+1}] \\
& - \left(\frac{1}{2}\right) \left(\frac{\Delta \tau}{L_p}\right)^{n+1} \left[\left(\frac{v}{1-v}\right)_1^{n+1} (\bar{\rho} u_{s\xi})_1^{n+1}\right] \\
& + \left(\frac{\Delta \tau}{2}\right) \left(\frac{v}{1-v}\right)_1^{n+1} [1 - \left(\frac{\bar{\rho}}{\rho_s}\right)_1^{n+1}] (\dot{M}_s)_1^{n+1} \quad (4.63)
\end{aligned}$$

Projectile Base Boundary Predictor

$$\begin{aligned}
\bar{\rho}_{IL}^{n+1} = & \bar{\rho}_{IL}^n + \left(\frac{\Delta \tau}{L_p}\right)^n \left(\frac{1}{\Delta \xi}\right) \{U_p^n \left[\left(\frac{3}{2}\right) \bar{\rho}_{IL}^n - (2) \bar{\rho}_{IL-1}^n + \left(\frac{1}{2}\right) \bar{\rho}_{IL-2}^n\right] \\
& - \left[\left(\frac{3}{2}\right) (\bar{\rho} \bar{u})_{IL}^n - (2) (\bar{\rho} \bar{u})_{IL-1}^n + \left(\frac{1}{2}\right) (\bar{\rho} \bar{u})_{IL-2}^n\right] \\
& + \left(\frac{\bar{\rho}}{1-v}\right)_{IL}^n (\bar{u} - u_s)_{IL}^n \left[\left(\frac{3}{2}\right) v_{IL}^n - (2) v_{IL-1}^n + \left(\frac{1}{2}\right) v_{IL-2}^n\right] - \left(\frac{\Delta \tau}{L_p}\right)^n \left\{\left(\frac{a}{A}\right)_{IL}^n \right. \\
& + (k_{\rho u \xi})_{IL}^n (\bar{\rho} \bar{u})_{IL}^n + \left(\frac{v}{1-v}\right)_{IL}^n \bar{\rho}_{IL}^n [(u_{s\xi})_{IL}^n + \left(\frac{a}{A}\right)_{IL}^n (u_s)_{IL}^n] \} \\
& + \Delta \tau \left(\frac{v}{1-v}\right)_{IL}^n [1 - \left(\frac{\bar{\rho}}{\rho_s}\right)_{IL}^n] (\dot{M}_s)_{IL}^n \quad (4.64)
\end{aligned}$$

Projectile Base Boundary Corrector

$$\begin{aligned}
\bar{\rho}_{IL}^{n+1} = & \frac{1}{2} (\bar{\rho}_{IL}^n + \bar{\rho}_{IL}^{n+1}) + \left(\frac{1}{2}\right) \left(\frac{\Delta \tau}{L_p}\right) \left(\frac{1}{\Delta \xi}\right) \{U_p^{n+1} \left[\left(\frac{3}{2}\right) \bar{\rho}_{IL}^{n+1} - (2) \bar{\rho}_{IL-1}^{n+1} \right. \\
& + \left.\left(\frac{1}{2}\right) \bar{\rho}_{IL-2}^{n+1}\right] - \left[\left(\frac{3}{2}\right) (\bar{\rho} \bar{u})_{IL}^{n+1} - (2) (\bar{\rho} \bar{u})_{IL-1}^{n+1} + \left(\frac{1}{2}\right) (\bar{\rho} \bar{u})_{IL-2}^{n+1}\right] \\
& + \left(\frac{\bar{\rho}}{1-v}\right)_{IL}^{n+1} (\bar{u} - u_s)_{IL}^{n+1} \left[\left(\frac{3}{2}\right) v_{IL}^{n+1} - (2) v_{IL-1}^{n+1} + \left(\frac{1}{2}\right) v_{IL-2}^{n+1}\right] \}
\end{aligned}$$

$$\begin{aligned}
& - \left(\frac{1}{2}\right) \left(\frac{\Delta \tau}{L_p}\right)^{n+1} \left[\left(\frac{a}{A}\right)_{IL}^{n+1} + (k_{pu\xi})_{IL}^{n+1} \right] (\bar{\rho} \bar{u})_{IL}^{n+1} \\
& + \left(\frac{v}{1-v}\right)_{IL}^{n+1} \frac{\bar{\rho}^{n+1}}{\rho_{IL}^{n+1}} \left[(u_{s\xi})_{IL}^{n+1} + \left(\frac{a}{A}\right)_{IL}^{n+1} (u_s)_{IL}^{n+1} \right] \\
& + \left(\frac{\Delta \tau}{2}\right) \left(\frac{v}{1-v}\right)_{IL}^{n+1} \left[1 - \left(\frac{\bar{\rho}}{\rho_s}\right)_{IL}^{n+1} \right] (\dot{M}_s)_{IL}^{n+1} \quad (4.65)
\end{aligned}$$

Conservation of Momentum for the Combustion Gas

Breech Boundary Predictor

$$(\bar{\rho} \bar{u})_1^{n+1} = 0 \quad (4.66)$$

Breech Boundary Corrector

$$(\bar{\rho} \bar{u})_1^{n+1} = 0 \quad (4.67)$$

Projectile Boundary Predictor

$$(\bar{\rho} \bar{u})_{IL}^{n+1} = \bar{\rho}_{IL}^{n+1} u_p^{n+1} \quad (4.68)$$

Projectile Boundary Corrector

$$(\bar{\rho} \bar{u})_{IL}^{n+1} = \bar{\rho}_{IL}^{n+1} u_p^{n+1} \quad (4.69)$$

Conservation of Energy for the Combustion Gas

Breech Boundary Predictor

$$\begin{aligned}
\bar{e}_1^{n+1} = & \bar{e}_1^n + \left(\frac{\Delta \tau}{L_p}\right)^n \left(\frac{1}{\Delta \xi}\right) \{ [(2)(\bar{e}u)_2^n - (\frac{1}{2})(\bar{e}u)_3^n] - [(2)(P\bar{u})_2^n \\
& - (\frac{1}{2})(P\bar{u})_3^n] \} - \left(\frac{\Delta \tau}{L_p}\right)^n \left(\frac{v}{1-v}\right)_1^n (\bar{e}u_{s\xi})_1^n \\
& + \Delta \tau \left(\frac{v}{1-v}\right)_1^n (\dot{M}_s)_1^n \{ [h_{sg} - C_{ps}(T_{ig} - T_{init}) - h(\bar{T}_1^n) \\
& - h(T_{ig})] \} - \left(\frac{\bar{e}}{\rho_s}\right)_1^n - \left(\frac{\Delta t}{1-v}\right)_1^n (q_w)_1^n \left(\frac{2}{R}\right)_1
\end{aligned} \quad (4.70)$$

Breech Boundary Corrector

$$\begin{aligned}
\bar{e}_1^{n+1} = & \frac{1}{2} (\bar{e}_1^n + \bar{e}_1^{n+1}) + \left(\frac{1}{2}\right) \left(\frac{\Delta \tau}{L_p}\right) \left(\frac{1}{\Delta \xi}\right) \{ [(2)(\bar{e}u)_2^{n+1} - (\frac{1}{2})(\bar{e}u)_3^{n+1}] \\
& - [(2)(P\bar{u})_2^{n+1} - (\frac{1}{2})(P\bar{u})_3^{n+1}] \} - \left(\frac{1}{2}\right) \left(\frac{\Delta \tau}{L_p}\right)^{n+1} \left(\frac{v}{1-v}\right)_1^{n+1} (\bar{e}u_{s\xi})_1^{n+1} \\
& + \left(\frac{\Delta \tau}{2}\right) \left(\frac{v}{1-v}\right)_1^{n+1} (\dot{M}_s)_1^{n+1} \{ [h_{sg} - C_{ps}(T_{ig} - T_{init}) - h(\bar{T}_1^{n+1}) \\
& - h(T_{ig})] \} - \left(\frac{\bar{e}}{\rho_s}\right)_1^n - \left(\frac{1}{2}\right) \left(\frac{\Delta \tau}{1-v}\right)_1^{n+1} (q_w)_1^{n+1} \left(\frac{2}{R}\right)_1
\end{aligned} \quad (4.71)$$

Projectile Base Boundary Predictor

$$\begin{aligned}
\bar{e}_{IL}^{n+1} = & \bar{e}_{IL}^n + \left(\frac{\Delta \tau}{L_p}\right)^n \left(\frac{1}{\Delta \xi}\right) \{ U_p^n \left[\left(\frac{3}{2}\right) \bar{e}_{IL}^n - (2) \bar{e}_{IL-1}^n + \left(\frac{1}{2}\right) \bar{e}_{IL-2}^n \right] \\
& - \left[\left(\frac{3}{2}\right) (\bar{e}u)_{IL}^n - (2) (\bar{e}u)_{IL-1}^n + \left(\frac{1}{2}\right) \bar{e}_{IL-2}^n \right] - \left[\left(\frac{3}{2}\right) (P\bar{u})_{IL}^n - (2) (P\bar{u})_{IL-1}^n \right]
\end{aligned}$$

$$\begin{aligned}
& + \left(\frac{1}{2}\right)(\bar{P}\bar{u})_{IL-2}^n + \left(\frac{1}{1-v}\right)_{IL}^n [(\bar{e}\bar{u})_{IL}^n - (\bar{e}u_s)_{IL}^n + (\bar{P}\bar{u})_{IL}^n] \left[\left(\frac{3}{2}\right)v_{IL}^n \right. \\
& - (2)v_{IL-1}^n + \left(\frac{1}{2}\right)v_{IL-2}^n \left. \right] - \left(\frac{v}{1-v}\right)_{IL}^n (\bar{e}u_{s\xi})_{IL}^n - \left(\frac{\Delta\tau}{L_p}\right)^n \{ (k_{eu\xi} \bar{e}\bar{u})_{IL}^n \\
& + [(\bar{e}\bar{u})_{IL}^n + \left(\frac{v}{1-v}\right)_{IL}^n (\bar{e}u_s)_{IL}^n + (\bar{P}\bar{u})_{IL}^n] \left(\frac{a}{A}\right)_{IL}^n + \left(\frac{v}{1-v}\right)_{IL}^n (eu_{s\xi})_{IL}^n \} \\
& + \Delta\tau \left(\frac{v}{1-v}\right)_{IL}^n (\dot{M}_s)_{IL}^n - C_{Ps}(T_{ig} - T_{init}) - (h(\bar{T}_{IL}^n) - h(T_{ig})) \\
& - \left(\frac{\bar{e}}{\rho_s}\right)_{IL}^n - \left(\frac{\Delta\tau}{1-v}\right)_{IL}^n (q_w)_{IL}^n \left(\frac{2}{R}\right)_{IL} \quad (4.72)
\end{aligned}$$

Projectile Base Boundary Corrector

$$\begin{aligned}
\bar{e}_{IL}^{n+1} &= \frac{1}{2} (\bar{e}_{IL}^n + \bar{e}_{IL}^{n+1}) + \left(\frac{1}{2}\right) \left(\frac{\Delta\tau}{L_p}\right)^{n+1} \left(\frac{1}{\Delta\xi}\right) \{ U_p^{n+1} \left[\left(\frac{3}{2}\right)\bar{e}_{IL}^{n+1} - (2)\bar{e}_{IL-1}^{n+1} \right. \right. \\
& + \left.\left(\frac{1}{2}\right)\bar{e}_{IL-2}^{n+1} \right] - \left[\left(\frac{3}{2}\right)(\bar{e}\bar{u})_{IL}^{n+1} - (2)(\bar{e}\bar{u})_{IL-1}^{n+1} + \left(\frac{1}{2}\right)(\bar{e}\bar{u})_{IL-2}^{n+1} \right] \\
& - \left[\left(\frac{3}{2}\right)(\bar{P}\bar{u})_{IL}^{n+1} - (2)(\bar{P}\bar{u})_{IL-1}^{n+1} + \left(\frac{1}{2}\right)(\bar{P}\bar{u})_{IL-2}^{n+1} \right] \\
& + \left(\frac{1}{1-v}\right)_{IL}^{n+1} [(\bar{e}\bar{u})_{IL}^{n+1} - (\bar{e}u_s)_{IL}^{n+1} + (\bar{P}\bar{u})_{IL}^{n+1}] \left[\left(\frac{3}{2}\right)v_{IL}^{n+1} \right. \\
& - (2)v_{IL-1}^{n+1} + \left(\frac{1}{2}\right)v_{IL-2}^{n+1} \left. \right] + \left(\frac{1}{2}\right) \left(\frac{\Delta\tau}{L_p}\right)^{n+1} \{ (k_{eu\xi} \bar{e}\bar{u})_{IL}^{n+1} + [(\bar{e}\bar{u})_{IL}^{n+1} \\
& + \left(\frac{v}{1-v}\right)_{IL}^{n+1} (\bar{e}u_s)_{IL}^{n+1} + (\bar{P}\bar{u})_{IL}^{n+1}] \left(\frac{a}{A}\right)_{IL}^{n+1} + \left(\frac{v}{1-v}\right)_{IL}^{n+1} (eu_{s\xi})_{IL}^{n+1} \} \\
& + \left(\frac{\Delta\tau}{2}\right) \left(\frac{v}{1-v}\right)_{IL}^{n+1} (\dot{M}_s)_{IL}^{n+1} \{ [h_{sg} - C_{Ps}(T_{ig} - T_{init}) - (h(\bar{T}_{IL}^{n+1}))
\end{aligned}$$

$$- h(\tau_{ig})) - (\bar{e}_s)_{IL}^{n+1} - \left(\frac{1}{2}\right) \left(\frac{\Delta \tau}{1-v}\right)_{IL}^{n+1} (q_w)_{IL}^{n+1} \left(\frac{2}{R}\right)_{IL} \quad (4.73)$$

Summary of the Solution Procedure

At this point all the equations needed to specify the viscous interior ballistic problem have been developed. A solution procedure for this problem proceeds as follows:

- I) Specify the input parameters listed in table 4.1 for all grid points i and i^* .
- II) Specify initial values for the dependent variables v , \bar{p} , $\bar{\rho}u$ and \bar{e} for all grid points i and i^* .
- III) Find the values of the dependent variables at the predictor time level $\overline{n+1}$ in the following manner:

Predictor

- 1) Find $v_{i^*}^{n+1}$, and v_i^{n+1} .
 - a) find $v_{i^*}^{n+1}$ at all i interior points by using Eq. (4.36)
 - b) find $v_{i^*}^{n+1}$ by using Eq. (4.58)
 - c) find v_{IL}^{n+1} by using Eq. (4.60)
 - d) find v_i^{n+1} at all i grid points by interpolating between $v_{i^*}^{n+1}$ values at i^* grid points (see Appendix A)
 - e) store all values of $v_{i^*}^{n+1}$ and v_i^{n+1} for use in the corrector FDE's

- 2) Find $\overline{\rho}_1^{n+1}$, $(\overline{\rho u})_1^{n+1}$, and \overline{e}_1^{n+1} .
- find $\overline{\rho}_1^{n+1}$, $(\overline{\rho u})_1^{n+1}$, and \overline{e}_1^{n+1} at all i interior grid points by using Eqs. (4.38), (4.40) and (4.42)
 - find $\overline{\rho}_1^{n+1}$ and $\overline{\rho}_{IL}^{n+1}$ by using Eq. (4.62) and Eq. (4.64)
 - find $(\overline{\rho u})_1^{n+1}$ by using Eq. (4.66)
 - guess the value of $(\overline{\rho u})_{IL}^{n+1}$ by using a one-sided difference version of Eq. (4.40)
 - find \overline{e}_1^{n+1} and \overline{e}_{IL}^{n+1} by using Eq. (4.70) and Eq. (4.72)
- 3) Find \overline{u}_1^{n+1} , \overline{T}_1^{n+1} , and \overline{p}_1^{n+1} .
- find \overline{u}_1^{n+1} at all i grid points by dividing $(\overline{\rho u})_1^{n+1}$ by $\overline{\rho}_1^{n+1}$
 - find \overline{T}_1^{n+1} at all i grid points by applying the internal energy equation (Eq. (4.8)) in Eq. (4.6) where all variables are discretized (i) predictor variables and \overline{e}_1^{n+1} , $\overline{\rho}_1^{n+1}$, and \overline{u}_1^{n+1} are known
 - find \overline{p}_1^{n+1} at all i grid points by using Eq. () where $\overline{\rho}_1^{n+1}$ and \overline{T}_1^{n+1} are now known
- 4) Find \overline{U}_p^{n+1} , $(\overline{\rho u})_{IL}^{n+1}$, and \overline{L}_p^{n+1} .
- find \overline{P}_f^{n+1} (the projectile frontal pressure) by using Eq. (2.30) or Eq. (2.31)
 - find \overline{U}_p^{n+1} by using Eq. (4.21) or Eq. (4.33) where all variables are discretized (i) predictor variables

- c) find $(\bar{\rho u})_{IL}^{n+1}$ by using Eq. (4.68)
- d) find L_p^{n+1} by using Eq. (4.24) where all variables are discretized (i) predictor variables
- 5) Find $(CD_1)_i^{n+1}$, U_s^{n+1} , and L_s^{n+1} .
- a) find $(CD_1)_i^{n+1}$ at all i grid points by using Eq. (4.14) or Eq. (4.16) where all variables are discretized (i) predictor variables
- b) solve for U_s^{n+1} and L_s^{n+1} by using the iterative method described in Appendix A
- 6) Find $(u_s)_i^{n+1}$, $(u_s)_{i*}^{n+1}$, $(u_{s\xi})_{i*}^{n+1}$, and $(u_{s\xi})_i^{n+1}$.
- a) find $(u_s)_i^{n+1}$ at all i grid points by using Eq. (4.7) where all variables are discretized (i) predictor variables
- b) find $(u_s)_{i*}^{n+1}$ at all i* grid points by interpolating between $(u_s)_{i*}^{n+1}$ values at i grid points (see Appendix A)
- c) find $(u_{s\xi})_{i*}^{n+1}$ at all i* grid points by using backward differencing of $(u_s)_{i*}^{n+1}$ for grid points $(2 \leftrightarrow IL)^*$ and one-sided differencing of $(u_s)_{i*}^{n+1}$ at grid point 1
- d) find $(u_{s\xi})_i^{n+1}$ at all i grid points by interpolating between $(u_{s\xi})_{i*}^{n+1}$ values at i* grid points (see Appendix A)

7) Find $(\dot{M}_s)_i^{n+1}$ and $(\dot{M}_s)_{i*}^{n+1}$.

a) find $(\dot{M}_s)_i^{n+1}$ at all i grid points by using Eq. (4.17)

or Eq. (4.18) where all variables are discretized (i)

predictor variables and $(r_b)_i$ depends on p_i^{n+1}

b) find p_{i*}^{n+1} at all $i*$ grid points by interpolating

between p_i^{n+1} values at i grid points (see Appendix A)

c) find $(\dot{M}_s)_{i*}^{n+1}$ at all $i*$ grid points by using Eq. (4.17)

or (4.18) where all variables are discretized ($i*$)

predictor variables and $(r_b)_{i*}$ depends on p_{i*}^{n+1}

8) Find R_i^{n+1} , A_i^{n+1} , and a_i^{n+1} .

a) use the set of equations which corresponds to the

chosen tube geometry (see Tables 2.1-2.3) to find

R_i^{n+1} , A_i^{n+1} and a_i^{n+1}

9) Find R_{i*}^{n+1} , A_{i*}^{n+1} , and a_{i*}^{n+1} .

a) find R_{i*}^{n+1} , A_{i*}^{n+1} and a_{i*}^{n+1} at all $i*$ grid points by

interpolating between R_i^{n+1} , A_i^{n+1} , and a_i^{n+1} values

respectively at i grid points (see Appendix A)

10) Find the dissipative terms $(\tau_w)_i^{n+1}$, D_i^{n+1} , and $(q_w)_i^{n+1}$.

a) find $(\tau_w)_i^{n+1}$ at all i grid points by using Eq. (4.26)

where all variables are discretized (i) predictor variables

b) find D_i^{n+1} at all i grid points by using Eq. (4.27)

where all variables are discretized (1) predictor variables

- c) find $(q_w)_i^{n+1}$ at all i grid points by using Eq. (4.28)

where all variables are discretized (1) predictor variables, or by using heat flux information obtained from a boundary layer analysis of this problem

- 11) Find the K-factors and derivatives of K-factors by using Eq. (4.31) and Eqs. (4.44)-(4.48) or by using K-factor information obtained from a boundary layer analysis of this problem.

IV) Find the values of the dependent variables at the corrector time level of $n+1$ in the following manner:

Corrector

- 1) Find v_{i*}^{n+1} , v_i^{n+1} .
 - a) find v_{i*}^{n+1} at all i interior points by using Eq. (4.37)
 - b) find v_{i*}^{n+1} by using Eq. (4.59)
 - c) find v_{IL*}^{n+1} by using Eq. (4.61)
 - d) find v_i^{n+1} at all i grid points by interpolating between v_{i*}^{n+1} values at i^* grid points (see Appendix A)
 - e) store all values of v_{i*}^{n+1} and v_i^{n+1} for use in the predictor FDE's.
- 2) Find $\bar{\rho}_i^{n+1}$, $(\bar{\rho}u)_i^{n+1}$, and \bar{e}_i^{n+1} .
 - a) find $\bar{\rho}_i^{n+1}$, $(\bar{\rho}u)_i^{n+1}$ and \bar{e}_i^{n+1} at all i interior grid points by using Eqs. (4.39), (4.41) and (4.43)

- b) find $\bar{\rho}_1^{n+1}$ and $\bar{\rho}_{IL}^{n+1}$ by using Eq. (4.63) and Eq. (4.65)
 - c) find $(\bar{\rho}\bar{u})_1^{n+1}$ by using Eq. (4.67)
 - d) guess the value of $(\bar{\rho}\bar{u})_{IL}^{n+1}$ by using a one-sided difference version of Eq. (4.41)
 - e) find \bar{e}_1^{n+1} and \bar{e}_{IL}^{n+1} by using Eq. (4.71) and Eq. (4.73)
- 3) Find \bar{u}_1^{n+1} , \bar{T}_1^{n+1} , and P_1^{n+1} .
- a) find \bar{u}_1^{n+1} at all i grid points by dividing $(\bar{\rho}\bar{u})_1^{n+1}$ by $\bar{\rho}_1^{n+1}$
 - b) find \bar{T}_1^{n+1} at all i grid points by applying the internal energy equation (Eq. (4.8)) in Eq. (4.6) where all variables are discretized (i) corrector variables and \bar{e}_1^{n+1} , $\bar{\rho}_1^{n+1}$ and \bar{u}_1^{n+1} are known
 - c) find P_1^{n+1} at all i grid points by using Eq. (4.5) where $\bar{\rho}_1^{n+1}$ and \bar{T}_1^{n+1} are now known
- 4) Find U_p^{n+1} , $(\bar{\rho}\bar{u})_{IL}^{n+1}$, and L_p^{n+1} .
- a) find P_f^{n+1} (the projectile frontal pressure) by using Eq. (2.30) or Eq. (2.31)
 - b) find U_p^{n+1} by using Eq. (4.21) or Eq. (4.23) where all variables are discretized (i) corrector variables
 - c) find $(\bar{\rho}\bar{u})_{IL}^{n+1}$ by using Eq. (4.69)
 - d) find L_p^{n+1} by using Eq. (4.24) where all variables are discretized (i) corrector variables
- 5) Find $(CD_1)_1^{n+1}$, U_s^{n+1} , and L_s^{n+1} .
- a) find $(CD_1)_1^{n+1}$ at all i grid points by using Eq. (4.14) or Eq. (4.16) where all variables are discretized (i) corrector variables
 - b) solve for U_s^{n+1} and L_s^{n+1} by using the iterative method

described in Appendix A

- 6) Find $(u_s)_i^{n+1}$, $(u_s)_{i*}^{n+1}$, $(u_{s\xi})_{i*}^{n+1}$, and $(u_{s\xi})_i^{n+1}$.
 - a) find $(u_s)_i^{n+1}$ at all i grid points by using Eq. (4.7) where all variables are discretized (i) corrector variables
 - b) find $(u_s)_{i*}^{n+1}$ at all $i*$ grid points by interpolating between $(u_s)_i^{n+1}$ values at i grid points (see Appendix A)
 - c) find $(u_{s\xi})_{i*}^{n+1}$ by using forward differencing of $(u_s)_{i*}^{n+1}$ for grid points $(1 \leftrightarrow IL-1)*$ and one-sided differencing of $(u_s)_{i*}^{n+1}$ at grid point $1*$
 - d) find $(u_{s\xi})_i^{n+1}$ by interpolating between $(u_{s\xi})_{i*}^{n+1}$ values at $i*$ grid points (see Appendix A)
- 7) Find $(\dot{M}_s)_i^{n+1}$ and $(\dot{M}_s)_{i*}^{n+1}$.
 - a) find $(\dot{M}_s)_i^{n+1}$ at all i grid points by using Eq. (4.17) or Eq. (4.18) where all variables are discretized (i) corrector variables and $(r_b)_i$ depends on P_i^{n+1}
 - b) find P_{i*}^{n+1} at all $i*$ grid points by interpolating between P_i^{n+1} values at i grid points (see Appendix A)
 - c) find $(\dot{M}_s)_{i*}^{n+1}$ at all $i*$ grid points by using Eq. (4.17) or Eq. (4.18) where all variables are discretized ($i*$) corrector variables and $(r_b)_{i*}$ depends on P_{i*}^{n+1}
- 8) Find R_i^{n+1} , A_i^{n+1} , and a_i^{n+1} .
 - a) use the set of equations which corresponds to the chosen tube geometry (see tables ()-()) to find R_i^{n+1} , A_i^{n+1} and a_i^{n+1}
- 9) Find R_{i*}^{n+1} , A_{i*}^{n+1} , and a_{i*}^{n+1} .

- a) find R_{i*}^{n+1} , A_{i*}^{n+1} and a_{i*}^{n+1} at all i^* grid points by interpolating between R_i^{n+1} , A_i^{n+1} and a_i^{n+1} values respectively at i grid points
- 10) Find the dissipative terms $(\tau_w)_i^{n+1}$, D_i^{n+1} , and $(q_w)_i^{n+1}$.
- a) find $(\tau_w)_i^{n+1}$ at all i grid points by using Eq. (4.26) where all variables are discretized (i) corrector variables
- b) find D_i^{n+1} at all i grid points by using Eq. (4.27) where all variables are discretized (i) corrector variables
- c) find $(q_w)_i^{n+1}$ at all i grid points by using Eq. (4.28) where all variables are discretized (i) corrector variables, or by using heat flux information obtained from a boundary layer analysis of this problem
- 11) Find the K-factors and derivatives of K-factors by using Eq. (4.31) and Eqs. (4.44)-(4.48) or by using K-factor information obtained from a boundary layer analysis of this problem.

V) Repeat steps III and IV until the projectile has traveled a prescribed length L_f .

4.5 Results

In this section, the results of several computer simulations of viscous interior ballistic flow are presented and compared. Salient gun performance parameters were determined and conclusions were drawn about their significance.

Description of Cases

A case study which isolated the effect of a parameter on gun performance was made for the viscous interior ballistic problem. Table 4.2 lists the values or equations of parameters which did not change in these case studies. The assumptions common to all the viscous interior ballistic case studies are listed as follows:

- 1) Combustion gas flow is unsteady and one-dimensional in the axial direction (where radial effects are accounted for by the K-factor approach).
- 2) Combustion gas pressure varies in the axial direction only.
- 3) All K-factors are set to 1.0 and all derivatives of K-factors are set to 0.0.
- 4) The tube assembly is a straight tube.

Table 4.3 lists the equations of parameters which were varied in the viscous interior ballistics case studies. The sum of the parameters listed in Tables 4.2 and 4.3 specify the viscous interior ballistic problem.

Table 4.2

Specification in MKS units of parameters (and equations) which remain the same for all viscous interior ballistic case studies

Projectile Parameters

$$U_{p0} = 0.0$$

$$P_{or} = 6.895 \times 10^6$$

Air Parameters

$$T_{atm} = 300$$

$$P_{atm} = 1.0 \times 10^5$$

$$\gamma_{atm} = 1.41$$

$$R_{atm} = 296.82$$

Combustion Gas Parameters

$$m_{mass} = 24.0728$$

$$T_0 = 300$$

$$P_0 = 3.449 \times 10^6$$

$$U_0 = 0.0$$

μ is given by Eq. (A.93)

k is given by Eq. (A.94)

Pr is given by Eq. (A.95)

$$f = 0.02$$

Propellant Parameters

$$\text{type} = \text{CIL 3352}$$

grain geometry = cylindrical,
single perforate

$$m_{c0} = 0.148$$

$$\rho_s = 1660.820$$

$$w_0 = 86.868 \times 10^{-5}$$

$$d_{i0} = 22.352 \times 10^{-5}$$

$$l_0 = 205.740 \times 10^{-5}$$

$$C_{ps} = 1539.25$$

$$T_{init} = 300$$

$$T_{ig} = 600$$

$$h_{sg} = 4171.998 \times 10^3$$

$$U_{s0} = 0.0$$

$$C_D = 1.0$$

Tube Wall Parameters

$$T_{w0} = 300$$

α is given by Eq. (A.98)

Table 4.3
Parameters and equations which were varied in the
viscous interior ballistic case studies

| Case | CD_1 | D | \dot{P} | τ_w | Q_w |
|------|-------------------------|------------------------|-------------------------|-------------------------|-------------------------|
| BA | 0.0 | given by Eq. (4.27) | 0.0 | 0.0 | 0.0 |
| BB | given by Eq. (4.14)* | given by Eq. (4.27) | 0.0 | 0.0 | 0.0 |
| BC | 1.0* | given by Eq. (4.27) | 0.0 | 0.0 | 0.0 |
| BD | 1.0 | given by Eq. (4.27) | given by Eq. (4.74)* | 0.0 | 0.0 |
| BE | 1.0 | given by Eq. (4.27) | given by Eq. (4.74) | given by Eq. (4.26)* | 0.0 |
| BF | 1.0 | given by Eq. (4.27) | given by Eq. (4.74) | given by Eq. (4.26) | given by Eq. (4.29)* |

* Indicates a change in value from the previous case.

Case BA was the simplest viscous interior ballistic case study. In addition to the general assumptions listed previously, the following simplifying assumptions were used to analyze this case:

- 1) The propellant grain-combustion gas velocity ratio (CD_1) is 0.0.
- 2) There is no momentum generation.
- 3) There is no tube wall shear stress.
- 4) There is no heat transfer.

The rest of the viscous interior ballistic cases reduce these simplifying assumptions one-by-one in the following manner:

- 1) Case BB is the same as case BA except that CD_1 is described by Eq. 4.14 and varies between 0.0 and 1.0.
- 2) Case BC is the same as case BB except that CD_1 is set equal to 1.0.
- 3) Case BD is the same as case BC except that momentum generation described by the equation

$$\dot{P} = A \left(\frac{v}{1-v} \right) \dot{M}_s CD_1 \bar{u} \quad (4.74)$$

is considered.

- 4) Case BE is the same as case BD except that tube wall shear stress, τ_w (given by Eq. (4.26)), is considered.
- 5) Case BF is the same as case BE except that tube wall heat flux, q_w (given by Eq. (4.29)), is considered.

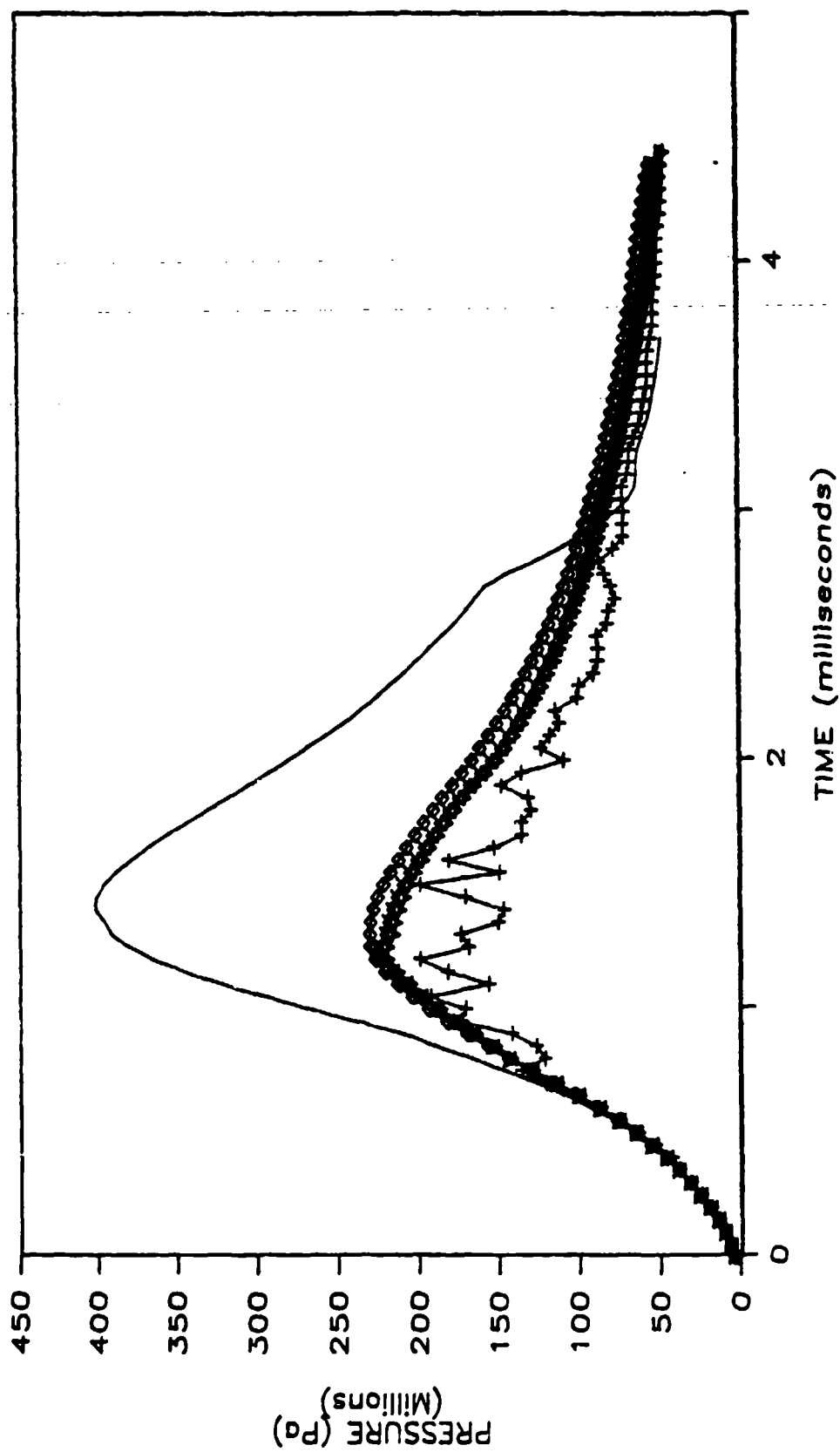


Figure 4.1

Breech pressure as a function of time for the viscous interior ballistic cases BA-BF.

- denotes case BA, + denotes case BB, \diamond denotes case BC, Δ denotes case BD,
- x denotes case BE, and ∇ denotes case BF.

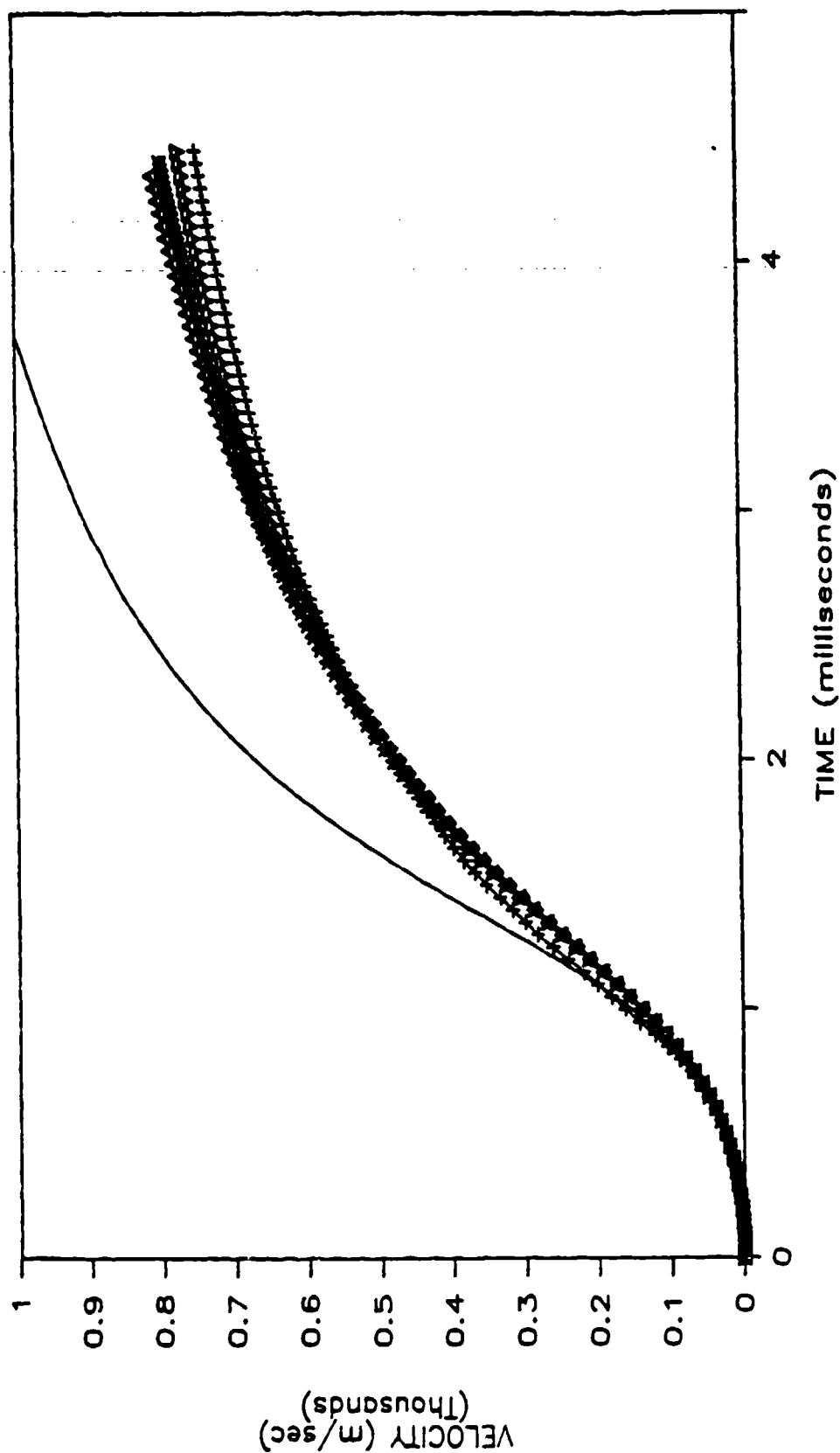


Figure 4.2

Projectile velocity as a function of time for the viscous interior ballistic cases BA-BF. - denotes case BA, + denotes case BB, \diamond denotes case BC, Δ denotes case BD, x denotes case BE, and ∇ denotes case BF.

Table 4.4

Muzzle velocity, peak breech pressure, time of occurrence of peak breech pressure and percent differences for an actual gun firing and for the viscous interior ballistic cases BA-BF

| Case | U_{pf} (m/sec) | % Dif. | Peak P (10^5 Pa) | % Dif. | Time ($P_k P$) (milli-sec) | % Dif. |
|------|---------------------|--------|------------------------|--------|---------------------------------|--------|
| BA | 997 | | 4009 | | 1.40 | |
| BB | 747 | -25.1 | 1987 | -50.4 | 1.20 | -14.3 |
| BC | 793 | 6.2 | 2293 | 15.4 | 1.30 | 8.3 |
| BD | 807 | 1.8 | 2222 | -3.1 | 1.25 | -3.8 |
| BE | 795 | -1.5 | 2224 | <0.1 | 1.25 | 0.0 |
| BF | 770 | -3.1 | 2183 | -1.9 | 1.20 | -4.0 |
| EXP | 960 | | 3187 | | 1.20 | |

Case Performance

Figure 4.1 shows a plot of breech pressure versus time for cases BA-BF while Fig. 4.2 shows a plot of projectile velocity versus time for cases BA-BF. Table 4.4 lists the muzzle velocity, the peak breech pressure and the time of occurrence of peak breech pressure for cases BA-BF. It also lists the percent difference (from the previous case) of each of these quantities.

The effect of the propellant grain drag force can be seen by comparing the viscous case BA with the inviscid case AD (see section 2.5) since the only difference between these two cases is the addition of a drag force term. When compared to case AD, case BA shows a negligible difference in muzzle velocity, peak breech pressure and the time needed to reach peak breech pressure.

The effect of a variable propellant grain-combustion gas velocity ratio on the numerical solution can be seen by comparing cases BA and BB. When compared to case AA, case BB shows a 25.1% decrease in muzzle velocity, a 50.4% decrease in peak pressure and a 14.3% decrease in the time needed to reach peak breech pressure.

When CD_1 is near 1.0, the propellant grain velocity is nearly that of the gas. There is a discontinuity at position L_g where the number of propellant grains drops suddenly from a finite value to zero. The effect of the discontinuity seems to be to produce pressure pulses as seen in Fig. 4.1. These pulses are not a physical phenomenon, but are produced when the propellant grain and combustion gas grids move past each other. The magnitude of these pulses was observed to increase when the distance between the discontinuity and the projectile base decreases.

The maximum effect of the propellant grain-combustion gas velocity ratio (CD_1) can be seen by comparing cases BA and BC. When compared to case BA, case BC shows a 20.4% decrease in muzzle velocity, a 42.8% decrease in peak breech pressure and a 7.1% decrease in the time needed to reach peak breech pressure. This is the largest performance difference observed in the viscous interior ballistic case studies.

Cases BA and BC also bracket the experimentally obtained muzzle velocity and peak pressure for an actual gun firing (see Table 4.4). The parameters which specify the viscous interior ballistic flow problem were chosen to match the experimental conditions as closely as possible [Refs. 14,29].

The effect of momentum generation can be seen by comparing case BC and BD. When compared to case BC, case BD shows a 1.8% increase in muzzle velocity, a 3.1% decrease in peak breech pressure and a 3.8% decrease in the time needed to reach peak breech pressure. This is the only case comparison in which there is a decrease in peak breech pressure when the corresponding muzzle velocity increases.

The effect of tube wall shear stress can be seen by comparing cases BD and BE. When compared to case BD, case BE shows a 1.5% decrease in muzzle velocity and negligible changes in peak breech pressure and time needed to reach peak breech pressure.

The effect of tube wall heat transfer can be seen by comparing cases BE and BF. When compared to case BE, case BF shows a 3.1% decrease in muzzle velocity, a 1.9% decrease in peak breech pressure and a 4% decrease in the time needed to reach peak breech pressure. This indicates that the effects of heat transfer should be considered when constructing a detailed and accurate model of interior ballistic flow.

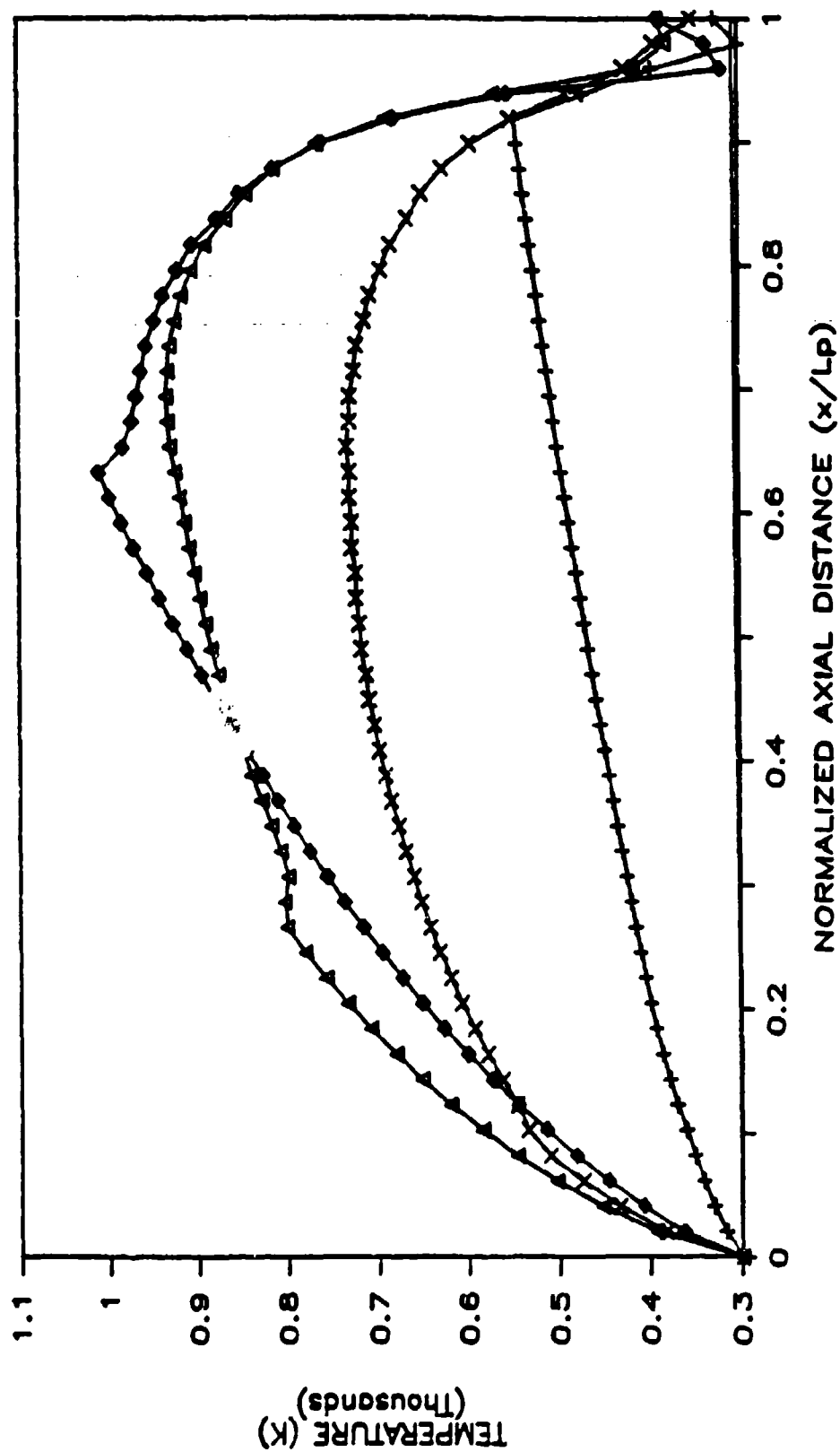


Figure 4.3

Tube wall temperature as a function of normalized distance at five times (t) where

- indicates $t = 0.24$ msec, + indicates $t = 0.74$ msec, \diamond indicates 1.34 msec,

Δ indicates 2.34 msec, and x indicates 4.39 msec.

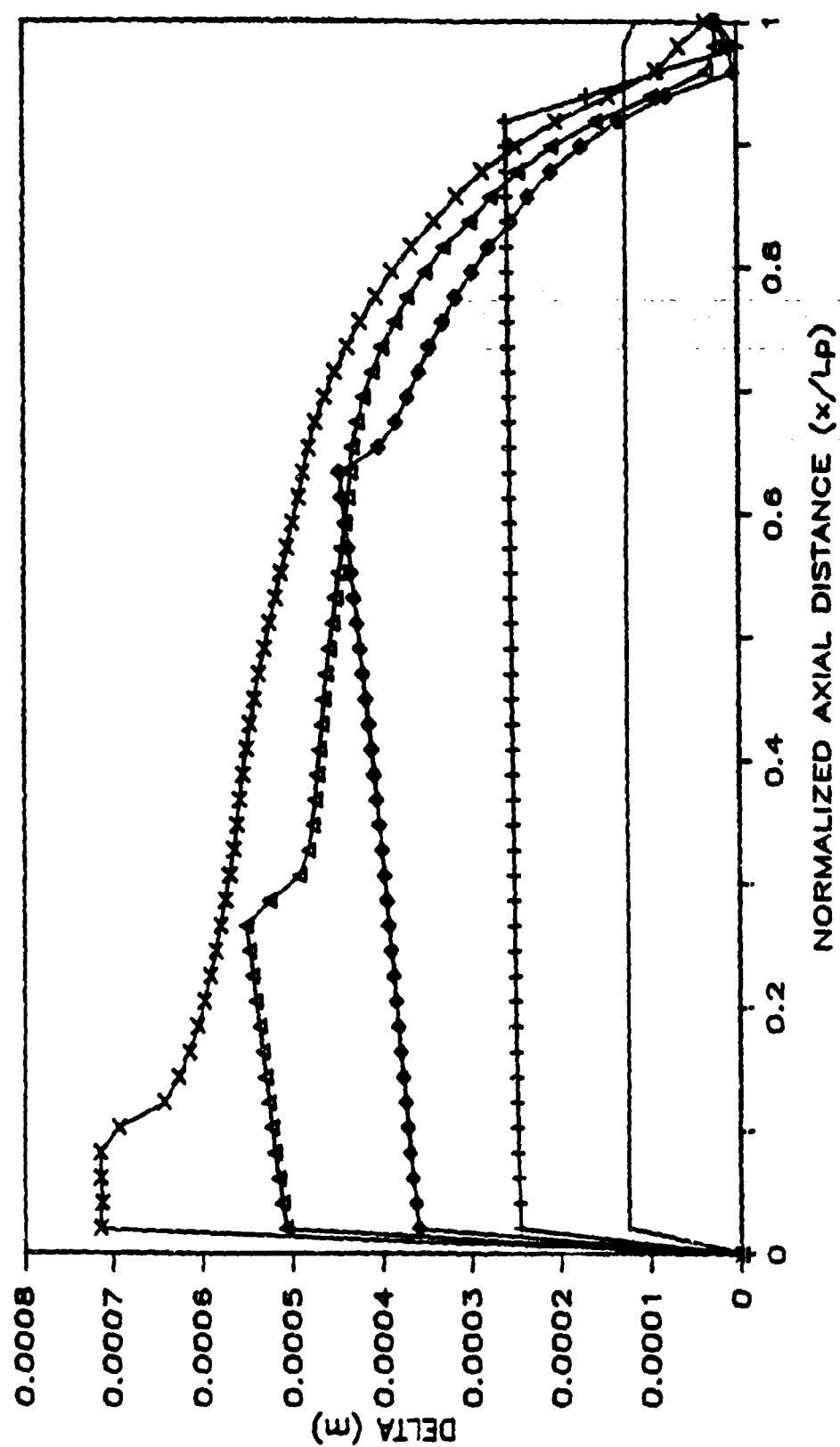


Figure 4.6

Heat penetration distance as a function of normalized distance at five times (t)

where $-$ indicates $t=0.24$ msec, $+$ indicates $t=0.74$ msec, \diamond indicates $t=1.34$ msec,

Δ indicates $t=2.34$ msec, and x indicates $t=4.39$ msec.

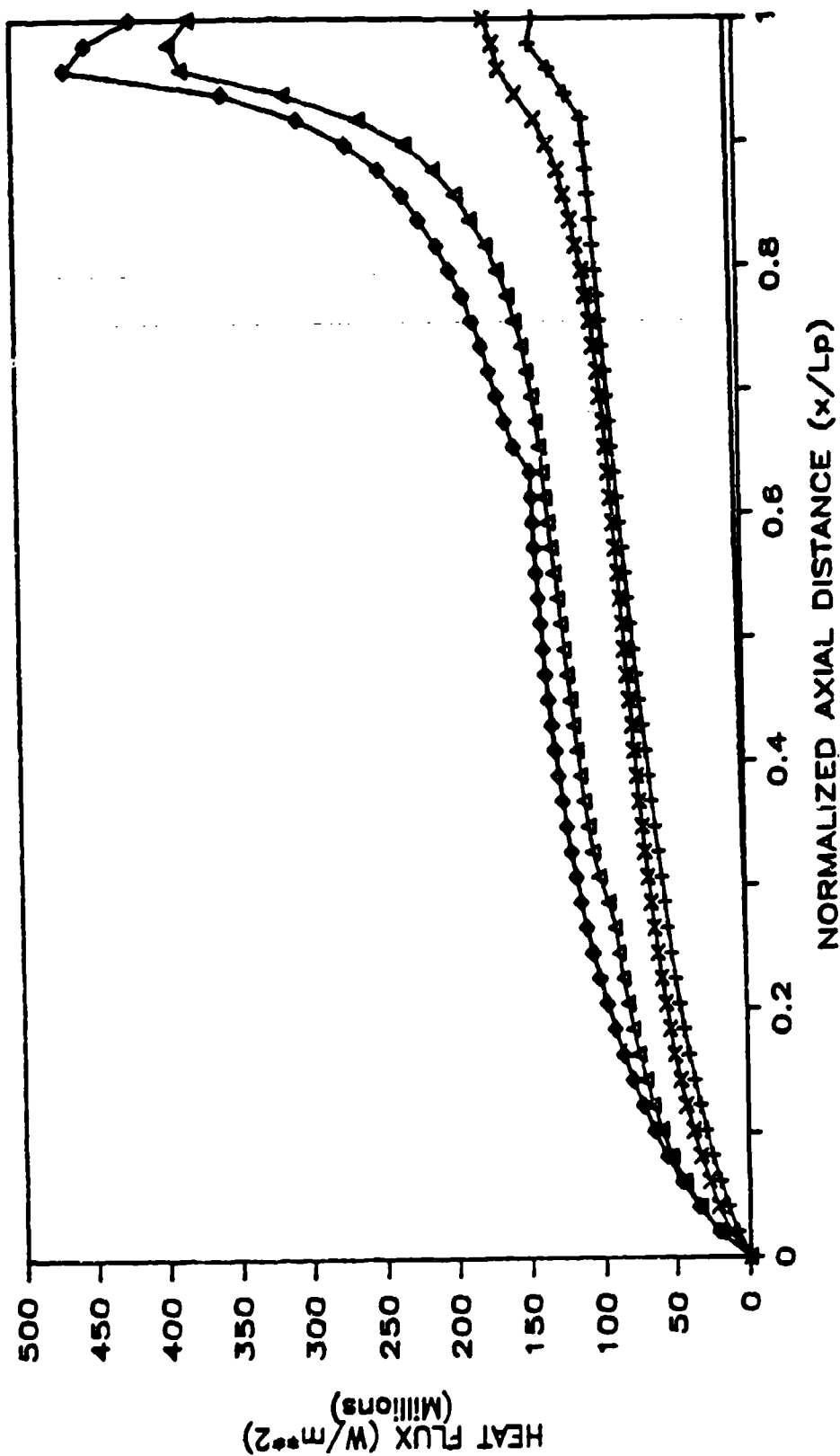


Figure 4.5

Tube wall heat flux as a function of normalized distance at five times (t) where

- indicates $t=0.24$ msec, + indicates $t=0.74$ msec, \diamond indicates 1.34 msec,

Δ indicates 2.34 msec, and x indicates 4.39 msec.

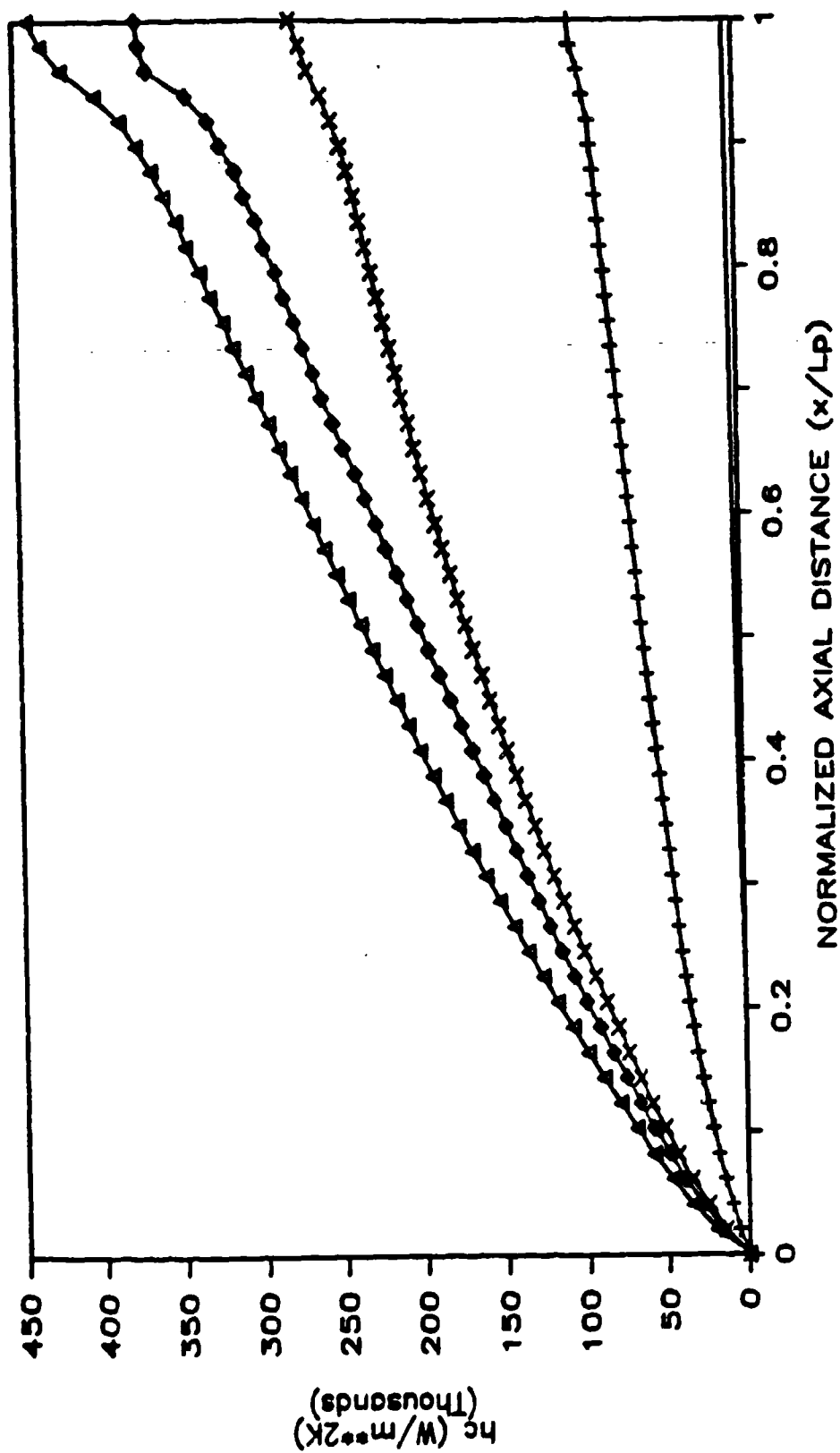


Figure 4.4

Convection coefficient as a function of normalized distance at five times (t) where

- indicates $t = 0.24$ msec, + indicates $t = 0.74$ msec, \diamond indicates 1.34 msec,
- Δ indicates 2.34 msec, and x indicates 4.39 msec.

Tube Wall Heat Transfer

Heat transfer data generated from case BF was chosen to illustrate the unsteady interior ballistic heat transfer problem. This heat transfer problem was modeled as a 1-D conduction problem with unsteady boundary conditions of the third kind. The details of the derivation of the heat transfer equations used here are given in Appendix A and the results of using these equations are presented as follows:

Figure 4.3 shows tube wall temperature plotted against normalized axial distance at five times (t) during the viscous interior ballistic cycle. The maximum tube wall temperature of 1020 K was achieved by adjusting the convection coefficient until the maximum calculated tube wall temperature agreed well with the experimentally obtained maximum tube wall temperature of 1050 K [Ref. 22].

Figure 4.3 shows that the highest tube wall temperatures develop near but not at the base of the projectile. The high temperatures near the projectile base are accounted for by the large value of the convection coefficient in this region (see Fig. 4.4). The sudden drop-off in tube wall temperature at the base of the projectile occurs because relatively cold (ambient temperature) tube wall is being uncovered as the projectile travels down the tube.

Inspection of Fig. 4.3 also shows that the maximum tube wall temperature of 1020 K occurs at $t=1.34$ milliseconds, which coincides with the time at which peak pressure, maximum propellant burning rate, and maximum combustion gas temperature occur. As the shot progresses and combustion gas temperature decreases, tube wall temperature, as shown in Fig. 4.3, correspondingly decreases.

Figure 4.4 shows the convection coefficient (h_c) plotted against normalized axial distance at five times during the viscous interior ballistic cycle. The formula used to calculate h_c was based on a modified version of the Sieder-Tate Nusselt number formula and the details of its derivation are given in Appendix A.

Figure 4.4 shows the strong similarity between the axial convection coefficient profile and the axial combustion gas momentum profile. Also noteworthy are the large magnitudes predicted for the convection coefficient.

A drawback in the model used here to calculate h_c is that it does not take into consideration the fact that the thermal and momentum boundary layer thicknesses decrease to zero at the base of the projectile. This boundary phenomenon would tend to accentuate h_c near the base of the projectile more than is shown in Fig. 4.4.

Figure 4.5 shows tube wall heat flux plotted against normalized axial distance at five times during the viscous interior ballistic cycle.

Very large magnitudes of tube wall heat flux are indicated by Fig. 4.5 with the highest values occurring at $t=1.34$ milliseconds (which is when peak combustion gas temperatures occur).

The most interesting aspect of the heat flux distributions shown in Fig. 4.5 are the sharply increased values near the base of the projectile. This is the result of the combined effects of uncovering previously unexposed tube wall area (which results in low tube wall temperatures) and the increasingly large values of h_c near the base of the projectile.

Figure 4.6 shows the heat penetration distance into the tube

wall (δ) plotted against axial distance at five times during the viscous interior ballistic cycle. These plots again show the effect of uncovering previously unexposed tube wall area as the projectile moves down the tube. The highest value of δ occurs in the region of the tube assembly which has been transferring heat the longest; namely, the original chamber volume. The maximum value of δ shown in Fig. 4.6 is 0.72 millimeters and is typical of a 30 mm gun firing at ambient conditions [Ref. 22].

Chapter V PRESSURE AND DENSITY GRADIENTS IN UNSTEADY TUBE FLOWS

5.1 Physical Mechanisms Causing Pressure and Density Gradients

The physical mechanism which causes a pressure difference between the breech and projectile is the acceleration of the projectile. As the projectile accelerates, it produces a series of expansion waves behind it. The pressure drops from breech to projectile through these waves.

The ballistic cycle begins as combustion occurs within the chamber bounded by the breech, tube wall, and projectile and increases the pressure. Because the burning rate of the propellant increases with increased pressure, high pressures are quickly produced. These high pressures accelerate the projectile producing a series of expansion waves behind it. These waves accelerate the gases behind the projectile to the velocity of the projectile. They travel toward the breech, reflect, and return to the projectile distributing the velocities of the gases between the breech and the projectile.

As the projectile accelerates, the gases behind the projectile also accelerate. This acceleration produces a gradient of pressure, density, and temperature behind the projectile. Subsequently, the pressure at the base of the projectile is lower than that at the breech.

The pressure drop is then governed by the acceleration of the piston. After the acceleration stops, the pressure drop from the stationary end of the cylinder to the moving piston goes to zero. In a typical ballistic system the acceleration begins low, it then increases

rapidly to a peak and drops off with movement of the projectile. It would then be reasonable that the drop of pressure from breech to projectile would be dependent on the acceleration history of the recent past. The recent past would be defined as the time between formation of an expansion wave and when that wave has reflected and returned to the piston. Once the expansion wave has returned to the piston, its remaining effect is only to lower the pressure of the gas in the chamber.

5.2 Equations of Motion for Unsteady Flows

The breech to projectile gradients of pressure, density and temperature are governed by the conservation equations of mass, momentum and energy. One dimensional forms of these equations were solved using simplifying assumptions to determine analytical relationships between the projectile acceleration and the gradients. The derivation of these relationships can be found in Appendix C. The equations of motion for a mixture of gas and solids are the conservation of mass and the conservation of momentum.

$$\frac{\partial}{\partial t} (\rho_s (1-v') + \rho v') + \frac{\partial}{\partial x} (\rho_s (1-v') u_s + \rho v' u) = 0 \quad (5.1)$$

$$\frac{\partial}{\partial t} (u_s \rho_s (1-v') + u \rho v') + \frac{\partial}{\partial x} (u_s^2 \rho_s (1-v') + u^2 \rho v') = - \frac{\partial P}{\partial x} \quad (5.2)$$

It was assumed that the velocity of the solids is related to the velocity of the gas by a constant ratio throughout the tube at any particular instant. No friction or heat transfer effects were included. The two equations were combined to give an equation which has a form similar to the unsteady Bernoulli equation.

$$\frac{\rho_{ml}}{\rho_m} \int_0^x \frac{\partial u}{\partial t} dx + \left(\frac{\rho_{ml} u}{\rho_m} \right)^2 \frac{1}{2} \Big|_x = - \int_{P_b}^x \frac{dP}{\rho_m} \quad (5.3)$$

The terms on the left hand side of Eqn 5.3 are acceleration terms. The integrated acceleration produces the pressure difference from breech to projectile. The right hand side represents the pressure gradient produced by the acceleration.

Acceleration Term

The acceleration term was evaluated for solids and gases. A linear profile of velocity with distance was assumed for both the velocities of gas and solids. The velocity of the solids was assumed to lag that of the gas by the ratio u_s/u_g . This approach was used because several different models including the XNOVA code [Ref. 40] indicated that the velocity profile was quite linear.

When the acceleration of the piston is zero, the linear velocity model seems to predict that the velocity past a point is always decreasing. When $a_p > v^2/L$, the velocity past a point will increase with time. When $a_p < v^2/L$, the velocity past a point will decrease with time. This does not mean however, that the velocity of a particle is slowing down. As one follows a particle it continues on at the same or greater

velocity depending on the level of acceleration of the piston.

Assuming a linear velocity profile and integrating the acceleration side of equation 5.3 gave

$$\left[\frac{\rho_{m1}}{\rho_m} \frac{L a_p}{2} + \frac{u_p^2}{2} \left(\left(\frac{\rho_{m1}}{\rho_m} \right)^2 - \left(\frac{\rho_{m1}}{\rho_m} \right) \right) \right] \xi^2 = - \int_{P_b}^P \xi \frac{dP}{\rho_m} \quad (5.4)$$

$$\text{or } \frac{L a_p}{2} \xi^2 = - \int_{P_b}^P \xi \frac{dP}{\rho_m} \quad (5.5)$$

The most significant portion of the acceleration side is $L a_p / 2$. The factor ρ_{m1}/ρ_m accounts for solids which are not accelerating as fast as the gas. The projectile velocity squared portion of the acceleration side will always have a minus sign in front of it because ρ_{m1}/ρ_m is always less than 1. When there are no longer any solids, ρ_{m1}/ρ_m goes to 1 and the entire acceleration term goes to $L a_p / 2$.

The effect of the lagging behind of the solids is contained in the term ρ_{m1}/ρ_m .

$$\rho_m = \rho_s (1 - v') + \rho v'$$

$$\rho_{m1} = \rho_s (1 - v') u_s / v' + \rho v'$$

This ratio is determined knowing the porosity, the gas density, and u_s/u .

u_s/u was estimated as a constant along the barrel at any instant in time. It was assumed to change with time. The ratio of average acceleration of the solids over the average acceleration of the gas was assumed to be equal to u_s/u . The drag force on the cylindrical grain was

assumed proportional to $(u-u_s)^2$ and equal to the acceleration of the solid grain times its mass.

u_s/u was solved for as a function of a nondimensional acceleration number, Fa . Fa has been formulated to be a function of the easily determined parameters.

$$Fa = \frac{2C_{Dp} \rho_p U^2}{3\pi r_o \rho'_s a_p}$$

$$\frac{u_s}{u} = 1 + \frac{1}{2Fa} (1 - \sqrt{4Fa + 1}) \quad (5.6)$$

The assumption of a linear velocity profile was tested using an inviscid computer model of gas flow in a tube between breech and projectile. The projectile was driven by estimates of accelerations from experimental shots 536 and 571 which will be discussed later. The ratio of the integrated particle acceleration (left hand side of equation 5.3) divided by $a_p L/2$ was plotted against time in Figures 5.1 and 5.2. If the velocity profile was linear, the ratio would be 1. In Figure 5.1 the last 70% of the time has a ratio of 0.98. This indicates that the integrated acceleration estimate of $a_p L/2$ is 2% high. Figure 5.2 is for a case with a 30% higher peak pressure. This higher pressure causes increased acceleration. This increased acceleration rate is the probable cause of the hump in Figure 5.2 that starts at 0.002 seconds. The peak of the hump, 1.07, indicates that the integrated acceleration estimate of $a_p L/2$ is 7% low.

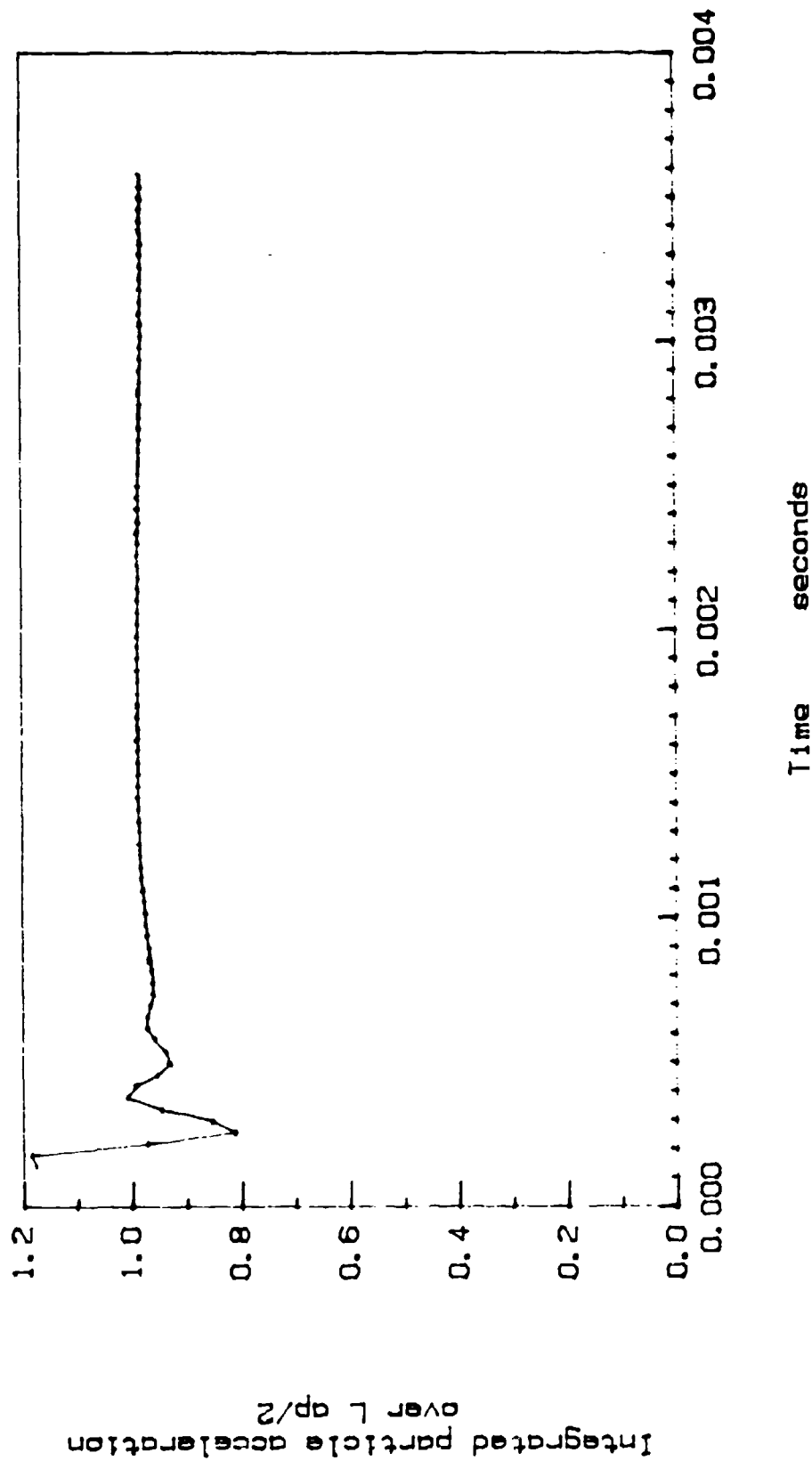
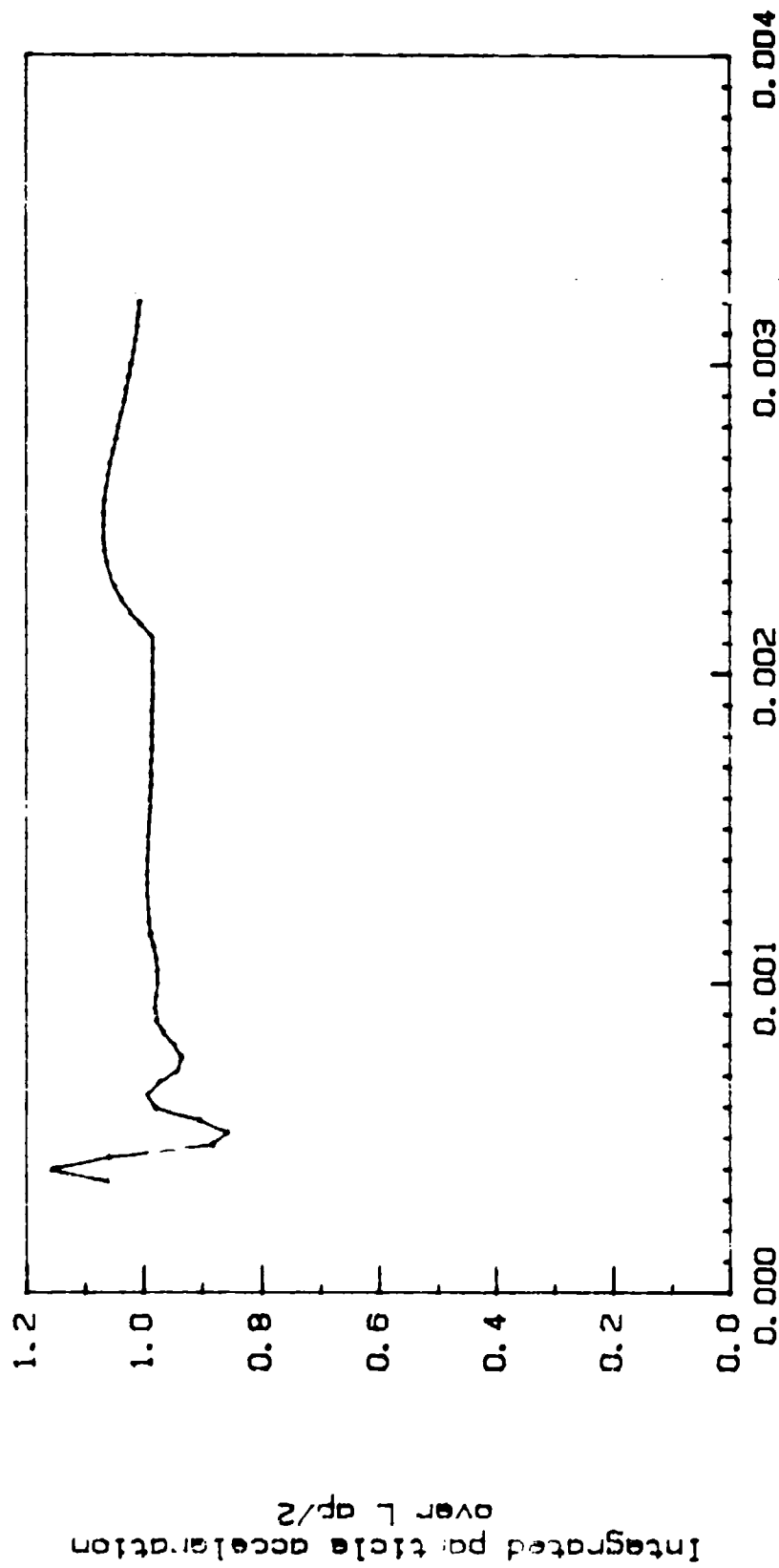


Fig. 5.1 Instantaneous particle acceleration integrated from breech to projectile over $L a_p/2$ calculated using inviscid theory of a compressible gas and using the acceleration of the projectile from shot 536.



Time seconds

Fig. 5.2 Instantaneous particle acceleration integrated from breech to projectile over $L a / 2$ calculated using inviscid theory of a compressible gas using acceleration of the projectile from shot 571.

Pressure Gradient Term

The pressure gradient term was evaluated for the two cases of gas only and of gas and solids. The pressure was integrated by assuming an isentropic relationship between pressure and density. The details of the two derivations are given in appendix C.

The integration of the gas only case stated in terms of temperature and density directly yielded

$$\frac{P_{\xi}}{P_b} = \left(1 - \frac{(\gamma-1)(1-\rho_b n) L a_p \xi^2}{\gamma R T_b} \right)^{\frac{\gamma}{\gamma-1}} \quad (5.7a)$$

When stated in terms of pressure and density it yielded

$$\frac{P_{\xi}}{P_b} = \left(1 - \frac{(\gamma-1) \rho_b L a_p \xi^2}{\gamma P_b} \right)^{\frac{\gamma}{\gamma-1}} \quad (5.7b)$$

The gas and solids case was integrated using a linearized form of the term $(P/P_b)^{(1/\gamma)}$. The equation was stated in terms of temperature and density

$$\frac{P_{\xi}}{P_b} = 1 + \gamma \left(\frac{\rho_s (1/v' - 1)}{\rho_b} + 1 \right) \left[\exp \left(\frac{-v' (1-\rho_b n) L a_p \xi^2}{2 \gamma R T_b} \right) - 1 \right] \quad (5.8a)$$

It was also stated in terms of temperature and density.

$$\frac{P_{\xi}}{P_b} = 1 + \gamma \left(\frac{\rho_s (1/v' - 1)}{\rho_b \rho_s (1/v' - 1)} + 1 \right) \left[\exp \left(\frac{-v' \rho_b L a_p \xi^2}{2 \gamma P_b} \right) - 1 \right] \quad (5.8b)$$

The multiplier term $\left(\frac{\rho_s (1/v' - 1)}{\rho_b \rho_s (1/v' - 1)} + 1 \right)$ can greatly increase the pressure

drop from breech to projectile over the gas only case. This is because the large forces are needed to accelerate the solids which have a density much greater than the gases. The average pressure can be determined by integration of a series expansion of 5.8b.

$$\frac{P_{ave}}{P_0} = 1 - K_1 \left(-\frac{K_2}{3} + \frac{K_2^2}{10} - \frac{K_2^3}{42} + \frac{K_2^4}{216} - \frac{K_2^5}{1320} \right) \quad (5.9)$$

$$K_1 = \left(\frac{\rho_s (1/v' - 1)}{\rho_b} + 1 \right) \gamma$$

$$K_2 = \frac{v' (1 - \rho_b N) La_p^*}{2 \gamma R T_b}$$

Kinetic Energy in the Gases

The ratio of kinetic energy in the gas solid mixture to the kinetic energy of the same mass moving at the projectile velocity is $1/\delta$. δ was obtained using a linear velocity distribution and a density distribution obtained from the pressure distribution Eqn. 5.8.

$$\delta = 3 \frac{\frac{\rho_s (1-v')}{\rho_b v'} + \left(1 - \frac{\rho_p}{3\rho_b}\right)}{\frac{\rho_s (1-v')}{\rho_b v'} \left(\frac{u_s}{u}\right)^2 + \left(1 - \frac{3\rho_p}{5\rho_b}\right)} \quad (5.10)$$

The case of gas only reduces 5.10 to 5.11.

$$\delta = \frac{3 \left(1 - \frac{\rho_p}{3\rho_b}\right)}{\left(1 - \frac{3}{5} \frac{\rho_p}{\rho_b}\right)} \quad (5.11)$$

5.3 Comparisons of Analytical Model with Experimental Data

The equations just described in were compared with experimental data from Eglin AFB for firings with muzzle velocities of 1000 m/s. Comparisons were also made with computer modelled predictions obtained from Eglin AFB and the Ballistics Research Lab. The experimental data came from two series of shots of 30 mm aircraft cannon. Each series consisted of four shots. These runs were evaluated by shifting the time scales to make the peak pressures coincide and then comparing the measured pressures in time. The two pressure time traces which best matched each other were then used as the standard data for each series.

Each set of data consisted of time and for pressure readings. The first reading was called the chamber pressure reading. It was not taken at the breech but just in front of the initial position of the rotating band. The three other readings were taken at three downbore locations.

The data in a nondimensional form was used for the comparison with analytical equations (5.7 and 5.8). The pressures at the three downbore locations were normalized by the chamber pressure reading. The resulting pressure ratio was less than 1 because the downstream pressures were always lower than the chamber pressure.

The analytical pressure ratio was determined using equation 5.8 to find the downbore pressure with respect to the breech pressure for both the chamber location and the downbore location. Values of the variables in equation 5.8 were obtained from an interior ballistics program of Heiney [Ref 14]. The variables needed were average porosity, breech density and pressure, projectile acceleration, and breech to projectile length. The analytical pressure ratio was determined as a function of

time for each downbore pressure tap location beginning from the time that each tap was passed by the projectile.

The results are quite encouraging. Comparisons with the 536 experimental data is shown in Figures 5.3-5.5. The experimental data is the jagged line. The other two lines are the results of calculations from equation 5.8 with the upper line being a gas only calculation and the lower line being the calculation when solids are included. At 1700 microseconds in Figure 5.3 one can see that the solids theory agrees quite well with the data.

At a later time of 2500 microseconds in Figure 5.4 the gas only theory seems to be a better estimate than that of the solids. This is probably due to the fact that the solids do not follow directly behind the projectile but lag it. The ξ squared term in equation 5.8, causes the majority of the pressure drop to occur in the 30% of the length just behind the projectile. If the solids concentration is very low in this region, the pressure will drop less and will better follow the gas only theory.

The last figure in the 536 series is Figure 5.5. It shows good agreement between theory and experiment for either gas only or gas and solids. The two theoretical lines are very close because at 3000 microseconds there are very few solids left.

Comparisons of 571 experimental data with theory are shown in Figures 5.6-5.8. This shot had a muzzle velocity 7% higher than the previous 536 shot. This was produced by a thinner grain web thickness. Figure 5.6 shows the pressure ratio for downbore tap 2. Burning has occurred more quickly and few solids remain so that the gas and solids lines are very close. Predicted pressures are lower than those

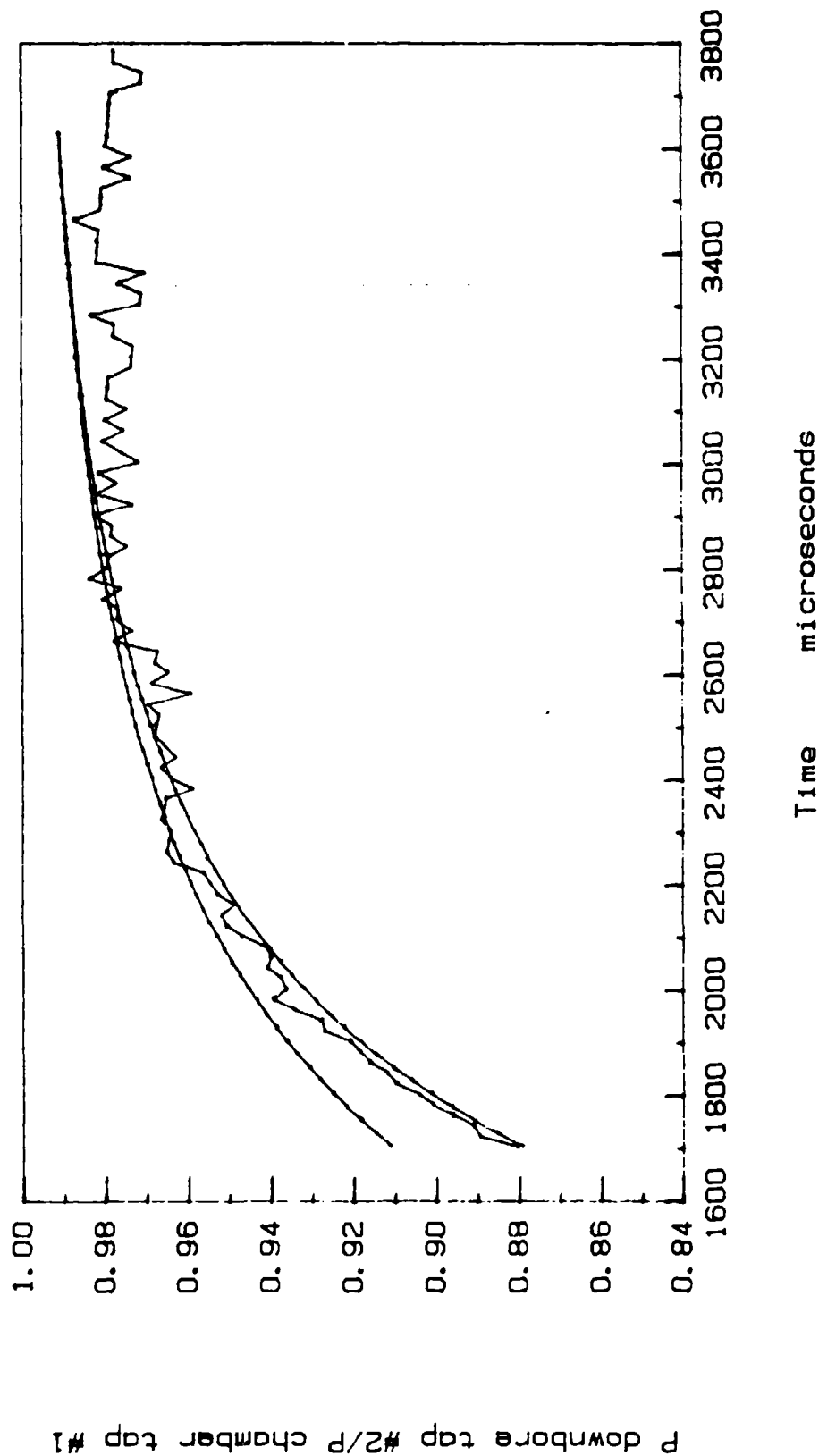


Fig. 5.3 Pressure at downbore tap #2 over pressure at chamber tap #1 as a function of time. Jagged line is experimental data of shot 536. Upper smooth line is gas only theory. Lower smooth line is solids and gas theory.

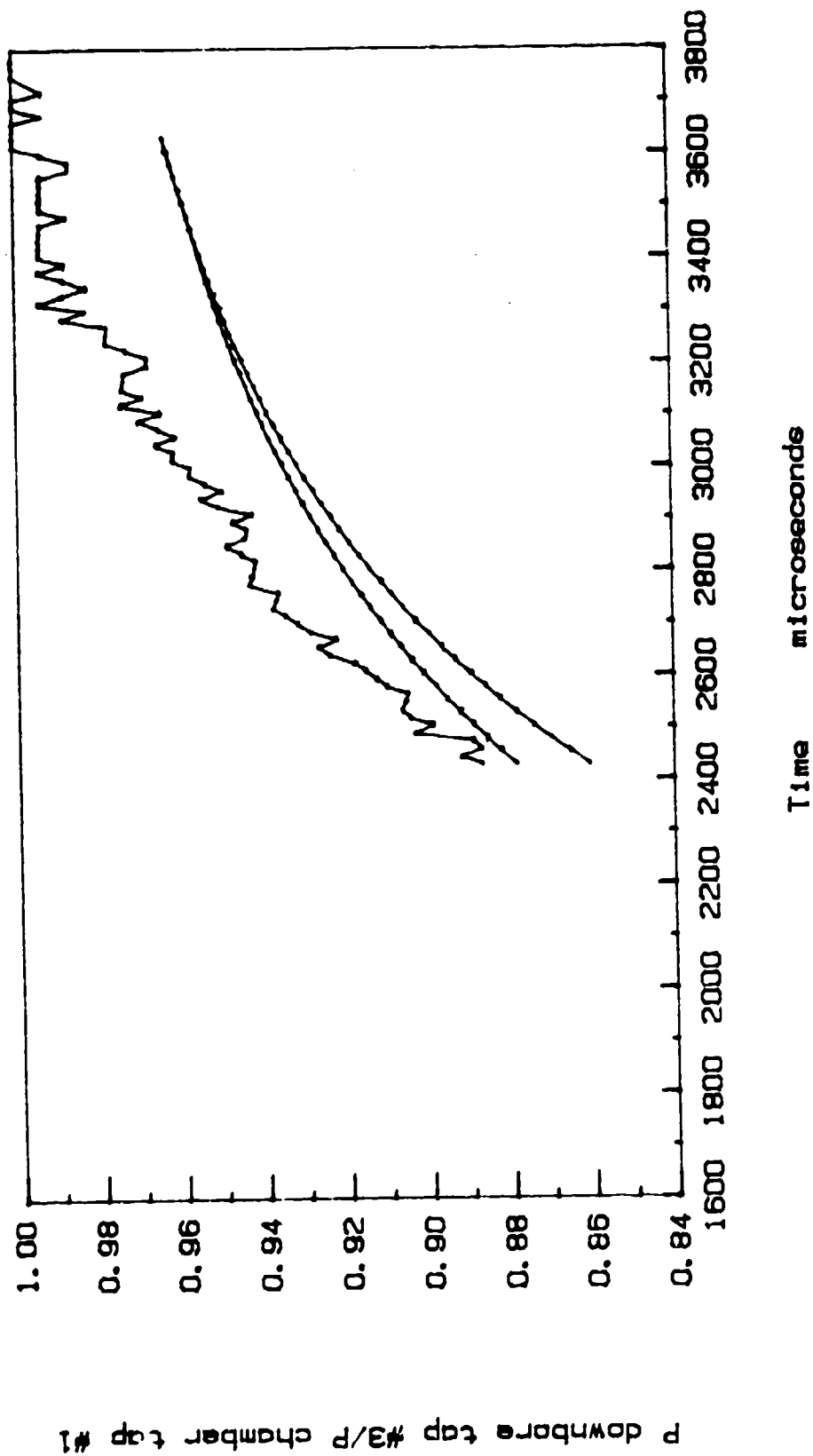


Fig. 5.4 Pressure at downbore tap #3 over pressure at chamber tap #1 as a function of time. Jagged line is experimental data of shot 536. Upper smooth line is gas only theory. Lower smooth line is solids and gas theory.

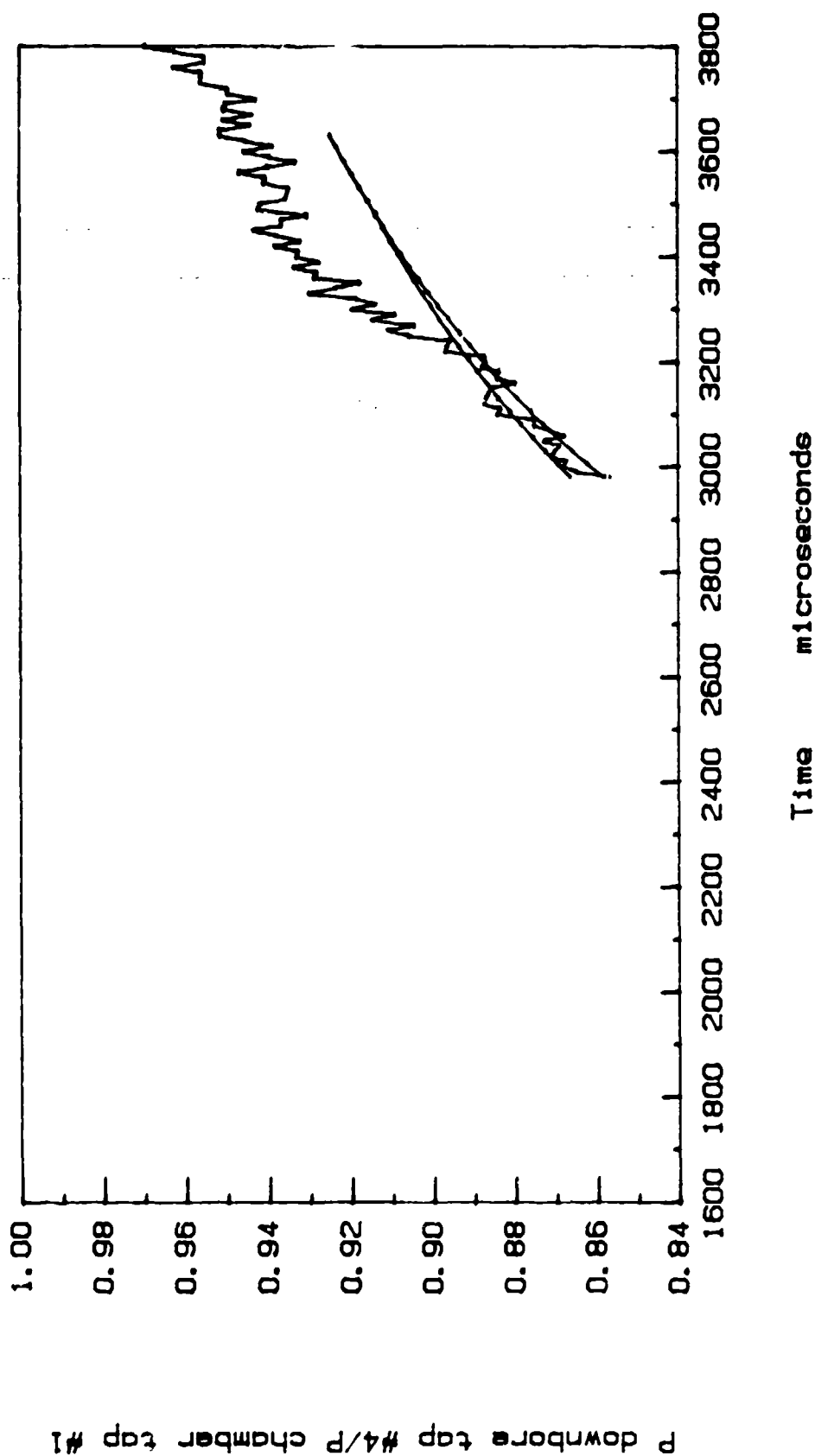


Fig. 5.5 Pressure at downbore tap #4 over pressure at chamber tap #1 as a function of time. Jagged line is experimental data of shot 536. Upper smooth line is gas only theory. Lower smooth line is solids and gas theory.

measured. One explanation may be lack of time for the velocity profile to become linear after then time of peak pressure.

Figure 5.7 shows quite good agreement with the experimental data over the last half of the time of the run. Figure 5.8 shows a pressure ratio higher than the data. This may be caused by the hump in acceleration ratio shown in Figure 5.2

Two higher speed cases were compared with theory. Experimental data was not available for either of these. However, computer predictions were available using two different codes which model the flow of both solid and gas as the solids burn. Input conditions were not available for these run so that the model of Chapter 2 could not also be compared.

The first case was a 1400 m/s run. Combustion was complete and gas only theory was compared. Pressure at the projectile base over pressure at the breech was compared when the projectile was at the muzzle. The computer prediction of the pressure ratio was 0.707 and the pressure ratio of the theory of this work was 0.665.

The second case was a large diameter round with a 1450 m/s muzzle velocity. Combustion was complete and the pressure ratios was compared when the projectile was at the muzzle. The computer prediction of the pressure ratio was 0.731 and the pressure ratio of the theory of this work was 0.747.

In both of these cases the theory matched the computer predictions well. The Mach number of the gases behind the projectile in both of the last two cases is near 1.5 indicating that the flow is supersonic.

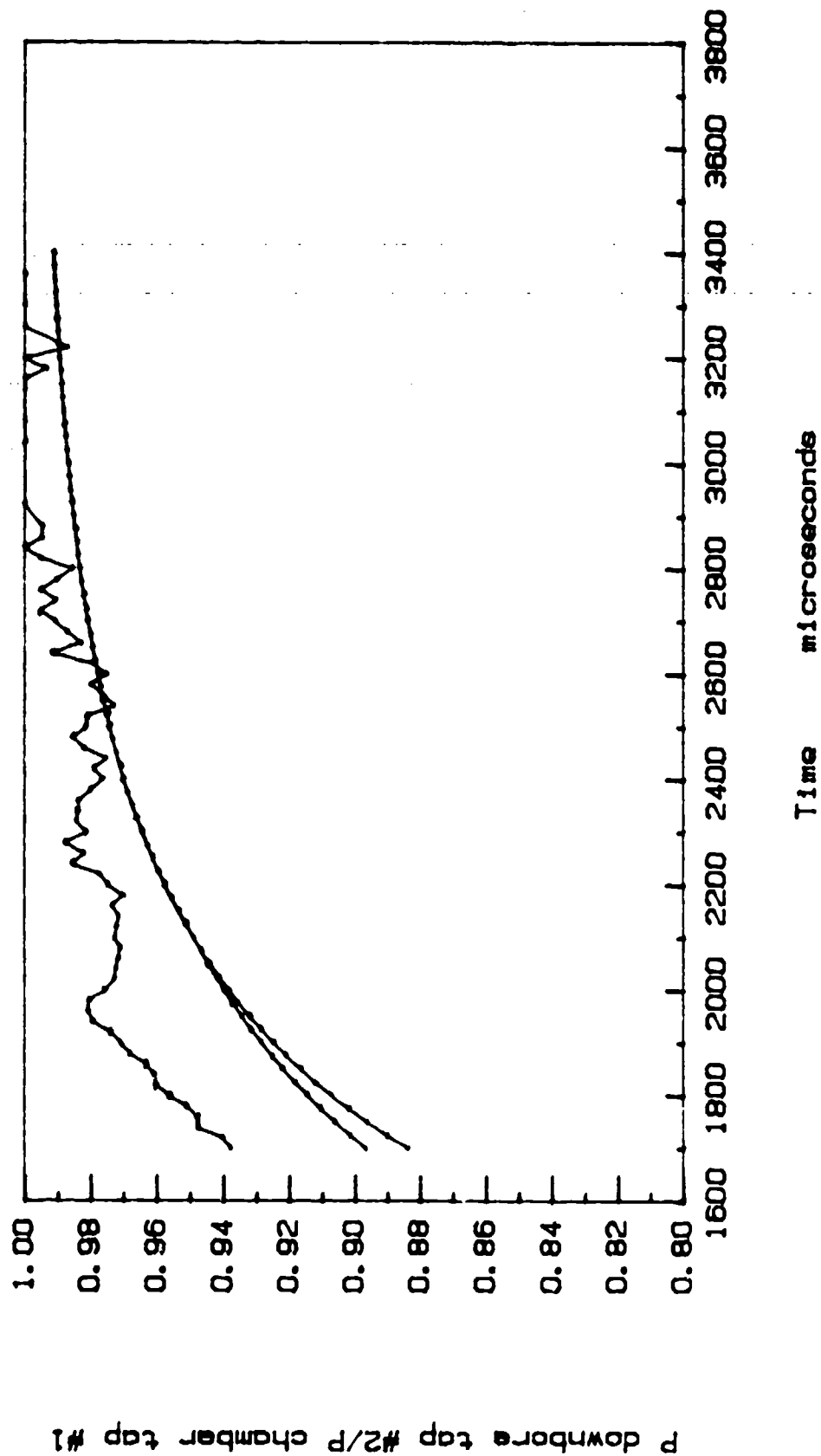


Fig. 5.6 Pressure at downbore tap #2 over pressure at chamber tap #1 as a function of time. Jagged line is experimental data of shot 571. Upper smooth line is gas only theory. Lower smooth line is solids and gas theory.

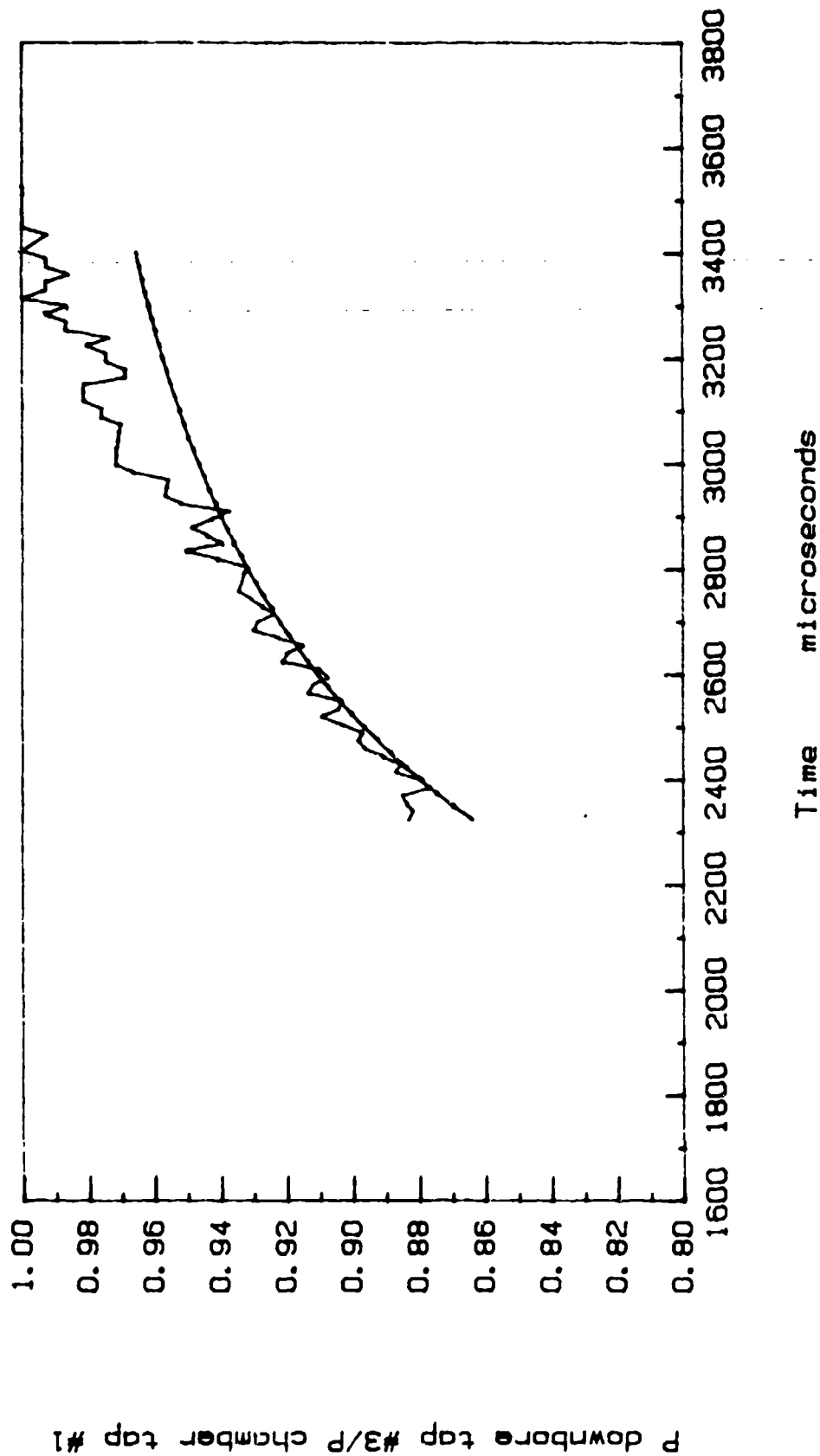


Fig. 5.7 Pressure at downbore tap #3 over pressure at chamber tap #1 as a function of time. Jagged line is experimental data of shot 571. Smooth line is gas only theory and solids and gas theory.

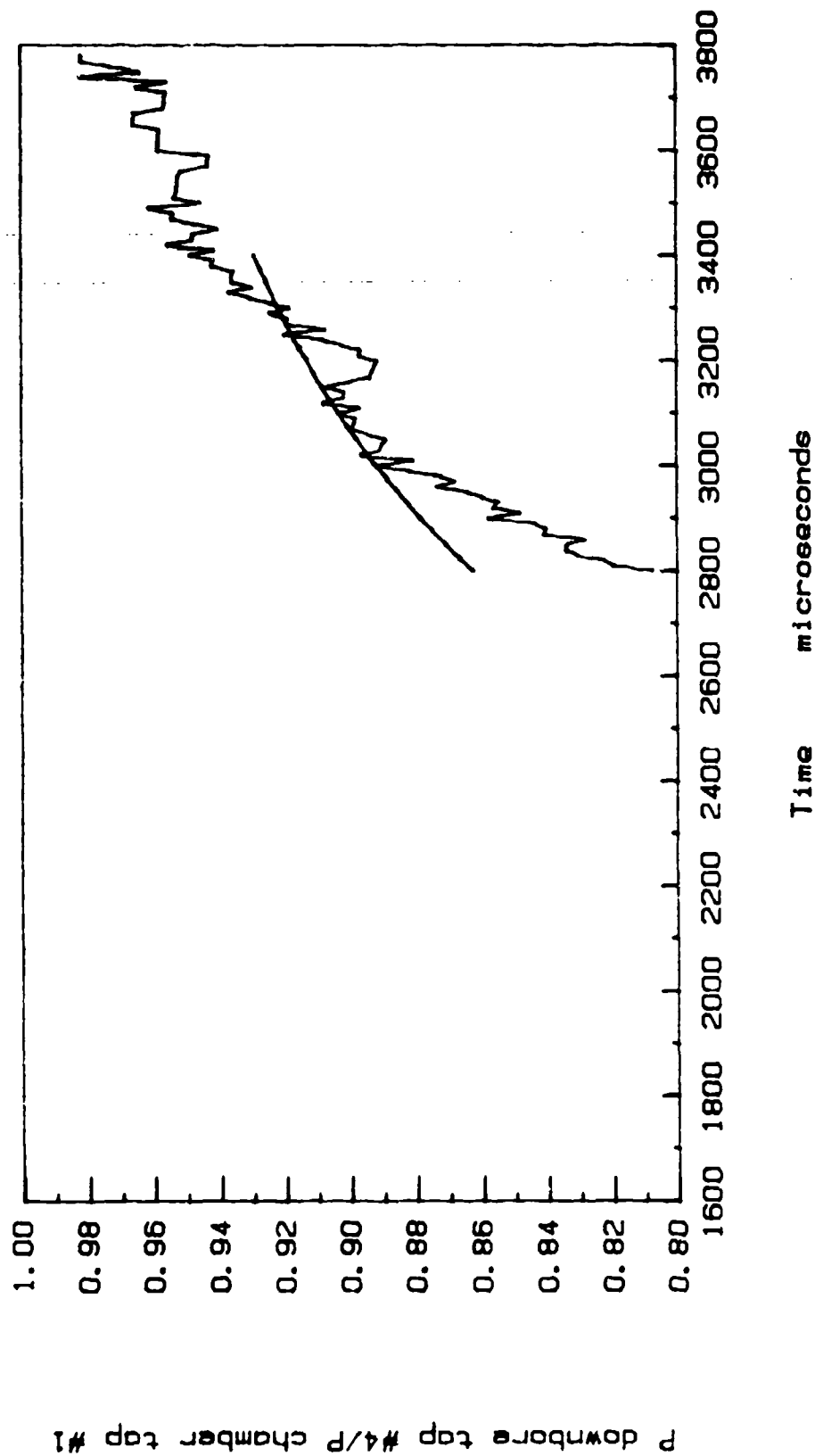


Fig. 5.8 Pressure at downbore tap #4 over pressure at chamber tap #1 as a function of time. Jagged line is experimental data of shot 571. Smooth line is gas only theory and solids and gas theory.

Chapter 6

SUMMARY OF ACCOMPLISHMENTS AND DISCOVERIES

In this chapter, the accomplishments and discoveries made are summarized.

Accomplishments

Four interior ballistic models were developed to analyze the flowfields inside tubes that launch high-speed projectiles. The first model developed was for analyzing unsteady, one-dimensional inviscid flow inside tubes that launch high-speed projectiles. This model can account for changes in the cross-sectional area along the tube and the effect of temperature on the ratio of the specific heats.

The second interior ballistic model developed was for analyzing the unsteady, two-dimensional, compressible, momentum and thermal boundary layers next to tube walls of ballistic devices.

The third interior ballistic model developed was for analyzing unsteady, one-dimensional viscous flow inside tubes that launch high-speed projectiles. This model can account for (a) variations of velocity, density, and temperature in the radial direction; (b) interphase drag between the combustion gas and the propellant grains; (c) momentum generated due to burning of propellants; (d) heat transfer to the propellants; and (e) unsteady heat transfer to the tube wall.

The fourth interior ballistic model developed was an analytical model for analyzing how density and pressure vary from the breech to the base of the projectile.

The results obtained by using the interior ballistic models developed in this study were compared with experimental data.

Discoveries

Parameters having significant effects on the physics occurring inside ballistic devices are presented here in descending order of importance:

1. The covolume of the gas.
2. The tube cross-sectional area changes as a function of axial distance.
3. Relative velocity between the propellant grains and the combustion gas.
4. The ratio of specific heats as a function of local temperature.
5. Friction and heat transfer in the boundary layer.
6. The propellant burning rate as a function of local pressure.

Important effects occurring in the boundary layer include:

1. The displacement thickness is negative indicating that the streamlines in the boundary layer turn toward the tube wall.
2. The cooling of the gas near the wall produces a significant change in the effective volume which lowers the chamber pressure.
3. The thickness of the momentum and thermal boundary layers goes to zero at the breech and the base of the projectile.

4. Profiles in both the momentum and thermal boundary layers are nonsimilar.

Parameters affecting axial gradients of pressure and density were determined to be

1. Gradients of pressure and density are governed by the product, $a_p L$, projectile acceleration times breech-to-projectile distance.
2. Acceleration of the propellant grains has a significant effect on the pressure and density gradients.
3. Supersonic interior ballistic flow exist and can be modelled by the method described in Chapter 5.

ACKNOWLEDGEMENTS

We would like to thank Dr. L. Caveny, Dr. R. Vondra, and Dr. J. Tishkoff for their encouragement and their management of this project. The technical assistance provided by O. K. Heiney is acknowledged. Finally the financial support provided by the Air Force Office of Scientific Research grant AFOSR-85-0113 is also gratefully acknowledged.

REFERENCES

1. Sugot, G., Ballistique Interieure Theorique et Tables Numeriques, Gouthier-Villars, Paris, 1928.
2. "Interior Ballistics of Guns," Army Material Command, Engineering Design Handbook, Ballistic Ser., Pamphlet AMCP 706-150, 1965.
3. Whyte, B., "Interior Ballistics," General Electric Armament Dept., Burlington, Utah, Letter Rept., Feb. 1969.
4. Goldstein, S., "Interior Ballistic Modelling Applied to Small-Arms Systems," in Interior Ballistics of Guns, Editor: H. Krier and M. Summerfield, Progress in Astronautics and Aeronautics, Vol. 66, AIAA, 1979, pp. 67-86.
5. Baer, P. G., "Practical Interior Ballistic Analysis of Guns," in Interior Ballistics of Guns, Editor: H. Krier and M. Summerfield, Progress in Astronautics and Aeronautics, Vol. 66, AIAA, 1979, pp. 37-66.
6. Love, A. E. H. and Pidduck, F. B., "Lagrange's Ballistic Problem," Philosophical Transactions, Vol. A222, March 1922, pp. 167-216.
7. Kent, R. H., "The Motion of Powder Gas, I and II," Ballistic Research Lab., Repts. 36 and 37, 1936.
8. Kent, R. H., "Some Special Solutions for the Motion of the Powder Gas," Physics, Vol. 7, September 1936, pp. 319-324.
9. Baer, P. G. and Stals, J., "A Comparison of Gun Interior Ballistic Computer Programs," Ballistic Research Lab., 1978.
10. Trafton, T. R., "An Improved Interior Ballistic Model for Small Arms Using Deterred Propellants," Ballistics Research Lab., Rept. 1624, 1972.
11. Smith, C. M., "An Interior Ballistic Model for Rolled Ball Propellant, Part II, A Computer Implementation (IMBRB)," Frankford Arsenal, MR M71-7-1, 1971.
12. Heppner, L., "Final Report of Special Study of Electronic Computer Program for Interior Ballistics," U.S. Army, Test and Evaluation Command, DPS-1711, 1965.

13. Heiney, O. K., "Analytical and Experimental Interior Ballistics of Closed Breech Guns," Air Force Armament Lab., AFATL TR-69-42, 1969.
14. Heiney, O. K. and West, R. J., "Interior Ballistics, Muzzle Flash and Gas Gradients of Aircraft Cannon," Air Force Armament Lab., AFATL TR-76-34, 1976.
15. Heiney, O. K., "Ballistics Applied to Rapid-Fire Guns," in Interior Ballistics of Guns, Editor: H. Krier and M. Summerfield, Progress in Astronautics and Aeronautics, Vol. 66, AIAA, 1979, pp. 87-112.
16. Peterson, E. G., "Interior Ballistics of Guns," Hercules Inc., Bacchus Works, Magna, Utah, 1967.
17. Nusbaum, M. S., Barbarek, L. A. C., and Zimmerman, F. J., "Hypervelocity Weapon Feasibility Study," Air Force Systems Command Eglin Air Force Base, FL, Rept. ATL TDR-64-35, 1964.
18. Schlenker, G., "Update of Cannon Interior Ballistics," U.S. Army Weapons Command, Rock Island Arsenal, TN RDF 73-1, 1973.
19. Voltis, P. M., "Digital Computer Simulation of the Interior Ballistic Process in Guns," Watervliet Arsenal, Rept. TR-6615, 1966.
20. Seigel, A. E., "The Theory of High Speed Guns," AGARDograph 91, NATO, 1965.
21. Seigel, A. E., "Theory of High-Muzzle-Velocity Guns," in Interior Ballistics of Guns, Editor: H. Krier and M. Summerfield, Progress in Astronautics and Aeronautics, Vol. 66, AIAA, 1979, pp. 135-175.
22. Shelton, S., Bergles, A., and Saha, P., "Study of Heat Transfer and Erosion in Gun Barrels," Air Force Armament Lab., AFATL TR-73-69, 1971.
23. Gough, P. S., "The Flow of a Compressible Gas through an Aggregate of Mobile, Reacting Particles," Ph.D. Dissertation, Dept. of Mechanical Engineering, McGill University, 1974.
24. Gough, P. S., "The Predictive Capability of Models of Interior Ballistics," Proceedings of the 12th JANNAF Combustion Meeting, 1975.
25. Gough, P. S. and Zwarts, F. J., "Modeling Heterogeneous Two-Phase Reacting Flow," AIAA Journal, Vol. 17, 1979, pp. 17-25.
26. Gough, P. S., "Two-Dimensional, Two-Phase Modeling of Multi-Increment Bagged Artillery Charges," Contract Report ARBRL-CR-00503, Ballistic Research Laboratory, Aberdeen Proving Ground, Maryland, February 1983.

27. Gough, P. S., "Modeling of Rigidized Gun Propelling Charges," Contract Report ARBRL-CR-00518, Ballistic Research Laboratory, Aberdeen Proving Ground, Maryland, November 1983.
28. Clayton, H., Bartley, C. E., and Mills, M. M., Solid Propellant Rockets, Princeton University Press, New Jersey, 1960.
29. Heiney, O., Personal Communication, 1986.
30. Sonntag, R. E. and Van Wylen, G. J., Introduction to Thermodynamics, Classical and Statistical, John Wiley and Sons, New York, 1982.
31. Wark, K., Thermodynamics, McGraw-Hill Book Company, New York, 1983.
32. Shapiro, A. H., The Dynamics and Thermodynamics of Compressible Fluid Flow, Vol. 1, John Wiley and Sons, New York, 1953.
33. Shih, T. I-P., Finite-Difference Methods in Computational Fluid Dynamics, to be published by Prentice-Hall, Englewood Cliffs, New Jersey.
34. Mirels, H., "Boundary Layer Behind Shock or Thin Expansion Wave Moving into Stationary Fluid," NACA TN 37 12, 1956.
35. Yalamanchili, R. and Reddy, K. C., "Numerical Simulation of General Purpose Boundary Layers," Numerical/Laboratory Computer Methods in Fluid Mechanics, ASME, 1976, pp. 111-127.
36. Cook, W. J. and Chapman, G. T., "Characteristics of Unsteady Shock-Induced Laminar Boundary Layer on a Flat Plate," The Physics of Fluids, Vol. 15, 1972, pp. 2129-2139.
37. Kwon, O. K., Pletcher, R. H., and Delaney, R. A., "Solution Procedure for Unsteady Two-Dimensional Boundary Layers," AIAA/ASME 4th Fluid Mechanics, Plasma Dynamics and Laser Conference, May 12-14, 1985.
38. Incropera, F. P. and DeWitt, D. P., Fundamentals of Heat Transfer, John Wiley and Sons, New York, 1981.
39. Ozisik, M. N., Heat Conduction, John Wiley and Sons, New York, 1980.
40. Gough, P. S., "XNOVA - An Express Version of the NOVA Code," Contract Report N00174-82-M-8048, Naval Ordnance Station, Indian Head, Maryland, November 1983.

Appendix A

Derivation of Governing and Auxilliary Equations for Inviscid and Viscous Flow inside Tubes.

Introduction

In this appendix, conservation equations which describe high speed unsteady compressible flow in tubes with combustion are developed and presented first. These equations were derived using a control volume approach where a typical control volume is shown in Fig. A.1.

Next, auxilliary equations which describe the volumetric rate of propellant consumption (\dot{M}_s), the propellant grain-combustion gas velocity ratio (CD_1), tube wall heat flux (q_w) and propellant grain displacement (L_s) are developed and presented.

Last of all, auxilliary equations are presented for two interpolative schemes which allow variable values to be mapped to and from the i and i^* grid point systems.

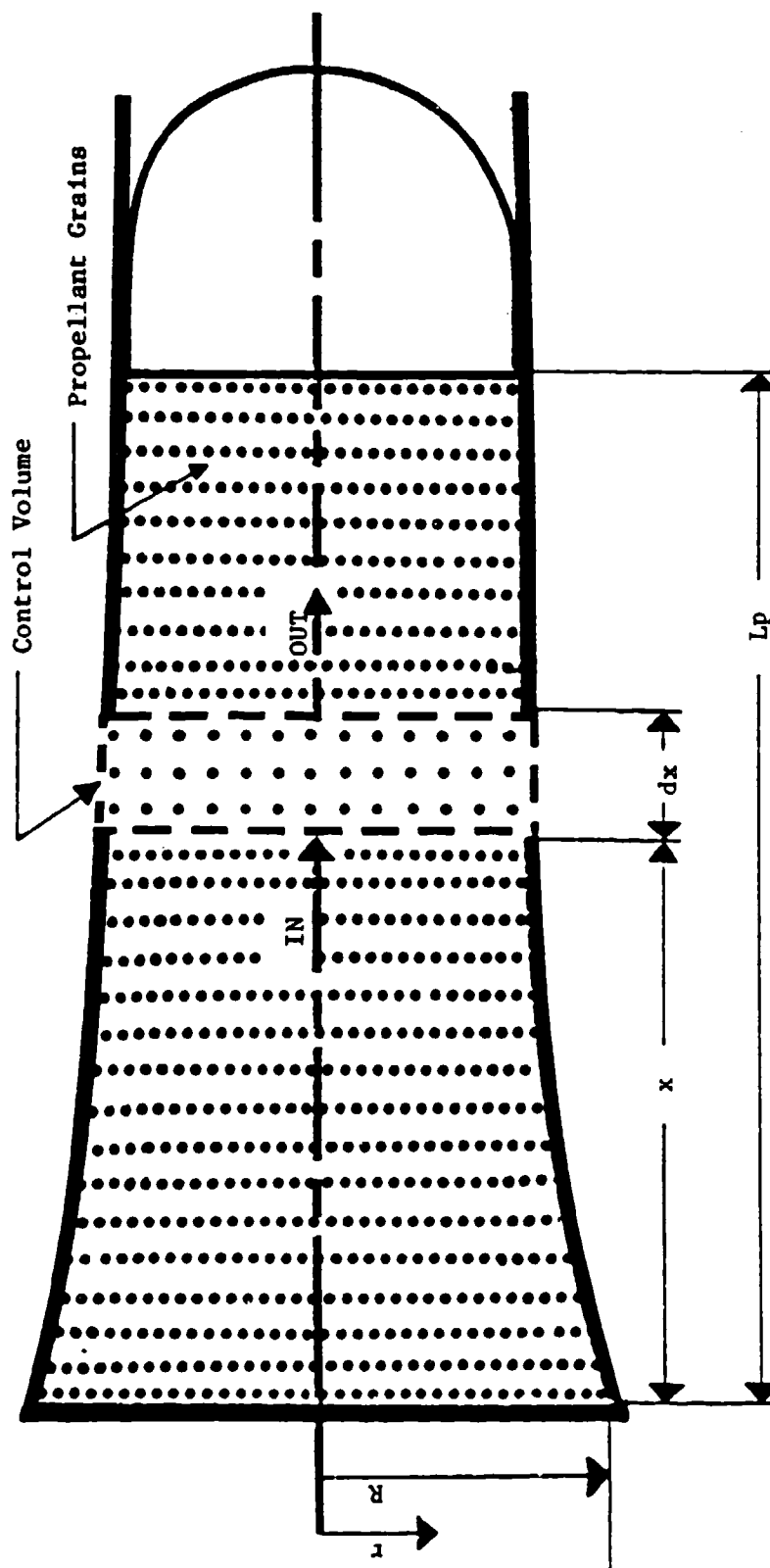


Figure A.1
Schematic of an infinitesimal control volume.

Continuity of Propellant Grains

The following assumptions were used in deriving the continuity equation for the propellant grains:

- 1) The propellant grains are incompressible.
- 2) The propellant grains are distributed homogeneously throughout the control volume.
- 3) The propellant grains can be treated as a continuum.
- 4) The problem is unsteady and one-dimensional (in the axial direction along the tube).

Under these assumptions, the propellant continuity equation can be written as

$$\left| \begin{array}{l} \text{the time rate} \\ \text{of change of} \\ \text{mass of propellant} \\ \text{within the control} \\ \text{volume} \end{array} \right| = \left| \begin{array}{l} \text{the rate of} \\ \text{propellant} \\ \text{influx} \end{array} \right| - \left| \begin{array}{l} \text{the rate of} \\ \text{propellant} \\ \text{efflux} \end{array} \right| + \left| \begin{array}{l} \text{the generation of} \\ \text{propellant mass} \\ \text{within the control} \\ \text{volume} \end{array} \right|$$

or,

$$\left| \frac{\partial \dot{M}_s}{\partial t} \right| = \left| \dot{m}_s \right| - \left| \left(\dot{m}_s + \frac{\partial \dot{M}_s}{\partial x} dx \right) \right| + \left| (-\dot{M}_s v A dx) \right| \quad (A.1)$$

where the terms of Eq. (A.1) are defined as follows:

- 1) $A = \pi R^2$ = the tube cross-sectional area
- 2) $v = A_s/A$ = the ratio of propellant cross-sectional area to tube cross-sectional area
- 3) \dot{M}_s = the volumetric rate of propellant consumption within the control volume

$$4) \quad \dot{M}_s = \left[\int_A \rho_s v dA \right] dx = \rho_s v \left[\int_A dA \right] dx = \rho_s v A dx \quad (A.2)$$

$$5) \quad \dot{m}_s = \int_A \rho_s v u_s dA = \rho_s v u_s \int_A dA = \rho_s v u_s A \quad (A.3)$$

Substitution of Eqs. (A.2) and (A.3) into Eq. (A.1) yields

$$\frac{\partial}{\partial t} (\rho_s v A) dx = - \frac{\partial}{\partial x} (\rho_s u_s A) dx - \dot{M}_v A dx \quad (A.4)$$

which can be rearranged to give

$$\frac{\partial v}{\partial t} = -v \frac{\partial u_s}{\partial x} - u_s \frac{\partial v}{\partial x} - \frac{v u_s}{A} \frac{\partial A}{\partial x} - \frac{\dot{M}_s v}{\rho_s} \quad (A.5)$$

Continuity of the Combustion Gas

The following assumption was used in deriving the continuity equation for the combustion gas:

- 1) The problem is unsteady and one-dimensional (in the axial direction along the tube) where radial effects are accounted for by the K factor approach.

Under this assumption, the combustion gas continuity equation can be written as

$$\left| \begin{array}{l} \text{the time rate of} \\ \text{change of combustion} \\ \text{gas mass within the} \\ \text{control volume} \end{array} \right| = \left| \begin{array}{l} \text{the rate of} \\ \text{combustion} \\ \text{gas influx} \end{array} \right| - \left| \begin{array}{l} \text{the rate of} \\ \text{combustion} \\ \text{gas efflux} \end{array} \right| + \left| \begin{array}{l} \text{the generation} \\ \text{of combustion gas} \\ \text{mass within the} \\ \text{control volume} \end{array} \right|$$

or,

$$\left| \frac{\partial M}{\partial t} \right| = \left| \dot{m}_g \right| - \left| \dot{m}_g + \frac{\partial \dot{m}_g}{\partial x} dx \right| + \left| \dot{M}_g (1-v) A dx \right| \quad (A.6)$$

where the terms of Eq. (A.6) are defined as follows:

$$1) \quad \dot{M}_g = \dot{M}_s \left(\frac{v}{1-v} \right) \quad (A.7)$$

$$2) \quad \dot{M} = \left[\int_A \rho(1-v) dA \right] dx = (1-v) \left[\int_A \rho dA \right] dx = (1-v) \bar{\rho} A dx \quad (A.8)$$

$$3) \quad \dot{m}_g = \int_A \rho u (1-v) dA = (1-v) \int_A \rho u dA = (1-v) \bar{\rho} \bar{u} K_{\rho u} A \quad (A.9)$$

Substitution of Eqs. (A.7)-(A.9) into Eq. (A.6) yields the equation

$$\frac{\partial}{\partial t} [(1-v) \bar{\rho} A] dx = - \frac{\partial}{\partial x} [(1-v) K_{\rho u} \bar{\rho} \bar{u} A] dx + v \dot{M}_s A dx \quad (A.10)$$

which can be rearranged to give

$$\frac{\partial \bar{\rho}}{\partial t} + \frac{1}{A} \frac{\partial}{\partial x} (K_{\rho u} \bar{\rho} \bar{u} A) = \dot{M}_s \left(\frac{v}{1-v} \right) + \frac{\bar{\rho}}{(1-v)} \left[\frac{\partial v}{\partial t} + K_{\rho u} \bar{u} \frac{\partial v}{\partial x} \right] \quad (A.11)$$

Substitution of the Propellant Continuity Equation (Eq. (A.5)) into Eq. (A.11) and subsequent rearranging yield the final form of the combustion gas continuity equation

$$\begin{aligned} \frac{\partial \bar{\rho}}{\partial t} = & -K_{\rho u} \frac{\bar{\rho} \bar{u}}{A} \frac{\partial A}{\partial x} - \bar{\rho} \bar{u} \frac{\partial K_{\rho u}}{\partial x} - K_{\rho u} \frac{\partial (\bar{\rho} \bar{u})}{\partial x} + \frac{\dot{M}_s}{(1-v)} [(K_{\rho u} \bar{u} - u_s) \frac{\partial v}{\partial x} \\ & - v \left(\frac{\partial u_s}{\partial x} + \frac{u_s}{A} \frac{\partial A}{\partial x} \right)] \end{aligned} \quad (A.12)$$

For the case of inviscid flow, all K-factors in Eq. (A.12) are set to 1.0 and all derivatives of K-factors are set to 0.0.

Momentum Equation for the Combustion Gas

The following assumptions were used in deriving the momentum equation for the combustion gas:

- 1) The problem is unsteady and one-dimensional (in the axial direction along the tube) where radial effects are accounted for by the K factor approach.

2) The tube wall friction caused by the propellant grains is negligible.

3) Pressure varies in the axial direction only.

Under these assumptions, the combustion gas momentum equation can be written as

$$\left| \begin{array}{l} \text{the time rate} \\ \text{of change of} \\ \text{combustion} \\ \text{gas momentum} \\ \text{within the} \\ \text{control} \\ \text{volume} \end{array} \right| = \left| \begin{array}{l} \text{the rate} \\ \text{of combus-} \\ \text{tion gas} \\ \text{momentum} \\ \text{influx} \end{array} \right| - \left| \begin{array}{l} \text{the rate} \\ \text{of combus-} \\ \text{tion gas} \\ \text{momentum} \\ \text{efflux} \end{array} \right| + \left| \begin{array}{l} \text{the genera-} \\ \text{tion of} \\ \text{combustion} \\ \text{gas momen-} \\ \text{tum within} \\ \text{the control} \\ \text{volume} \end{array} \right| + \left| \begin{array}{l} \text{the net exter-} \\ \text{nal force im-} \\ \text{posed on the} \\ \text{combustion gas} \\ \text{within the} \\ \text{control volume} \end{array} \right|$$

or,

$$\left| \frac{\partial(Mu)}{\partial t} \right| = |\dot{m}u| - \left| \dot{m}u + \frac{\partial(\dot{m}u)}{\partial x} dx \right| + |\dot{P} dx| + |\Sigma F_{ext}| \quad (A.13)$$

where the terms of Eq. (A.13) are defined as follows:

$$1) \quad Mu = \left[\int_A \rho u (1-v) dA \right] dx = \left[(1-v) \int_A \rho u dA \right] dx = (1-v) \bar{\rho} \bar{u} K_{\rho u} A dx \quad (A.14)$$

$$2) \quad \dot{m}u = \int \rho u^2 (1-v) dA = (1-v) \int \rho u^2 dA = (1-v) \bar{\rho} \bar{u}^2 K_{\rho u^2} A \quad (A.15)$$

$$3) \quad \dot{P} = CD_1 \dot{M}_g v A \bar{u} \quad (A.16)$$

$$4) \quad \Sigma F_{ext} = F_{net}(\text{pressure}) + F(\text{wall shear}) + F(\text{particle drag})$$

where, referring to Fig. (A.1)

$$\begin{aligned} a) \quad F_{net}(\text{pressure}) &= F(\text{pressure})|_x - F(\text{pressure})|_{x+dx} \\ &\quad - F(\text{pressure})|_{x+dx/2} \\ &= PA(1-v) - \{PA(1-v) + \frac{\partial}{\partial x} [PA(1-v)] dx\} \\ &\quad + [P + \frac{\partial P}{\partial x} \frac{dx}{2}] (1-v) dA \\ &= - \frac{\partial}{\partial x} [PA(1-v)] dx + (1-v) PdA \\ &= - \frac{\partial}{\partial x} [PA(1-v)] dx + (1-v) P \frac{\partial A}{\partial x} dx \\ &= -(1-v) P \frac{\partial A}{\partial x} dx - A \frac{\partial [P(1-v)]}{\partial x} dx + (1-v) P \frac{\partial A}{\partial x} dx \end{aligned}$$

therefore,

$$F_{\text{net}}(\text{pressure}) = -A \frac{\partial [P(1-v)]}{\partial x} dx \quad (\text{A.17})$$

$$\text{b) } F(\text{wall shear}) = -\tau_w 2\pi R dx \quad (\text{A.18})$$

where a model for the wall shear stress (τ_w) is presented in Section 4.3

$$\text{c) } F(\text{particle drag}) = -D dx \quad (\text{A.19})$$

where a model for the particle drag (D) is presented in Section 4.3

Therefore, the net external force acting on the combustion gas in the control volume may be expressed as

$$\Sigma F_{\text{ext}} = -A \frac{\partial [P(1-v)]}{\partial x} dx - \tau_w 2\pi R dx - D dx \quad (\text{A.20})$$

Substitution of Eqs. (A.14)-(A.19) into Eq. (A.13) yields the following equation

$$\begin{aligned} \frac{\partial}{\partial t} [(1-v) \bar{\rho} \bar{u} K_{\rho u} A] dx &= - \frac{\partial}{\partial x} [(1-v) \bar{\rho} \bar{u}^2 K_{\rho u}^2 A] dx + CD_1 \dot{M}_s v \bar{u} dx \\ &- A \frac{\partial}{\partial x} [(1-v) P] dx - \tau_w 2\pi R dx - D dx \end{aligned} \quad (\text{A.21})$$

which can be rearranged to give

$$\begin{aligned} \frac{\partial (\bar{\rho} \bar{u})}{\partial t} &= \left(\frac{K_{\rho u}^2}{K_{\rho u}} \right) \left\{ - \frac{\partial (\bar{\rho} \bar{u}^2)}{\partial x} - \frac{\bar{\rho} \bar{u}^2}{A} \frac{\partial A}{\partial x} + \frac{\bar{\rho} \bar{u}^2}{(1-v)} \frac{\partial v}{\partial x} \right\} + \frac{\bar{\rho} \bar{u}}{(1-v)} \frac{\partial v}{\partial t} \\ &+ \left(\frac{1}{K_{\rho u}} \right) \left\{ - \bar{\rho} \bar{u} \frac{\partial K_{\rho u}}{\partial t} - \bar{\rho} \bar{u}^2 \frac{\partial K_{\rho u}^2}{\partial x} + CD_1 \dot{M}_s \frac{\bar{u} v}{(1-v)} - \frac{\partial P}{\partial x} \right\} \end{aligned}$$

$$+ \frac{1}{(1-v)} \left[P \frac{\partial v}{\partial x} - \frac{\tau_w 2\pi R}{A} - \frac{D}{A} \right] \quad (A.22)$$

Substitution of Eq. (A.5), the propellant continuity equation, into Eq. (A.22) and subsequent rearranging yield the final form of the combustion gas momentum equation:

$$\begin{aligned} \frac{\partial(\bar{\rho}\bar{u})}{\partial t} = & \frac{1}{K_{\rho u}} \left\{ -K_{\rho u}^2 \frac{\partial(\bar{\rho}\bar{u}^2)}{\partial x} + \frac{[\bar{\rho}\bar{u} (K_{\rho u}^2 \bar{u} - K_{\rho u} u_s) + P]}{\rho u^2 (1-v)} \frac{\partial v}{\partial x} - \frac{\partial P}{\partial x} \right\} \\ & - \frac{\bar{\rho}\bar{u}}{K_{\rho u}} \left\{ \frac{[K_{\rho u}^2 \bar{u} + (\frac{v}{1-v}) K_{\rho u} u_s]}{A} \frac{\partial A}{\partial x} + \left[\frac{\partial K_{\rho u}}{\partial t} + u \frac{\partial K_{\rho u}^2}{\partial x} \right. \right. \\ & \left. \left. + (\frac{v}{1-v}) K_{\rho u} \frac{\partial u_s}{\partial x} \right] \right\} + \left\{ \frac{\bar{u}}{K_{\rho u}} \frac{v}{(1-v)} \dot{M}_s [CD_1 - K_{\rho u} \rho/\rho_s] \right. \\ & \left. + \frac{1}{K_{\rho u}(1-v)} \left[\tau_w 2\pi R/A + D/A \right] \right\} \quad (A.23) \end{aligned}$$

For the case of inviscid flow, all K-factors in Eq. (A.23) are set to 1.0 and all derivatives of K-factors are set to 0.0. Also, the dissipative terms τ_w and D are set to 0.0.

Energy Equation for the Combustion Gas

The following assumptions were used in deriving the energy equation for the combustion gas:

- 1) The problem is unsteady and one-dimensional (in the axial direction along the tube) where radial effects are accounted for by the K factor approach.
- 2) Heat transfer in the axial direction is negligible.
- 3) Pressure varies only in the axial direction only.

Under these assumptions, the combustion gas energy equation can be

written as

$$\left| \begin{array}{l} \text{the time rate} \\ \text{of change of} \\ \text{combustion} \\ \text{gas energy} \\ \text{within the} \\ \text{control} \\ \text{volume} \end{array} \right| = \left| \begin{array}{l} \text{the rate of} \\ \text{combustion} \\ \text{gas energy} \\ \text{influx} \end{array} \right| - \left| \begin{array}{l} \text{the rate of} \\ \text{combustion} \\ \text{gas energy} \\ \text{efflux} \end{array} \right| + \left| \begin{array}{l} \text{the generation} \\ \text{of combustion} \\ \text{gas energy} \\ \text{within the} \\ \text{control volume} \end{array} \right| - \left| \begin{array}{l} \text{the rate} \\ \text{of energy} \\ \text{transferred} \\ \text{across the} \\ \text{control} \\ \text{volume} \\ \text{boundaries} \end{array} \right|$$

or,

$$|E| = |\dot{E}| - \left| \dot{E} + \frac{\partial \dot{E}}{\partial x} dx \right| + |\dot{Q}| - |\dot{Q}_w| \quad (\text{A.24})$$

where the terms of Eq. (A.24) are defined as follows:

$$1) \quad E = \left[\int_A \rho (\hat{u} + u^2/2) (1-v) dA \right] dx = \left[(1-v) \int_A e dA \right] dx = (1-v) \bar{e} A dx \quad (\text{A.25})$$

$$\begin{aligned} 2) \quad \dot{E} &= \int_A [\rho (\hat{u} + u^2/2) + P] u (1-v) dA = (1-v) \int_A (e + P) u dA \\ &= (1-v) A [K_{eu} \bar{e} u + P \bar{u}] \end{aligned} \quad (\text{A.26})$$

$$3) \quad \dot{Q} = \left| \begin{array}{l} \text{the rate} \\ \text{of chemi-} \\ \text{cal energy} \\ \text{release} \\ \text{within the} \\ \text{control} \\ \text{volume} \end{array} \right| - \left| \begin{array}{l} \text{the energy rate} \\ \text{needed to raise} \\ \text{the temperature of} \\ \text{the propellant} \\ \text{within the control} \\ \text{volume up to the} \\ \text{ignition temperature} \end{array} \right| - \left| \begin{array}{l} \text{the energy rate needed} \\ \text{to bring the newly} \\ \text{released gas within} \\ \text{the control volume up} \\ \text{to the temperature of} \\ \text{the surrounding} \\ \text{combustion gas} \end{array} \right|$$

or,

$$\dot{Q} = |\dot{Q}_r| - |\dot{Q}_{ig}| - |\dot{Q}_{gs}| \quad (\text{A.27})$$

where the terms of Eq. (A.27) are defined as follows:

$$a) \quad \dot{Q}_r = \dot{M}_s v A h_{sg} dx \quad (\text{A.28})$$

$$b) \quad \dot{Q}_{ig} = C_{Ps} (T_{ign} - T_{init}) \dot{M}_s v A dx \quad (\text{A.29})$$

$$c) \quad \dot{Q}_{gs} = [h(\bar{T}) - h(T_{ign})] \dot{M}_s v A dx \quad (\text{A.30})$$

therefore,

$$\dot{Q} = \dot{M}_s v A \{ h_{sg} dx - C_{Ps} (T_{ign} - T_{init}) - [h(\bar{T}) - h(T_{ign})] \} dx \quad (A.31)$$

$$4) \quad \dot{Q}_w = q_w 2\pi R(x) dx \quad (A.32)$$

Substitution of Eqs. (A.25)-(A.32) into Eq. (A.24) yields the equation

$$\begin{aligned} \frac{\partial[(1-v)\bar{A}\bar{e}]}{\partial t} = & - \frac{\partial}{\partial x} \{ (1-v)A[K_{eu}\bar{e}\bar{u} + P\bar{u}] \} dx - q_w 2\pi R dx \\ & - \dot{M}_s v A \{ h_{sg} - C_{Ps} (T_{ign} - T_{init}) - [h(\bar{T}) - h(T_{ign})] \} dx \quad (A.33) \end{aligned}$$

which can be rearranged to give

$$\begin{aligned} \frac{\partial \bar{e}}{\partial t} = & -K_{eu} \frac{\partial(\bar{e}\bar{u})}{\partial x} - (\bar{e}\bar{u}) \frac{\partial(K_{eu})}{\partial x} - \frac{(K_{eu}\bar{e}\bar{u} + P\bar{u})}{A} \frac{\partial A}{\partial x} - \frac{\partial(P\bar{u})}{\partial x} + \left(\frac{1}{1-v}\right) \{\bar{e} \frac{\partial v}{\partial t} \\ & + (K_{eu}\bar{e}\bar{u} + P\bar{u}) \frac{\partial v}{\partial x} - q_w \frac{2}{R} + v \dot{M}_s [h_{sg} - C_{Ps} (T_{ign} - T_{init}) \\ & - (h(\bar{T}) - h(T_{ign}))]\} \quad (A.34) \end{aligned}$$

Substitution of Eq. (A.5), the propellant continuity equation, into Eq. (A.34) and subsequent rearranging yield the final form of the combustion gas energy equation.

$$\begin{aligned} \frac{\partial \bar{e}}{\partial t} = & -K_{eu} \frac{\partial(\bar{e}\bar{u})}{\partial x} + \frac{1}{(1-v)} (K_{eu}\bar{e}\bar{u} + P\bar{u} - \bar{e}u_s) \frac{\partial(v)}{\partial x} - \frac{\partial(P\bar{u})}{\partial x} - \bar{e}\bar{u} \frac{\partial(K_{eu})}{\partial x} \\ & - \frac{[(K_{eu}\bar{e}\bar{u} + P\bar{u}) + (\frac{v}{1-v})\bar{e}\bar{u}]}{A} \frac{\partial A}{\partial x} - \frac{\bar{e}v}{(1-v)} \frac{\partial(u_s)}{\partial x} + \frac{v}{(1-v)} \dot{M}_s [h_{sg} \end{aligned}$$

$$- C_{Ps}(T_{ign} - T_{init}) - (h(\bar{T}) - h(T_{ign})) - \frac{\bar{\theta}}{\rho_s} - \left(\frac{1}{1-v}\right) q_w \frac{2}{R} \quad (A.35)$$

For the case of inviscid flow, all K-factors in Eq. (A.35) are set to 1.0 and all derivatives of K-factors are set to 0.0. Also, the dissipative term q_w is set to 0.0.

Derivation of the Volumetric Rate of Propellant Consumption Equation

In this section, two formulas for the volumetric rate of propellant consumption (\dot{M}_g) are derived. First, a formula for the linear burning speed (r_b) is given and then two formulas for the local burning surface area (A_b) are developed. For the development of the first burning surface formula, a control volume approach is used to relate the cross-sectional area fraction of propellant (v) to the local burning surface area. Figure (A.1) shows a control volume of cross-sectional area A and length dx .

For the development of the second burning surface formula, the assumptions of constant total burning surface area and constant propellant grain burning surface area are dropped. Therefore, this formulation should more closely model the real burning process.

Calculation of the linear burning speed

The linear burning speed is the speed at which the surface area of a propellant grain regresses due to combustion. During combustion, the propellant grain radius (r) decreases a distance dr in a time interval dt . The linear burning speed is therefore given by

$$r_b = \frac{dr}{dt} \quad (A.36)$$

The linear burning speed is known to be primarily a function of pressure. Table A-1 shows experimentally obtained linear burning speeds for CIL 3331 propellant at different pressures [Ref. 14]. Values for the linear burning speed at specific pressures are found by linear interpolation between the listed burning speeds.

Calculation of the local burning surface area

The propellant grains chosen for this study are single perforate and cylindrically shaped with the following dimensions:

- 1) r_i = the inner radius of the propellant grain
- 2) r_o = the outer radius of the propellant grain
- 3) l = the initial length of the propellant grain

The following assumptions are used to obtain the first equation for the propellant grain burning surface area:

- 1) The propellant grains are incompressible.
- 2) The burning surface area of the ends of a propellant grain are small in comparison to the burning surface area of the inner and outer cylindrical surfaces of the propellant grain.
- 3) The number of propellant grains per unit volume (n) is a function of time and distance along the combustion tube axis, i.e., $n = n(x, t)$.
- 4) The total surface burning area (A_{bt}) is constant.

Under these assumptions, the volumetric burning surface area may be expressed as

$$A_b = \{2\pi l[r_i(t=0) + \int_0^t \frac{dr}{dt} dt] + 2\pi l[r_o(t=0) - \int_0^t \frac{dr}{dt} dt]\}n \quad (A.37)$$

TABLE A-1

Linear burning speeds for CIL 3331 propellant at various pressures

| r_b (10^{-3} m/sec) | Pressure (10^5 Pa) |
|-----------------------------|--------------------------|
| 0.0 | 0.0 |
| 3.30 | 20.7 |
| 5.08 | 34.5 |
| 7.11 | 48.3 |
| 9.65 | 69.0 |
| 13.21 | 103.5 |
| 17.27 | 138.0 |
| 20.57 | 172.4 |
| 24.38 | 206.9 |
| 30.48 | 275.9 |
| 36.83 | 344.9 |
| 43.69 | 413.9 |
| 55.88 | 551.8 |
| 68.58 | 689.8 |
| 116.84 | 1379.5 |
| 170.18 | 2069.3 |
| 210.18 | 2759.1 |
| 243.84 | 3448.9 |
| 309.88 | 9828.4 |
| 401.32 | 6897.7 |
| 635.00 | 13795.4 |

or

$$A_b = 2\pi l(r_i(t=0) + r_o(t=0))n \quad (A.38)$$

Because the propellant grain geometry and assumptions chosen for this analysis result in a constant total burning surface area, it is convenient to recast Eq. (A.38) in the following way:

- 1) multiply Eq. (A.38) by ρ_s/ρ_s where ρ_s is the propellant grain density.
- 2) define a quantity known as the web thickness (w) where $w = (r_o(t) - r_i(t))$ and multiply Eq. (A.38) by w/w .

Equation (A.38) can then be rewritten as

$$A_b = \frac{2\pi l \rho_s (r_o^2 - r_i^2) n}{\rho_s w} \quad (A.39)$$

If n refers to the number of propellant grains contained within a control volume of size Adx (see Fig. (A-1)), then the equation for the local volumetric burning surface area becomes

$$A_b = \frac{2m_{scv}}{\rho_s w} \quad (A.40)$$

where m_{scv} = the mass of the propellant per unit volume contained within the control volume.

If n refers to the total number of propellant grains, the equation

for total burning surface area becomes

$$A_{bt} = \frac{2m_{st}}{\rho_s w} \quad (A.41)$$

where m_{st} = the mass of the propellant charge per unit volume at time t .

Since A_{bt} is a constant, it may also be expressed as

$$A_{bt} = \frac{2m_{c0}}{\rho_s w_0} \quad (A.42)$$

where

m_{c0} = the initial mass of the propellant charge per unit volume.

w_0 = the initial web thickness of the propellant grains.

Equations (A.40)-(A.42) may then be combined to give A_b in terms of a constant and a mass ratio, i.e.,

$$A_b = A_{bt} \frac{m_{scv}}{m_{st}} \quad (A.43)$$

where,

$$m_{scv} = \rho_s v A dx \quad (A.44)$$

$$m_{st} = \rho_s \int_0^L v A dx \quad (A.45)$$

Substituting Eqs. (A.44) and (A.45) into Eq. (A.43) yields the final form of the first equation for the local burning surface area

$$A_b = A_{bt} \left[\frac{\int_0^L v A dx}{\int_0^L v A dx} \right] \quad (A.46)$$

The second formula derived for the propellant grain local burning surface area uses only assumptions 1 and 3 of the previous derivation. Under these assumptions, the local burning surface area may be expressed as

$$A_b = 2\pi \left\{ \left[1_\phi - \int_0^t \frac{dr}{dt} dt \right] \left[r_1(t=0) + \int_0^t \frac{dr}{dt} dt \right] + \left[r_\phi(t=0) - \int_0^t \frac{dr}{dt} dt \right] \right. \\ \left. + 2\pi \left\{ \left[r_\phi(t=0) - \int_0^t \frac{dr}{dt} dt \right]^2 - \left[r_\phi(t=0) + \int_0^t \frac{dr}{dt} dt \right]^2 \right\} n \right\} \quad (A.47)$$

By using Eq. (A.36), the definition of web thickness, and rearranging, Eq. (A.47) can be rewritten as

$$A_b = 2\pi \left\{ [w_\phi + 2r_1(t=0)] \left[1_\phi - \int_0^t r_b dt + w_\phi \right] - 2w_\phi \int_0^t r_b dt \right\} n \quad (A.48)$$

Referring to Fig. (A.1), it can be seen that the number of propellant grains per unit volume in the control volume may be written as

$$n_{cv} = \frac{[\text{propellant mass in CV}/\text{volume of CV}]}{\text{mass of propellant grain}} \quad (A.49)$$

or

$$n_{cv} = \frac{[\rho_s A dx / A dx]}{\rho_s \pi \left\{ [w_\phi + 2r_1(t=0)] w_\phi - 2w_\phi \int_0^t r_b dt \right\} \left[1_\phi - \int_0^t r_b dt \right]} \quad (A.50)$$

Simplifying Eq. (A.56) and substituting it into Eq. (A.47) results in

the second formula for the local burning surface area:

$$A_b = \frac{2\{[w_0 + 2r_i(t=0)][1_0 - \int_0^t r_b dt + w_0] - 2w_0 \int_0^t r_b dt\}}{w_0\{[w_0 + 2r_i(t=0) - 2 \int_0^t r_b dt][1_0 - \int_0^t r_b dt]\}} \quad (A.51)$$

Calculation of the local volumetric rate of propellant consumption

The local volumetric rate of propellant consumption (\dot{M}_s) may be found by multiplying the propellant density by the local volume of propellant consumed in time interval dt , i.e.,

$$\dot{M}_s = \rho_s A_b r_b \quad (A.52)$$

Formulation of the Propellant Grain-Combustion Gas Velocity Ratio

In this section, a relation is found between propellant grain velocity and combustion gas velocity. The relation derived is of an approximate nature and is intended to express only the most dominant physics. The main concept of this derived relationship between propellant grain velocity and combustion gas velocity is that propellant grain velocity can be expressed simply as

$$u_s = CD_1 u \quad (A.53)$$

where

- 1) u_s = the propellant grain velocity
- 2) CD_1 = a parameter which describes the ratio of propellant

grain velocity

- 3) u = the combustion gas velocity

To derive an equation for CD_1 , the following assumptions were made:

- 1) Quasi-steady conditions are valid for all time dependent variables.
- 2) All other forces felt by a propellant grain are negligible in comparison to the pressure drag force, i.e.,

$$F_{net} = F_d \quad (A.54)$$

- 3) At any time, u is a linear function of the projectile velocity U_p and the projectile displacement (L_p), i.e.,

$$u = \frac{x}{L_p} U_p \quad (A.55)$$

where x is the axial distance from the breech.

- 4) At any time, the combustion gas spatial density gradient is negligible, i.e.,

$$\frac{\partial \rho}{\partial x} = 0 \quad (A.56)$$

- 5) The spatial gradient of the propellant grain-combustion gas velocity ratio is negligible at any time, i.e.,

$$\frac{\partial CD_1}{\partial x} = 0 \quad (A.57)$$

- 6) The propellant grains are incompressible.
- 7) The temporal gradient CD_1 has a much smaller magnitude than either the temporal gradient u_g or the temporal gradient of u ,

i.e.,

$$\left| \frac{\partial CD_1}{\partial t} \right| \ll \left| \frac{\partial u_s}{\partial t} \right| \text{ or } \left| \frac{\partial u}{\partial t} \right| \quad (\text{A.58})$$

- 8) The propellant grains are single perforate cylinders with a time averaged radius \bar{r} and constant length l .

The first step in finding an expression for CD_1 is to find an expression for the acceleration of the propellant particles (a_s) in terms of known variables. To do this, a force balance is applied to a propellant grain at an instant in time. Using assumption 1, the drag force felt by the propellant grain can be expressed in the following way:

$$F_d = C_D \rho (u - u_s)^2 (2r1) \quad (\text{A.59})$$

where

- 1) C_D = a drag coefficient for a propellant grain
- 2) ρ = the combustion gas density
- 3) $2r1$ = the frontal area of the propellant grain

Making use of assumption 2, the drag force (F_d) may also be expressed by Newton's Second Law:

$$F_d = (\pi r^2 l \rho_s) a_s \quad (\text{A.60})$$

where ρ_s = the propellant grain density. Combining Eqs. (A.59) and

(A.60) results in the following formula for a_s :

$$a_s = \frac{C_D (u - u_s)^2}{\pi r} \frac{\rho}{\rho_s} \quad (\text{A.61})$$

The desired final form of an expression for propellant grain acceleration is found by combining Eqs. (A.53) and (A.61):

$$a_s = \frac{C_D u^2 (1 - CD_1)^2}{\pi r} \frac{\rho}{\rho_s} \quad (\text{A.62})$$

The second step used to find an expression for CD_1 was to derive expressions for the spatial average propellant grain acceleration (\bar{a}_s) and the spatial average combustion gas acceleration (\bar{a}). Equation (A.62) can be integrated in the axial direction and divided by the integration interval ($L_p - 0$) to find \bar{a}_s :

$$\bar{a}_s = \frac{1}{L_p} \int_0^{L_p} \left[\frac{C_D u^2 (1 - CD_1)^2}{\pi r} \frac{\rho}{\rho_s} \right] dx \quad (\text{A.63})$$

Using Eq. (A.55) from assumption 3, Eq. (A.56) from assumption 4, Eq. (4.57) from assumption 5, and assumption 6, Eq. (A.63) can be rewritten as

$$\bar{a}_s = \frac{C_D (1 - CD_1)^2}{\pi r} \frac{\rho}{\rho_s} \frac{u_p^2}{L_p^3} \int_0^{L_p} x^2 dx \quad (\text{A.64})$$

Performing the indicated integration results in the desired expression for \bar{a}_s :

$$\bar{a}_s = \frac{C_D (1 - CD_1)^2}{\pi r} \frac{\rho}{\rho_s} \frac{u_p^2}{3} \quad (\text{A.65})$$

Differentiating Eq. (A.55) with respect to time gives the following expression for the combustion gas acceleration:

$$a = \frac{x}{L_p} a_p \quad (\text{A.66})$$

where $a_p =$ the projectile acceleration $\left(\frac{\partial U}{\partial t}\right)_p$

Equation (A.66) can be integrated in the axial direction and divided by the integration interval (L_p-0) to find \bar{a} :

$$\bar{a} = \frac{1}{L_p} \int_0^{L_p} \frac{x}{L_p} a_p dx \quad (\text{A.67})$$

Performing the indicated integration results in the desired expression for \bar{a} :

$$\bar{a} = \frac{1}{2} a_p \quad (\text{A.68})$$

The last step needed to find an expression for CD_1 was to relate \bar{a}_s and \bar{a} . This was done by making use of assumption 7 in the differentiation of Eq. (A.68) with respect to time. The resulting equation is

$$a_s = CD_1 a \quad (\text{A.69})$$

Integrating Eq. (A.69) in the axial direction, dividing by the integration interval (L_p-0) , and using assumption 5 results in the equation

$$\frac{1}{L_p} \int_0^{L_p} a_s dx = \frac{1}{L_p} \int_0^{L_p} CD_1 a dx \quad (\text{A.70})$$

Performing the indicated integration results in the equation

$$\bar{a}_s = CD_1 \bar{a} \quad (A.71)$$

Substituting Eq. (A.65) and Eq. (A.68) into Eq. (A.71) results in the equation

$$\frac{C_D (1 - CD_1)^2}{\pi r} \frac{\rho}{\rho_s} \frac{U_p^2}{3} = \frac{1}{2} a_p CD_1 \quad (A.72)$$

where the acceleration ratio of propellant grains to combustion gas is

$$Fa = \frac{2C_D \rho U_p^2}{3\pi r \rho_s a_p} \quad (A.73)$$

Substituting Eq. (A.73) into Eq. (A.72) yields the desired expression for the propellant grain-combustion gas velocity ratio:

$$CD_1 = 1 + \frac{1}{2Fa} (1 - \sqrt{4Fa+1}) \quad (A.74)$$

To check the validity of this expression, the following typical interior ballistic values were chosen:

- 1) $r = 0.035 \text{ in} = 0.0009 \text{ m}$
- 2) $\rho_s = 0.06 \text{ lbm/in}^3 = 1664 \text{ kg/m}^3$
- 3) $\rho = 0.009 \text{ lbm/in}^3 = 250 \text{ kg/m}^3$
- 4) $C_D = 1.0$

Table A.2 lists values for CD_1 for typical values of U_p and a_p . The CD_1 ratios shown in table (A.2) are typical of those observed in interior

Table A.2
Values for CD_1

| $\frac{2C_D \rho_g}{3\pi \rho_s} (1/m)$ | $U_p (m/sec)$ | $a_p (m/sec^2)$ | Fa | CD_1 |
|---|---------------|-----------------|-------|--------|
| 35.37 | 200 | 600,000 | 2.36 | 0.53 |
| 35.37 | 600 | 400,000 | 31.8 | 0.84 |
| 35.37 | 1000 | 100,000 | 353.7 | 0.95 |

ballistic simulations.

Tube Wall Heat Flux

In this section, a formula for tube wall heat flux (q_w) is derived. The first part of this heat flux analysis is concerned with developing formulas for the thermal properties of the combustion gas and tube wall. Next, a formula is derived for the heat transfer coefficient h_c . Finally, an integral approach is used to find the heat penetration length (δ) into the tube wall and the tube wall boundary temperature at some axial location [Ref. 34].

With this information, the heat flux can be found by using a form of the formula

$$q_w = h_c(\bar{T} - T_w) \quad (A.75)$$

where

- 1) \bar{T} is the average combustion gas temperature at some axial location.
- 2) T_w is the tube wall boundary temperature at the same axial location.

Combustion gas and tube wall properties

In order to find the heat flux for the interior ballistic problem, the relevant combustion gas and tube wall properties must be known. Here, it is assumed that the relevant properties vary linearly with

temperature according to the equation

$$F = mT + b \quad (\text{A.76})$$

where

- 1) F = a temperature dependent property
- 2) T = temperature
- 3) m = a constant
- 4) b = a constant

Table (A.3) shows the MKS values of μ , k and Pr at two temperatures for H_2 , CO , H_2O , CO_2 and N_2 . Applying Eq. (A.76) to these sets of data results in the following formulas:

Properties of H_2

$$1) \quad \mu_{H_2}(T) = 0.135 \times 10^{-7}(T) + 49.259 \times 10^{-7} \quad (\text{A.77})$$

$$2) \quad k_{H_2}(T) = 0.409 \times 10^{-3} + 60.353 \times 10^{-3} \quad (\text{A.78})$$

$$3) \quad Pr_{H_2}(T) = -2.353 \times 10^{-5}(T) + .708 \quad (\text{A.79})$$

Properties of CO

$$1) \quad \mu_{CO}(T) = 0.336 \times 10^{-7}(T) + 74.200 \times 10^{-7} \quad (\text{A.80})$$

$$2) \quad k_{CO}(T) = 0.0610 \times 10^{-3}(T) + 6.700 \times 10^{-3} \quad (\text{A.81})$$

$$3) \quad Pr_{CO}(T) = -5.000 \times 10^{-5}(T) + 0.745 \quad (\text{A.82})$$

Properties of H_2O

$$1) \quad \mu_{H_2O}(T) = 0.361 \times 10^{-7}(T) + 10.185 \times 10^{-7} \quad (\text{A.83})$$

Table A.3
Gas properties at various temperatures

| Constituent Gas | Temperature (T) (K) | Viscosity (μ) $(\frac{N \cdot s}{m^2})$ | Conductivity (k) $(\frac{W}{m \cdot K})$ | Prantl number (Pr) (dimensionless) |
|--------------------|------------------------|--|---|---------------------------------------|
| H_2 | 300 | 89.6×10^{-7} | 183×10^{-3} | 0.701 |
| | 2000 | 318.2×10^{-7} | 878×10^{-3} | 0.661 |
| CO | 300 | 175×10^{-7} | 25.0×10^{-3} | 0.730 |
| | 800 | 343×10^{-7} | 55.5×10^{-3} | 0.705 |
| H_2O | 380 | 127.1×10^{-7} | 24.6×10^{-3} | 1.06 |
| | 850 | 296.9×10^{-7} | 63.7×10^{-3} | 1.02 |
| CO ₂ | 300 | 149×10^{-7} | 16.55×10^{-3} | 0.766 |
| | 800 | 337×10^{-7} | 55.1×10^{-3} | 0.716 |
| N_2 | 300 | 178.2×10^{-7} | 25.9×10^{-3} | 0.716 |
| | 1300 | 466.2×10^{-7} | 81.0×10^{-3} | 0.701 |

$$2) \quad k_{H_2O}(T) = 0.0832 \times 10^{-3}(T) - 7.013 \times 10^{-3} \quad (A.84)$$

$$3) \quad Pr_{H_2O}(T) = -8.511 \times 10^{-5}(T) + 1.092 \quad (A.85)$$

Properties of CO₂

$$1) \quad \mu_{CO_2}(T) = 0.376 \times 10^{-7}(T) + 36.200 \times 10^{-7} \quad (A.86)$$

$$2) \quad k_{CO_2}(T) = 0.0771 \times 10^{-3}(T) - 6.580 \times 10^{-3} \quad (A.87)$$

$$3) \quad Pr_{CO_2}(T) = -1.000 \times 10^{-4}(T) + 0.796 \quad (A.88)$$

Properties of N₂

$$1) \quad \mu_{N_2}(T) = 0.288 \times 10^{-7}(T) + 91.800 \times 10^{-7} \quad (A.89)$$

$$2) \quad k_{N_2}(T) = 0.0551 \times 10^{-3}(T) + 9.370 \times 10^{-3} \quad (A.90)$$

$$3) \quad Pr_{N_2}(T) = -1.500 \times 10^{-5}(T) + 0.721 \quad (A.91)$$

After finding formulas for μ , k and Pr for the constituents of the combustion gas, the mass averaging formula

$$\begin{aligned} F_{ave} = & (.011)F_{H_2} + (.524)F_{CO} + (.142)F_{H_2O} \\ & + (.183)F_{CO_2} + (.140)F_{N_2} \end{aligned} \quad (A.92)$$

was used to obtain the following combustion gas properties for CIL 3331 propellant:

$$1) \quad \mu_{CIL} = 0.338 \times 10^{-7}(T) + 57.412 \times 10^{-7} \quad (A.93)$$

$$2) \quad k_{CIL} = 0.0703 \times 10^{-3}(T) + 3.322 \times 10^{-3} \quad (A.94)$$

$$3) \quad Pr_{CIL} = -5.893 \times 10^{-5}(T) + 0.800 \quad (A.95)$$

Table A.4
Tube wall properties

| Tube Wall Material | Temperature (T) (K) | Specific Heat | | Thermal |
|-----------------------|------------------------|--------------------------------------|--|---|
| | | Capacity (Cp) ($\frac{J}{kgK}$) | Conductivity (k) ($\frac{W}{mK}$) | Diffusivity (α) ($\frac{m^2}{sec}$) |
| Carbon Steel | 400 | 487 | 56.7 | 14.82×10^{-6} |
| | 1000 | 1169 | 30.0 | 3.27×10^{-6} |

Table A.4 shows the MKS values of C_p , k and α at two temperatures for plain carbon steel. Applying Eq. (A.76) to this set of data results in the following formulas:

$$1) \quad C_{p_{st}}(T) = 1.137(T) + 32.330 \quad (A.96)$$

$$2) \quad k_{st}(T) = -0.0445(T) + 74.500 \quad (A.97)$$

$$3) \quad \alpha_{st}(T) = -0.0193 \times 10^{-6}(T) + 22.520 \times 10^{-6} \quad (A.98)$$

A convection coefficient model

A reasonable value for the convection coefficient h_c is needed in order to find the heat transferred into the tube wall from the combustion gas. The formula for h_c presented here is of an approximate nature for the interior ballistic flow problem. This is because of the assumptions needed to use a modified version of the Sieder-Tate Nusselt number formula. The necessary assumptions are as follows:

- 1) Quasi-steady state conditions hold.
- 2) The flow in the tube is fully developed.
- 3) The combustion gas flow in the tube is turbulent (i.e., it has a Reynolds number, Re_D , in excess of 2300).
- 4) The Prantl number (Pr) for the combustion gas is greater than 0.5.

By using the above assumptions, the Nusselt number of the combustion gas at some axial location x_a along the tube and time t can be expressed as

$$Nu_D(x_a, t) = A Re_D^{4/5} Pr^{1/3} \left(\frac{\mu}{\mu_s} \right)^{0.14} \quad (A.99)$$

where the temperature dependent properties Pr and μ are given by Eq. (A.95) and Eq. (A.93), respectively, and evaluated at $\bar{T}_m = [\bar{T}(x_a, t) +$

$T_w(x_a, t)]/2$, the viscosity at the tube wall surface μ_s is given by Eq. (A.93) and evaluated at $T_w(x_a, t)$, and A is chosen such that the calculated peak tube wall temperature agrees well with the experimentally obtained peak tube wall temperature of 1050 K [Refs. 22,38]. For this analysis of the interior ballistic problem, a value of 0.075 was chosen for A .

The convection coefficient of the combustion gas at some axial location x_a along the tube and time t can be expressed as

$$h_c(x_a, t) = Nu_D(x_a, t) \frac{k}{D} \quad (A.100)$$

where k is the thermal conductivity of the combustion gas given by Eq. (A.94) and D is the tube diameter. Substituting Eq. (A.99) into Eq. (A.100) results in the formula

$$h_c(x_a, t) = [0.075 Re_D^{4/5} Pr^{1/3} (\frac{\mu}{\mu_s})^{0.14}] (\frac{k}{D}) \quad (A.101)$$

The Reynolds number in Eq. (A.101) is given by

$$Re_D = \frac{\bar{\rho}(x_a, t) \bar{u}(x_a, t) D}{\mu} \quad (A.102)$$

An integral method to find heat flux

Figure A.1 shows the geometry and coordinate system used to analyze the tube wall heat transfer problem. The axial distance along the tube is measured along the x axis and the distance into the tube

wall is measured along the y axis where

$$y = R-r \quad (A.103)$$

The following assumptions were used to derive an expression for tube wall heat transfer:

- 1) The heat transfer taking place in the tube wall is conduction heat transfer in the y direction.
- 2) The effects of tube wall curvature may be neglected since the heat penetration distance into the tube wall, $\delta(t)$, is small.
- 3) The tube wall thermal properties are functions of temperature only.
- 4) The temperature profile in the tube wall at any axial location can be expressed as a second degree polynomial function of temperature.
- 5) Quasi-steady conditions hold for the convection coefficient h_c .

Using assumptions 1 and 2, the governing equation for tube wall heat transfer at a fixed axial location x_a and time t can be written as

$$\frac{1}{\alpha_{st}} \frac{\partial T(x_a, y, t)}{\partial t} = \frac{\partial^2 T(x_a, y, t)}{\partial y^2} \quad (A.104)$$

with the initial condition

$$T(x_a, t, 0) = T_i \quad (A.105)$$

and the boundary condition

$$-k_{st} \frac{\partial T_w(x_a, t)}{\partial y} + hT_w(x_a, t) = h\bar{T}(x_a, t) \quad (A.106)$$

where

$T_w(x_a, t)$ is the temperature at the tube wall boundary

and

$\bar{T}(x_a, t)$ is the combustion gas temperature.

Using assumptions 3 and 4, the temperature profile in the tube wall can be expressed as

$$T(x_a, y, t) = a + bT + cT^2 \quad (\text{A.107})$$

subject to the constraints

$$\frac{\partial T(x_a, \delta, t)}{\partial y} = 0 \quad (\text{A.108})$$

$$T(x_a, \delta, t) = T_1 \quad (\text{A.109})$$

By applying the constraints due to the heat penetration length (Eqs. (A.108) and (A.109)) and the tube wall boundary condition (Eq. (A.106)), the terms a , b and c in Eq. (A.107) may be found. The resulting tube wall temperature profile equation is

$$T(x_a, y, t) - T_1 = \left(\frac{h}{k_{st}}\right) [\bar{T}(x_a, t) - T_w(x_a, t)] \left[\frac{\delta}{2} - y + \frac{y^2}{2\delta}\right] \quad (\text{A.110})$$

By integrating the governing equation (Eq. (A.104)) across the region of heat penetration, using assumption 2, and applying the heat

penetration length constraint Eq. (A.108), the governing equation can be rewritten as

$$\frac{1}{\alpha_{st}} \int_0^{\delta} \left[\frac{\partial T(x_a, y, t)}{\partial y} \right] dy = - \frac{\partial T_w(x_a, t)}{\partial y} \quad (A.111)$$

By using Liebnitz's rule and the heat penetration length constraint Eq. (A.109), the following two relations may be found:

$$\frac{\partial}{\partial t} \int_0^{\delta} T(x_a, y, t) dy = T_i \frac{\partial \delta}{\partial t} + \int_0^{\delta} \left[\frac{\partial T(x_a, y, t)}{\partial y} \right] dy \quad (A.112)$$

$$T_i \frac{\partial \delta}{\partial t} = \frac{\partial}{\partial t} \int_0^{\delta} T_i dy \quad (A.113)$$

Substitution of Eqs. (A.112) and (A.113) into Eq. (A.111) and subsequent rearranging results in the following integral form of the governing equation:

$$\frac{\partial}{\partial t} \int_0^{\delta} [T(x_a, y, t) - T_i] dy = -\alpha_{st} \frac{\partial T_w(x_a, t)}{\partial y} \quad (A.114)$$

Substituting the tube wall temperature profile equation (Eq. (A.110)) into Eq. (A.114) and performing the indicated integration yields the following equation:

$$\frac{\partial}{\partial t} \left\{ \frac{h}{k_{st}} [\bar{T}(x_a, t) - T_w(x_a, t)] \frac{1}{6} \delta^2 \right\} = -\alpha_{st} \frac{\partial T_w(x_a, t)}{\partial y} \quad (A.115)$$

Differentiating Eq. (A.110) with respect to y and applying the result at

the tube wall boundary ($y=0$) yields the relation:

$$\frac{\partial T_w(x_a, t)}{\partial y} = \frac{h_c}{k_{st}} [\bar{T}(x_a, t) - T_w(x_a, t)] \quad (\text{A.116})$$

By substituting Eq. (A.116) into Eq. (A.115) and using assumption 5, Eq. (A.116) can be rewritten as

$$\frac{\partial}{\partial t} \{ [\bar{T}(x_a, t) - T_w(x_a, t)] \frac{1}{6} \delta^2 \} = \alpha_{st} [\bar{T}(x_a, t) - T_w(x_a, t)] \quad (\text{A.117})$$

The solution of Eq. (A.117) yields a value for δ at time t and some axial location x_a along the tube. Performing an integration of Eq. (A.117) by use of a summation approximation yields the following solution for δ at time level $n+1$:

$$\delta((n+1)\Delta t) = \left| \frac{\sum_{j=1}^{n+1} \delta(\alpha_{st})_j [\bar{T}(x_a, j\Delta t) - T_w(x_a, j\Delta t)] \Delta t}{[\bar{T}(x_a, (n+1)\Delta t) - T_w(x_a, (n+1)\Delta t)]} \right|^{1/2} \quad (\text{A.118})$$

where $(\alpha_{st})_j$ is given by Eq. (A.98) at the average tube wall temperature

$$(T_{ave})_j = \frac{T_w(x_a, j\Delta t) + T_i}{2} \quad (\text{A.119})$$

For Eq. (A.118), the term $T_w(x_a, (n+1)\Delta t)$ can be approximated as $T_w(x_a, n\Delta t)$. If higher accuracy is desired, an iteration technique can be used to update the value of $\delta((n+1)\Delta t)$.

Once $\delta((n+1)\Delta t)$ is known, it can be substituted into the tube wall temperature profile equation to find a value for the tube wall boundary

temperature at some axial location x_a and time $(n+1)\Delta t$. The resulting equation is

$$T_w(x_a, (n+1)\Delta t) = \frac{T_i + \left(\frac{h_c}{2k_{st}}\right)\delta((n+1)\Delta t)\bar{T}(x_a, (n+1)\Delta t)}{\left[1 + \left(\frac{r_c}{2k_{st}}\right)\delta((n+1)\Delta t)\right]} \quad (A.120)$$

where k_{st} is given by Eq. (A.97) at the tube wall boundary temperature corresponding to time level n . Finally, the heat flux at time level $n+1$ at some axial location x_a along the tube can be written as

$$q_w(x_a, (n+1)\Delta t) = h_c[\bar{T}(x_a, (n+1)\Delta t) - T_w(x_a, (n+1)\Delta t)] \quad (A.121)$$

Propellant grain displacement

In order to properly scale the transformed spatial domain of the propellant grains, the propellant grain displacement (L_g) must be known.

To find L_g , an iterative procedure was used. The essence of this procedure is to find an i grid point which corresponds to the IL^* grid point as shown in Fig. A.2. Once the location of this i grid point is known, velocity information from the combustion gas problem can be used to find U_g (the propellant grain velocity at point IL^*). After U_g is determined, L_g can be found in a manner analogous to that used to find L_p (see Section 2.3).

A step-by-step description of the iterative procedure used to find L_g is given here and proceeds as follows:

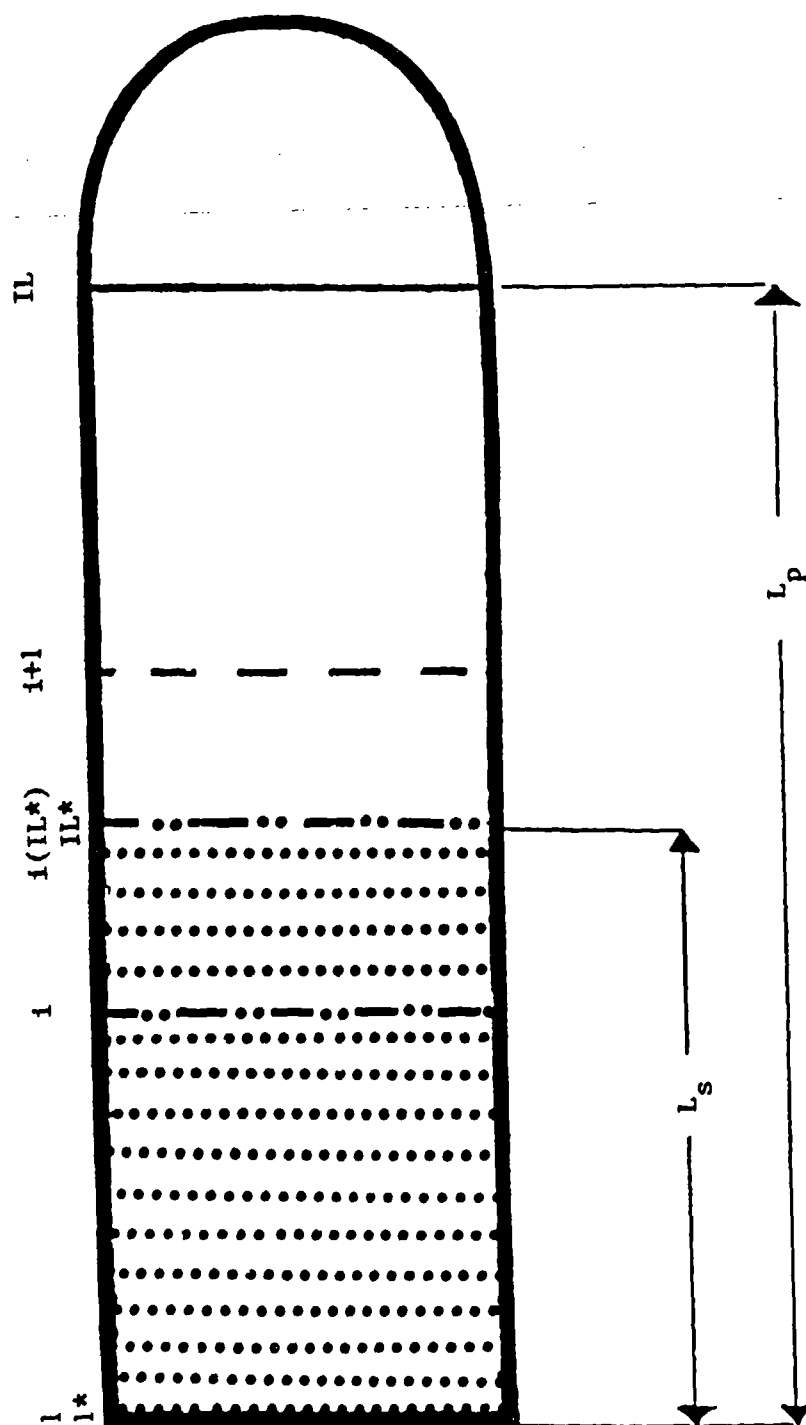


Figure A.2

Propellant grain displacement (L_s) and projectile displacement (L_p) where
 i grid points correspond to the discretized combustion gas spatial domain
 and i^* grid points correspond to the discretized propellant
 grain spatial domain.

- 1) Find the i grid point which corresponds to $(IL^*)^{n+1}$ by using the formula

$$ir' = (IL-1) \frac{L_{s'}}{L_p^{n+1}} + 1 \quad (A.122)$$

where initially

$$L_{s'} = L_s^n \quad (A.123)$$

- 2) Find the integer value i which corresponds to the value of ir' by using the formula

$$i = \text{INT}(ir') \quad (A.124)$$

where INT indicates an integer value

- 3) Calculate a ratio (PHE) which indicates the position of the point ir' relative to the positions of the points i and $i+1$ (see Fig. A-2) by using the formula

$$\text{PHE} = ir' - i \quad (A.125)$$

- 4) Find the combustion gas velocity and the propellant grain-combustion gas velocity ratio at point ir' by using the formulas

$$\bar{u}(ir') = (1 - \text{PHE})\bar{u}(i) + (\text{PHE})\bar{u}(i+1) \quad (A.126)$$

$$CD_1(ir') = (1 - \text{PHE})CD_1(i) + (\text{PHE})CD_1(i+1) \quad (A.127)$$

- 5) Find the propellant grain velocity at point ir' by using the formula

$$U_g(ir') = CD_1(ir')\bar{u}(ir') \quad (A.128)$$

- 6) Guess the value of the propellant grain displacement (L_g) at

time level $n+1$ by using the formula

$$L_s^{n+1} = L_s^n + \frac{[U_s^n + U_s(i r')]}{2} \Delta t \quad (\text{A.129})$$

- 7) Check to see whether the difference between $L_s(i r')$ in Eq. (A.129) and L_s in Eq. (A.122) is less than some small value ϵ . If this difference is less than ϵ , then Eq. (A.129) has yielded an acceptable value for L_s^{n+1} . If this difference is still greater than ϵ , then repeat steps 1-7 using the updated value of L_s found in Eq. (A.129).

A Conservative Scheme for Mapping i^* Values onto the i Grid Point System

When mapping i^* values onto the i grid point system (see Fig. A.3), it is important that the mapping procedure be conservative. This is because of the very significant influence of i^* variables on the interior ballistic problem and the large number of times that this mapping procedure must be carried out in the numerical solution procedure.

The mapping procedure developed ensures conservation by requiring the spatial integral of whatever variable is to be mapped to have the same value in both grid point systems. A step-by-step description of the mapping procedure is given below:

- 1) Find the i^* point which equals the corresponding i point (see Fig. A.3) by using the formula

$$i^* r = 1 + L_p / L_s (i-1) \quad (\text{A.130})$$

- 2) Calculate a ratio (PHE) which indicates the position of the point $i^* r$ relative to the positions of point i^* and $(i+1)^*$

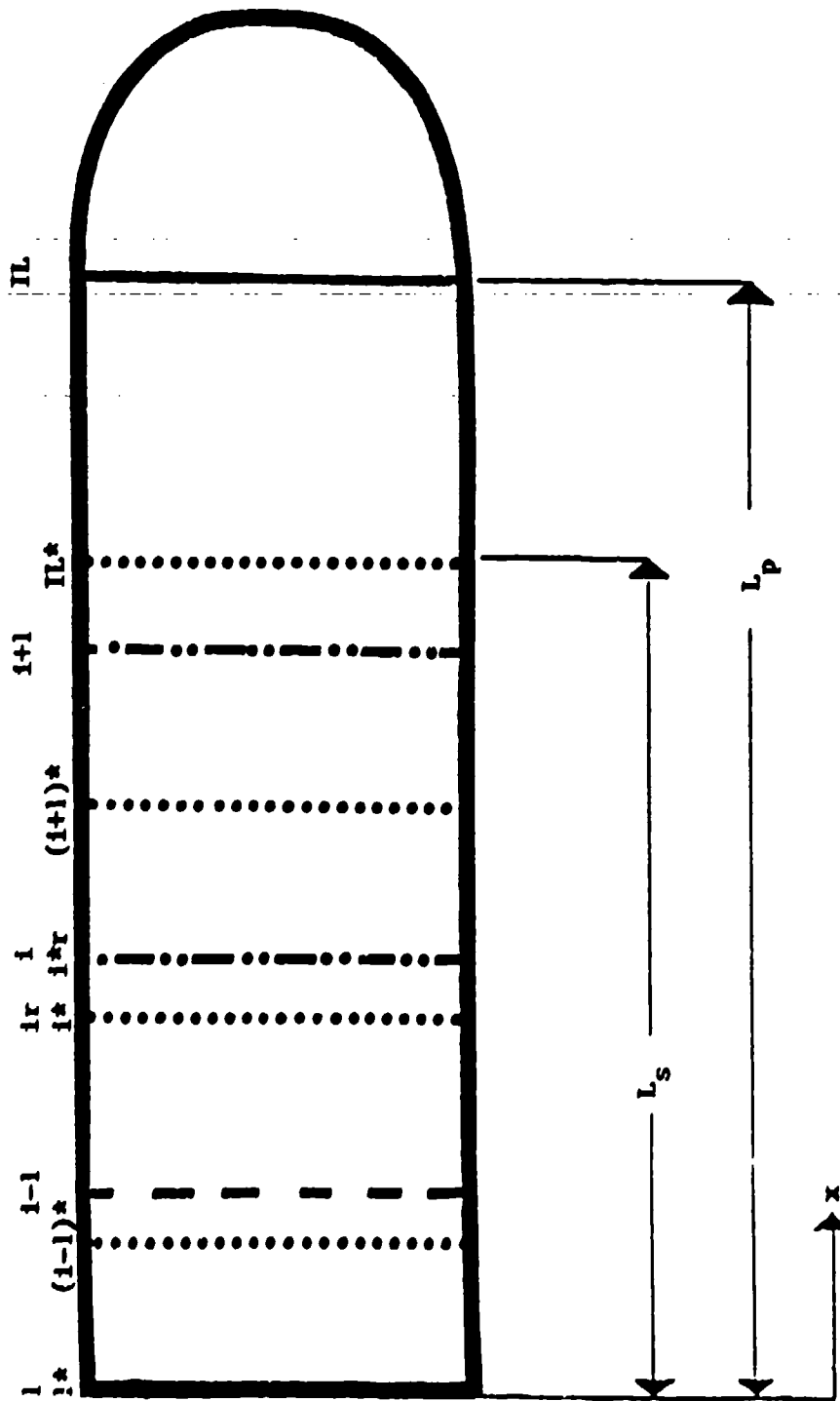


Figure A.3

The discretized propellant grain spatial domain (indicated by 1^* grid points) superimposed on the discretized combustion gas spatial domain (indicated by i grid points).

(see Fig. A.3) by using the formula

$$PHE = (i-1) \frac{L_p}{L_s} - \frac{INT[1 + L_p/L_s (i-1)] - 1}{L_s} \quad (A.131)$$

where INT indicates an integer value.

- 3) Find the interpolated value at point i^*r (equivalently point i) by using the formula

$$VAL(i^*r) = (1-PHE)VAL(i^*) + (PHE)VAL(i+1)^* \quad (A.132)$$

- 4) To ensure conservation of values mapped from the i^* grid point system to the i grid point system, the integral relation

$$\int_0^{x(i^*r)} VAL^*(x) dx = \int_0^{x(i)} VAL(x) dx \quad (A.133)$$

is used in the following manner:

- a) the left side of Eq. (A.133) is numerically approximated as

$$\begin{aligned} \int_0^{x(i^*r)} VAL^*(x) dx &\approx \sum_{i^*=2}^{INT(i^*r)} \frac{1}{2} [VAL(i-1)^* + VAL(i^*)] \frac{L_s}{(IL^*-1)} \\ &+ \frac{1}{2} [VAL(i^*) + VAL(i^*r)] \left[\frac{[(i-1)L_p - (i^*-1)L_s]}{(IL-1)} \right] \end{aligned} \quad (A.134)$$

- b) the right side of Eq. (A.133) is numerically approximated as

$$\int_0^{x(i)} VAL(x) dx \approx \sum_{i=2}^I \frac{1}{2} [VAL(i-1) + VAL(i)] \frac{L_p}{(IL-1)} \quad (A.135)$$

where

$$I = (i^*r-1) \frac{L_s}{L_p} + 1 \quad (\text{A.136})$$

c) by combining Eqs. (A.133)-(A.135), rearranging and recognizing that IL is numerically equivalent to IL*, i* values can be conservatively mapped onto the i grid point system by the formula

$$\begin{aligned} \text{VAL}(i) = & \left\{ \sum_{i^*=2}^{\text{INT}(i^*r)} (L_s/L_p) [\text{VAL}(i-1)^* + \text{VAL}(i^*)] \right\} \\ & - \left\{ \sum_{i=2}^{I-1} [\text{VAL}(i-1) - \text{VAL}(i)] \right\} + [1 - (i^*-1)(L_s/L_p) \\ & - 1][\text{VAL}(i^*) + \text{VAL}(i^*r)] - \text{VAL}(i-1) \end{aligned} \quad (\text{A.137})$$

5) Increment the value of i and repeat steps 1-4 until

$$i = \text{IL} \quad (\text{A.138})$$

A Non-Conservative Scheme for Mapping i Values onto the i* Grid Point System

Since the i grid point system is inherently less accurate than the i* grid point system (because $\Delta x \geq \Delta x^*$) conservative mapping of i values onto the i* grid point system is not appropriate. Therefore, a simpler mapping scheme was developed and is presented here in a step-by-step manner:

- 1) Find the i_r point which equals the corresponding $(IL^* - i^*)$ point (see Fig. A.3) by using the formula

$$i_r = (IL^* - i^*) \left(\frac{L_s}{L_p} \right) + 1 \quad (A.139)$$

- 2) Find the integer value i which corresponds to the value of i_r , i.e.,

$$i = \text{INT}(i_r) \quad (A.140)$$

- 3) Calculate a ratio (PHE) which indicates the position of the point i_r relative to the positions of points i and $i+1$ (see Fig. A.3) by using the formula

$$\text{PHE} = i_r - i \quad (A.141)$$

- 4) Map the i value onto the i^* grid point system by using the formula

$$\text{VAL}(IL^{*+1} - i^*) = (1 - \text{PHE})\text{VAL}(i) + (\text{PHE})\text{VAL}(i+1) \quad (A.142)$$

- 5) Increment the value of i^* and repeat steps 1-4 until

$$i^* = IL^* \quad (A.143)$$

APPENDIX B

B.1 Boundary Layer Equations

The physical coordinate system for the interior ballistic cycle is shown in Fig. C.1. An axisymmetric tube is closed on one end by the fixed breech wall and bounded on the other end by the movable projectile. An axial coordinate (x) is set on the breech and oriented toward the projectile. A radial coordinate (r) is set on the tube centerline and oriented toward the tube wall. The partial differential equations which govern boundary layer flow in this coordinate system are as follows:

Continuity

$$\frac{\partial \rho}{\partial t} + \frac{\partial(\rho v)}{r \partial r} + \frac{\partial(\rho u)}{\partial x} = 0 \quad (\text{B.1})$$

Momentum

$$\rho \left(\frac{\partial u}{\partial t} + v \frac{\partial u}{\partial r} + u \frac{\partial u}{\partial x} \right) = \frac{\partial}{r \partial r} (r \mu \frac{\partial u}{\partial r}) - \frac{\partial p}{\partial x} \quad (\text{B.2})$$

Energy

$$\begin{aligned} \rho \left(\frac{\partial H}{\partial t} + u \frac{\partial H}{\partial x} + v \frac{\partial H}{\partial r} \right) - \frac{\partial p}{\partial t} - u \frac{\partial p}{\partial x} \\ = \frac{\partial}{r \partial r} \left[r \left[\left(\frac{\mu}{Pr} + \frac{\mu_T}{Pr_T} \right) \frac{\partial H}{\partial r} + \left(\mu \left(1 - \frac{1}{Pr} \right) + \mu_T \left(1 - \frac{1}{Pr_T} \right) \right) u \frac{\partial u}{\partial r} \right] \right] \end{aligned} \quad (\text{B.3})$$

Static Enthalpy

$$H_1 = H - (u^2)/2 \quad (\text{B.4})$$

Gas Properties

$$T = T(H_1) \quad (\text{B.5})$$

Equation of State

$$P = \rho * R_{cg} * T \quad (B.6)$$

It is desired to perform calculations in a new coordinate system. This new coordinate system is shown in Fig. C.2. An axial coordinate λ is set on the projectile and oriented toward the breech. A radial coordinate (y) is set on the tube wall and oriented toward the tube centerline. Another radial coordinate ζ is parallel to (y) and clusters grid points near the wall to capture the wall velocity gradients and wall thermal gradients. The computational coordinate system is functionally dependent on the physical coordinate system by the following relationships:

$$y = R - r$$

$$\tau = t$$

$$\lambda = \lambda(x, t)$$

$$\zeta = \zeta(y)$$

By the chain rule:

$$\frac{\partial ()}{\partial r} = \frac{\partial y}{\partial r} \frac{\partial \zeta}{\partial y} \frac{\partial ()}{\partial \zeta} = -\zeta_y \frac{\partial ()}{\partial \zeta} \quad \frac{\partial y}{\partial r} = -1$$

$$\frac{\partial ()}{\partial z} = \frac{\partial \lambda}{\partial z} \frac{\partial ()}{\partial \lambda} = \lambda_z \frac{\partial ()}{\partial \lambda}$$

$$\frac{\partial ()}{\partial t} = \frac{\partial \tau}{\partial t} \frac{\partial ()}{\partial \tau} + \frac{\partial \lambda}{\partial t} \frac{\partial ()}{\partial \lambda} = \frac{\partial ()}{\partial \tau} + \lambda_t \frac{\partial ()}{\partial \lambda}$$

The previous equations (B.1) to (B.6) are thus transformed:

Continuity

$$\frac{\partial \rho}{\partial \tau} + \lambda_t \frac{\partial \rho}{\partial \lambda} - \frac{1}{r} \zeta_y \frac{\partial (r \rho v)}{\partial \zeta} + \lambda_z \frac{\partial (\rho u)}{\partial \lambda} = 0 \quad (B.7)$$

Momentum

$$\begin{aligned} & \rho \left(\frac{\partial (u)}{\partial t} + (\lambda_t + \lambda_z u) \frac{\partial (u)}{\partial \lambda} - v \zeta_y \frac{\partial (u)}{\partial \zeta} \right) \\ &= \frac{1}{r} \zeta_y \frac{\partial}{\partial \zeta} (r (\mu + \mu_T) \zeta_y \frac{\partial (u)}{\partial \zeta}) - \lambda_z \frac{\partial P}{\partial \lambda} \end{aligned} \quad (B.8)$$

Energy

$$\begin{aligned} & \rho \left(\frac{\partial H}{\partial t} + (\lambda_t + \lambda_z u) \frac{\partial H}{\partial \lambda} - v \zeta_y \frac{\partial H}{\partial \zeta} \right) - \frac{\partial P}{\partial t} - (\lambda_t + \lambda_z u) \frac{\partial P}{\partial \lambda} \\ &= \frac{1}{r} \zeta_y \frac{\partial}{\partial \zeta} \left[r \left[\left(\frac{\mu}{Pr} + \frac{\mu_T}{Pr_T} \right) \zeta_y \frac{\partial H}{\partial \zeta} \right. \right. \\ & \quad \left. \left. + \left[\mu \left(1 - \frac{1}{Pr} \right) + \mu_T \left(1 - \frac{1}{Pr_T} \right) \right] u \zeta_y \frac{\partial (u)}{\partial \zeta} \right] \right] \end{aligned} \quad (B.9)$$

Static Enthalpy

$$H_1 = H - \frac{u^2}{2} \quad (B.10)$$

Gas Properties

$$T = T(H_1) \quad (B.11)$$

Equation of State

$$P = \rho * R_{cg} * T \quad (B.12)$$

By boundary layer principles, it is necessary that the longitudinal velocity "sweep" in the direction of the computational coordinate λ . The calculation velocity U is chosen as $U = u - u_p$. The projectile velocity is not spatially dependent:

$$\frac{\partial u_p}{\partial \lambda} = 0 \quad \frac{\partial u}{\partial \lambda} = \frac{\partial (u + u_p)}{\partial \lambda} = \frac{\partial U}{\partial \lambda}$$

$$\frac{\partial u_p}{\partial \zeta} = 0 \quad \frac{\partial u}{\partial \zeta} = \frac{\partial (u + u_p)}{\partial \zeta} = \frac{\partial U}{\partial \zeta}$$

The partial differential equations which govern boundary layer flow in the computational coordinate system simplify to:

Continuity

$$\frac{\partial \rho}{\partial t} + \lambda_t \frac{\partial \rho}{\partial \lambda} - \frac{1}{r} \zeta_y \frac{\partial}{\partial \zeta} (r \rho v) + \lambda_z \frac{\partial}{\partial \lambda} (\rho U + \rho u_p) = 0 \quad (B.13)$$

Momentum

$$\begin{aligned} & \rho \left(\frac{\partial}{\partial t} (U + u_p) + (\lambda_t + \lambda_z (U + u_p)) \frac{\partial}{\partial \lambda} (U) \right) - v \zeta_y \frac{\partial}{\partial \zeta} (U) \\ &= \frac{1}{r} \zeta_y \frac{\partial}{\partial \zeta} (r (\mu + \mu_T) \zeta_y \frac{\partial}{\partial \zeta} (U)) - \lambda_z \frac{\partial P}{\partial \lambda} \end{aligned} \quad (B.14)$$

Energy

$$\begin{aligned} & \rho \left(\frac{\partial H}{\partial t} + (\lambda_t + \lambda_z (U + u_p)) \frac{\partial H}{\partial \lambda} \right) - v \zeta_y \frac{\partial H}{\partial \zeta} - \frac{\partial P}{\partial t} - (\lambda_t + \lambda_z (U + u_p)) \frac{\partial P}{\partial \lambda} \\ &= \frac{1}{r} \zeta_y \frac{\partial}{\partial \zeta} \left[r \left[\left(\frac{\mu}{Pr} + \frac{\mu_T}{Pr_T} \right) \zeta_y \frac{\partial H}{\partial \zeta} \right. \right. \\ & \quad \left. \left. + \left(\mu \left(1 - \frac{1}{Pr} \right) + \mu_T \left(1 - \frac{1}{Pr_T} \right) \right) (U + u_p) \zeta_y \frac{\partial}{\partial \zeta} (U) \right] \right] \end{aligned} \quad (B.15)$$

Static Enthalpy

$$H_1 = H - \frac{(U + u_p)^2}{2} \quad (B.16)$$

Gas Properties

$$T = T(H_1) \quad (B.17)$$

Equation of State

$$P = \rho * R_{cg} * T \quad (B.18)$$

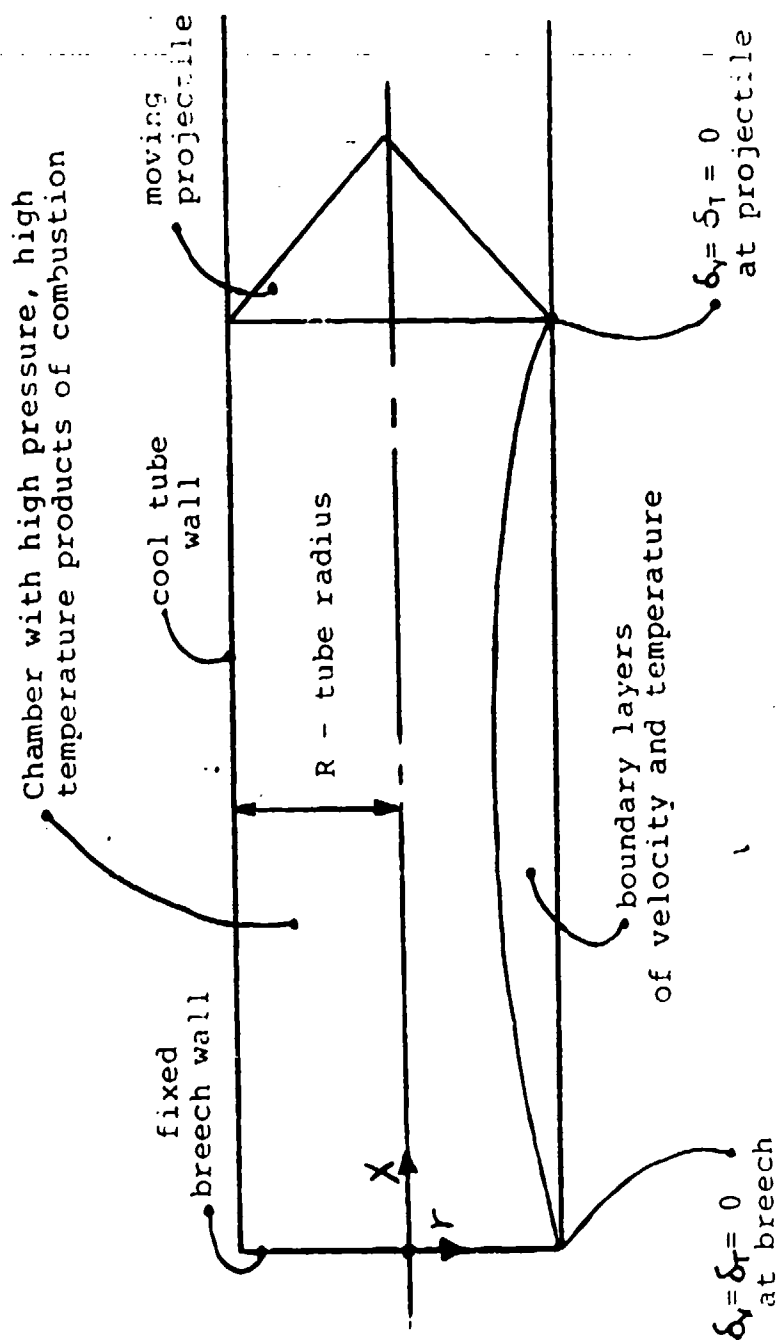


Fig. B.1 Physical coordinate system for the interior ballistic problem

B.2 Numerical Method of Solution

In the previous section, the equations (B.13) to (B.18) were developed to describe the boundary layer flow of the interior ballistic cycle. There is no analytical solution to this set of non-linear partial differential equations. To solve these coupled equations on a digital computer requires that the continuous physical grid be discretized and that the partial differentials be replaced with finite difference formulas. Typical for boundary layer flows, the following techniques were applied to the momentum and energy equations:

- 1) Partial derivatives in time are forward differenced, involving only the current time step and the next time step forward in time.
- 2) Partial derivatives in the longitudinal direction are all of first order. Backward differencing is applied across the current grid point and the preceeding grid point.
- 3) Partial derivatives in the radial direction use at most three grid points, and are central differenced where possible.

The following techniques typical for boundary layer flows were applied to the continuity equation:

- 1) Partial derivatives in time are forward differenced, involving only the current time step and the next time step forward in time.
- 2) Partial derivatives in the longitudinal direction are all of first order. To aid in properly determining mass flux, backward differencing is applied across the current grid point and the preceeding grid point, and across the respective pair of points nearer the tube wall.
- 3) Partial derivatives in the radial direction are all of first order. Backward differencing is applied across the current grid point and the neighboring point nearer the wall.

Except for the partial time derivative, some choice must be made for the time level of each term in the finite difference equations. An implicit scheme is used where all the spatial derivatives are sought at the next time level (n+1). The resulting finite differenced equations are as follows:

Continuity

$$\begin{aligned}
 & \left[\frac{1}{4\Delta t} \right] \left[\begin{array}{cccc} (\rho_{i,j})^{n+1} & + (\rho_{i-1,j})^{n+1} & + (\rho_{i,j-1})^{n+1} & + (\rho_{i-1,j-1})^{n+1} \\ -(\rho_{i,j})^n & -(\rho_{i-1,j})^n & -(\rho_{i,j-1})^n & -(\rho_{i-1,j-1})^n \end{array} \right] \\
 & + \left[\frac{\lambda_{ti}}{2\Delta\lambda} + \frac{\lambda_{zi}u_p}{\Delta\lambda} \right] \left[\begin{array}{cc} (\rho_{i,j})^{n+1} & -(\rho_{i-1,j})^{n+1} \\ +(\rho_{i,j-1})^{n+1} & -(\rho_{i-1,j-1})^{n+1} \end{array} \right] \\
 & - \left[\frac{\zeta_{y,j}}{r_j\Delta\zeta} \right] \left[r_j(\rho_{i,j}v_{i,j})^{n+1} - r_{j-1}(\rho_{i,j-1}v_{i,j-1})^{n+1} \right] \\
 & + \left[\frac{\lambda_{zi}}{\Delta\lambda} \right] \left[\begin{array}{cc} (\rho_{i,j}u_{i,j})^{n+1} & -(\rho_{i-1,j}u_{i-1,j})^{n+1} \\ +(\rho_{i,j-1}u_{i,j-1})^{n+1} & -(\rho_{i-1,j-1}u_{i-1,j-1})^{n+1} \end{array} \right] = 0 \quad (B.19)
 \end{aligned}$$

Momentum

$$\begin{aligned}
 & \left[\frac{(\rho_{i,j})^{n+1}}{\Delta\tau} \right] \left[(u_{i,j})^{n+1} - (u_{i,j})^n + (u_{pi,j})^{n+1} - (u_{pi,j})^n \right] \\
 & + \left[\frac{(\rho_{i,j})^{n+1}}{\Delta\lambda} \right] \left[(\lambda_{ti} + \lambda_{zi}(u_{i,j} + u_p))^{n+1} \right] \left[(u_{i,j})^{n+1} - (u_{i-1,j})^{n+1} \right] \\
 & - \left[\frac{(\rho_{i,j}v_{i,j})^{n+1}}{2\Delta\zeta} \right] \left[\zeta_{y,j} (u_{i+1,j} - u_{i-1,j})^{n+1} \right]
 \end{aligned}$$

$$\begin{aligned}
&= \frac{\zeta_{y,j}}{\Delta \zeta \tau_j} \left[(r_{j+1/2}) \left(\frac{\mu_{1,j+1} + \mu_{1,j}}{2} + \frac{\mu_{T1,j+1} + \mu_{T1,j}}{2} \right) \zeta_{y,j+1/2} \frac{(u_{1,j+1} - u_{1,j})^{n+1}}{\Delta \zeta} \right. \\
&\quad \left. - (r_{j-1/2}) \left(\frac{\mu_{1,j} + \mu_{1,j-1}}{2} + \frac{\mu_{T1,j} + \mu_{T1,j-1}}{2} \right) \zeta_{y,j-1/2} \frac{(u_{1,j} - u_{1,j-1})^{n+1}}{\Delta \zeta} \right] \\
&\quad - \left[(\lambda_{z1})^{n+1} \right] \left[\frac{(P_1 - P_{1-1})^{n+1}}{\Delta \lambda} \right]
\end{aligned} \tag{B.20}$$

Energy

$$\begin{aligned}
&\left[(\rho_{1,j})^{n+1} \right] \left[(H_{1,j})^{n+1} - (H_{1,j})^n \right] \\
&+ \left[\frac{(\rho_{1,j})^{n+1}}{\Delta \lambda} \right] \left[(\lambda_{t1} + \lambda_{z1} (U_{1,j} + u_p))^{n+1} \right] \left[(H_{1,j})^{n+1} - (H_{1-1,j})^{n+1} \right] \\
&- \left[\frac{(\rho_{1,j} v_{1,j})^{n+1}}{2 \Delta \zeta} \right] \left[\zeta_{y,j} \right] \left[(H_{1,j+1} - H_{1,j-1})^{n+1} \right] \\
&= \frac{\zeta_{y,j}}{r_j \Delta \zeta} \left\{ \left[r_{j+1/2} \right] \left(\frac{\mu_{1,j+1} + \mu_{1,j}}{Pr_{1,j+1} + Pr_{1,j}} + \frac{\mu_{T1,j+1} + \mu_{T1,j}}{Pr_{T1,j+1} + Pr_{T1,j}} \right) \right. \\
&\quad \left. \left[\zeta_{y,j+1/2} \right] \frac{(H_{1,j+1} - H_{1,j})^{n+1}}{\Delta \zeta} \right\} \\
&+ \left[\frac{\mu_{1,j+1} + \mu_{1,j}}{2} \right] \left(1 - \frac{2}{Pr_{1,j} + Pr_{1,j+1}} \right) + \left[\frac{\mu_{T1,j+1} + \mu_{T1,j}}{2} \right] \left(1 - \frac{2}{Pr_{T1,j+1} + Pr_{T1,j}} \right) \\
&\quad \left(\frac{U_{1,j+1} - U_{1,j} + u_p}{2} \right)^{n+1} \left(\zeta_{y,j+1/2} \right) \frac{(U_{1,j+1} - U_{1,j})^{n+1}}{\Delta \zeta}
\end{aligned}$$

$$\begin{aligned}
& - \left[\bar{x}_{j-1/2} \right] \left(\frac{\mu_{1,j} + \mu_{1,j-1}}{Pr_{1,j} + Pr_{1,j-1}} + \frac{\mu_{T1,j} + \mu_{T1,j-1}}{Pr_{T1,j} + Pr_{T1,j-1}} \right) \\
& \quad \left[\zeta_{y j-1/2} \right] \left[\frac{(H_{1,j} - H_{1,j-1})^{n+1}}{\Delta \zeta} \right] \\
& - \left\{ \left[\frac{\mu_{1,j} + \mu_{1,j-1}}{2} \left(1 - \frac{2}{Pr_{1,j} + Pr_{1,j-1}} \right) + \frac{\mu_{T1,j} + \mu_{T1,j-1}}{2} \left(1 - \frac{2}{Pr_{T1,j} + Pr_{T1,j-1}} \right) \right] \right. \\
& \quad \left. \left(\frac{U_{1,j} - U_{1,j-1} + u_p}{2} \right)^{n+1} \right\} \left(\zeta_{y j-1/2} \right) \left(\frac{U_{1,j} - U_{1,j-1}}{\Delta \zeta} \right)^{n+1} \\
& + \left[(P_1)^{n+1} - (P_1)^n + (\lambda_{t1} + \lambda_{z1} (U_{1,j} + u_p))^{n+1} \right] \left[\frac{(P_{1,j})^{n+1} - (P_{1-1,j})^{n+1}}{\Delta \lambda} \right]
\end{aligned} \tag{B.21}$$

Static Enthalpy

$$(H1_{1,j})^{n+1} = (H_{1,j})^{n+1} - \frac{((U_{1,j} + u_p)^{n+1})^2}{2} \tag{B.22}$$

Gas Properties

$$(T_{1,j})^{n+1} = T((H1_{1,j})^{n+1}) \tag{B.23}$$

Equation of State

$$(P_{1,j})^{n+1} = (\rho_{1,j})^{n+1} * R_{cg} * (T_{1,j})^{n+1} \tag{B.24}$$

The subscript (i) refers to the axial location of a computational grid point. This subscript (i) ranges from i=1 to i=IL, where IL is the number of axial grid points.

The subscript (j) refers to the radial location of a computational grid point. This subscript (j) ranges from j=1 to j=JL, where JL is the number of radial grid points.

The solution to the finite difference equations is obtained by marching in time. For a given time, calculations sweep in the λ direction, from the projectile to the breech. This is in the same direction as the flow, propagating information to the next i-station. At a give i-station,

unknowns in the finite difference equations occur at the $(j-1)$, (j) , and $(j+1)$ gridpoints.

The continuity, energy, static enthalpy, and gas property equations and the ideal gas equation of state are all linear and can be efficiently solved on a digital computer. However, the momentum equation is non-linear in calculation velocity (U) at the gridpoint (i,j) . To efficiently solve the momentum equation on a digital computer, this $(U_{i,j})^2$ term must be linearized. Newton linearization is used. The resulting linearized momentum equation is:

$$\begin{aligned}
 & \left[\frac{(\rho_{i,j})^{n+1}}{\Delta t} \right] \left[(U_{i,j})^{n+1} - (U_{i,j})^n + (u_{p1,j})^{n+1} - (u_{p1,j})^n \right] \\
 & + \left[\frac{(\rho_{i,j})^{n+1}}{\Delta \lambda} \right] \left[(\lambda_{t1} + \lambda_{z1} u_p)^{n+1} \right] \left[(U_{i,j})^{n+1} - (U_{i-1,j})^{n+1} \right] \\
 & + \left[\frac{(\rho_{i,j})^{n+1}}{\Delta \lambda} \right] \left[(\lambda_{z1})^{n+1} \right] \left[-(\hat{U}_{i,j})^{n+1} - (2U_{i,j} \hat{U}_{i,j})^{n+1} + (U_{i,j} U_{i-1,j})^{n+1} \right] \\
 & - \left[\frac{(\rho_{i,j} v_{i,j})^{n+1}}{2 \Delta \zeta} \right] \left[\zeta_{y,j} \right] \left[(U_{i+1,j} - U_{i-1,j})^{n+1} \right] \\
 & = \frac{\zeta_{y,j}}{\Delta \zeta r_j} \left[(r_{j+1/2}) \left(\frac{\mu_{1,j+1} + \mu_{1,j}}{2} + \frac{\mu_{T1,j+1} + \mu_{T1,j}}{2} \right) \zeta_{y,j+1/2} \frac{(u_{1,j+1} - u_{1,j})^{n+1}}{\Delta \zeta} \right. \\
 & \quad \left. (r_{j-1/2}) \left(\frac{\mu_{1,j} + \mu_{1,j-1}}{2} + \frac{\mu_{T1,j} + \mu_{T1,j-1}}{2} \right) \zeta_{y,j-1/2} \frac{(u_{1,j} - u_{1,j-1})^{n+1}}{\Delta \zeta} \right] \\
 & - \left[\frac{(\lambda_{z1})^{n+1}}{\Delta \lambda} \right] \left[(P_i - P_{i-1})^{n+1} \right]
 \end{aligned} \tag{B.25}$$

Here $\hat{U}_{1,j}$ is the predicted value of calculation velocity, taken to be $U_{1,j}$ from the most recent iteration. The use of Newton linearization for the $(U_{1,j})^2$ term of the momentum equation necessitates the use of iteration in obtaining a solution at a given i -station. Since small time steps are taken, the solution should change only slightly from one time step to the next. The iteration procedure starts with values of T , u , p , and v from the most recent time step. The projectile acceleration and increase in chamber length require adjustment of the calculation variables H and U . To use the temperature from the most recent time step as an initial guess to the solution of stagnation enthalpy:

$$\begin{aligned}
 (H_{1,j})^{n+1} &\approx (H_{1,j})^n \\
 \left(H_{1,j} - \frac{(U_{1,j} + u_p)^2}{2} \right)^{n+1} &\approx \left(H_{1,j} - \frac{(U_{1,j} + u_p)^2}{2} \right)^n \\
 (H_{1,j})^{n+1} &\approx (H_{1,j})^n - \left(\frac{(U_{1,j} + u_p)^2}{2} \right)^n + \left(\frac{(U_{1,j} + u_p)^2}{2} \right)^{n+1} \quad (B.26)
 \end{aligned}$$

To use the axial velocity from the most recent time step as an initial guess to the solution of the calculation velocity:

$$\begin{aligned}
 (u_{1,j})^{n+1} &\approx (u_{1,j})^n \\
 (U_{1,j} - u_p)^{n+1} &\approx (U_{1,j} - u_p)^n \\
 (U_{1,j})^{n+1} &\approx (U_{1,j})^n + (u_p)^{n+1} - (u_p)^n \quad (B.27)
 \end{aligned}$$

The energy equation is solved for stagnation enthalpy (H). All other variables are assumed known:

$$[A] (H_{1,j-1})^{n+1} + [B] (H_{1,j})^{n+1} + [C] (H_{1,j+1})^{n+1} = [D] \quad (B.28)$$

$$\text{where: } [A] = \left[\frac{(\rho_{1,j} V_{1,j})^{n+1}}{2\Delta\zeta} \right] \zeta_{y,j}$$

$$- \left[\frac{r_{j-1/2}}{r_j} \right] \left[\frac{\zeta_{y,j} \zeta_{y,j-1/2}}{(\Delta\zeta)^2} \right] \left[\frac{\mu_{1,j} + \mu_{1,j-1}}{Pr_{1,j} + Pr_{1,j-1}} + \frac{\mu_{T1,j} + \mu_{T1,j-1}}{Pr_{T1,j} + Pr_{T1,j-1}} \right]$$

$$[B] = \left[\frac{(\rho_{1,j})^{n+1}}{\Delta\tau} \right] + \left[\frac{(\rho_{1,j})^{n+1}}{\Delta\lambda} \right] \left[(\lambda_{t1} + \lambda_{z1} (U_{1,j} + u_p))^{n+1} \right]$$

$$+ \left[\frac{(\rho_{1,j} V_{1,j})^{n+1}}{2\Delta\zeta} \right] \zeta_{y,j}$$

$$- \left[\frac{r_{j+1/2}}{r_j} \right] \left[\frac{\zeta_{y,j} \zeta_{y,j+1/2}}{(\Delta\zeta)^2} \right] \left[\frac{\mu_{1,j+1} + \mu_{1,j}}{Pr_{1,j+1} + Pr_{1,j}} + \frac{\mu_{T1,j+1} + \mu_{T1,j}}{Pr_{T1,j+1} + Pr_{T1,j}} \right]$$

$$+ \left[\frac{(\rho_{1,j} V_{1,j})^{n+1}}{2\Delta\zeta} \right] \zeta_{y,j}$$

$$- \left[\frac{r_{j-1/2}}{r_j} \right] \left[\frac{\zeta_{y,j} \zeta_{y,j-1/2}}{(\Delta\zeta)^2} \right] \left[\frac{\mu_{1,j} + \mu_{1,j-1}}{Pr_{1,j} + Pr_{1,j-1}} + \frac{\mu_{T1,j} + \mu_{T1,j-1}}{Pr_{T1,j} + Pr_{T1,j-1}} \right]$$

$$[C] = - \left[\frac{(\rho_{1,j} V_{1,j})^{n+1}}{2\Delta\zeta} \right] \zeta_{y,j}$$

$$- \left[\frac{r_{j+1/2}}{r_j} \right] \left[\frac{\zeta_{y,j} \zeta_{y,j+1/2}}{(\Delta\zeta)^2} \right] \left[\frac{\mu_{1,j+1} + \mu_{1,j}}{Pr_{1,j+1} + Pr_{1,j}} + \frac{\mu_{T1,j+1} + \mu_{T1,j}}{Pr_{T1,j+1} + Pr_{T1,j}} \right]$$

$$\begin{aligned}
[D] = & \left[\frac{(p_{1,j})^{n+1}}{\Delta \tau} \right] (H_{1,j})^n \\
& + \left[(p_{1,j})^{n+1} \right] \left[\frac{(\lambda_{t1} + \lambda_{z1} (U_{1,j} + u_p))^{n+1}}{\Delta \lambda} \right] (H_{1-1,j})^{n+1} \\
& + \left[\left(\frac{\mu_{1,j+1} + \mu_{1,j}}{2} \right)^{1-\frac{2}{Pr_{1,j+1} + Pr_{1,j}}} \right. \\
& \quad * \left(\frac{\mu_{T1,j+1} + \mu_{T1,j}}{2} \right)^{1-\frac{2}{Pr_{T1,j+1} + Pr_{T1,j}}} \\
& \quad * \frac{(U_{1,j+1} - U_{1,j} + u_p)^{n+1}}{2} \zeta_{y_{j+1/2}} \frac{(U_{1,j+1} - U_{1,j})^{n+1}}{\Delta \zeta} \\
& + \left[\left(\frac{\mu_{1,j} + \mu_{1,j-1}}{2} \right)^{1-\frac{2}{Pr_{1,j} + Pr_{1,j-1}}} \right. \\
& \quad * \left(\frac{\mu_{T1,j} + \mu_{T1,j-1}}{2} \right)^{1-\frac{2}{Pr_{T1,j} + Pr_{T1,j-1}}} \\
& \quad * \frac{(U_{1,j} - U_{1,j-1} + u_p)^{n+1}}{2} \zeta_{y_{j-1/2}} \frac{(U_{1,j} - U_{1,j-1})^{n+1}}{\Delta \zeta} \\
& + \left[(\lambda_{t1} + \lambda_{z1} (U_{1,j} + u_p))^{n+1} \right] \left[\frac{(p_{1,j})^{n+1} - (p_{1-1,j})^{n+1}}{\Delta \lambda} \right] \\
& + \left[\frac{(p_1)^{n+1} - (p_1)^n}{\Delta \tau} \right]
\end{aligned}$$

The values of H at the wall and boundary layer edge are known. A coupled set of equations results for H which is efficiently solved using a Thomas algorithm matrix solver.

The linearized momentum equation is solved for calculation velocity (U). All other variables are assumed known:

$$[A] (U_{1,j-1})^{n+1} + [B] (U_{1,j})^{n+1} + [C] (U_{1,j+1})^{n+1} = [D] \quad (B.29)$$

$$\text{where: } [A] = \left[\frac{(p_{1,j-1} V_{1,j-1})^{n+1} \zeta_{y_{j-1/2}}}{2 \Delta \zeta} \right]$$

$$\begin{aligned}
& - \left[\frac{r_{j-1/2}}{r_j} \right] \left[\frac{\zeta_{y_j} \zeta_{y_{j-1/2}}}{(\Delta \zeta)^2} \right] \left(\frac{\mu_{1,j} + \mu_{1,j-1}}{2} + \frac{\mu_{T1,j} + \mu_{T1,j-1}}{2} \right) \\
[B] & = \left[\frac{(\rho_{1,j})^{n+1}}{\Delta \tau} \right] + \left[\frac{(\rho_{1,j})^{n+1}}{\Delta \lambda} (\lambda_{t1} + \lambda_{z1} u_p)^{n+1} \right] \\
& + \left[\frac{(\rho_{1,j} \lambda_{z1})^{n+1}}{\Delta \lambda} \right] (2(\hat{u}_{1,j})^{n+1} - (\hat{u}_{1-1,j}^2)^{n+1}) \\
& - \left[\frac{r_{j+1/2}}{r_j} \right] \left[\frac{\zeta_{y_j} \zeta_{y_{j+1/2}}}{(\Delta \zeta)^2} \right] \left(\frac{\mu_{1,j+1} + \mu_{1,j}}{2} + \frac{\mu_{T1,j+1} + \mu_{T1,j}}{2} \right) \\
& + \left[\frac{(\rho_{1,j} v_{1,j})^{n+1}}{2 \Delta \zeta} \right] \zeta_{y_j} \\
& - \left[\frac{r_{j-1/2}}{r_j} \right] \left[\frac{\zeta_{y_j} \zeta_{y_{j-1/2}}}{(\Delta \zeta)^2} \right] \left(\frac{\mu_{1,j} + \mu_{1,j-1}}{2} + \frac{\mu_{T1,j} + \mu_{T1,j-1}}{2} \right) \\
[C] & = - \left[\frac{(\rho_{1,j} v_{1,j})^{n+1}}{2 \Delta \zeta} \right] \zeta_{y_j} \\
& - \left[\frac{r_{j+1/2}}{r_j} \right] \left[\frac{\zeta_{y_j} \zeta_{y_{j+1/2}}}{(\Delta \zeta)^2} \right] \left(\frac{\mu_{1,j+1} + \mu_{1,j}}{2} + \frac{\mu_{T1,j+1} + \mu_{T1,j}}{2} \right) \\
[D] & = \left[\frac{(\rho_{1,j})^{n+1}}{\Delta \tau} \right] ((U_{1,j})^n - (u_p)^{n+1} + (u_p)^n) \\
& + \left[\frac{(\rho_{1,j})^{n+1}}{\Delta \lambda} \right] \frac{(\lambda_{t1} + \lambda_{z1} (U_{1,j} + u_p))^{n+1}}{\Delta \lambda} (U_{1-1,j})^{n+1} \\
& + \left[\frac{(\lambda_{z1})^{n+1}}{\Delta \lambda} \right] \left[\frac{(\rho_{1,j} (U_{1,j})^2)^{n+1} + (P_1)^{n+1} - (P_{1-1})^{n+1}}{\Delta \lambda} \right]
\end{aligned}$$

The values of U at the wall and boundary layer edge are known. A coupled set of equations results for U which is

efficiently solved using a Thomas algorithm matrix solver.

The ideal gas equation of state is solved for density (ρ). All other variables are assumed known:

$$(\rho_{i,j})^{n+1} = \frac{(P_i)^{n+1}}{R_{cg} * (T_{i,j})^{n+1}}$$

The value of density is explicitly found at each grid point. The continuity equation is solved for radial velocity (v). All other variables are assumed known:

$$(v_{i,j})^{n+1} = \left[\frac{r_{j-1} (\rho_{i,j-1} v_{i,j-1})^{n+1}}{r_j (\rho_{i,j})^{n+1}} \right] + \frac{\Delta \zeta}{\zeta_{y,j} (\rho_{i,j})^{n+1}} * \\ \left[\frac{1}{4\Delta t} \begin{bmatrix} (\rho_{i,j})^{n+1} + (\rho_{i-1,j})^{n+1} + (\rho_{i,j-1})^{n+1} + (\rho_{i-1,j-1})^{n+1} \\ -(\rho_{i,j})^n - (\rho_{i-1,j})^n - (\rho_{i,j-1})^n - (\rho_{i-1,j-1})^n \end{bmatrix} \right. \\ \left. + \left[\frac{\lambda_{ti}}{2\Delta \lambda} + \frac{\lambda_{zi} u_p}{\Delta \lambda} \right] \begin{bmatrix} (\rho_{i,j})^{n+1} - (\rho_{i-1,j})^{n+1} \\ + (\rho_{i,j-1})^{n+1} - (\rho_{i-1,j-1})^{n+1} \end{bmatrix} \right. \\ \left. + \left[\frac{\lambda_{zi}}{\Delta \lambda} \right] \begin{bmatrix} (\rho_{i,j} u_{i,j})^{n+1} - (\rho_{i-1,j} u_{i-1,j})^{n+1} \\ + (\rho_{i,j-1} u_{i,j-1})^{n+1} - (\rho_{i-1,j-1} u_{i-1,j-1})^{n+1} \end{bmatrix} \right]$$

The value of v at the wall is known. Other values of v are explicitly found by sweeping from the wall to the tube centerline. The new values of H , U , ρ , and v are used as initial values for the next iteration and the iteration process is repeated until an acceptable solution is obtained. An acceptable solution for the time level $(n+1)$ at the given i -station requires convergence by one of two criteria:

- 1) If the number of iterations for a given station reaches 30, oscillation around the correct answer is assumed. The oscillated values from the two most recent iterations

are averaged to provide the answer at this i-station for this time level.

2) For every variable, at every (i,j) gridpoint:

a) If the absolute value for a variable at a point is less than $1E-4$, then convergence at this point, for this variable, for this time level is met.

or b) If the difference between successive iterations for a variable at a point is less than 00.01%, convergence at this point, for this variable, for this time level is met.

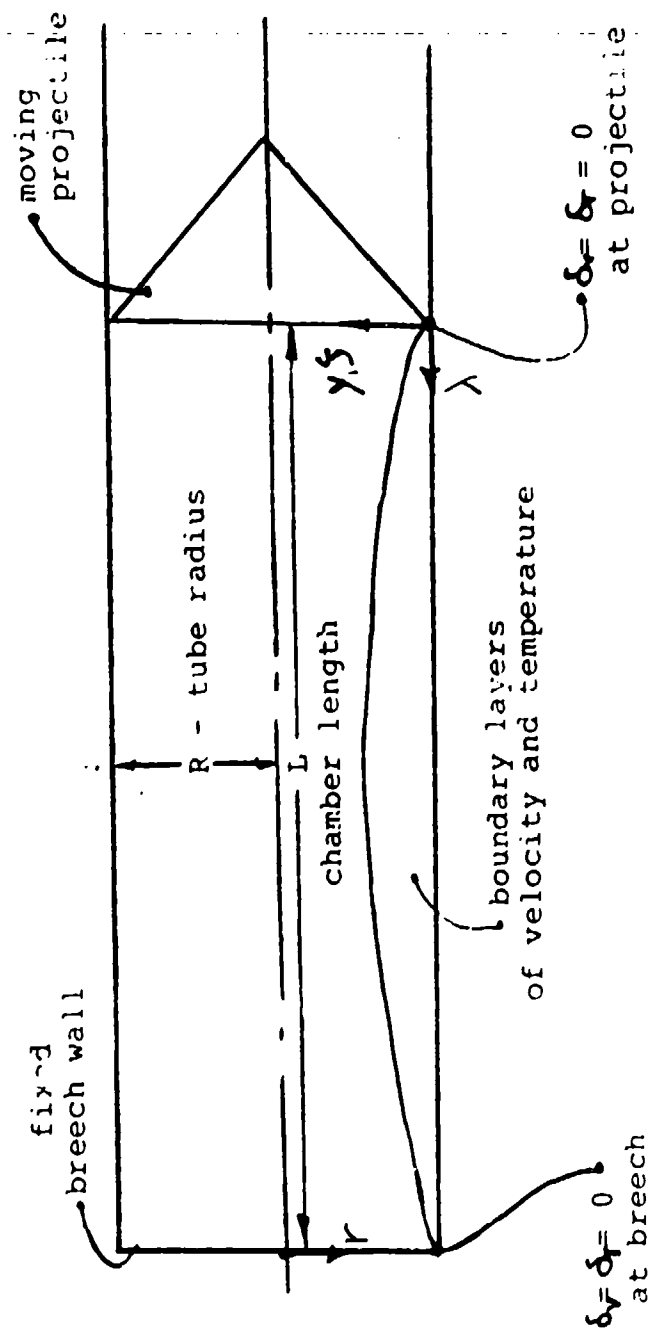


Fig. B.2 Computational coordinate system for the interior ballistic problem

B.3 Boundary Layer Thicknesses

It is difficult to indicate a velocity or thermal boundary layer thickness in a universal way. The influence of viscosity and compressibility of high speed flow in tubes decreases asymptotically from the wall to the centerline. Defining the edge of a boundary layer equates to defining when radial gradients are negligible. For this study, the velocity boundary layer edge is defined to be the first point away from the wall where $u \geq 0.95 * u(\text{core})$. The temperature boundary layer edge is defined to be the first point away from the wall where $T \geq 0.95 * T(\text{core})$. Such definition is arbitrary and varies among problems. There are better parameters which describe the viscous and thermal effects of high speed boundary layer flow in tubes. These parameters are the displacement, momentum, energy, and density thicknesses.

Displacement Thickness

A meaningful measure of the viscous and thermal effects for high speed flow in tubes is the displacement thickness. As shown in Figure B.3, the displacement thickness is a decrease in effective tube radius caused by a mass flux defect. The actual flow containing radial gradients in velocity and density is replaced by an ideal flow of identical mass flux where radial gradients are absent. The resulting change in tube radius, conventionally defined as positive toward the core flow, is the displacement thickness.

The mass flux for the ideal flow is lessened by the decrease in tube radius:

$$\int_{r=R}^{r=R-\delta_1} \rho_e u_e dA \quad \text{where } dA = 2\pi r dr$$

The subscript e refers to the boundary layer edge or core conditions. The loss of mass flux in the boundary layer, as compared with the ideal flow, is given by:

$$\int_{r=R}^{r=R-\delta_v} (\rho_e u_e - \rho u) dA \quad \text{where } dA = 2\pi r dr$$

The integrand of the preceeding integral is zero from $r=R-\delta_v$ to $r=0$. An equivalent expression for the loss of mass flux in the boundary layer, as compared to the ideal flow, is given by:

$$\int_{r=R}^{r=0} (\rho_e u_e - \rho u) dA \quad \text{where } dA = 2\pi r dr$$

Equating the mass flux lost in the ideal flow and the mass flux defect in the actual flow:

$$\int_{r=R}^{r=R-\delta_1} \rho_e u_e 2\pi r dr = \int_{r=R}^{r=0} (\rho_e u_e - \rho u) 2\pi r dr$$

The displacement thickness for compressible viscous flow in tubes is given by:

$$\frac{\delta_1}{R} = 1 - \sqrt{1 + \frac{2}{R^2} \int_{r=R}^{r=0} \left[1 - \frac{\rho u}{\rho_e u_e} \right] r dr}$$

The integral within the equation for displacement thickness was numerically integrated using the trapezoidal rule:

$$\frac{2}{R^2} \int_{r=R}^{r=0} \left[1 - \frac{\rho u}{\rho_e u_e} \right] r dr = \frac{2}{R} \sum_{j=2}^{JL} \left[1 - \frac{\rho_{ave} u_{ave}}{\rho_e u_e} \right] \frac{r_{j-1/2}}{R} (r_j - r_{j-1})$$

where:

$$\rho_{ave} = (\rho_j + \rho_{j-1})/2$$

$$u_{ave} = (u_j + u_{j-1})/2$$

ρ_e = the density along the centerline

u_e = the axial velocity along the centerline

$r_{j-1/2}$ = the radius of the half point between the (j) and (j-1) gridpoints.

$r_j - r_{j-1}$ = the differential change in radius consistent with the limits of integration.

A unit of tube radius R was placed inside the integral to normalize the variable r and reduce computational roundoff error.

Momentum Thickness

The momentum thickness (Fig. B.3) is a measure of the momentum flux defect. The actual flow containing radial gradients in velocity and density is replaced by an ideal flow of identical momentum flux where radial gradients are absent. The resulting change in tube radius, conventionally defined as positive toward the core flow, is the momentum thickness.

The momentum flux for the ideal flow is lessened by the decrease in tube radius:

$$\int_{r=R}^{r=R-\delta_2} \rho_e u_e^2 dA \quad \text{where } dA = 2\pi r dr$$

The loss of momentum flux in the boundary layer, as compared with the ideal flow, is given by:

$$\int_{r=R}^{r=R-\delta_v} \rho u (u_e - u) dA \quad \text{where } dA = 2\pi r dr$$

The integrand of the above integral is zero from $r=R-\delta_v$ to $r=0$. An equivalent expression for the loss of momentum flux in the boundary layer, as compared to the ideal flow, is given by:

$$\int_{r=R}^{r=0} \rho u (u_e - u) dA \quad \text{where } dA = 2\pi r dr$$

Equating the momentum flux lost in the ideal flow and the momentum flux defect in the actual flow:

$$\int_{r=R}^{r=R-\delta_2} \rho_e u_e^2 2\pi r dr = \int_{r=R}^{r=0} \rho u (u_e - u) 2\pi r dr$$

The momentum thickness for compressible viscous flow in tubes is given by:

$$\frac{\delta_2}{R} = 1 - \sqrt{1 + \frac{2}{R^2} \int_{r=R}^{r=0} \left[\frac{\rho u}{\rho_e u_e} \right] \left[1 - \frac{u}{u_e} \right] r dr}$$

The integral within the equation for momentum thickness was numerically integrated using the trapezoidal rule:

$$\frac{2}{R^2} \int_{r=R}^{r=0} \left[\frac{\rho u}{\rho_e u_e} \right] \left[1 - \frac{u}{u_e} \right] r dr$$

$$= \frac{2}{R} \sum_{j=2}^{JL} \left[\frac{\rho_{ave} u_{ave}}{\rho_e u_e} \right] \left[1 - \frac{u_{ave}}{u_e} \right] \frac{r_{j-1/2}}{R} (r_j - r_{j-1})$$

where ρ_{ave} , ρ_e , u_{ave} , and u_e have been previously defined.

Energy Thickness

The energy thickness (Fig B.3) is a decrease in effective tube radius caused by an energy flux defect. The actual flow containing radial gradients in velocity and density is replaced by an ideal flow of identical energy flux where radial gradients are absent. The resulting change in tube radius, conventionally defined as positive toward the core flow, is the energy thickness.

The energy flux for the ideal flow is lessened by the decrease in tube radius:

$$\int_{r=R}^{r=R-\delta_3} \rho_e u_e^3 dA \quad \text{where } dA = 2\pi r dr$$

The loss of energy flux in the boundary layer, as compared with the ideal flow, is given by:

$$\int_{r=R}^{r=R-\delta_v} \rho u (u_e^2 - u^2) dA \quad \text{where } dA = 2\pi r dr$$

The integrand of the above integral is zero from $r=R-\delta_v$ to $r=0$. An equivalent expression for the loss of energy flux in the boundary layer, as compared to the ideal flow, is given by:

$$\int_{r=R}^{r=0} \rho u (u_e^2 - u^2) dA \quad \text{where } dA = 2\pi r dr$$

Equating the energy flux lost in the ideal flow and the energy flux defect in the actual flow:

$$\int_{r=R}^{r=R-\delta_3} \rho_e u_e^3 2\pi r dr = \int_{r=R}^{r=0} \rho u (u_e^2 - u^2) 2\pi r dr$$

The energy thickness for compressible viscous flow in tubes is given by:

$$\frac{\delta_3}{R} = 1 - \sqrt{1 + \frac{2}{R^2} \int_{r=R}^{r=0} \left[\frac{\rho u}{\rho_e u_e} \right] \left[1 - \frac{u^2}{u_e^2} \right] r dr}$$

The integral within the equation for energy thickness was numerically integrated using the trapezoidal rule:

$$\begin{aligned} & \frac{2}{R^2} \int_{r=R}^{r=0} \left[\frac{\rho u}{\rho_e u_e} \right] \left[1 - \frac{u^2}{u_e^2} \right] r dr \\ & \approx \frac{2}{R} \sum_{j=2}^{JL} \left[\frac{\rho_{ave} u_{ave}}{\rho_e u_e} \right] \left[1 - \frac{u_{ave}^2}{u_e^2} \right] \frac{r_{j-1/2}}{R} (r_j - r_{j-1}) \end{aligned}$$

where ρ_{ave} , ρ_e , u_{ave} , and u_e have been previously defined.

Density Thickness

A new useful measure of the thermal effects occurring in a boundary layer is the density thickness. The density thickness (Fig. B.3) is a decrease in effective tube radius caused by a density flux defect. The actual flow containing radial gradients in density is replaced by an ideal flow of identical density flux where radial gradients are absent. The density thickness is the resulting change in tube radius and is defined as positive toward the core flow.

The density flux for the ideal flow is lessened by the decrease in tube radius:

$$\int_{r=R}^{r=R-\delta_v} \rho_e dA \quad \text{where } dA = 2\pi r dr$$

The loss of density flux in the boundary layer, as compared with the ideal flow, is given by:

$$\int_{r=R}^{r=R-\delta_p} (\rho_e - \rho) dA \quad \text{where } dA = 2\pi r dr$$

The integrand of the above integral is zero from $r=R-\delta_v$ to $r=0$. An equivalent expression for the loss of density flux in the boundary layer, as compared to the ideal flow, is given by:

$$\int_{r=R}^{r=0} (\rho_e - \rho) dA \quad \text{where } dA = 2\pi r dr$$

Equating the density flux lost in the ideal flow and the density flux defect in the actual flow:

$$\int_{r=R}^{r=R-\delta_p} \rho_e 2\pi r dr = \int_{r=R}^{r=0} (\rho_e - \rho) 2\pi r dr$$

The density thickness for compressible viscous flow in tubes is given by:

$$\frac{\delta_p}{R} = 1 - \sqrt{1 + \frac{2}{R^2} \int_{r=R}^{r=0} \left[1 - \frac{\rho}{\rho_e} \right] r dr}$$

The integral within the equation for density thickness was numerically integrated using the trapezoidal rule:

$$\frac{2}{R^2} \int_{r=R}^{r=0} \left[1 - \frac{\rho}{\rho_e} \right] r dr \approx \frac{2}{R} \sum_{j=2}^{JL} \left[1 - \frac{\rho_{ave}}{\rho_e} \right] \frac{r_{j-1/2}}{R} (r_j - r_{j-1})$$

where ρ_{ave} and ρ_e have been previously defined.

Effective volume change

The objective of the interior ballistic problem is to accelerate a projectile. This objective is accomplished by the high chamber pressure. The cool tube wall has the effect of increasing the effective chamber volume and decreasing the effective pressure which acts on the projectile. The final result is a decrease in the muzzle exit velocity of the projectile.

The density thickness provides a measure of this effective volume increase. An assumption made of the interior ballistic cycle was that the mass in the chamber was constant. For the proper density flux at any given cross section, the one dimensional model must increase the effective tube radius since density thickness is negative. As the effective volume increases, the effective pressure must decrease, assuming the combustion gas acts as an ideal gas:

$$P * V = m * R * T = \text{constant}$$

For a given time, the percent change in effective volume is given by:

$$\begin{aligned} \frac{V_{new} - V_{old}}{V_{old}} &= \frac{\int \pi (R - \delta_\rho)^2 dx - \int \pi R^2 dx}{\int \pi R^2 dx} \\ &= \frac{\int \pi (R - \delta_\rho)^2 dx - \pi R^2 L}{\pi R^2 L} = \frac{1}{L} \int_0^L \left[1 - \frac{\delta_\rho}{R} \right]^2 dx - 1 \end{aligned}$$

The integral in the last expression was numerically determined using the trapezoidal rule:

$$\frac{1}{L} \int_0^L \left[1 - \frac{\delta_p}{R} \right]^2 dx = \frac{1}{IL-1} \sum_{i=2}^{IL} \left[1 - \frac{\delta_{p_{ave}}}{R} \right]^2 \frac{L}{(IL-1)}$$

where $\delta_{p_{ave}} = (\delta_{p_i} + \delta_{p_{i-1}}) / 2$

B.4 K Factors

The work of Chapter 4 modelled the interior ballistic problem as one-dimensional. In this model, integral averages over a cross sectional area remove radial dependence, so that mass, momentum, and energy are only axially dependent. To study the validity of this one-dimensional model, three ratios are examined:

$$K_{\rho u} = \frac{[1/A \int \rho u \, dA]}{[1/A \int \rho \, dA] [1/A \int u \, dA]}$$

$$K_{\rho u^2} = \frac{[1/A \int \rho u^2 \, dA]}{[1/A \int \rho \, dA] [1/A \int u^2 \, dA]}$$

$$K_{eu} = \frac{[1/A \int e u \, dA]}{[1/A \int e \, dA] [1/A \int u \, dA]}$$

where e is the total energy:

$$e = \rho(u(T) + 0.5u^2) = \rho \left[\frac{h - P}{\rho} + 0.5u^2 \right]$$

The pressure P is assumed independent of the radial coordinate and can be removed from within the respective integrals. Simplifying $K_{\rho u}$:

$$K_{eu} = \frac{[1/A \int \rho h u \, dA] + [P/A \int u \, dA] + [1/2A \int u^3 \, dA]}{[1/A \int \rho h \, dA - P + 1/2A \int u^2 \, dA] [1/A \int u \, dA]}$$

If $K_{\rho u}$, $K_{\rho u^2}$, K_{eu} are close to unity, the one-dimensional model is good. The interior ballistic cycle occurs in an axisymmetric tube, so that $A = \pi R^2$, $dA = 2\pi r dr$, and the limits of integration go from the centerline ($r=0$) to the tube wall ($r=R$).

The numerical integrations used the trapezoidal rule:

$$K_{pu} = \frac{R^2}{2} \frac{\left[\sum_{j=2}^{JL} \rho_{ave} u_{ave} r_{j-1/2} (r_j - r_{j-1}) \right]}{\left[\sum_{j=2}^{JL} \rho_{ave} r_{j-1/2} (r_j - r_{j-1}) \right] \left[\sum_{j=2}^{JL} u_{ave} r_{j-1/2} (r_j - r_{j-1}) \right]}$$

$$K_{pu^2} = \frac{R^2}{2} \frac{\left[\sum_{j=2}^{JL} \rho_{ave} u_{ave}^2 r_{j-1/2} (r_j - r_{j-1}) \right]}{\left[\sum_{j=2}^{JL} \rho_{ave} r_{j-1/2} (r_j - r_{j-1}) \right] \left[\sum_{j=2}^{JL} u_{ave}^2 r_{j-1/2} (r_j - r_{j-1}) \right]}$$

$$K_{eu} = \frac{R^2}{2} \frac{\left[\sum_{j=2}^{JL} \rho_{ave} h_{ave} u_{ave} r_{j-1/2} (r_j - r_{j-1}) \right.}{\left[\sum_{j=2}^{JL} \rho_{ave} h_{ave} r_{j-1/2} (r_j - r_{j-1}) \right.} \frac{\left. P \sum_{j=2}^{JL} u_{ave} r_{j-1/2} (r_j - r_{j-1}) + 1 \sum_{j=2}^{JL} u_{ave}^3 r_{j-1/2} (r_j - r_{j-1}) \right]}{\left. + 1 \sum_{j=2}^{JL} u_{ave}^2 r_{j-1/2} (r_j - r_{j-1}) \right.} \left. - P * R^2 / 2 \right]$$

where ρ_{ave} , ρ_e , u_{ave} , and u_e have been previously defined. The variable h_{ave} is defined to be $(h_j + h_{j-1})/2$. The differential change in radius $(r_j - r_{j-1})$ is consistent with the limits of integration.

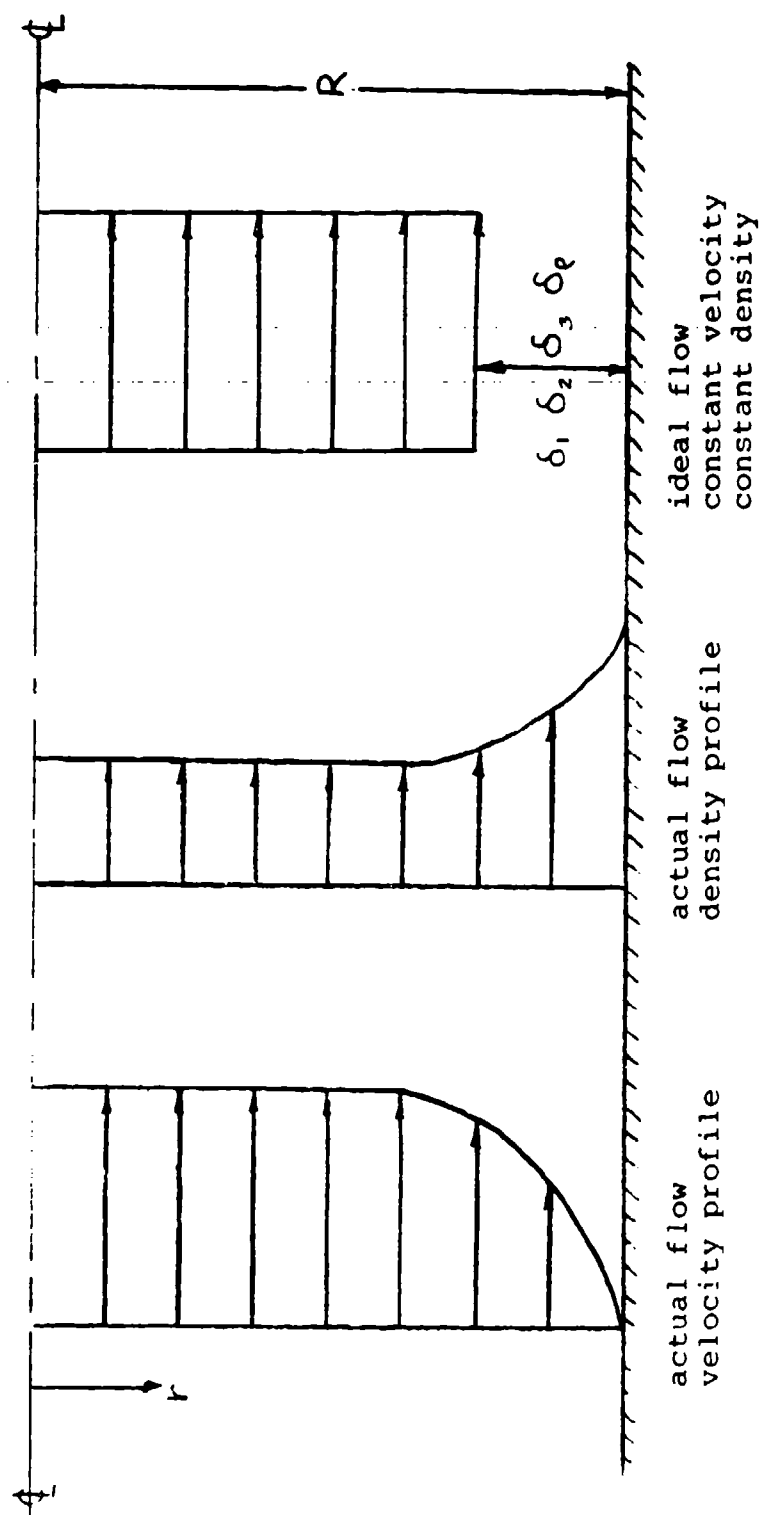


Fig. B.3 Illustration of displacement thickness, momentum thickness, energy thickness, and density thickness for high speed compressible flow in tubes.

APPENDIX C SIMPLIFIED ANALYSIS OF PRESSURE AND DENSITY GRADIENTS

Unsteady Equations of Motion

The flow of the combustion gas behind the projectile during the interior ballistic cycle was modeled using the one dimensional conservation equation of mass and momentum.

$$\frac{\partial}{\partial t} (\rho_s (1-v') + \rho v') + \frac{\partial}{\partial x} (\rho_s (1-v') u_s + \rho v' u) = 0 \quad (C.1)$$

$$\frac{\partial}{\partial t} (u_s \rho_s (1-v') + u \rho v') + \frac{\partial}{\partial x} (u_s^2 \rho_s (1-v') + u^2 \rho v') = - \frac{\partial P}{\partial x} \quad (C.2)$$

The flow is composed of solids, s, and gas. The acceleration and velocity are assumed to be related by the ratio u_s/u . Several mean densities are defined for use in equations D.1 and D.2.

$$\rho_m = \rho_s (1-v') + \rho v'$$

$$\rho_{m1} = \rho_s (1-v') u_s/u + \rho v'$$

$$\rho_{m2} = \rho_s (1-v') u_s^2/u^2 + \rho v'$$

For typical values of ρ_m and u_s/u , ρ_{m2}/ρ_{m1} was approximately equal to ρ_{m1}/ρ_m . Substituting the mean density definitions and ratios into C.1 and C.2 gives C.3 and C.4.

$$\frac{\partial}{\partial t} (\rho_m) + \frac{\partial}{\partial x} \left(\frac{\rho_{m1}}{\rho_m} \rho_m u \right) = 0 \quad (C.3)$$

$$\frac{\partial}{\partial t} \left(\frac{\rho_{m1}}{\rho_m} \rho_m u \right) + \frac{\partial}{\partial x} \left(\left(\frac{\rho_{m1}}{\rho_m} \right)^2 \rho_m u^2 \right) = - \frac{\partial p}{\partial x} \quad (C.4)$$

The two left hand terms of C.4 were expanded.

$$\begin{aligned} \rho_m \frac{\partial}{\partial t} \left(\frac{\rho_{m1}}{\rho_m} u \right) + \frac{\rho_{m1}}{\rho_m} u \frac{\partial \rho_m}{\partial t} + \frac{\rho_{m1}}{\rho_m} \rho_m u \frac{\partial}{\partial x} \left(\frac{\rho_{m1}}{\rho_m} u \right) \\ + \frac{\rho_{m1}}{\rho_m} u \frac{\partial}{\partial x} \left(\frac{\rho_{m1}}{\rho_m} \rho_m u \right) = - \frac{\partial p}{\partial x} \end{aligned} \quad (C.5)$$

The second and fourth terms were eliminated by subtracting $\rho_{m1}u/\rho_m$ times equation C.3.

$$\rho_m \frac{\partial}{\partial t} \left(\frac{\rho_{m1}}{\rho_m} u \right) + \rho_m u \frac{\partial}{\partial x} \left(\frac{\rho_{m1}}{\rho_m} u \right) = - \frac{\partial p}{\partial x} \quad (C.6)$$

ρ_{m1}/ρ_m was assumed to vary slowly with time so it can be brought outside the derivative.

$$\frac{\rho_{m1}}{\rho_m} \left(\frac{\partial u}{\partial t} + \frac{\partial}{\partial x} \left(\frac{\rho_{m1}}{\rho_m} \right)^2 \frac{u^2}{2} \right) = - \frac{1}{\rho_m} \frac{\partial p}{\partial x} \quad (C.7)$$

Equation (C.7) was integrated in the x direction from breech ($x=0$, $u=0$) to an arbitrary location downstream.

$$\frac{\rho_{m1}}{\rho_m} \int_0^x \frac{\partial u}{\partial t} dx + \left(\frac{\rho_{m1} u}{\rho_m} \right)^2 \frac{1}{2} \Big|_x = - \int_{p_b}^p \frac{dp}{\rho_m} \quad (C.8)$$

The left hand side of the equation represents the acceleration of the gases. The first term in the instantaneous acceleration and the second

is the convective acceleration. In steady flows the second term drives the pressure drop given by the right hand side.

Acceleration of the Gases and Solids

The acceleration of the solids and gases (left hand side of C.8) causes the pressure to drop from breech to projectile and is related to the piston acceleration. The velocity of the gas is approximated as $u = u_p x/L$ based on numerical simulations of this and other work. After the first one third of the ballistic cycle, the velocity distribution is very linear.

The coordinate $\xi = x/L$ was used along with the following coordinate stretching function.

$$\frac{\partial}{\partial t} = \frac{\partial}{\partial \tau} - \frac{\xi u_p}{L} \frac{\partial}{\partial \xi} \quad (C.9)$$

It was applied to the time derivative of term in equation C.8.

$$\frac{\rho_{m1}}{\rho_m} \int_0^x \left(\frac{\partial u}{\partial \tau} - \frac{\xi u_p}{L} \frac{\partial u}{\partial \xi} \right) dx + \left(\frac{\rho_{m1} u^2}{\rho_m} \right) \frac{1}{2} \Big|_x = - \int_{P_b}^P \frac{1}{\rho_m} \frac{dP}{dx} \quad (C.10)$$

Using $u = u_p \xi$, $x = L\xi$, and $a_p = \partial u_p / \partial t$ the acceleration term (left hand side of C.10) was tied to the piston acceleration and velocity.

$$\left[\frac{\rho_{m1}}{\rho_m} \frac{L a_p}{2} + \frac{u_p^2}{2} \left(\left(\frac{\rho_{m1}}{\rho_m} \right)^2 - \left(\frac{\rho_{m1}}{\rho_m} \right) \right) \right] \xi^2 = - \int_{P_b}^P \xi \frac{dP}{\rho_m} \quad (C.11)$$

$$\text{or } \frac{L a_p}{2} \xi^2 = - \int_{P_b}^P \xi \frac{dP}{\rho_m} \quad (C.12)$$

When combustion is complete, $\rho_{m1}/\rho_m = 1$ and a_p^* is the acceleration of the projectile, a_p . If the projectile were accelerated from zero to a_p over a distance L , it would have the kinetic energy $m_p U_p^2/2$. The energy to accelerate it would be force times distance, $m_p(a_p/2)L$. This then means that $a_p L/2 = U_p^2/2$.

The pressure drop from breech to projectile is then controlled by the projectile acceleration. This is logical because it is the expansion waves behind the accelerating projectile which lower the pressure.

The solids affect the acceleration term in equation B.11 through ρ_{m1}/ρ_m . ρ_{m1}/ρ_m becomes less than one when u_s/u is less than one.

The assumption was made that $u_s/u = \bar{a}_s/\bar{a}_g$. The solids are accelerated by the drag forces of the faster gas. The drag force on the grain was estimated assuming it to be a cylinder in cross flow.

$$\text{Drag} = C_D \rho (u^2 - u_s^2) 2rL/2 \quad (C.13)$$

This force accelerates the grain where ρ'_s is the average density of the grain including its gas filled perforations.

$$\begin{aligned} \pi r_o^2 L \rho'_s a_s &= C_D \rho (u^2 - u_s^2) 2r_o L/2 \\ \text{or } a_s &= \frac{C_D u^2 (1 - (\frac{u_s}{u})^2)}{\pi r_o} \frac{\rho}{\rho'_s} \end{aligned} \quad (C.14)$$

The gas velocity was assumed as $u = U_p \xi$. The solids velocity, u_s , was assumed to be related to u . The spatial averages of the solids and gas accelerations were obtained.

$$\int_0^1 a_s d\xi = \frac{C_D (1 - (\frac{u_s}{u})^2) \rho}{\pi r_o \rho'_s} u_p \int_0^1 \xi^2 d\xi \quad (C.15)$$

$$\bar{a}_s = \frac{u_p^2 C_D (1 - (\frac{u_s}{u})^2) \rho}{3\pi r_o \rho'_s} \quad (C.15)$$

$$\int_0^1 a_g d\xi = \int_0^1 a_p \xi d\xi$$

$$\bar{a}_g = \frac{a_p}{2} \quad (C.16)$$

$$\frac{\bar{a}_s}{\bar{a}_g} = \frac{u_p^2 C_D (1 - (\frac{u_s}{u})^2) \rho (2)}{3\pi r_o \rho'_s a_p} = \frac{u_s}{u} \quad (C.17)$$

C.17 was solved for u_s/u in terms of Fa an acceleration ratio.

$$\frac{u_s}{u} = 1 + \frac{1}{2Fa} (1 - \sqrt{4Fa + 1}) \quad (C.18)$$

$$Fa = \frac{2C_D \rho u_p^2}{3\pi r_o \rho'_s a_p}$$

Pressure Distribution

The acceleration of solids and gas in equation C.12 causes the pressure to drop from breech to projectile.

$$\frac{La_p^*}{2} \xi^2 = - \int_{P_b}^P \xi \frac{dP}{\rho_m} \quad (C.12)$$

Assuming $\rho_m = \rho$ and $P = p^Y$ constant allowed integration of the right hand side.

$$\frac{La_p^*}{2} \xi^2 = \frac{\gamma}{(\gamma-1)} \frac{P_b}{\rho_b} \left(1 - \left(\frac{P_\xi}{P_b}\right)^{\frac{\gamma-1}{\gamma}}\right) \quad (C.19)$$

The equation of state was used to replace P_b/ρ_b .

$$P/\rho = RT / (1-pn) \quad (C.20)$$

$$\frac{La_p^*}{2} \xi^2 = \frac{\gamma R T_b}{(\gamma-1)(1-\rho_b n)} \left(1 - \left(\frac{P_\xi}{P_b}\right)^{\frac{\gamma-1}{\gamma}}\right) \quad (C.21)$$

or

$$\frac{P_\xi}{P_b} = \left(1 - \frac{(\gamma-1)(1-\rho_b n) La_p^* \xi^2}{\gamma R T_b}\right)^{\frac{\gamma}{\gamma-1}} \quad (C.22)$$

$\rho_m = \rho_s(1-v') + v'\rho$ and $P = \rho^\gamma C$ were assumed and C.12 was integrated.

$$\frac{La_p^*}{2} \xi^2 = - \int_{P_b}^{P_\xi} \frac{dP}{\rho_s(1-v') + v'\rho} \quad (C.23)$$

$$\frac{La_p^*}{2} \xi^2 = - \frac{P_b}{\rho_b v'} \int_{P_b}^{P_\xi} \frac{d\left(\frac{P}{P_b}\right)}{\frac{\rho_s(1/v'-1)}{\rho_b} + \left(\frac{P}{P_b}\right)^{1/\gamma}} \quad (C.18)$$

$(P/P_b)^{1/\gamma}$ was linearized as $1 + (P/P_b - 1)/\gamma$ and equation (5.18) was integrated.

$$\frac{La_p^*}{2} \xi^2 = \frac{\gamma R T_b}{v'(1-\rho_b n)} \ln \left[1 / \left(1 + \left(\frac{P_\xi}{P_b} - 1\right) / (\gamma(\rho_s(1/v'-1)/\rho_b + 1))\right)\right] \quad (C.25)$$

or

$$\frac{P_\xi}{P_b} = 1 + \gamma \left(\frac{\rho_s(1/v'-1)}{\rho_b} + 1\right) \left[\exp\left(\frac{-v'(1-\rho_b n) La_p^* \xi^2}{2\gamma R T_b}\right) - 1\right] \quad (C.26)$$

P_{ave}/P_o was obtained by integrating equation 5.20.

$$\frac{P_{ave}}{P_b} = \int_0^1 \left[1 + \gamma \left(\frac{\rho_s(1/v'-1)}{\rho_b} + 1\right) \left[\exp\left(\frac{-v'(1-\rho_b n) La_p^* \xi^2}{2\gamma R T_b}\right) - 1\right]\right] d\xi$$

$$\frac{P_{ave}}{P_b} = \int_0^1 [1 + K_1 (\exp(-K_2 \xi^2) - 1)] d\xi$$

$$K_1 = \left(\frac{\rho_s (1/v' - 1)}{\rho_b} + 1 \right) \gamma$$

$$K_2 = \frac{v' (1 - \rho_b N) La^*}{2 \gamma R T_b} \cdot \frac{p}{p_0}$$

The exponential term is expanded in a series to facilitate integration

$$\frac{p_{ave}}{p_0} = 1 - K_1 \left(-\frac{K_2}{3} + \frac{K_2^2}{10} - \frac{K_2^3}{42} + \frac{K_2^4}{216} - \frac{K_2^5}{1320} \right) \quad (C.27)$$

Kinetic Energy in Gas and Solids

The ratio of the density of the gas-solid mixture times $u_p^2/2$ divided by the kinetic energy of the gas is δ .

$$\delta = \frac{\frac{u_p^2}{2} a_c L \int_0^1 \rho_\xi d\xi}{a_c L \int_0^1 \left(\rho_s (1 - v') \frac{u_s^2}{2} + v' \frac{\rho u^2}{2} \right) d\xi} \quad (C.28)$$

u_s was assumed as a fraction of u , $u = u_p \xi$. The density ratio distribution was approximated as parabolic, $\rho_\xi / \rho_b = 1 - (1 - \frac{\rho_p}{\rho_b}) \xi^2$. Integrating gave

$$\delta = 3 \frac{\frac{\rho_s (1 - v')}{\rho_b v'} + (1 - \frac{\rho_p}{3\rho_b})}{\frac{\rho_s (1 - v')}{\rho_b v'} \left(\frac{u_s}{u} \right)^2 + (1 - \frac{3\rho_p}{5\rho_b})} \quad (C.29)$$

When there are no solids, $v' = 1$ and C.23 becomes C.24.

$$\delta = \frac{3(1 - \frac{\rho_p}{3\rho_b})}{(1 - \frac{3}{5} \frac{\rho_p}{\rho_b})} \quad (C.30)$$

END

7-87

DTIC